

Nanoscopy in nonlinear scanning fluorescence imaging systems

THÈSE N° 6905 (2016)

PRÉSENTÉE LE 11 MARS 2016

À LA FACULTÉ DES SCIENCES ET TECHNIQUES DE L'INGÉNIEUR

LABORATOIRE D'OPTIQUE

PROGRAMME DOCTORAL EN BIOTECHNOLOGIE ET GÉNIE BIOLOGIQUE

ÉCOLE POLYTECHNIQUE FÉDÉRALE DE LAUSANNE

POUR L'OBTENTION DU GRADE DE DOCTEUR ÈS SCIENCES

PAR

Grégoire Pierre Jean LAPORTE

acceptée sur proposition du jury:

Prof. B. Deplancke, président du jury

Prof. D. Psaltis, directeur de thèse

Prof. R. Grange, rapporteuse

Dr C. Sheppard, rapporteur

Prof. A. Radenovic, rapporteuse



ÉCOLE POLYTECHNIQUE
FÉDÉRALE DE LAUSANNE

Suisse
2016

Acknowledgements

The main part of this work has been done in the Optics Laboratory of EPFL under the supervision of Professor D. Psaltis. I would like to express my gratitude to him for giving me the opportunity to work in such a great research environment. I also would like to thank him for his ideas, advises and guidance without which the completion of this thesis would not have been possible.

Also I would like to thank Professor C. Sheppard and Professor R. Piestun for their contribution on my PhD thesis. I had the opportunity to collaborate with each of them. I would like to thank each of them for their constructive criticisms and helpful discussions.

The beginning of this project has been tumultuous. It was initially centered on the protein-DNA interaction analysis with high-resolution optical imaging of fluorescence proteins. After major difficulties with the stability of stretched DNA molecules in microfluidic channels, I focused my research on the imaging methods. Nevertheless, I would like to thank very especially Prof. B. Deplancke. He was one of the project initiator, gave me full access to his lab and allow me to discover the basics of genetics research for more than one year. Even during hard times, he supported me, encouraged me and let me chose the best for the progress of my PhD. I wish our collaboration could have been more fruitful, however, thanks to him, my future projects will probably have a flavor of biology.

I also would like to address a special thanks to Carole Berthet that with her patience and proficiency make our everyday life easier.

Special thanks also to Nicolino Stasio and Donald Conkey that helped me more than their contributions to the papers we published together. I had with them, Yannis Papadopoulos and Alexandre Goy fruitful exchanges about science and also a true friendly relationship. Thank you also to Andreas Vasdekis for his precious help and his strong support at the beginning of this project.

Some images presented in this thesis have been acquired in the Bioimaging facility. I would like to thank all the BIOP team for their kindness and their expertise, especially Romain Guet for his help with the cell sample preparation.

I would like to mention all the member of the Laboratory of Optics, past and present: Ye Pu, (thank you for his patience to answer my questions, it was a great help all along my PhD), Rachel Grange (thank you for giving me the opportunity to discover Optics Laboratory during my Master project and giving the first insight about Swiss culture), Chia-Lung Hsieh (thank you for his disponibility and advises in nonlinear optics), Salma Fahari (thanks for her advises and cheerfulness), Laurent Decloux (thank you for his help with Labview codes), Marcin Zielinski, Jae-Woo Choi, Miguel Modestino, Julien Cuennet, Xin Yang, Thomas Lanvin, Mohammad Hashemi, Wuzhou Song, Marilisa Romito and Mortesa Hashani Shoreh. Finally, thanks to all LAPD team for their joy of living and the good atmosphere in the building.

Lausanne, November the 5th 2015.

Remerciements

L'essentiel des travaux de cette thèse ont été effectués au laboratoire d'Optique de l'EPFL sous la supervision du professeur D. Psaltis. Je souhaiterais lui exprimer ici toute ma gratitude pour m'avoir donné l'opportunité de travailler dans un environnement de recherche d'une telle qualité. Je voudrais également le remercier pour ses idées, ses conseils et ses encouragements, sans lesquels la réalisation de ce travail n'aurait pas été possible.

J'aimerais également remercier les professeurs C. Sheppard, R. Piestun et C. Moser pour leur contribution à ma thèse. J'ai eu l'opportunité de collaborer avec chacun d'entre eux. Je souhaiterais les remercier pour l'intérêt qu'ils ont porté à mon travail et pour les discussions constructives qui ont facilité la réalisation respectivement de l'illumination structurée point par point, de la lecture de profondeur en double hélice et de l'endoscopie à excitation saturée.

Ce projet a connu un début chaotique. Il était initialement centré sur l'observation à haute résolution de protéines fluorescentes pour l'analyse des interactions ADN-protéines. Suite à des difficultés majeures de stabilité des brins d'ADN dans les canaux micro-fluidiques, je me suis tourné vers l'amélioration des méthodes d'imagerie. Je tiens néanmoins à remercier tout particulièrement le Prof. B. Deplancke. Il était à l'origine de ce projet, m'a ouvert son laboratoire et permis de découvrir les bases de la recherche en génétique. Même dans les temps difficiles, il m'a supporté, encouragé et laissé libre de faire au mieux pour le succès de ma thèse. Je regrette que notre collaboration n'ait pu être plus fructueuse mais je pense que grâce à lui mes futurs projets auront un parfum de biologie.

Je souhaiterais aussi remercier Carole Berthet pour sa patience et son aide dans toutes les démarches administratives qui rendent notre vie plus facile.

Un grand merci également à mes collègues Nicolino Stasio and Donald Conkey qui m'ont aidé bien au-delà de leur contribution scientifique aux travaux que nous avons publiés ensemble. J'ai passé avec eux ainsi qu'avec Yannis Papadopoulos et Alexandre Goy de nombreux bon moments au laboratoire et en dehors et je les considère maintenant comme des amis. Je me permets aussi de témoigner ici mon affection et ma reconnaissance au professeur Andreas Vasdekis pour son aide précieuse et son support indéfectible depuis le commencement de ce projet.

Certaines des images présentées dans ce mémoire ont été acquises au complexe de bio-imagerie de l'EPFL. J'aimerais remercier l'ensemble de l'équipe du BIOP pour leur gentillesse et leur expertise et plus spécialement Romain Guiet pour son aide avec la préparation des échantillons à base de cellules.

Je tiens à remercier tous mes camarades de recherche qui se sont succédés lors de mon passage dans le laboratoire : Ye Pu, (merci pour la patience avec laquelle tu as répondu à toutes mes questions, ça a été d'une grande aide tout au long de mon doctorat), Rachel Grange (merci de m'avoir fait découvrir le laboratoire d'optique ainsi que la culture suisse durant mon stage de Master), Chia-Lung Hsieh (merci pour ta disponibilité et tes conseils en optique non-linéaire), Salma Fahari (merci pour tes conseils et ta gaieté), Laurent Decloux (merci pour ton aide avec Labview), Marcin Zielinski, Jae-Woo Choi, Miguel Modestino, Julien Cuenet, Xin Yang, Thomas Lanvin, Mohammad Hashemi, Wuzhou Song, Marilisa Romito and Mortesa Hashani Shoreh. Enfin, merci à toute l'équipe du LAPD pour leur joie de vivre et la bonne atmosphère qu'ils propagent dans les bureaux alentours.

Lausanne, le 5 novembre 2015

Abstract

In the last 30 years, superresolution in optical microscopy has been a major field of research. During this time, different techniques have been created to break the diffraction limit in order to make observations at a nanometric scale. Given that optical microscopy is non-invasive, those superresolution methods pave the way for a better understanding of biological mechanism at a molecular level. Most of those methods are based on a nonlinear interaction between the excitation light intensity and the sample response (often fluorescent signal).

In the same time, nanodiamonds containing fluorescent defects have been proven to be a choice probe for superresolution nanoscopy since they exhibit a strong and stable fluorescent signal even under high light intensities exposure (often required to obtain nonlinear photoresponse). Nanodiamonds containing Nitrogen Vacancy (NV) defects that exhibit a red fluorescent signal had been previously shown to be a viable biomarker for STED superresolved image. First, we demonstrated that green fluorescent nanodiamonds containing Nitrogen-Vacancy-Nitrogen (NVN) defects can be used with a Stimulated Emission Depletion (STED) superresolution microscope. Then, we implemented a STED microscope in our lab and compared the properties of NVN and NV centers for STED imaging. We conclude that even if nanodiamonds with NVN defects are less intense, they can be used as a second color nonbleaching biomarker. To illustrate the potential use of green nanodiamonds as bio-compatible probe, we superresolved them internalized into a cell with STED microscopy.

Second, we tried to work on one of the main limitation in STED nanoscopy: the lack of information in the axial direction within a single scan. We combined our home made STED microscope with a Double Helix phase mask that modifies the detection point spread function in order to obtain axial localization of the superresolved emitters. We achieved three dimensional localization of nanometric fluorescent emitters but we note that photobleaching was the main limitation of this approach with organic dyes. We discussed different solutions to limit the photobleaching and their feasibility.

We also worked on a different superresolution technique that we named Computational Nonlinear Saturated (CNS) microscopy. We showed that with digital post treatment of the acquired data, a nonlinear photoresponse can be harnessed to any scanning microscope equipped with a camera detector to enhance the resolution. We demonstrated that increasing the excitation power and inducing fluorescence saturation, it is possible to break the diffraction limit in a conventional confocal microscope (after data post-treatment). However, with this method, we did not obtain a gain in resolution as high as with other superresolution techniques involving fluorescence saturation, such as saturated structured illumination microscopy. To understand the origin of this limitation, we carried out simulation to investigate the performance of CNS microscopy in noisy environments compared with wide field techniques. We propose alternative implementation and quantify the possible resolution gain with simulations.

Finally, we demonstrated how a technique, initially created for optical microscopy, can be adapted to lensless endoscopic imaging. Recently in our laboratory, ultrathin endoscopy has been implemented with phase conjugation through multimode fiber. We demonstrate how the resolution of this endoscopic imaging technique can be improved by saturated excitation and temporal modulation of the excitation beam. Moreover, we demonstrate the presence of optical sectioning with this method. We show image contrast improvement provided by saturated excitation sectioning and discuss its use in thick biological sample.

Keywords

Microscopy, superresolution, stimulated emission depletion microscopy, double-helix localization, confocal microscopy, structured illumination microscopy, endoscopic imaging, saturated excitation microscopy.

Résumé

Les techniques de microscopies optiques super-résolues permettent des observations à l'échelle nanométrique au-delà de la limite classique de diffraction. Elles ouvrent donc la voie, sans être invasives, à une meilleure compréhension des mécanismes biologiques au niveau moléculaire. La plupart de ces méthodes d'imagerie super-résolues reposent sur une interaction non-linéaire entre l'intensité lumineuse envoyée à l'échantillon et le signal réémis (en général de fluorescence).

Dans ce cadre, des diamants de tailles nanométriques contenant des défauts fluorescents très stables ont été récemment développés. En premier lieu, nous avons démontré que des nanodiamants (ND) verts avec des défauts azote-lacune-azote (NVN) pouvaient être utilisés avec un microscope à super-résolution commercial de type STED (Stimulated Emission Depletion). Nous avons ensuite construit un microscope STED et comparé les propriétés des défauts NVN avec les défauts azote-lacune (NV) qui ont été utilisés précédemment pour des images STED d'échantillons biologiques. Nous avons ainsi démontré que bien que moins intenses que les défauts NV, les défauts NVN sont également des marqueurs appropriés.

Dans un deuxième temps, nous avons tenté d'apporter une réponse à une des limitations inhérente des techniques non-linéaires de microscopie à balayage: le manque d'information sur la profondeur de l'échantillon lors d'un balayage. Nous avons amélioré un microscope STED en l'équipant d'un masque de phase qui modifie la fonction d'étalement du point afin d'obtenir en un seul scan une localisation axiale de l'échantillon super-résolu latéralement. Nous avons constaté que la limitation principale de la technique est le photo-blanchiment avec les colorants organiques. Nous proposons donc des alternatives et discutons leur faisabilité.

D'autre part nous avons développé une technique différente de microscopie à super-résolution que nous avons baptisé CNS (Computational Nonlinear Scanning) microscopy. Nous avons ainsi démontré comment le post traitement des images d'un microscope à balayage équipé d'une détection à champs large combiné à une photo-réponse non-linéaire de l'échantillon peut conduire à un gain en résolution. Ainsi, la simple augmentation de l'intensité d'excitation dans un microscope confocal, entraînant la saturation de la fluorescence réémise, permet d'obtenir des images super-résolues (après traitement des données). Cependant, les gains en résolution obtenus expérimentalement sont limités comparés par exemple à la microscopie à illumination structurée utilisant également la saturation comme phénomène non-linéaire. Pour déterminer les causes de cette observation, nous avons mené une analyse de l'influence du bruit sur la résolution obtenu et montré en quoi elle était inférieure aux techniques d'imagerie en champs large. Nous proposons des modifications de la forme du faisceau d'excitation et prédisons les gains en performances obtenus à travers des simulations.

Enfin, nous avons démontré qu'une de ces techniques à super-résolution originalement développée pour des microscopes classiques pouvaient être utilisée pour améliorer la résolution d'imagerie endoscopique. Nous avons utilisé la technique de conjugaison de phase à travers une fibre multimode développée dans le laboratoire, pour obtenir un endoscope très fin sans lentille. D'une part nous présentons l'amélioration de la résolution par modulation temporel du faisceau d'excitation. D'autre part, nous rendons compte de l'obtention de coupe optique avec cette même méthode. Nous démontrons l'amélioration du contraste d'imagerie grâce à la coupe optique puis nous discutons ses possibilités réelles d'applications dans des échantillons biologiques épais.

Mots-clés

Microscopie, super-résolution, microscopie à déplétion par émission stimulée, fonction d'étalement du point en forme de double hélice, microscopie confocale, microscopie à illumination structurée, imagerie endoscopique, microscopie à excitation saturée.

Contents

Nanoscopy in nonlinear scanning fluorescence imaging systems.	i
Acknowledgements	iii
Remerciements	v
Abstract	vii
Keywords	vii
Résumé	ix
Mots-clés	ix
Contents	xi
List of Figures	xv
List of Abbreviations	xix
Chapter 1 Introduction	1
Chapter 2 Nonlinear fluorescence scanning microscopy with non-bleaching probes and characterization of the NVN defect in nanodiamonds for STED microscopy.	5
2.1 A few definitions: resolution limit in fluorescence scanning microscopy	5
2.2 Breaking the diffraction limit: nonlinear fluorescence scanning microscopy	7
2.3 Gold standard in nonlinear fluorescence scanning microscopy: STED microscopy	10
2.3.1 General principle	10
2.3.2 Resolution gain by stimulated emission depletion	10
2.3.3 A nonbleaching nanometric label for STED microscopy: Fluorescent nanodiamonds:	13
2.4 Implementation of a STED microscope for FNDs imaging:	15
2.4.1 Setup	15
2.4.2 NV defects depletion by stimulated emission	16
2.4.3 Generation of donut-shaped beam	16
2.4.4 STED imaging of FNDs:	19
2.5 Characterization of a new material for STED microscopy: green nanodiamonds	21
2.5.1 Stimulated emission characteristics of gNDs:	22
2.5.2 STED imaging	26
2.5.3 Cell imaging	26
2.5.4 Conclusion:	27
2.6 Conclusion:	28
Chapter 3 Double Helix axial localization in STED microscopy	29
3.1 Introduction	29

3.2	Principle	30
3.2.1	Rotating beam	31
3.2.2	Detection Point spread function	33
3.2.3	PSF-design for axial localization in fluorescence scanning microscopy	38
3.3	DH-STED of red nanodiamonds	40
3.3.1	Setup	40
3.3.2	Three dimensional imaging of superresolved nanodiamonds	41
3.4	DH-STED with organic dye emitters	44
3.4.1	Photobleaching limitation in STED microscopy	44
3.4.2	Setup	46
3.4.3	Photobleaching characterization	46
3.4.4	Three dimensional imaging of fluorescent beads (containing organic dyes)	47
3.5	Discussion	49
3.6	Conclusion	50
Chapter 4	Computational nonlinear scanning microscopy.	51
4.1	Introduction	51
4.2	Underlying principle	51
4.2.1	Structured Illumination Microscopy	51
4.2.2	Structured Illumination in Scanning microscopy	53
4.3	Method	54
4.3.1	Setup	54
4.3.2	Post-processing algorithms	55
4.3.3	Digital post-processing implementation with sample scan:	56
4.4	Comparison of the linear algorithms:	57
4.5	Non-linear resolution enhancement method:	58
4.5.1	OTF spectrum elongation with fluorescence saturation	58
4.5.2	CNS reconstruction	60
4.6	CNS microscopy	62
4.7	SNR performance compared to wide field	63
4.8	Sectioning	65
4.9	Alternative Illumination patterns	66
4.10	Another nonlinear mechanism: stimulated emission depletion	69
4.10.1	CNS STED	69
4.10.2	STED as a ground truth for CNS microscopy	70
4.11	Conclusion	70
Chapter 5	Resolution enhancement in ultrathin endoscopy by saturated fluorescence excitation.	71
5.1	Introduction	71

5.2	Principle of the method	72
5.2.1	Scanning fluorescent imaging through multimode fiber using phase conjugation.	72
5.2.2	Saturated excitation microscopy.....	82
5.3	Enhanced resolution and optical sectioning through multimode fiber by saturated excitation	89
5.3.1	Experimental setup	89
5.3.2	Resolution improvement	90
5.3.3	Depth discrimination.....	92
5.3.4	SNR limitations	94
5.4	Conclusion	95
Chapter 6	Conclusion	97
6.1	Achieved results	97
6.2	Future developments	98
References.....		99
Appendix A: Analytical light distribution at the focus of a microscope objective and the validity of the approximations.		107
Appendix B: Fluorescence saturation under high power excitation.		109
Appendix C: Complete expression Gauss Laguerre modes.....		113
Appendix D: Influence of pulse width on depletion efficiency.....		115
Appendix E: Alignment procedure in digital phase conjugation.....		119
Appendix F: Numerical aperture in MMF		121
Appendix G Information confinement in single mode and multimode fiber		123
Appendix H: Analytical expression of SAX coefficient.....		125
Curriculum Vitae.....		126

List of Figures

Figure 1-1: Examples of microscopy methods breaking the optical diffraction limit.....	1
Figure 1-2 Examples of superresolution imaging.....	2
Figure 2-1 Resolution limit in scanning microscopy.....	6
Figure 2-2 An imaging system acts as a band pass filter in the spatial frequency domain.	7
Figure 2-3 Visualization of the limit of diffraction in the Fourier domain.....	8
Figure 2-4 Breaking the diffraction limit in nonlinear scanning microscopy: a single beam experimental demonstration.	9
Figure 2-5 Principle of STED microscopy.....	10
Figure 2-6 STED depletion energy diagram.....	11
Figure 2-7 Approximation used for analytical fit of excitation and depletion beams.....	12
Figure 2-8 Nanodiamonds containing NV defects.....	13
Figure 2-9 Fluorescence properties of red nanodiamonds	14
Figure 2-10 Simplified STED microscope setup.....	15
Figure 2-11 Luminescence inhibition of NV center by stimulated emission.	16
Figure 2-12 Calculated STED equivalent PSF for $I_{STED}^{max} = 50I_s$ and for different values of the depletion beam contrast.....	17
Figure 2-13 PSFs of the home-built CW STED microscope recorded with the backscattered light of a single 80 nm gold nanosphere (with a nonconfocal detection).....	18
Figure 2-14 Depletion beam contrast.	19
Figure 2-15 STED microscope performance.....	20
Figure 2-16 STED images of nonbleaching probes.	21
Figure 2-17 Nanodiamonds containing NVN defects.	22
Figure 2-18 Fluorescence saturation curve at 470 nm excitation	23
Figure 2-19 Absorption (green plot) and emission (red plot) spectra of green nanodiamonds.....	23
Figure 2-20 Fluorescence properties of green nanodiamonds.	24
Figure 2-21 Depletion efficiency with green nanodiamonds.	25
Figure 2-22 STED imaging of green nanodiamonds.	26
Figure 2-23 Superresolution imaging of gNDs uptaken into HeLa cell.....	27
Figure 3-1 Conventional STED vs 3D STED.	29
Figure 3-2 Principle of DH-STED.....	31
Figure 3-3 The GL basis.	32
Figure 3-4 Rotating beam properties.....	33
Figure 3-5 Axial localization with rotating PSF based microscope.	34
Figure 3-6 DH transfer function.	34
Figure 3-7 DH and conventional point spread functions around the focal plane.	35

Figure 3-8 Influence of the mode waist size (with respect to the pupil diameter) on the PSF width. .35	
Figure 3-9 DH transfer function optimization. 36	
Figure 3-10 Transfer function efficiency. 37	
Figure 3-11 Three dimensional localization of fluorescent beads, immobilized on a two level planar surface. 38	
Figure 3-12 Effect of wavelength on DH modulation..... 39	
Figure 3-13 Sectioning ability of scanning microscopes with DH localization.....40	
Figure 3-14 Schematic of the DH CW-STED setup..... 40	
Figure 3-15 Axial localization calibration with DH. 42	
Figure 3-16 Three dimensional imaging with DH-STED..... 43	
Figure 3-17 Immobilized NDs DH-STED three dimensional imaging. 44	
Figure 3-18 Depletion efficiency with pulsed STED..... 45	
Figure 3-19 Schematic of the DH pulsed STED setup. 46	
Figure 3-20 Photobleaching induced by depletion beam. 47	
Figure 3-21 Axial localization calibration of organic label with DH. 48	
Figure 3-22 Three dimensional imaging of a group of 100nm beads immobilized in a PDMS matrix. 49	
Figure 3-23 Phase contrast imaging with DH-STED setup. 50	
Figure 4-1 Principle of structured illumination microscopy 52	
Figure 4-2 Information loss during scanning imaging. 54	
Figure 4-3 CNS microscopy setup. 54	
Figure 4-4 Reconstruction steps to recreate a non-descanned modulated illumination.....57	
Figure 4-5 Linear imaging of FNDs with an 0.8 NA objective. 58	
Figure 4-6 Saturation of FNDs and corresponding saturated PSFs. 59	
Figure 4-7 Insensitivity of the temporal modulation algorithm to the beam shape. 61	
Figure 4-8 Resolution improvement with CNS microscopy..... 61	
Figure 4-9 Experimental demonstration of CNS microscopy on fluorescent NDs with a 0.8NA objective. 62	
Figure 4-10 Equivalent focused and sinusoidal illumination under saturated absorption.....63	
Figure 4-11 Simulated data on photon budget influence on linear imaging of fluorescent nanoparticles. 63	
Figure 4-12 Simulated data on photon budget influence on wide field and point scanning nonlinear imaging of fluorescent nanoparticles. 64	
Figure 4-13 Sectioning in CNS microscopy. 65	
Figure 4-14 Alternative illumination patterns for CNS microscopy..... 66	
Figure 4-15 Simulated data on photon budget influence on point scanning third harmonic nonlinear imaging of fluorescent nanoparticles with standard focus, Bessel beam and hexagonal pattern illuminations.67	
Figure 4-16 Experimental alternative patterns for CNS microscopy..... 68	
Figure 4-17 Linear imaging of FNDs with bessel beam illumination and with an 0.8 NA objective. 68	
Figure 4-18 Non-linear imaging of fluorescent NDs with a 1.4NA objective..... 69	
Figure 5-1 One solution to image deep into scattering materials (like biological tissues). 71	

Figure 5-2 Fiber waveguides outlook.	73
Figure 5-3 Principle of optical phase conjugation.	74
Figure 5-4 Off-axis digital holography setup and principle.	75
Figure 5-5 Reconstruction of the complex field at the output of the fiber.	77
Figure 5-6 Optical setup for focus generation through fiber by phase conjugation.	78
Figure 5-7 Focused excitation through multimode fiber by phase conjugation.	78
Figure 5-8 Influence of the excitation focus position on the phase conjugated spot.	79
Figure 5-9 Linear fluorescence scanning imaging through multimode fiber.	80
Figure 5-10 Numerical aperture of MMF and resolution of imaging through MMF.	81
Figure 5-11 Influence of light coherence and generation of a phase conjugated vortex beam.	82
Figure 5-12 Underlying principle of SAX microscopy.	84
Figure 5-13 Principle of SAX microscopy.	84
Figure 5-14 Calculated demodulated fluorescence intensity response.	85
Figure 5-15 Theoretical resolution improvement in SAX microscopy for a 0.39NA and 532nm excitation light.	86
Figure 5-16 Comparison of the PSF with different imaging method with a 0.39NA microscope for NV centers imaging.	87
Figure 5-17 Theoretical sectioning performance of SAX and two-photon microscopy.	88
Figure 5-18 1 Schematic of the SAX through MMF imaging setup.	89
Figure 5-19 Point spread function narrowing with saturated excitation endoscopy.	90
Figure 5-20 Peak intensity influence in SAX endoscopic imaging.	91
Figure 5-21 Fluorescence images of nanodiamonds immobilized on a glass slide.	92
Figure 5-22 Characterization of the sectioning performance: edge response of a Rhodamine 6G dye solution.	92
Figure 5-23 Improvement of image contrast by optical sectioning.	93
Figure 5-24 Experimentally measured relationship between demodulated fluorescence signal intensity and excitation intensity for two types of dye (fluorescent nanodiamonds with NV centers and Rhodamine 6G).	94
Figure 5-25 Detection of high saturation demodulated orders.	95

List of Abbreviations

AOM	Acousto-Optic Modulator
APD	Avalanche Photo-Diode
CCD	Charged Coupled Device (camera)
CMOS	Complementary Metal Oxide Semiconductor (camera)
CNS	Computational Nonlinear Microscopy (CNS)
CW	Continuous Wave
DC	Direct Current (signal)
DH	Double Helix
DNA	Deoxyribonucleic Acid
FND	Fluorescent Nanodiamonds
FWHM	Full Width Half Maximum
GL	Gauss-Laguerre
gND	green NanoDiamond
IR	Infra-Red
MMF	Multi Mode Fiber
NA	Numerical Aperture
ND	NanoDiamond
NV	Nitrogen Vacancy
NVN	Nitrogen Vacancy Nitrogen
OPO	Optical Parametric Oscillator
OTF	Optical Transfer Function
PALM	PhotoActivated Localization (microscopy)
PDMS	PolyDiMéthylSiloxane
PMT	PhotoMultiplifier (detector)
PSF	Point Spread Function
rND	red NanoDiamond
SAX	SATurated Excitation (microscopy)
SEM	Scanning Electron Microscopy
SIM	Structured Illumination Microscopy
SLM	Spatial Light Modulator
SNOM	Scanning Near-field Optical Microscopy
SNR	Signal to Noise Ratio
STED	Stimulated Emission Depletion
STM	Scanning Tunneling Microscopy
STORM	Stochastic Optical Reconstruction Microscopy
TEM	Transmission Electron Microscope
WF	Wide-Field

Chapter 1 Introduction

Optical microscopy is regarded as one of the most important tools in science history. Indeed, important discoveries in various disciplines resulted from the visualization of the fine structures that are invisible to the naked eye. These discoveries led to significant, scientific, economic and cultural progress throughout history. For example, in the 18th century the visualization of cells and bacteria led to great progress in medicine [1]. During the same period, the identification and classification of fungi was the first step towards crop protection from fungal pathogens and towards the isolation of penicillin [2]. During the 19th century, microscope observation was the main instrument for mineralogy and the control of polarization led to the identification of mineral internal composition [3]. The progress of modern research drives a never ending quest for higher resolution and deeper observation. In the last two decades the diffraction limit has been surpassed in optical microscopy. Thanks to superresolution fluorescence microscopy, current light microscopes allow for the dynamic observation of relatively large structures like cells assemblies with the visualization of molecular organization at the nanoscale. Thus, superresolution microscopy is an active research field that is growing because optical, nanometer resolution imaging is providing important insights about various biological systems and will lead in the future to further major advances.

On the advantages of far-field optical superresolution microscopy.

When confronted with the theoretical limit imposed by diffraction, researchers first opted for the obvious solution. In order to improve the resolution, the wavelength was decreased, and visible light was ultimately replaced by an electron beam to probe the sample. The Transmission Electron Microscope (TEM) and then the Scanning Electron Microscope (SEM) were developed in the 1930's not long after realizing the wave nature of electrons. Owing to the electron wavelength (\sim nm), electron microscopes reveal atomic organization of the materials and some subcellular structures with accuracy going to the angstrom range (Figure 1-1 (a)). In the 1980's different approaches were developed to observe beyond the diffraction limit without directly using a wave, but by probing the sample with an ultra-thin solid tip. Within this group are Atomic Force Microscopy (AFM), scanning tunneling microscopy (STM) and Scanning Near Field Optical Microscopy (SNOM). AFM and STM measure the interaction between the tip and the sample, respectively the contact forces and the tunneling current, to image the property of the sample at the tip. SNOM uses the evanescent light wave at the end of a fiber tip. The resolution obtained with those techniques is related to the size of the tip, AFM and STM provide typical resolution in the angstrom range while SNOM resolution is in the nanometer range (Figure 1-1 (b-c)) [4].

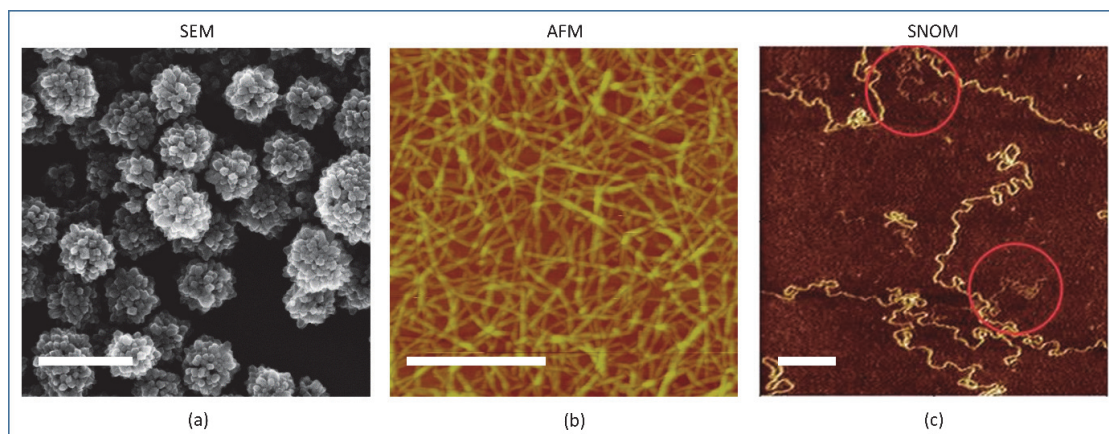


Figure 1-1: Examples of microscopy methods breaking the optical diffraction limit. (a) Scanning electron microscopy image of TiO_2 (Courtesy of M. Hashemi LO EPFL) (b-c) Scanning probe microscopy images. (b) AFM images of nanocellulose fibers (Wikipedia, public domain) (c) SNOM Topographical images of DNA molecules deposited onto mica surface. Single strand parts of DNA can be differentiated of double stranded DNA and are highlighted with red circles. (Courtesy of Dr. S. K. Sekatskii, LPMV EPFL.). Scale bars are 500 nm.

However, the very high resolution obtained with all those nanoscopy imaging techniques comes with strong restrictions. Electron microscopes impose strong limitations on the sample preparation that complicate the observation of organic samples and, until

recently, precluded the observation of live imaging [5]. SNOM, STM and AFM techniques are delivering very accurate surface profile of various samples but they remain limited to the imaging of single interfaces and do not provide volumetric images (Figure 1-1 (b)).

State of the art in superresolution microscopy.

The past two decades have seen the development of far field optical microscopy methods that have overcome the diffraction limit. All together, these techniques, usually referred to as “superresolution microscopy”, were recognized as an important breakthrough with the awarding of the 2014 Nobel Prize for chemistry. The main superresolution techniques are Stimulated Emission Depletion (STED) microscopy [6], Structured Illumination Microscopy (SIM) [7], Photo-Activated Localization Microscopy (PALM) [8] and Stochastic Optical Reconstruction Microscopy (STORM) [9](Figure 1-2). All these techniques rely on the same concept: as the minimal pattern size of the excitation light is limited by diffraction, further resolution improvement must come from the interaction between the light and the sample. In consequence most of these methods use fluorescent labelling and improve the resolution by modifying the fluorescence emission. For instance, STED drives the fluorophores to their ground state by stimulated emission except at a central point, thus confining the observation volume to a subdiffraction sized voxel. PALM and STORM are based on the sequential activation of single fluorescent molecules. The individual emitters are precisely localized sequentially and the image is reconstructed in a pointillistic way. On the other hand, SIM does not rely on light-matter interaction, but exploits frequency mixing between the spatial frequencies of the sample and the patterned illumination. The detected image is then demodulated to extract the sub-diffraction sample details.

The possibility of visualizing a sample with about one order of magnitude resolution enhancement over conventional light microscopy has led to numerous discoveries and applications, particularly in the life sciences. Numerous studies have refined our understanding of intra-cellular structures, in mitochondria, the nucleus or organelles [10]. They have confirmed previous observations made with electronic microscopy and have revealed new information thanks to the specificity of fluorescent labeling and the ability to image live cells. The distribution and dynamics of synaptic proteins have also been widely studied providing insight into the organization of proteins in the presynaptic zone and around the dendritic spines [10,11]. Another prominent example of superresolution microscopy application is the analysis of lipid-protein interaction in plasma membrane [10,11]. With a lower impact, the principles of superresolution microscopy have been applied to different fields, for example to improve photolithography fabrication resolution [12].

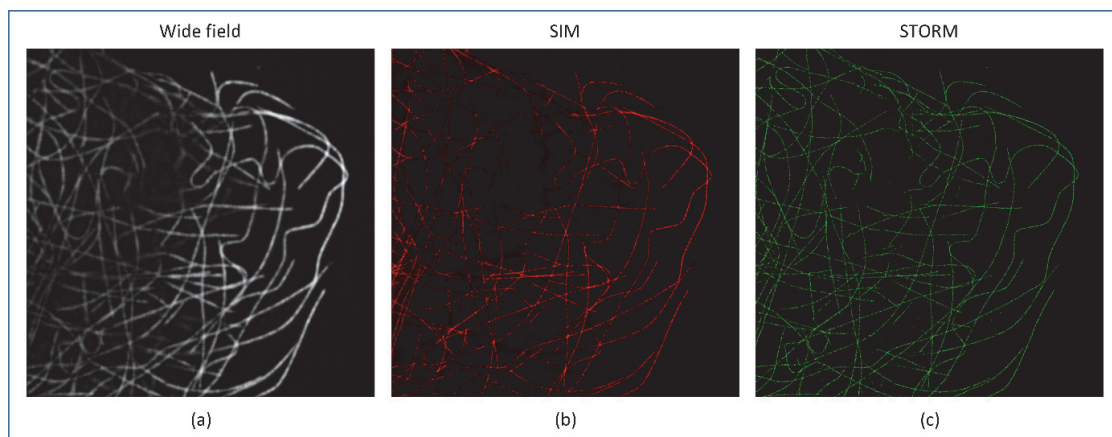


Figure 1-2 Examples of superresolution imaging. Courtesy of Bioimaging & Optics platform, EPFL. The same labelled cytoplasm microtubules imaged successively with wide-field microscopy (a), structured illumination microscopy (b) and stochastic optical reconstruction microscopy (c).

Nevertheless, superresolution microscopy, or nanoscopy, is still young and has continued to show significant improvement in the last few years. For example, PALM, STED and SIM were initially used for lateral resolution enhancement, but each of them has been modified to enable three dimensional superresolved imaging [13–15]. Also, several works have recently been presented to accelerate image acquisition speed, by technical refinement [16] or with focused illumination parallelization [17–20]. Recent publications have also focused on the imaging depth improvement by the use of nondiffracting beams [21], nonlinear excitation [22] and adaptive optics [23].

Future progress relies on the development of new probes with smaller size and more precise control of the photophysical characteristics for more precise labelling [10,24]. Progress also depends on new instrumental designs to address the current limitations. The existing methods are complementary as each offers advantages and disadvantages. However, further improvements to the nanoscopy methods are yet to come. The resolution needs to be improved beyond the current performance (20 to 40nm in biological samples). The discrepancy between lateral and axial resolution should be reduced for isotropic three dimensional imaging. Also, both biological and material science would benefit from superresolution imaging at increased depth to resolve thin details deep inside the samples. Finally, the time resolution must be improved to capture dynamic biological events in a sufficient field of view, which would provide environmental context and enrich data interpretation.

In a more general perspective, optical microscopy is an important tool because it is the non-invasive observation method with the highest resolution available up to date. However in order to understand the entire ensemble macroscopic behaviors, conventional microscopy is often insufficient. A deeper understanding is only possible by observing at the molecular level, which call for nanoscopy.

Outline:

In this thesis we study and implement different scanning methods that break the diffraction limit, each of them conveying a specific advantage compared to existing techniques.

In all superresolution techniques, the achievable resolution is intrinsically connected to the signal to noise ratio. This means that the strategies to further improve the resolution involve the development of fluorescent probes able to deliver more photons before bleaching. In Chapter 2, we propose and characterize a novel type of fluorescent label for nanoscopy: diamond nanocrystals containing Nitrogen Vacancy Nitrogen (NVN) defects. Indeed, lattice defects in diamond crystal have been identified as interesting fluorescence sources thanks to their uniquely high resistance to photobleaching [25]. A single type of point defect, namely the Nitrogen Vacancy (NV) defect has been used with STED microscopy. Thanks to the absence of photobleaching, it was imaged with resolution down to 5.8 nm [26]. These NV centers emit red light, however, many others crystal defects with many different colors are present in diamonds but have remained unused in superresolution microscopy. They all share the same outstanding photoreistance but exhibit different fluorescent properties and their compatibility with superresolution microscopy has not been investigated. Moreover, a second color diamond probe would open the door for two color superresolution imaging at very fine resolution (below 20nm) or long-term colocalization superresolution studies. With this goal in mind, we analyze the photophysical property of NVN defects that emit green light. We show that NVN centers are perfectly compatible with STED microscopy and we measure resolution improvement with the green fluorescent defects. The embedment of color centers into nanocrystals has also recently opened the door for their use as a biological label. To demonstrate the potential of NVN containing nanodiamonds as a nonbleaching probe for biological imaging, we imaged in vitro fluorescent particles up taken into a cancerous cell.

Superresolution methods like conventional light microscopy do not exhibit three dimension isotropic resolution: they suffer from a degraded axial resolution compared with the lateral one. It is especially true for conventional STED imaging where the resolution is enhanced only in the lateral dimension and the axial one remains dictated by diffraction. In Chapter 3, we record images with isotropic information in three dimension by combining STED imaging and a double helix point spread function axial localization [27]. The technique does not provide axial resolution improvement as has been demonstrated with three dimensional STED [15] or PALM [9]. However, this method is well suited for cases where a sample is resolved with lateral STED and confocal sectioning. The high resolution three dimensional images are obtained by post processing after a single lateral scan acquisition. Thus, in axially sparse samples, the technique has the potential for isotropic imaging, faster acquisition and consequently lower phototoxic side effects compared with three dimensional scanning techniques. As the method relies on scanning acquisition with an imaging sensor (a camera), the actual speed is still limited by the speed of available sensors. We discuss the current limitations in term of photobleaching together with the potential improvement with a fast camera sensor.

In Chapter 4 we present a method that uses the SIM mechanism of resolution enhancement but uses focused illumination. In fact, as we discussed above, SIM was one of the pioneering superresolution methods. In its linear implementation, SIM results in a resolution enhancement of a factor of two [7], but it exhibits a higher resolving power when combined with nonlinear fluorescence saturation [28]. Despite its potential advantage in terms of speed due to wide field detection, the difficulty to project very stable and precise sinusoidal fringes over the entire field of view has limited its popularity compared to STED or PALM. Recently, exploiting a similar principle as SIM as described in [29,30], the same resolution doubling has been demonstrated in scanning microscopy [31]. This renewed interest has been motivated by the simplicity of the method: by only using a camera detector in a standard confocal microscope, resolution gain could be obtained with digital post-treatment. Several publications have very recently shown the potential of the method for biological sample imaging after improvement of the acquisition speed by parallelization [19,20] and

of the contrast by two-photon excitation [19]. However, like linear SIM all those studies remained limited to an enhancement in resolution by a factor 2, while saturated SIM has been demonstrated to reach much higher resolution improvement [28]. In Chapter 4, we show how it is possible to harness the saturated SIM principle in confocal microscopy by using a different post treatment [32]. We demonstrate resolution enhancement above a factor of two obtained by only post-processing a scanning image acquired with a camera detector. We also investigate the theoretical resolution limit with this method and whether a resolution improvement comparable to saturated SIM can be obtained.

In Chapter 5 we present the use of fluorescence saturation for ultrathin endoscopy imaging. Indeed, optical resolution imaging deep inside scattering media (especially biological tissues for medical investigations) is still a major challenge. Scattering distortions and out of focus fluorescence complicates microscopic imaging, especially superresolution imaging. Recent progress has been made to increase imaging depth with adaptive optics, for example depletion beam aberrations have been dynamically corrected [23] and alternative methods like speckle scanning using the memory effect have been demonstrated [33,34]. However all those techniques limit the imaging depth to a few millimeters at most. The only existing solution to imaging deeper with very high resolution is then pretty basic: to use an endoscope to guide the light through the scattering medium and get closer to the part to be imaged. The trade-off is then different. Roughly, a larger endoscope provides better resolution, but it is more invasive to the penetrated tissue (usually human). In Chapter 5, we adapt a microscopy method to ultrathin (and thus minimally invasive) fiber based endoscopy [35] in order to improve the resolution. The method, called Saturated Excitation Microscopy (SAX) consists in using fluorescence saturation (as Computational Nonlinear Scanning microscopy in Chapter 4) combined with temporal modulation and demodulation of the fluorescence to enhance the resolution. We show how a 0.5 micron resolution can be obtained with 200 μm diameter endoscopes. In addition, we demonstrate that saturation excitation endoscopy also results in optical sectioning that can dramatically improve the contrast of the images.

Hence, each of the methods I investigated realizes of a specific advantage in term of speed, precision or imaging depth. These methods are our contribution to the quest for a live, inexpensive and versatile optical imaging method at the nanometer scale, before new breakthroughs, perhaps from novel concept like quantum imaging [36,37] or plasmonic imaging [38–40].

Chapter 2 Nonlinear fluorescence scanning microscopy with non-bleaching probes and characterization of the NVN defect in nanodiamonds for STED microscopy.

In this chapter, after introducing a few basic optical microscopy fundamental concepts, we describe how nonlinear scanning microscopy can break the classical diffraction limit. As an example, we detail the principle and implementation of one of the most popular nonlinear scanning techniques, i.e. STED microscopy. The experiments were performed with Fluorescent Nanodiamonds (FNDs), which have the distinct advantage of not photobleaching. Therefore, the performance of the STED method is limited only by the available power and imperfections of the optical system. We used a home-built system with 770 nm wavelength laser light for depletion. The maximum resolution was measured with Nitrogen-Vacancy (NV) FNDs to be about 50 nm, which is typical for CW-STED with the level of power used. Currently, STED imaging is the reference technique for superresolution in fluorescence scanning microscopy, so this study provides a point of comparison for the different studies described in this thesis. Moreover, we demonstrated for the first time the use of Nitrogen-Vacancy-Nitrogen (NVN) defect in diamond that emits green fluorescence with STED microscopy. We characterized the performance of green FNDs for STED imaging and investigated its possible use as a biomarker. The green FNDs are shown to have similar luminescence characteristics to the widely used red FNDs but the brightness is presently limited by the defect concentration.

2.1 A few definitions: resolution limit in fluorescence scanning microscopy

To quantify the performance of a microscope it is common to determine its Point Spread Function (PSF), which is the response of the imaging system to a point object. Any object can then be regarded as a superposition of point sources and its image through the microscope can be described as the sum over the contribution from each point. In an ideal, aberration free imaging system, this corresponds mathematically to a convolution. Thus, the image $Im(x,y)$ produced by a microscope of an object $Obj(x,y)$ can be written:

$$\begin{aligned} Im(x, y) &= \int_{-\infty}^{\infty} \int_{-\infty}^{\infty} Obj(x', y') \times PSF(x - x', y - y') dx' dy' \\ &= Obj(x, y) \otimes PSF(x, y) \end{aligned} \quad \text{Equation 2-1}$$

The convolution by the PSF blurs the object. Therefore, a sharper PSF (minimal spread) provides an image closer to the object. There are different types of microscopes with different imaging modalities. The idea of scanning microscopy is to illuminate the sample by a focused spot of light and to detect its response to light excitation (e.g. fluorescence or backscattering). By moving the focused spot at different points on the sample and recording the signal, an image is created. The spatial resolution of the image depends on the size of the probe that is used to scan the object. For example, in atomic force microscopy the object is scanned with a tip. A thinner tip provides higher resolution. Similarly, in far field optical microscopy, high resolution can be obtained by using a narrow illumination spot. The purpose of the STED method is to reduce the size of the probe beam below the classical diffraction limit. However, light is a wave and the diffraction imposes the minimal size of the light spot that can be obtained. In a typical microscope, the light is focused by an objective lens. The light distribution in the focal plane of a circularly symmetric and aberration free lens is given by [41] (p485-491):

$$I[\nu] = \left[\frac{2J_1(\nu)}{\nu} \right]^2 \cdot I_0 \text{ where, } \nu \text{ is the optical unit with } \nu = r \frac{2\pi}{\lambda} NA \text{ with } r = \sqrt{x^2 + y^2}$$

Equation 2-2

, NA is the numerical aperture and J_1 the Bessel function of the first kind.

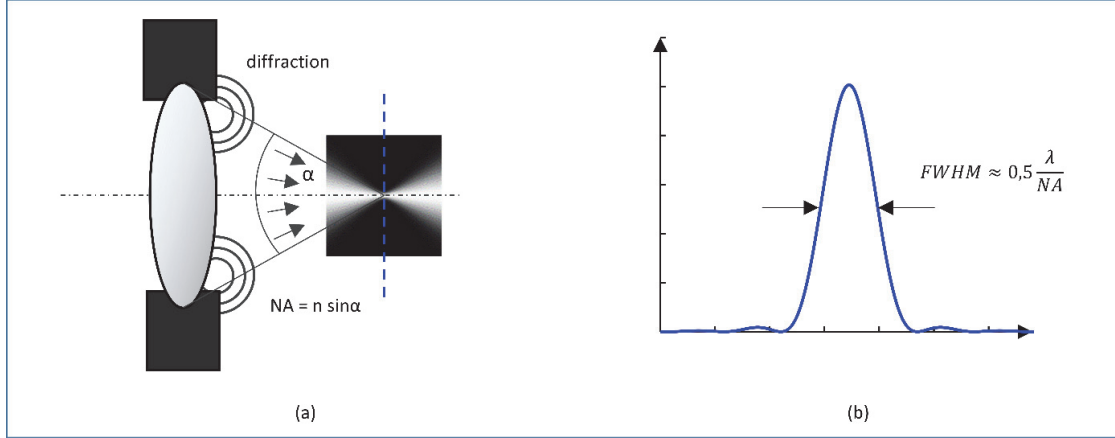


Figure 2-1 Resolution limit in scanning microscopy. (a) A light beam is focused by a lens: diffraction from the edge of the aperture of the lens results in spreading of the focused spot. (b) The intensity profile of the spot obtained at the focus of an ideal lens with a circular aperture is known as the Airy pattern. Its size (generally characterize with the Full Width Half Maximum (FWHM)) is limited by diffraction and is dependent on the numerical aperture of the lens and the wavelength of the light.

This classical result (Equation 2-2) for the focal distribution intensity follows from the Debye and paraxial approximation (Appendix A). As a result, it is not exact for a high numerical aperture but it still provides a good qualitative description to present the performance of optical scanning microscopy (Appendix A). In this section, we will consider a conventional scanning microscope, where all the light is collected for every object point (as opposed to confocal microscopy, for instance). In this way the optical systems that implements the collection does not contribute significantly to the image resolution and the PSF of the imaging system is the excitation PSF. In other words, the excitation beam itself is given by Equation 2-2, since we are considering here fluorescence imaging, we use the intensity PSF. The intensity map of the beam and its profile are displayed in Figure 2-1.

The resolution is the ability of a microscope to distinguish emitters close to each other. It can be defined as the minimal distance between two fluorophores that can be separated through the imaging system. The most common criterion is the Rayleigh one: it stands that under typical imaging condition two point emitters are resolved when the first diffraction minimum of the image of one point source coincides with the maximum of the other. Another reasonable approximation (that takes into account the shape of the PSF) is to consider that the resolution limit corresponds to the full width half maximum of the imaging PSF. The intensity profile given by Equation 2-2 is just a scaled version of the Airy formula that results from diffraction by a circular aperture. So, the Full Width Half Maximum (FWHM) and the position first lateral node (r_0) are given by:

$$r_0 = 0.61 \cdot \frac{\lambda}{NA} \text{ and } FWHM = 0.514 \cdot \frac{\lambda}{NA}$$

Equation 2-3

However, using the separation of two probes in the definition of resolution leads to confusion because it depends on the imaging conditions, especially on the Signal to Noise Ratio (SNR). It also requires an arbitrary criterion to define the resolution, as for example the one given in Eq. 2-3. An alternate way to quantify the resolving power of a microscope is to consider the Fourier Transform of the PSF, the so-called Optical Transfer Function (OTF). Analysis in the spatial frequency domain allows consideration of the action of the imaging system in terms of frequency filtering and is sometimes easier to interpret. Figure 2-2 displays the lateral OTF of an optical scanning microscope both in linear and logarithmic scales.

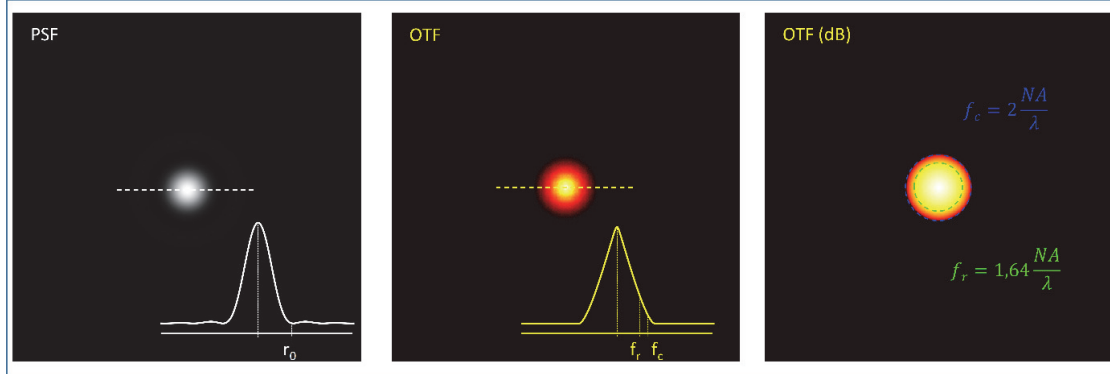


Figure 2-2 An imaging system acts as a low pass filter in the spatial frequency domain. (a) The systems impulse response: the point spread function. In the case of a scanning microscope the image of a point source is the excitation focus itself. The intensity profile of the focused spot is given by Equation 2-2. (b) The Fourier transform of the PSF called the optical transfer function. The profile of the OTF, shows that the spatial frequencies transmitted by the system are more and more attenuated up to the cut-off frequency (f_c). Above f_c no information is transmitted. (c) The OTF in logarithmic scale allows us to visualize the cut-off frequency. Outside of the blue circle, the optical system does not transmit the spatial frequencies it is the absolute resolution limit. However, close to the cut-off the OTF amplitude values are low: the green circle indicates the spatial frequency that corresponds to the resolution limit according to the Rayleigh criterion ($f_r = \left(0.61 \frac{\lambda}{NA}\right)^{-1} = 1.64 \frac{NA}{\lambda}$). The criterion is more severe than the absolute cut-off limit, so f_r is below f_c .

It can be seen in Figure 2-2 that the microscope acts as a low pass filter by transmitting the spatial frequencies only up to a cut-off frequency. In the spatial frequency domain, it is easier to see the absolute performance limit of the imaging system: no information is transmitted above the cut-off frequency. It corresponds to a physical limit of the lens which restricts the angle transmitted to those within the numerical aperture. This angular limit is difficult to visualize in the spatial domain. Obviously the PSF and OTF description are strictly equivalent. The amplitude value of the OTF shows to what extent the transmitted frequencies are attenuated which in practice limits the attainable frequency. The resolution will be then given by the minimum detectable amplitude value of the OTF. The green circle in Figure 2-2c shows the spatial frequency that corresponds to the Rayleigh resolution criterion.

2.2 Breaking the diffraction limit: nonlinear fluorescence scanning microscopy

In the previous paragraph, we stated that the achievable resolution in a scanning microscope is directly related to the numerical aperture of the focusing objective and is thus limited by diffraction from the aperture. We assumed that the sample photoresponse (fluorescence signal) was proportional to the excitation intensity. Therefore, the excitation PSF was equal to the focused excitation beam itself. In far field scanning microscopy, the solution to breaking the diffraction limit involves changing the photoresponse of the signal to make it nonlinear. Indeed, if the fluorescence sample response to the excitation intensity is non-linear it creates harmonics of the spatial frequencies present in the illumination PSF. These harmonics can have spatial frequencies higher than the cut-off frequency imposed by diffraction and extend the spatial frequency content of the effective PSF and as a result improve the resolution.

Here, the Fourier domain enables an easy visualization. The insets in Figure 2-3(a-d) show several possible shapes of focused illumination. They have been generated as linear combinations of high order Bessel beams (exact solution of the non-paraxial Helmholtz equation [42]). In Figure 2-3, it is clear that for any PSF spatial distribution the frequency content remains limited within the cutoff frequency (blue circle), which is the physical limit of the imaging system. Experimentally, this circular boundary would correspond to the back aperture of the microscope objective.

However, if a nonlinear transformation can be applied to the intensity PSF, the corresponding cut-off frequency varies. The simplest example is to consider the fundamental focused spot (inset, Figure 2-3(a)), raised to the power two (Figure 2-3(g)). The corresponding OTF to the squared PSF is the auto-convolution of the fundamental one. Thus, the cut-off frequency is multiplied by two (Figure 2-3(h)). Physically, this case corresponds to a two-photon microscope in which the sample is excited when two photons are absorbed together, so the fluorescence emission is proportional to the excitation intensity squared. In a more general case, if the fluorescence rate is proportional to a nonlinear function of the m^{th} degree, as the real space product corresponds to a Fourier space convolution it inserts m -times larger frequency in the corresponding effective OTF.

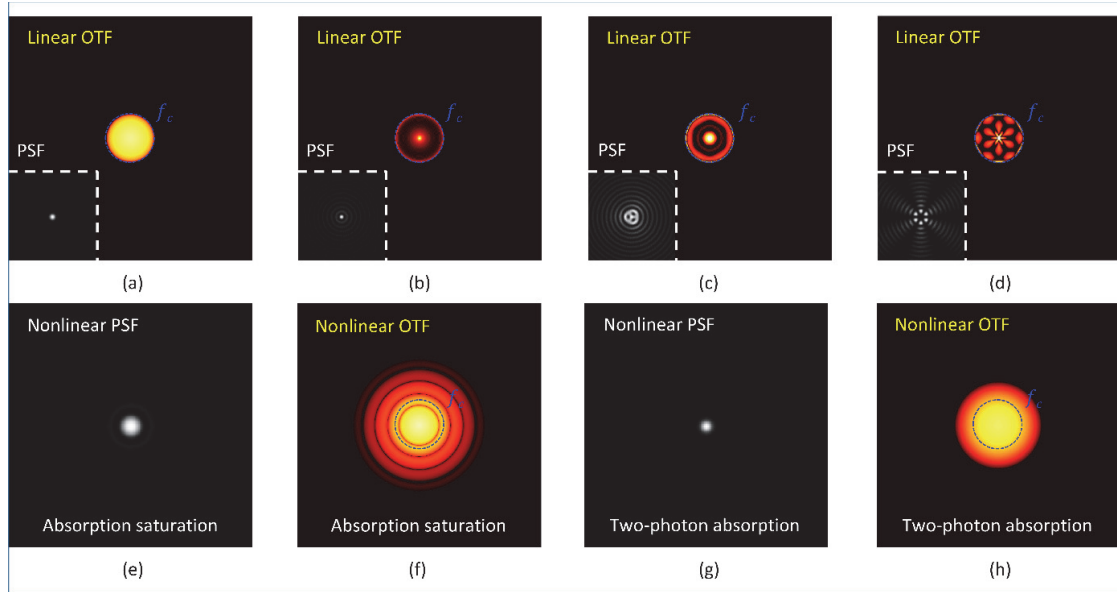


Figure 2-3 Visualization of the limit of diffraction in the Fourier domain.(a-d) Various PSFs (insets) and their corresponding OTFs. In (a), (b), (c) and (d) the PSFs are respectively generated as a focused beam (Airy pattern Equation 2-2), a zero-order Bessel beam, a superposition of higher-order Bessel beams ($l = +3$ and -3) and another higher-order Bessel beam superposition ($l = 1$ and 3). For the different PSFs with different shapes and thus different Fourier transforms, the cut-off frequency remains identical given by the numerical aperture of the system and bound to diffraction (the blue circle indicates the cut-off frequency (f_c)). (e-h) Non-linear microscopy breaks the diffraction limit. (e-f) Resulting PSF when the fluorescence sample saturates under high excitation and the corresponding OTF. (g-h) Resulting PSF when two-photon absorption fluorescence is used and the corresponding OTF. The two non-linear photoresponse mechanism (saturation and two-photon absorption) leads to a broader OTF, exceeding the linear cut-off frequency. Thus, a nonlinear fluorescence response creates higher frequencies information and allows to improve the resolution. All the PSF figures are normalized and shown with a linear scale, while all the OTF are shown with a logarithmic scale with a 130 dB range (that's why the saturated OTF does not appear infinite).

In two-photon microscopy the gain in resolution is immediate. As it can be observed in Figure 2-3(g), the extended frequency content in the OTF results in a narrower PSF and a gain in resolution by a factor $\sqrt{2}$ [43]. However, this is specific to this type of nonlinearity and this shape of PSF. Another way to obtain a nonlinear object response emission rate to the illumination is to increase the power so much that the ground state of the fluorophore becomes depleted, or in other words the fluorescence signal saturates. The fluorescence saturation, as any nonlinear relation, increases the width of the OTF. Fluorescence saturation is a non-polynomial nonlinearity so it has an infinite number of Taylor series terms (more details in Chapter 5, Appendix B and Appendix H). In consequence, as can be observed in Figure 2-3(f), the cut-off frequency increases much more than for two photon absorption. However, fluorescence saturation results in a broader PSF (Figure 2-3(e)), which leads to degraded images. This is the reason why it has been avoided for a long time in microscopy instrumentation [43]. Nevertheless, even if it is hidden in the PSF lobes, higher resolution information is still present and can be extracted. As proposed in [44], one way is to use a vortex beam with a donut shape. The saturation then reduces the size of the central node (the potential resolution gain can be visualize with the narrowing of this donut valley, Figure 2-4(c)). As it can be observed in Figure 2-4, a negative image with dark spots whose size is below the resolution limit can be obtained (Figure 2-4) and be reversed by deconvolution if the sample is sparse enough(Figure 2-4(d)).

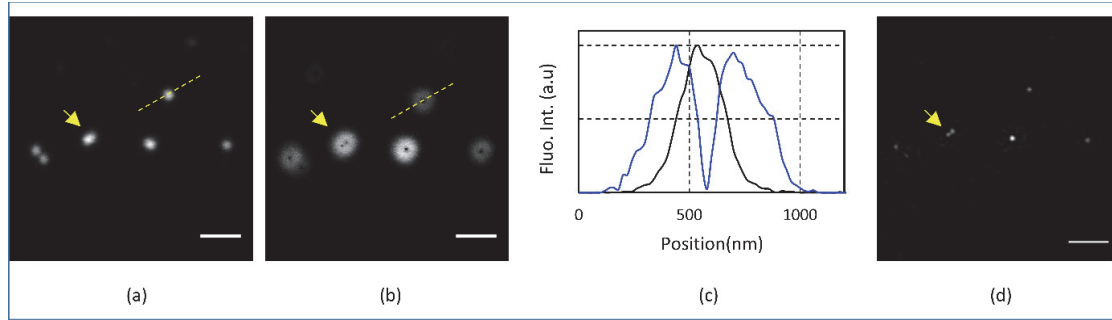


Figure 2-4 Breaking the diffraction limit in nonlinear scanning microscopy: a single beam experimental demonstration. (a) Linear (low excitation power) image of 10nm fluorescent particles immobilized on a glass slide. (b) Saturated (high excitation power $\approx 10\text{mW}$, focused with a 1.4NA objective) scanning image with a donut shaped excitation beam. The gain in resolution is visible on the particles pointed with the arrow. On the linear image the two particles cannot be distinguish while two dark spots are visible on the saturated one. (c) Intensity profile along the two the dashed lines on (a) and (b). It also illustrate the resolution gain with saturation: the FWHM of the saturated donut beam valley (110nm) is smaller than the FWHM of the conventional linear focused beam (240nm). (Because, the saturated PSF contains higher spatial frequencies) (d) Direct deconvolution of the image (b). The two particles pointed by the arrow, invisible in the linear image, are now resolved. All the scale bars are 1 μm .

We stated that a nonlinear mechanism is a fundamental requirement to overcome the diffraction limit. However, a large part of the literature is dedicated to methods that improve the resolution by a factor of two without a nonlinear mechanism. The most famous example is structured illumination microscopy (SIM). At first glance the two statements seem to be in conflict but there is no contradiction. Indeed, SIM methods all use two different imaging systems, one for illumination and one for the detection. Both the collection and the detection PSFs remain fundamentally limited by diffraction as we described previously, but their combination doubles the maximum spatial frequency of the equivalent PSF and as a result the resolution. Under this category, within scanning microscopy, confocal microscopy [45,46], subtraction microscopy [47,48] or tomographic microscopy [49] have all been demonstrated to improve the resolution by a factor of two.

Thus, linear methods remain fundamentally limited to a factor of two improvement in resolution. To completely break the resolution limit in microscopy and envisage higher gain in resolution, nonlinear response is the fundamental requirement. Any nonlinear mechanism can potentially be exploited. For instance, the metastable dark state of nitrogen vacancies in diamonds [50] and reverse saturation of scattering from gold nanoparticles [51,52] have been used. However, most of the scanning superresolution microscope methods that have been demonstrated (STED microscopy, saturation structured illumination, Ground State Depletion) [26,28,44,53,54] use some sort of saturation mechanism of the fluorescence signal. The major advantages which explain this predominance is that fluorescence provides high contrast and saturable transitions have a potentially unlimited resolution [55]. All of these transitions are known in the literature as REversible Saturable Optical Fluorescence Transitions (RESOLFT). In this thesis we will demonstrate various techniques all based on RESOLFT, with different architectures aiming at improving specific issues.

2.3 Gold standard in nonlinear fluorescence scanning microscopy: STED microscopy

2.3.1 General principle

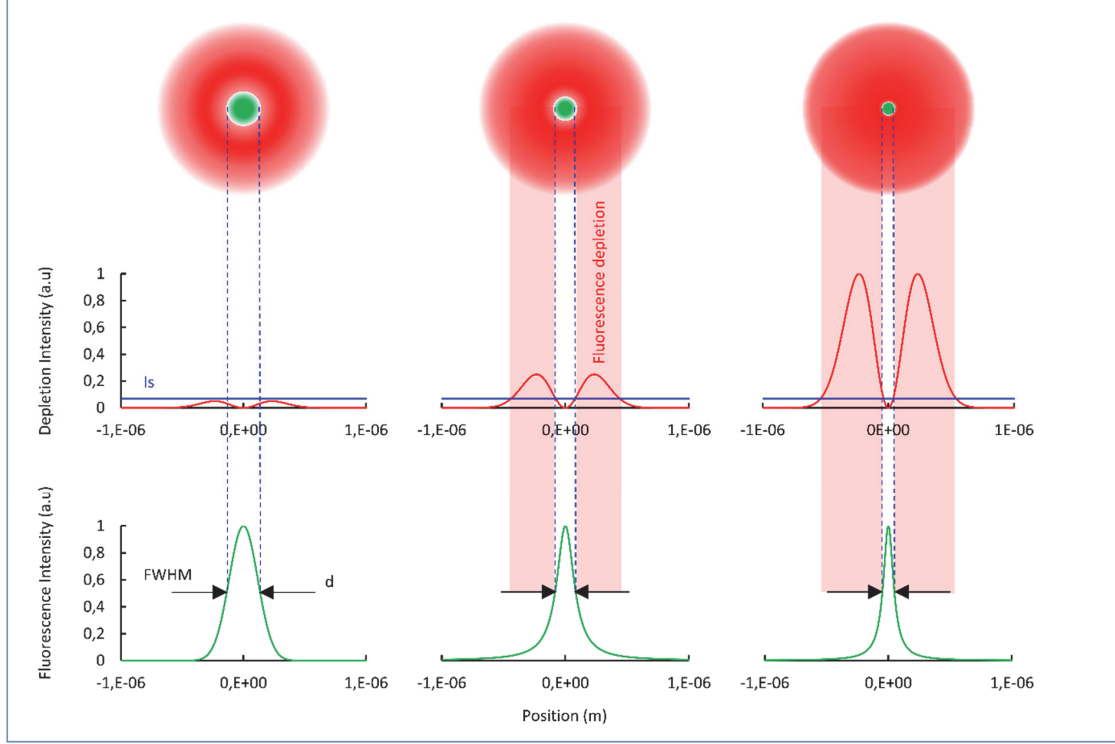


Figure 2-5 Principle of STED microscopy. (adapted from [56]) First row: 2D map of the two beams needed: one focused beam for the excitation (green) and one donut shaped focus beam for the depletion (red). Second row: Intensity profile of the depletion beam. The horizontal blue line indicates the value of the saturation intensity (I_s). The saturation intensity is the threshold intensity value above which more than half of the fluorescence is depleted. Third row: the resulting equivalent excitation intensity profile for STED imaging. All the rows, from left to right the depletion beam power increases. In a rough approximation (approximating the excitation beam to a plane wave and applying the Equation 2-14, details below), the value for which the depletion beam reaches I_s corresponds to the FWHM of the equivalent resulting excitation beam. The highest intensity value is at the donut crest, the more the depletion process saturates, and the narrower is the resulting PSF.

The principle of STED microscopy is to superimpose onto the excitation focused light beam another beam structured with an annular shape (the depletion beam) (Figure 2-5). This second beam inhibits the fluorescence of the sample by inducing stimulated emission. The fluorescence is only possible where the depletion beam intensity is the weaker and is completely quenched where the depletion beam intensity is higher. The center of the depletion beam is completely dark so by increasing the power of the beam, the intensity of the depletion beam increases and the volume where the fluorescence is possible decreases (Figure 2-5). In consequence, the resolution is improved.

In theory, by increasing the laser power indefinitely the resolution improvement would be infinite. In practice, the available power of laser source and imperfections in the depletion beam shape limits the resolution to nanometers [44].

2.3.2 Resolution gain by stimulated emission depletion

We explained in the previous section that, in imaging methods not limited by diffraction, the improvement in resolution results from a nonlinear photoresponse. In the case of STED microscopy, the fluorescence is depleted by stimulated emission and at high intensity the inhibition of the fluorescence saturates and depends nonlinearly on the depletion intensity. We derive here the expression for the suppression factor (residual fraction of fluorescence with both excitation and depletion beam on) and the corresponding resolution [56–58].

If we assume a stationary state and a four-level Jablonski diagram [59] (Figure 2-6(a)), the energy levels dynamic behavior is described by the equations in Figure 2-6(b):

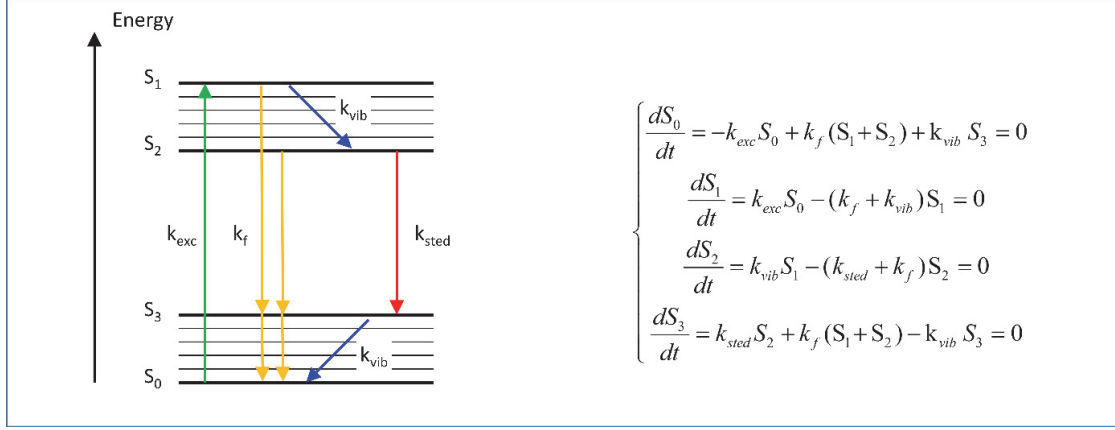


Figure 2-6 STED depletion energy diagram. (a) Jablonski diagram illustrating the transition involved in STED microscopy. k_{exc} and k_{sted} are the absorption rate for the excitation beam and the depletion beam respectively, k_f is the spontaneous fluorescence emission rate, k_{vib} is the a rate of the non-radiative transition between vibrational sub level (b) System of equation describing the dynamic of the energy states of the fluorescence molecule under CW illumination by the excitation and depletion beam.

To solve this system, we combine the second and the third equation of Figure 2-6 and we get:

$$S_2 = \frac{k_{vib} \cdot k_{exc}}{(k_{vib} + k_f)(k_{sted} + k_f)} S_0 \quad \text{Equation 2-4}$$

where, k_{exc} , k_{sted} , k_f and k_{vib} are defined in Figure 2-6.

Typical non-vibrational transitions have decay time of picoseconds, while the fluorescence decay time is of the order of nanosecond, so $k_{vib} \gg k_f$. Also, as long as I_{exc} is kept low $k_{exc} < k_f$ (we do not saturate the absorption), so $k_{vib} \gg k_{exc}$. As k_{vib} is much larger than the other rate, the states S_1 and S_3 are instantly unpopulated in the state S_2 and S_0 , so we can write:

$$S_1 = S_3 = 0 \Rightarrow S_0 + S_2 = 1 \quad \text{Equation 2-5}$$

Using Equation 2-4 and Equation 2-5 we obtain:

$$S_2 \left(1 + \frac{(k_{vib} + k_f)(k_{sted} + k_f)}{k_{vib} \cdot k_{exc}} \right) = 1 \quad \text{Equation 2-6}$$

From which, with $k_{vib} \gg k_{exc}$:

$$S_2 \left(1 + \frac{(k_{sted} + k_f)}{k_{exc}} \right) = 1 \Rightarrow S_2 = \frac{k_{exc}}{k_{sted} + k_f + k_{exc}} \quad \text{Equation 2-7}$$

Thus we can determine the suppression factor ($\eta(x)$) in continuous STED (i.e. the fraction of fluorescence which is not depleted):

$$\eta(x) = \frac{S_2(I_{STED}(x))}{S_2(I_{STED}(0))} = \frac{k_f + k_{exc}}{k_f + k_{exc} + k_{sted}} \quad \text{Equation 2-8}$$

Where I_{STED} is the depletion intensity profile. Under small enough excitation intensity ($k_{exc} \ll k_f$), it can be simplified:

$$\eta(x) = \frac{1}{1 + \frac{k_{STED}}{k_f}} = \frac{1}{1 + \frac{\sigma \cdot \lambda_{STED} \cdot I_{STED}(x)}{h \cdot c} \tau_f} = \frac{1}{1 + \frac{I_{STED}(x)}{I_{Sat}}} \quad \text{with } I_{Sat} = \frac{hc}{\sigma \lambda_{STED} \tau_f} \quad \text{Equation 2-9}$$

Where I_{sat} is the intensity needed to decrease the population of the excited state (S_2) (i.e. to deplete half of the fluorescence signal), h is the Planck constant, c the speed of light, λ_{STED} the STED wavelength, σ the STED cross-section and $\tau_f=1/k_f$ the fluorescence lifetime. Equation 2-9 indicates that the fluorescence rate is depending nonlinearly on the depletion intensity. As the relation is not polynomial, it can be expressed as an infinite Taylor series and it has the potential for unlimited improvement in resolution.

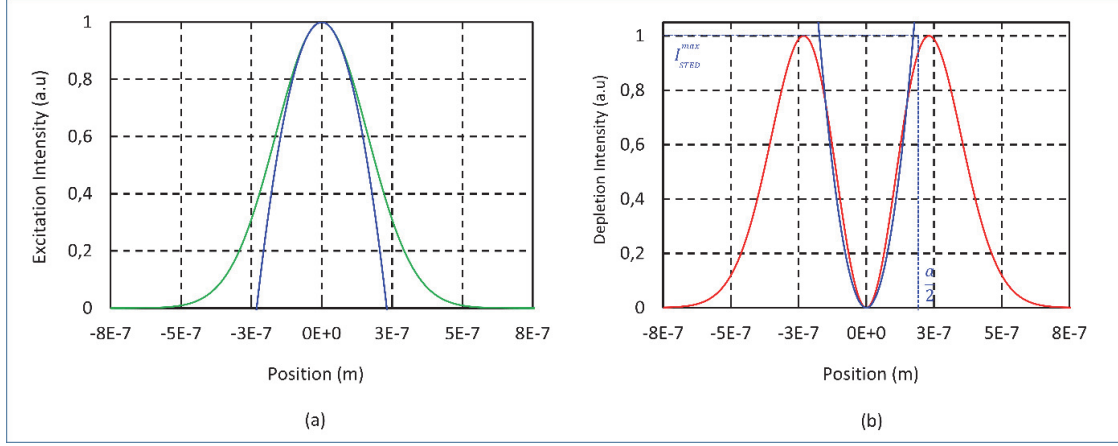


Figure 2-7 Approximation used for analytical fit of excitation and depletion beams (close to the center). (a) The numerically simulated excitation beam profile (green) is fitted with a negative parabola (blue) (Equation 2-10) (b) The numerically simulated depletion beam profile (red) is fitted with a parabola (blue) (Equation 2-11). The parabolic function is such that the position value $\frac{a}{2}$ corresponds to the maximum depletion beam intensity.

We can now calculate the resulting equivalent PSF with the excitation and depletion beam on. The intensity spatial profile of the excitation (I_{exc}) is well approximated with a Gaussian (with FWHM d_{exc}) and in the vicinity of the maximum is approximated by its Taylor expansion:

$$I_{exc}(x) \approx e^{-\ln 2 \left(\frac{2x}{d_{exc}} \right)^2} \sim 1 - \ln 2 \left(\frac{2x}{d_{exc}} \right)^2 \quad \text{Equation 2-10}$$

The spatial profile of the central hole of the donut (I_{sted}) is approximated by a parabola [57]:

$$I_{STED}(x) = 4I_{STED}^{max} \left(\frac{x}{a} \right)^2 \quad \text{Equation 2-11}$$

With a and I_{STED}^{max} constants defined in Figure 2-7. The resulting equivalent excitation PSF profile ($I_{exc,res}$) is given by the product:

$$I_{exc,res} = I_{exc} \cdot \eta(I_{STED}) \quad \text{Equation 2-12}$$

We determine the FWHM ($d_{exc,res}$), using Equation 2-9 to Equation 2-12 we solve:

$$I_{exc,res} \left(\frac{d_{exc,res}}{2} \right) = \frac{1}{2} \Rightarrow d_{exc,res} = \frac{d_{exc}}{\sqrt{\left(\frac{d_{exc}}{a} \right)^2 \frac{I_{STED}^{max}}{I_{Sat}} + 2 \ln 2}} \quad \text{Equation 2-13}$$

And if we approximate $d_{exc} \approx a$ and $2 \ln 2 \approx 1$, we find the square root dependency largely used in the literature [53,57]:

$$d_{exc,res} \approx \frac{d_{exc}}{\sqrt{1 + \frac{I_{STED}^{max}}{I_{Sat}}}}$$

Equation 2-14

Thus, we obtain an approximation of the FWHM $d_{exc,res}$ of the resulting equivalent excitation beam in STED microscopy. This value depends on the intensity of the depletion beam and the original width of the linear excitation beam. We can see that I_{sat} corresponds to the value to obtain a $\sqrt{2}$ gain in resolution. We can also see that with an infinite depletion intensity the resolution tends to zero. With careful implementation up to 6nm FWHM (with pulsed laser, [26]) has been demonstrated with STED nanoscopy. However, as we detail in the section 2.4, to avoid too much experimental imperfections, it needs some technical refinement.

2.3.3 A nonbleaching nanometric label for STED microscopy: Fluorescent nanodiamonds:

One of the major limitations of nonlinear microscopy techniques based on the saturation of a fluorescence transition is that it requires high laser intensity illumination, which induces photobleaching. Indeed, in STED microscopy, the depletion intensity required is of the order of 0.1-1 GW.cm⁻². At such a high illumination intensity, the creation of triplet state is enhanced [60]. As the triplet is long-lived with respect to the singlet excited state, it promotes the chemical interaction of the molecule with its environment, and the molecule can lose its ability to fluoresce. In order to limit photobleaching in STED microscopy, many solutions have been presented. The acceleration of the scanning speed reduces the dwell time and allows the acquisition of the images before the signal bleaches [61]. The reduction of the repetition rate limits the triplet-built up and increases the number of cycle fluorescent molecules can undergo before bleaching [60]. The use of cryogenic temperature improves the photo-bleaching resistivity [62]. Despite those improvements three-dimensional STED imaging requiring multi-stacks remains challenging and long-term studies are impractical.

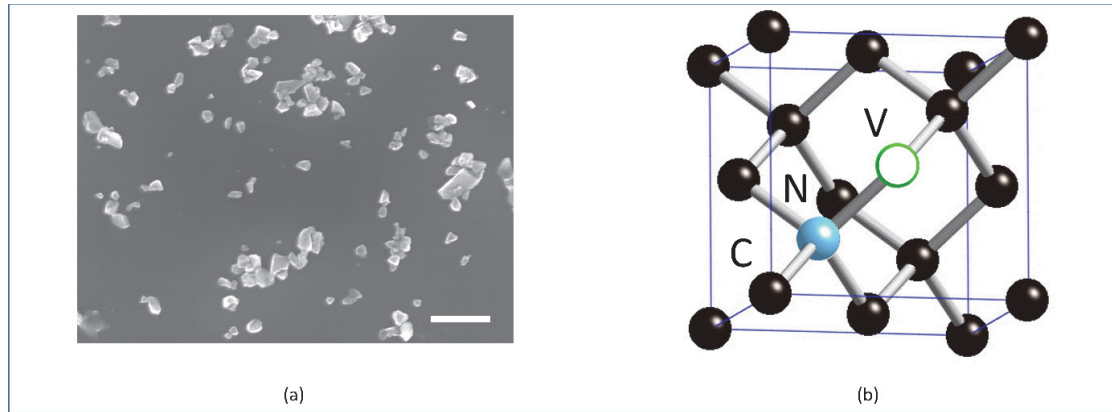


Figure 2-8 Nanodiamonds containing NV defects. (a) Scanning electron microscope image of NDs containing NDs dried on a silicon wafer (120 nm FNDs ordered from Adamas-Nano). Scale bar is 500 nm. (b) Schematic of the NV color center in the diamond lattice (black spheres). The NV center is composed of one vacancy (i.e. one missing carbon atom, green circle) next to one substitutional nitrogen atoms (blue sphere).

The development of fluorescent nanosized diamonds (FNDs), solves this problem since FNDs do not exhibit photobleaching even under high light intensity illumination. Indeed, diamond crystals contain defects consisting of missing atoms or of impurity atoms. Some of those defects called color center are fluorescent. As they are protected from their environment by the solid diamond matrix, they emit a perfectly photostable luminescence, free from blinking or bleaching behavior. The nitrogen-vacancy (NV) defect has been widely studied, and artificially generated inside nanodiamonds by protons beam irradiation [25]. The NV center is composed of one vacancy next to one substitutional nitrogen atom in the diamond lattice (Figure 2-8 (b)). As it can be observed in Figure 2-9 (a), it exhibits a fluorescence emission peak at 670 nm and red fluorescent nanodiamonds (rNDs) of different sizes are now commercially available (AdamasNano). Thanks to this absence of photobleaching rNDs (Figure 2-9 (b)) are excellent sources for STED microscopy and other non-linear techniques that requires high illumination intensities. A perfect photostability really changes the range of possible applications: single NV centers have been used as single photon source [63] but also to demonstrate the highest resolution (below 10 nm) in STED microscopy [26]. The absence of photobleaching also opens the door for different evolutions like the one we present in the next chapters: since milliseconds stationary illumination of the sample is not prohibited by bleaching, it allows the use of multi-pixel detectors (Chapter 3) or spatial light modulator based scanning systems (Chapter 5).

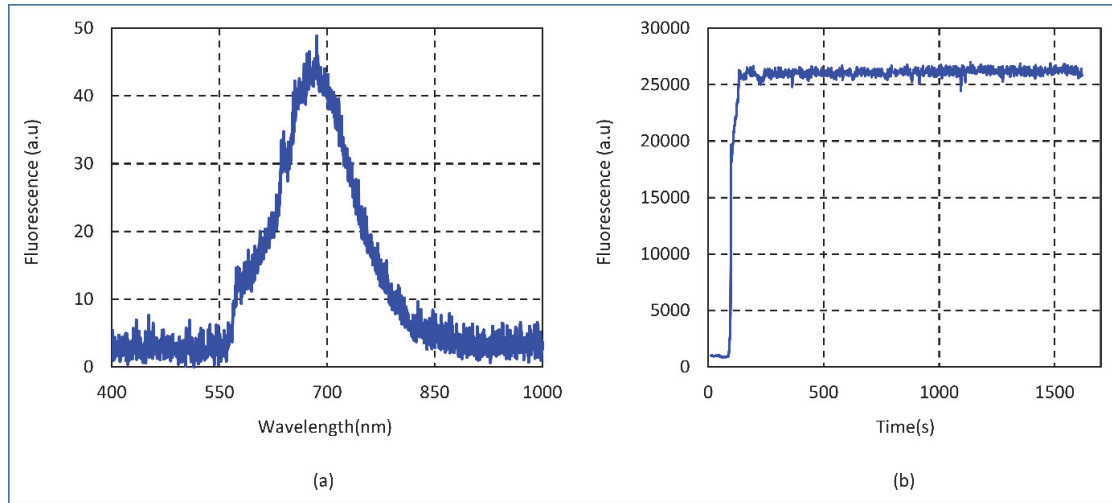


Figure 2-9 Fluorescence properties of red nanodiamonds (a) Emission spectrum of the NV color center. (b) Fluorescence signal under CW excitation of a single ND containing NV centers in function of time. The signal remains constant exhibiting no sign of photobleaching.

The development of FNDs probes for bioimaging is an active research field. Some limitations like the size and the brightness inhomogeneity remain. But FNDs are not only a nice characterization tool for novel superresolution techniques. Numerous studies have shown their low phototoxicity [25,64,65] and the synthesized particles are improving towards the ideal bio-compatible label. Some molecular sized FNDs have been obtained [66], making them non-perturbative thanks to a size comparable to a protein. Some surface functionalization have also been developed for targeted labelling [65,67]. The defects density has been increased to obtain higher brightness [65,68]. Different defects in FNDs have been investigating for multicolor labelling [69] (section (2.5)). Thus, it can be expected that FNDs will become an important and viable bio-label, especially for long term observation. In the next section, we use rNDs as a fluorescence sample to characterize the performance of our CW STED microscope. As illustrated in Figure 2-10, NV fluorescence can be excited with a green laser (Verdi V10 from coherent) and depleted with a near IR laser (Mira 900, from Coherent) which were directly available in our laboratory.

2.4 Implementation of a STED microscope for FNDs imaging:

2.4.1 Setup

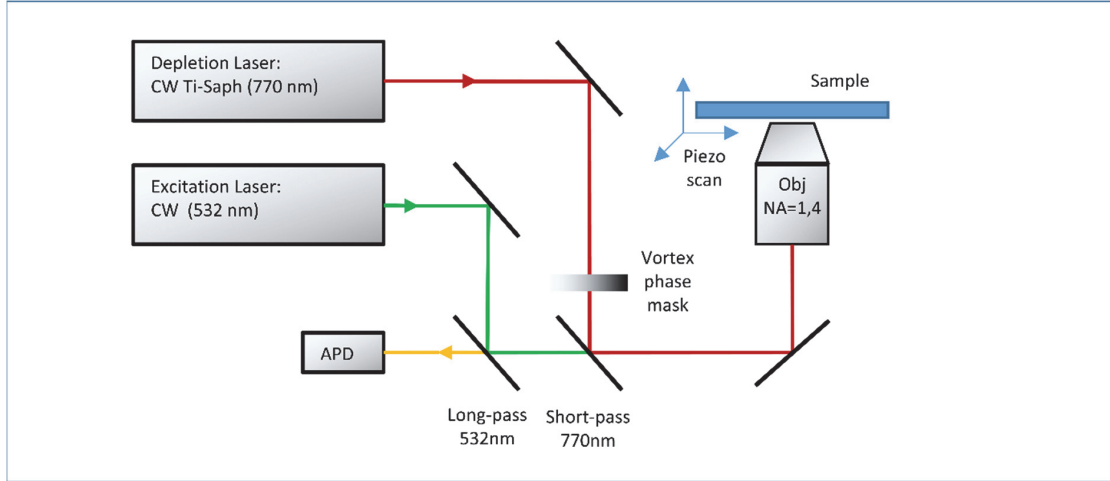


Figure 2-10 Simplified STED microscope setup. The excitation beam is taken from a 532nm DPSS laser. The depletion beam is taken from a Ti-Saph Mira laser tuned at 770 nm. The two beams are combined with dichroic mirrors and focused with a high NA objective. The sample is scanned with a fast piezo electric stage and the signal is collected with an avalanche photodiode.

The base of a STED microscope is a scanning fluorescence microscope on which the depletion laser line has been added. So, on our setup, two laser lines can be observed: the excitation beam and the depletion beam are both focused with a high numerical aperture lens. The sample is placed in the focal plane of the objective and moved with a piezo electric stage. The fluorescent image is acquired by recording point by point the fluorescence signal from the sample.

The most popular wavelength range for depletion in STED microscopy is the near infrared. First because the early demonstration [70] used high power pulsed laser (and Ti-Sapphire is the most common) and then because of the low scattering in tissue that allows to maintain a stable donut shape intensity profile. For our depletion laser we used a Titanium-Sapphire laser in continuous mode. The available output power is about 1W. To guarantee a clean intensity profile, the beam is spatially filtered with a precision pinhole resistant to high power. The beam is collimated so that its diameter is about twice the diameter of the objective back aperture (compromise in between overfilling objective aperture and minimizing the loss). It has been shown that in order to cancel the longitudinal component at the focus of a high NA objective and thus to obtain a good donut beam, the polarization should be circular of the same handedness than the helicoidal phase profile [71] (cf. 2.4.3). A half and a quarter wave plate are used to adjust the polarization just before the objective.

The excitation beam is also spatially filtered and expanded to overfill the objective back aperture. The collimation is adjusted to obtain the exact same focusing plane than for the depletion beam. It is critical to obtain a good alignment in the axial direction, otherwise (without a confocal pinhole), the section where the excitation is larger than the depletion beam results in a fluorescence halo around the STED PSF. Even if the objective used is corrected for chromatic aberration (Olympus, ApoPlan), the excitation beam used is slightly divergent before the objective in order to match axially with the depletion beam.

The detection is made with an avalanche photodiode (APD). The light is focused on the small APD sensor (50 μm) to make sure that there is no aperture effect (all the light collected by the objective is transmitted). Hence the detection does not contribute to the image formation and the excitation and depletion PSFs can be measured (with backscattered light from 80 nm gold particles). For fluorescent imaging, a pinhole of 0.8 Airy units can be placed in an intermediate plane (image plane of the objective focal plane) to obtain confocal sectioning.

2.4.2 NV defects depletion by stimulated emission

Before performing STED images, we measure the non-linear dependence of the depleted population of the excited molecule on STED laser beam intensity. To make sure that we are able to achieve complete suppression of the fluorescence, we remove the vortex phase plate and we place a single rFND under the co-aligned focused excitation and depletion beams.

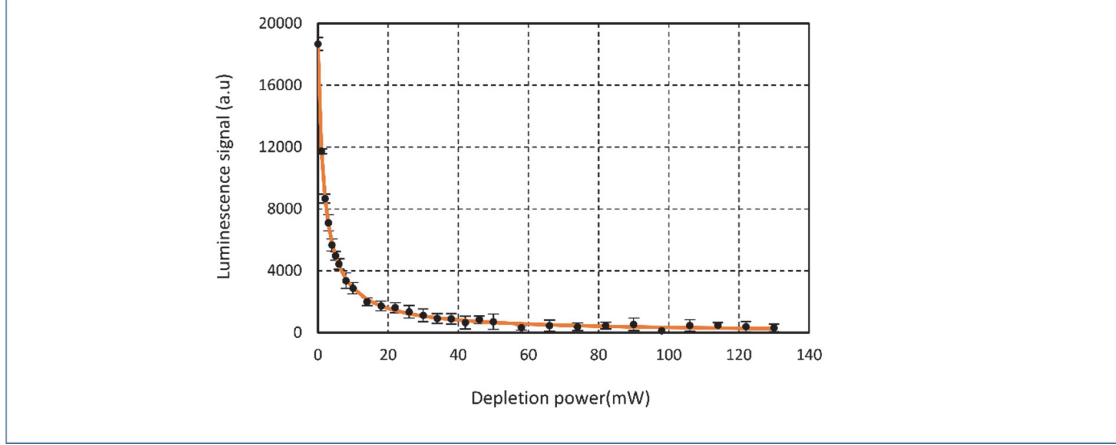


Figure 2-11 Luminescence inhibition of NV center by stimulated emission. One rND is excited with a low power beam (532nm) and the depletion beam (770 nm) with the same shape is superimposed. The fluorescence signal remaining in function of another NV. The curve is an average over 18 NDs. To determine the saturation depletion intensity (I_{sat}) the curve is fitted with Equation 2-15, and I_{sat} is found to be 1.87 mW.

To ensure that the excitation process does not compete with the depletion process, we excite the rND with a low laser power ($\approx 100 \mu W$). The fluorescence signal is recorded while the depletion beam power is increased. As detailed in the section 2.3.2, the dependency of the fluorescence signal on the depletion intensity can be written (from Equation 2-9) as:

$$I_{flu} = \frac{I_{flu}^0}{1 + \frac{I_{STED}(x)}{I_{Sat}}} \text{ with } I_{Sat} = \frac{hc}{\sigma \lambda_{STED} \tau_f} \quad \text{Equation 2-15}$$

Where I_{flu}^0 is the fluorescence signal with no depletion beam. It can be observed in Figure 2-11 that the fluorescence signal gets inhibited with increasing the STED intensity. As expected, above the threshold value (I_{sat}), stimulated emission is the dominant process with respect to spontaneous fluorescence emission, therefore at high depletion power the fluorescence signal is completely switched-off. To characterize the depletion efficiency and measure I_{sat} , the experimental points are fitted by the Equation 2-15 and I_{sat} is found to be 1.87 mW. According to Equation 2-14, the relatively low value of I_{sat} and the sharp edge transition in Figure 2-11 should lead to provide high spatial resolution with high STED intensity.

2.4.3 Generation of donut-shaped beam

We have demonstrated the possibility to deplete efficiently FNDs fluorescence with 770 nm laser wavelength. To exploit this sharp edged transition and improve the microscope resolution we now need to shape the beam. To obtain fine resolution with STED microscopy we generate a deep intensity valley around the excitation focus: the steeper is the node the higher will be the resolution (Figure 2-5). One of the critical parameter is to maintain the intensity in the center of the depletion ring as close as possible from zero even at high depletion intensity. Indeed, if we consider an imperfect donut with nonzero central intensity written as:

$$I_{STED}(x) = I_{STED}^{max} \left(4 \left(\frac{x}{a} \right)^2 + \varepsilon \right), \text{ with } \varepsilon \text{ being the depletion beam contrast defined as } \varepsilon = \frac{I_{STED}(0)}{I_{STED}^{max}} \quad \text{Equation 2-16}$$

Using the imperfect donut profile (Equation 2-16) and following the same derivation than in the paragraph 2.3.2 we find the resulting FWHM:

$$d_{exc, res, \epsilon} \approx \frac{d_{exc} \sqrt{1 + \epsilon \frac{I_{STED}^{max}}{I_s}}}{\sqrt{1 + \frac{I_{STED}^{max}}{I_s}}} \quad \text{Equation 2-17}$$

At moderate depletion beam intensity, $\epsilon I_{STED}^{max} = I_{STED}(0) < I_s$ and $I_{STED}^{max} > I_s$ so the resolution is improved when the depletion beam intensity is increased. But, in the limit of high depletion beam intensity, the resolution saturates at a minimum value:

$$d_{exc, res, \epsilon} \approx d_{exc} \sqrt{\epsilon} \quad \text{Equation 2-18}$$

In addition to this direct impact on the resolution, an imperfect central zero has a dramatic impact on the available signal. Indeed, the presence of depletion light in the center of the donut limits the brightness of the sample. Figure 2-12 displays calculated curves for the equivalent STED PSFs for $\epsilon = 0, 0.01, 0.02$ and 0.05 . The strong influence of an imperfect central zero intensity point is clearly visible. Already for $\epsilon = 0.02$ the fluorescence signal is quenched by 2 (This value depends of saturation level of the depletion process, it is obviously more sensitive for high depletion power. We took here $I_{STED}^{max} = 50I_s$). Even if the theoretical impact on resolution is limited, experimentally, it greatly limits the available SNR and so the image quality and the achievable resolution.

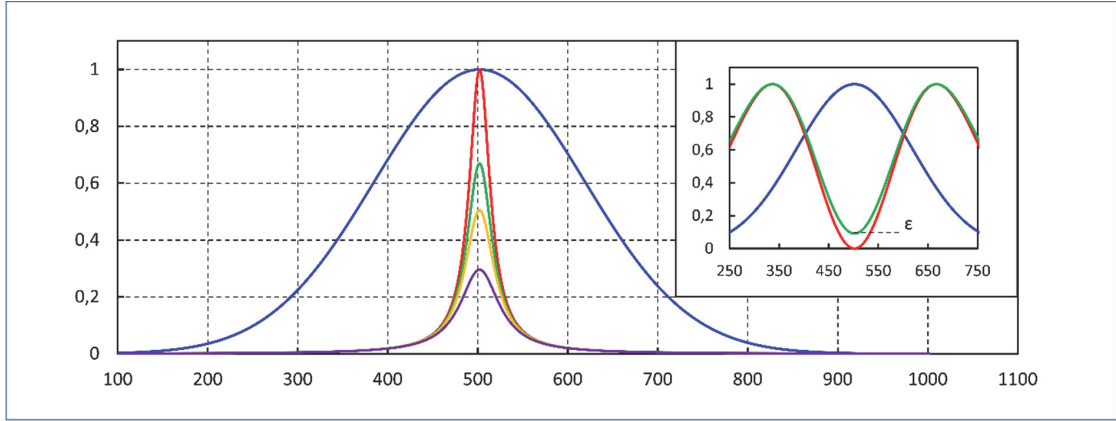


Figure 2-12 Calculated STED equivalent PSF for $I_{STED}^{max} = 50I_s$ and for different values of the depletion beam contrast. The red curve corresponds to a perfect “zero” in the center of the depletion beam. The green, yellow and purple curve correspond to imperfect central zero values of respectively $\epsilon=0.01$, $\epsilon=0.02$, $\epsilon=0.05$.

There are mainly two imperfection sources that can deteriorate the quality of the central zero: aberrations [72] and the polarization state [56,71] of the beam. In order to evaluate the quality of the beam, we recorded images with the backscattered light from a nanometric gold particle (80 nm) that acts like a point object. In order to avoid strong reflection at the air-glass interface we immobilized the bead on a glass coverslip surface treated with poly-L-lysine and we embedded them in immersion oil [73]. The intensity PSFs for excitation and depletion are displayed in Figure 2-13, the FWHM of the excitation beam (Figure 2-13(a)) is ≈ 220 nm. Such successive images are also used for the fine alignment to superimpose exactly the excitation peak and the center of the donut both axially and laterally.

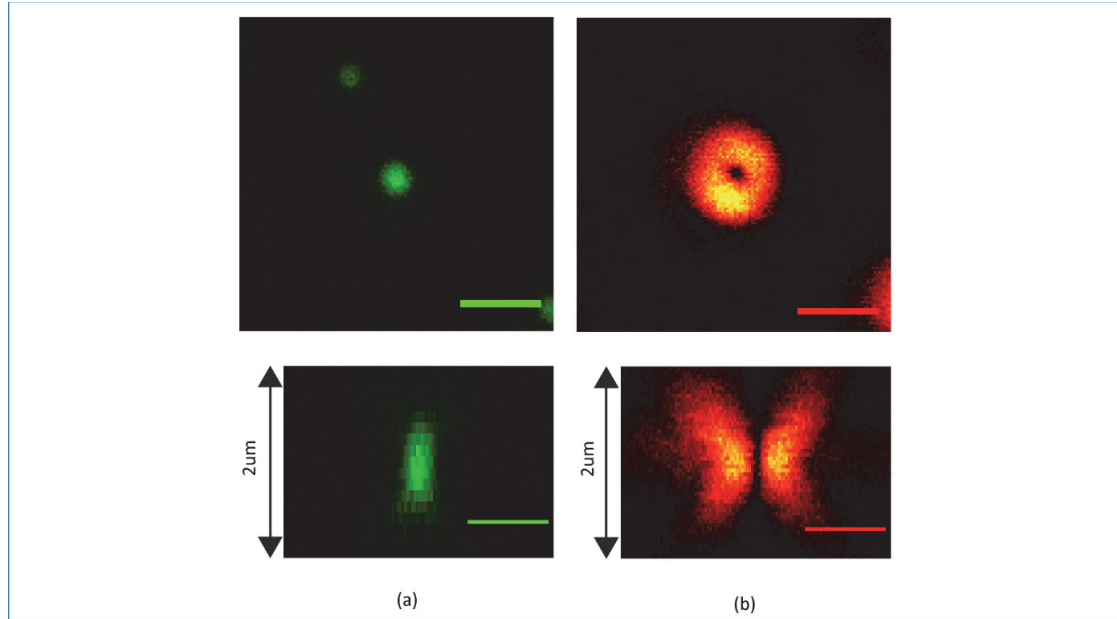


Figure 2-13 PSFs of the home-built CW STED microscope recorded with the backscattered light of a single 80 nm gold nanosphere (with a nonconfocal detection). (a) The excitation PSF (green). In the focal plane (up), the focused beam FWHM is measured to be 220 nm, close to the diffraction limit, indicating good refractive index match at the interfaces and minimal aberration. In the longitudinal profile (down), a slight spherical aberration can be observed. (b) The depletion PSF (hot red). After alignment of the depletion beam we obtain a pretty homogeneous repartition of the intensity around the donut ring in the focal plane (up). On the longitudinal profile (down), the propagation of the dark singularity along the optical axis can be observed. Scale bars are 750 nm.

-Aberrations

Some theoretical work has been done specifically on the aberrations propagation in the optical vortices and their consequences for STED nanoscopy when they are focused with high NA objective [72]. We use here their conclusions to detail the requirements for the practical generation of a high quality donut beam. In order to guarantee the quality of the central zero, all the components of the beam should destructively interfere, i.e. the circular symmetry of the phase profile should not be affected. In consequence, all the circularly asymmetric aberrations like astigmatism or coma should be avoided. In theory they are caused respectively by lateral or axial shift tilt of the beam compared to the optical axis (the objective axis). In consequence, they can be eliminated by working with a well-centered parallel beam, and then by placing the vortex phase mask in the center of the beam. After careful alignment of the incident beam spherical aberrations remain and are more complicated to eliminate (Figure 2-13(a)). Fortunately, spherical aberrations do not affect the circular symmetry of the beam, and thus they do not affect the quality of the central zero. However, it will tend to deteriorate the symmetry along the z axis and to elongate the beam [72]. This results in a lower maximal intensity at the focus and it leads to a lower gain in resolution. To minimize the spherical aberrations it is important to work with a well index matched immersion oil and mounting medium and the correct coverslip thickness (usually 150 μm for high NA objectives). It must be noted that systematic aberrations correction with adaptive optics has been used by other groups to avoid the tedious beam alignment [23], but this implies important power loss. This is especially relevant in three dimensional STED in order to maintain the best possible beam quality in thick media. It can be observed in the Figure 2-13(a) that the excitation beam exhibits a small asymmetry in the axial (z axis) direction and an elongation characteristic of spherical aberration. However, the available power from the laser allow to keep a level of intensity in focus sufficient to obtain high-resolution enhancement (cf Figure 2-15).

-Polarization effect

In STED microscopy, in order to have both the highest resolution before linear improvement and to get very high depletion intensity in the focal plane, high NA objectives are used. In consequence, the paraxial approximation does not apply and polarization effects affect the focused intensity profile. Indeed, if a linearly polarized with a $0-2\pi$ vortex phase profile beam is focused (inset Figure 2-14(a)), a non-negligible longitudinally polarized beam component is generated in the center of the beam [71] forbidding

any resolution improvement. To achieve a high contrast donut focal spot, the light after the phase plate at the input of the objective should have a circular polarization of the same handedness as the topological charge of the vortex phase plate [71]. Moreover, circular polarization of the depletion beam minimizes also photo-selection effects (influence of molecular orientation) that can reduce the efficiency of the depletion process [74]. Two successive half and quarter wave plates are used to obtain the desired polarization. The positions of the wave plates are optimized by using a rotating polarizer and a photodiode.

After optimization of the beam alignment and polarization profile, the depletion beam displayed in Figure 2-14(a) is obtained. As it can be seen on the profiles (Figure 2-14(b-c)) the generated donut beam exhibits peak to zero ratio intensity $\epsilon=0.011$ and $\epsilon=0.012$.

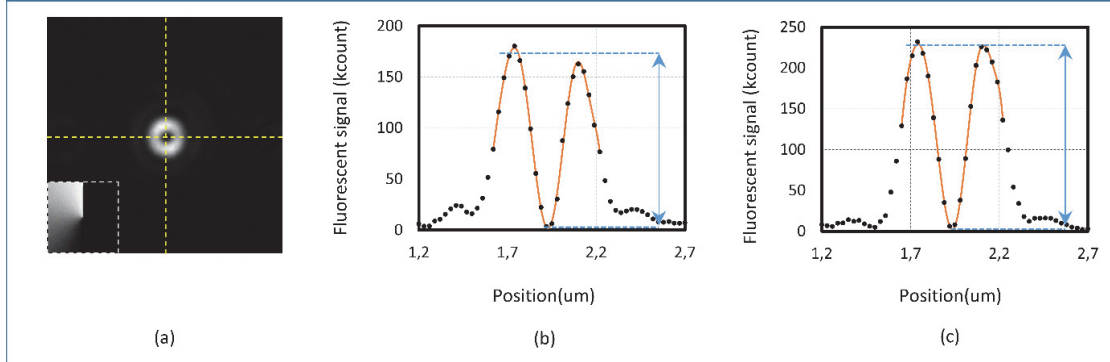


Figure 2-14 Depletion beam contrast. (a) Depletion beam obtained with a $0-2\pi$ vortex phase mask (Inset). The PSFs image is obtained like in Figure 2-13 by recording backscattered light from a single 80 nm gold particle. (b) and (c) Intensity profiles along the dashed line on (a). Each profile is fitted with a polynomial function. To estimate the donut contrast (i.e. the quality of the central “zero”) we measure the minimum of the fitted curve with respect to the average value of the two peaks.

2.4.4 STED imaging of FNDs:

In the previous section, we have detailed the implementation of a CW-STED microscope, its alignment procedure and the critical points to maximize its performance. In this section, we demonstrate resolution improvement and characterize the performance of the microscope.

To measure the performance of the STED microscope, we use 40 nm FNDs containing NV centers. The 40 nm crystals are small enough to disturb minimally the resolution measurement of the microscope (we consider them as point sources) and have still the advantage to be nonbleaching probe. Thus, we can use the maximum depletion power available in our system (≈ 250 mW) and a long dwell time (≈ 5 ms) to get a large signal to noise ratio (i.e. good fitting curves). Figure 2-15(a) shows a scanning fluorescent image of four isolated nanocrystals. The intensity profile of the excitation PSF is fitted with a Gaussian function of 200 nm FWHM (Figure 2-15(b)). The Figure 2-15(c) displays the image taken in STED mode. As expected, the depletion of the fluorescence around the excitation peak results in a sharper PSF. The profile is measured in Figure 2-15(d). By fitting with a Lorentzian function, the equivalent STED excitation PSF is measured to be about 60 nm. Those results are similar to the ones already presented in the literature with the same range of depletion power [53]. Higher resolution (about 10 nm) has been demonstrated with high energy pulsed laser systems [26,75]. With those systems, color centers have been resolved in bulk diamond [26] and inside nanodiamonds [75].

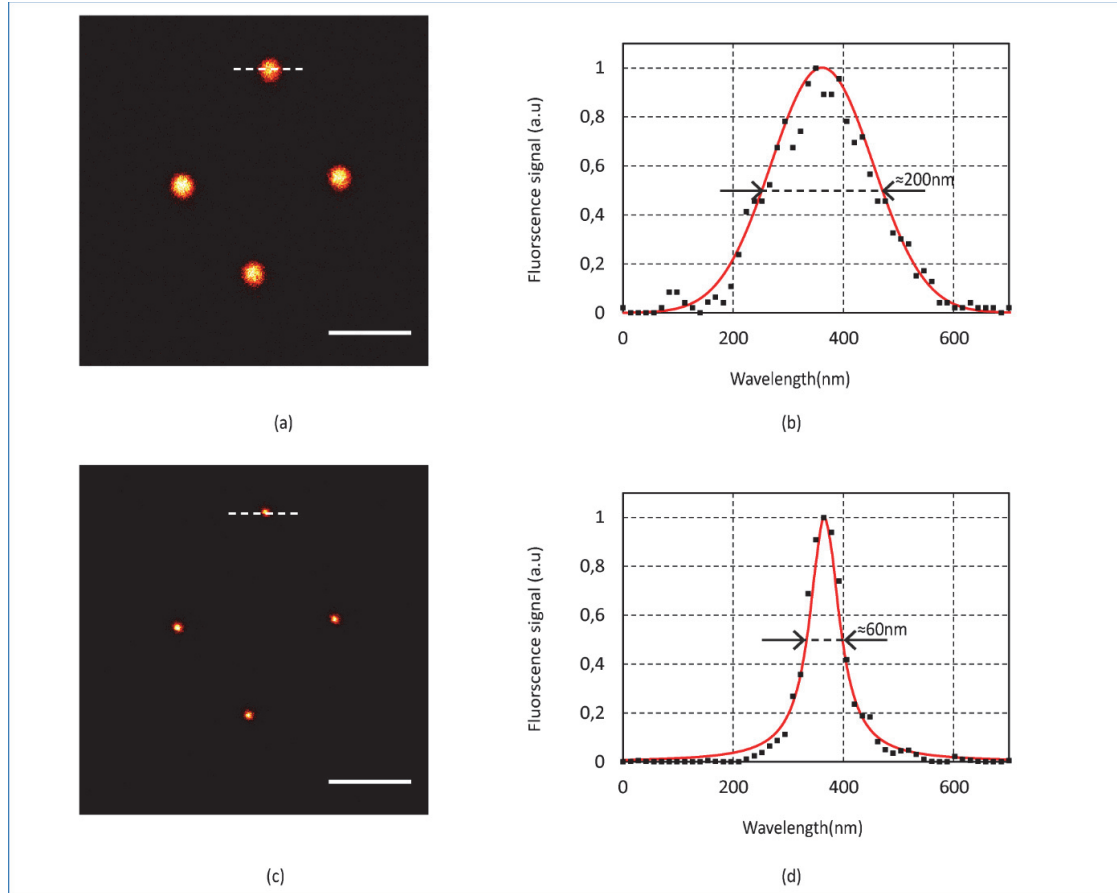


Figure 2-15 STED microscope performance. (a) Scanning fluorescence image of isolated 40 nm FNDs containing NV. (b) The intensity profile along the white dashed line of image (a). The FWHM is measured by fitting with a Gaussian function, it is found to be about 200 nm. (c) STED images of the same sample, the PSF width is clearly reduced. (d) To quantify the resolution improvement, we fit the intensity profile of the STED PSF with a Lorentzian function. The measured FWHM is about 60nm. Scale bars are 1 μm .

To illustrate the improvement in the image quality brought by the STED gain in resolution, we recorded successive conventional and STED images (Figure 2-16). The STED imaging allows the separation of individual nanocrystals that are not visible in the diffraction limited recording. A little halo of light can be observed around the crystals, this is characteristic of some residual fluorescence (even with high depletion power the inhibition is never perfect). This pedestal in the equivalent STED PSF can be removed with pulsed excitation and gated detection [76]. Nevertheless, the improved resolution obtained with CW modality allowed us to spatially distinguish nearby nanocrystals hidden by diffraction limit in the conventional recording (Figure 2-16). To date, STED microscopy is the far field microscopy method that provides the highest resolution at a speed of about 1 frame per second for 1cm^2 images in commercial microscopes (stochastic methods [8,9] provide similar resolution with lower illumination intensities, but with longer time frame). Those performances can be seen as a reference for the different nonlinear method presented in the rest of this thesis.

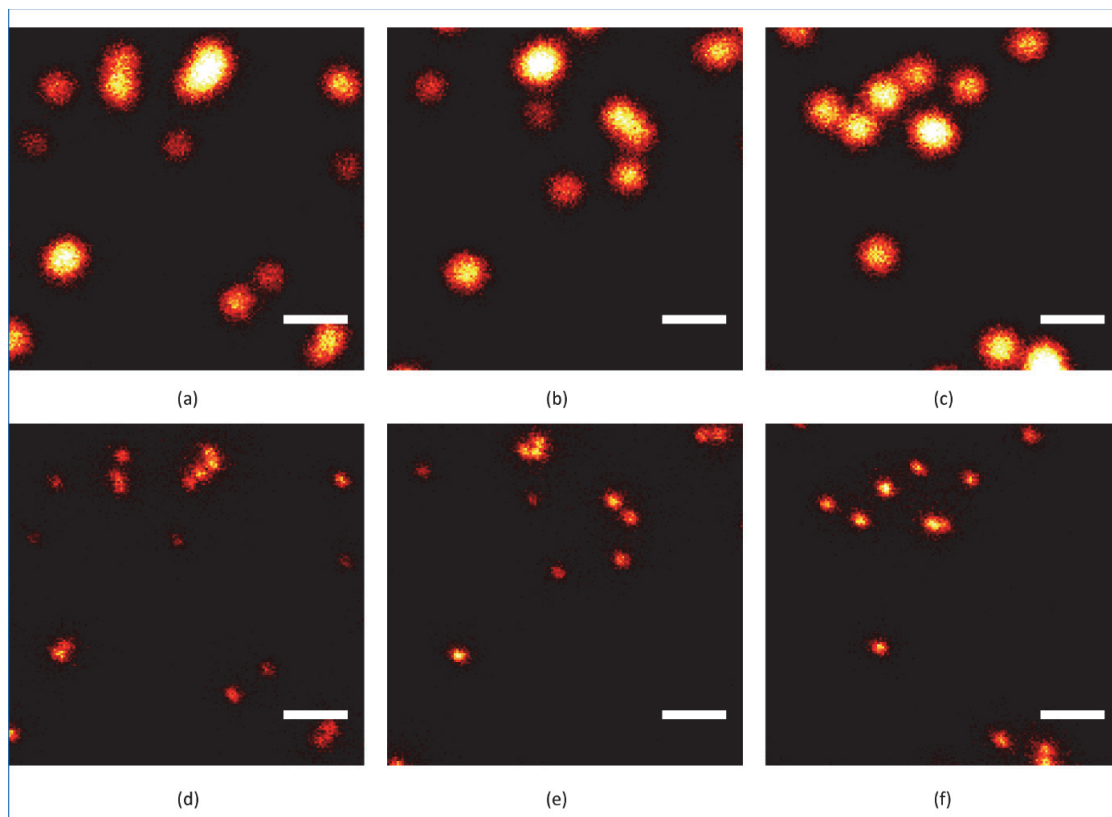


Figure 2-16 STED images of nonbleaching probes. (a) (b) and (c) Some FNDs containing NV centers immobilized on a glass slide are image both in conventional scanning microscopy mode. (d) (e) and (f) Same sample imaged the depletion beam switched on. By comparing the first and the second row, it can be observed that the STED mode allow to resolve details about the nanocrystals shapes and conformation that were invisible in the diffraction limited images. Scale bars are 500 nm.

2.5 Characterization of a new material for STED microscopy: green nanodiamonds

The color centers in diamond are comparable to artificial atoms trapped inside the diamond crystal. In this way, the fluorescent centers are perfectly isolated and protected from external environment. It results in the remarkable property we already emphasized for NV centers in nanodiamonds: they are exceptionally photostable [25]. In consequence, all the 500 different luminescent centers present in diamonds [77], emitting from the deep-ultraviolet to the far infrared (IR), are potential candidates for STED microscopy. However, to our knowledge, to date, only NV center were subject to superresolution techniques. The existence of only single color nonbleaching centers limits the possible observations. For instance it complicates spatial correlation studies with STED. For multicolor biological imaging, the commonly used channels are blue (Dapi...), green (GFP, Alexa-488...) and red (Texas-red...) staining. NV centers already provide red fluorescence and have been used in many STED microscopy studies. To provide a nonbleaching probe with different color, we focus our interest on another color center: the NVN defect that produces green fluorescence. In this section, we characterize the photophysical properties of fluorescent nanodiamonds containing NVN centers for STED imaging. By comparing with the properties of the NV centers extensively studied in the literature [26,53], we show that the NVN center is a viable source for STED nanoscopy. We demonstrate STED superresolution imaging of nanodiamonds with NVN defects and we show a resolution of 70 nm, which is the specified limit of our microscope system. Also, nanodiamonds have been shown to be highly biocompatible and have been used as bioimaging agents. They have been used for instance to probe intercellular transport of yolk protein [78], but also as intracellular probe to track the lung stem cell regeneration [79] and to label the neuronal differentiation [80]. Finally, in order to show the potential of green nanodiamonds (gNDs) as photostable biomarker tag in fluorescence nanoscopy, we finally acquired superresolved images of 70 nm sized diamond particle uptaken into Hela cells.

2.5.1 Stimulated emission characteristics of gNDs:

As we detailed in the section 2.2, all the superresolution imaging techniques that are not limited by diffraction rely on a nonlinear relationship between the excitation intensity and the fluorophores response. In the case of STED microscopy, the saturation of the emission depletion is exploited. The extent of this saturation determines the degree to which the effective PSF can be narrowed (Equation 2-14). In other words, the STED microscopy performance is directly related to the photophysical properties of the fluorescent probes. So, in order to estimate their applicability to STED microscopy, we characterize here the fluorescence properties of NVN center in nanodiamonds.

2.5.1.1 Absorption and Emission spectra:

The neutral NVN center is composed of one vacancy next to two substitutional nitrogen atoms in the diamond lattice. A solution of 70 nm gNDs was ordered from Adamas-Nanotechnologies. After dilution to a concentration of 0.01 mg.mL⁻¹ and it was dried on a glass slide for photophysical properties characterization. The sparsity of the sample prepared at such a concentration was checked using scanning electron microscopy (Figure 2-17 (a)). Thus, the recorded fluorescence was predominantly emitted by single nanocrystals. Scanning electron microscope images also allowed us to measure the size distribution of the particles. As specified, the most probable size of the nanodiamonds is found to be 70 nm and almost all the nanocrystals are larger than 50 nm (Figure 2-17 (b)).

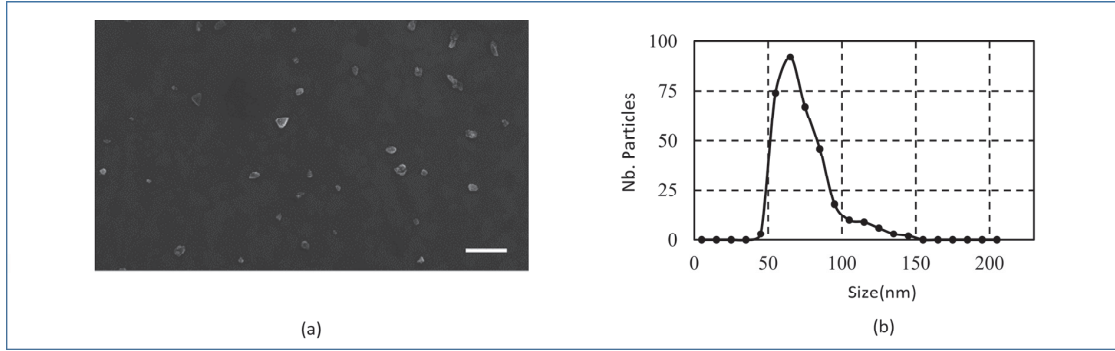


Figure 2-17 Nanodiamonds containing NVN defects. (a) Scanning electron microscope images of the gNDs. Sparse samples are obtained with gNDs solution of 0.01 mg.mL⁻¹. Scale bar is 500nm. (b) Size (diameter) distribution of the gNDs.

Absorption spectrum:

For organic dyes, optical absorption measurement are usually used to determine the absorption cross section (Beer Lambert law). However, the FNDs have a very high refractive index (≈ 2.4) that induces a lot of scattering and makes the absorption measurement challenging. But also and above all, those methods require the previous knowledge of the number of vacancies in the particle (that we don't have). So, as suggested in [81], we used the fluorescence absorption saturation to derive the absorption spectrum. Indeed, fluorescence saturation is directly related to the light absorbed (no interference of the scattered light) and independent of the number of color center. For fluorescence excitation, we used a white light laser (Fianum SC400) and a tunable filter that can deliver light over the whole visible and IR spectrum. For each excitation wavelength the fluorescence signal strength is recorded as the excitation power is increased (Figure 2-18). In order to estimate the absorption cross section we consider the simplified model proposed in [81], a two state energy level fluorescent color center (Appendix B). The white light source is a pulsed laser with a repetition rate (T_{rep}^{-1}) and a pulse width (T_p). We also consider a constant approximation rate k_{ex} during the pulse duration (T_p) and a constant fluorescence rate k_f . With those conditions, under steady state condition, the saturation of the fluorescence signal can be shown [82], to be proportional to:

$$I_{fluor} \propto \frac{e^{(-k_f T_p)} \left(e^{k_{ex} T_p + k_f (T_p + T_{rep})} k_{ex} (k_{ex} + k_f (k_{ex} + k_f) T_p) - k_{ex} \left(e^{(k_{ex} + 2k_f) T_p} k_{ex} + e^{k_f T_{rep}} k_{ex} + e^{k_f T_p} (-k_{ex} + k_f (k_{ex} + k_f) T_p) \right) \right)}{(-1 + e^{k_{ex} T_p + k_f T_{rep}}) k_f (k_{ex} + k_f)^2 T_{rep}} \quad \text{Equation 2-19}$$

The only unknown in Equation 2-19 is the excitation rate during the pulse, which can be expressed in function of the absorption cross section, $k_{ex} = \sigma_{abs} I_{exc} T_{rep} / T_p$. Thus, fitting our experimental data with this expression (Figure 2-18), we can determine the value of σ_{abs} for each wavelength.

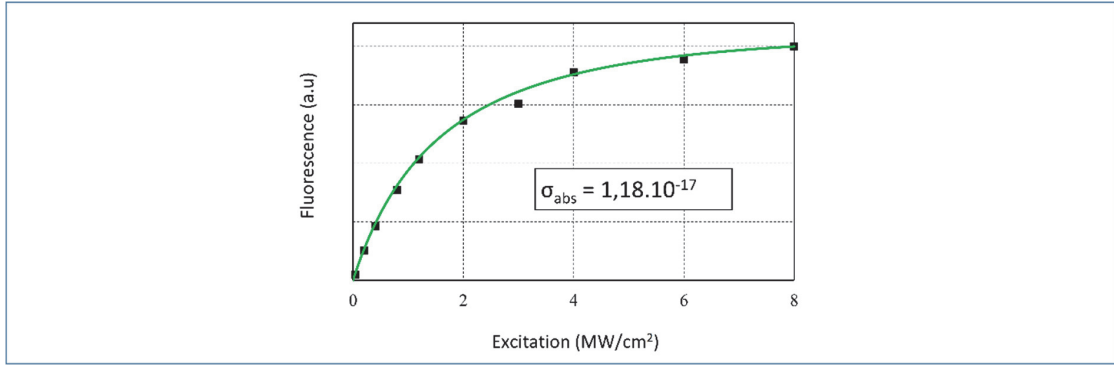


Figure 2-18 Fluorescence saturation curve at 470 nm excitation: the fluorescence signal emitted by a single gND in function of the average excitation intensity. For this experiment, we used a 2MHz repetition rate and 80 ps pulse width. For this nanodiamond, the fitting of experimental points with the (Equation 2-19) curve results in an absorption cross section of $1.18 \cdot 10^{-17} \text{ cm}^2$ (the detail calculation for Equation 2-19 is available in Appendix B).

We repeated the fluorescence saturation measurement (and the fit for the derivation of the absorption cross section) for 16 particles to obtain a statistical measurement on the absorption spectrum. It can be observed in Figure 2-19 that the uncertainty on the curve fitting leads to significant error bars. However, in good agreement with previous reports, the absorption spectrum exhibits a clear peak around 480 nm and allow us to select the excitation wavelength. The absorption cross section obtained at the peak is found to be $1.4 \cdot 10^{-17} \text{ cm}^2$ which is slightly lower than previous measurement [83].

Emission spectrum:

The emission spectrum was measured directly onto the confocal microscope for a fixed excitation wavelength at 458nm and changing the detection spectral window with an acousto-optic tunable filter.

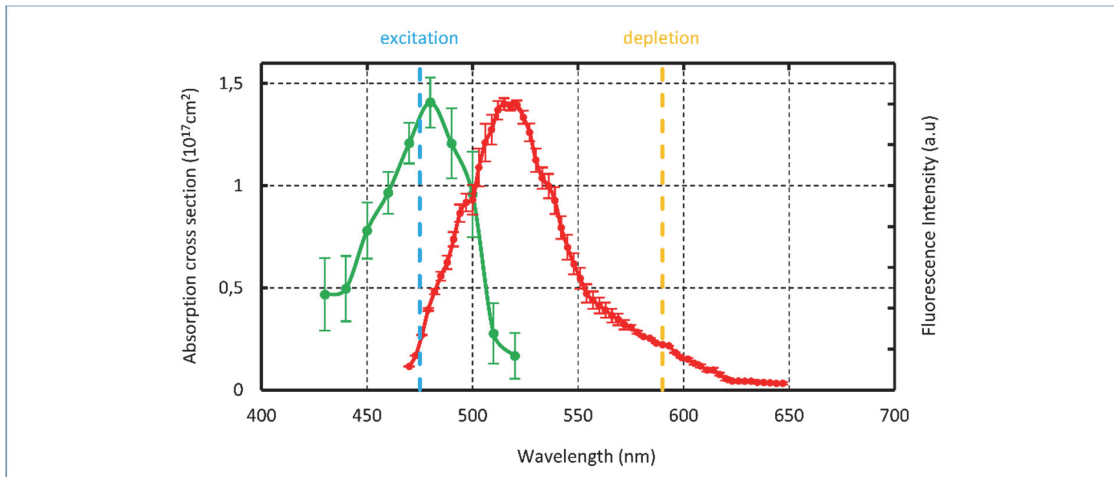


Figure 2-19 Absorption (green plot) and emission (red plot) spectra of green nanodiamonds. The absorption spectrum is deduced from the measurement of the luminescence saturation for each excitation wavelength (Figure 2-18). Each point of the absorption spectrum curve is the average value over 16 gNDs and the standard deviation is indicated with error bars. The luminescence spectrum shows a large tail at 600 nm. Each point of the emission curve is the average value over 30 gNDs and the standard deviation is indicated with error bars. The two vertical color lines indicate the wavelengths of the excitation and depletion beams used for the superresolution imaging

The Figure 2-19 displays the absorption and emission spectra of the nanodiamonds containing NVN color centers. The excitation of the NVN centers results in a broad fluorescence emission between 500 and 600 nm with a peak at about 530 nm [83]. The Stokes shift is larger than typical organic dye like Atto routinely used for STED imaging. This large Stokes shift eliminates any absorption of the depletion light. Moreover, the wide emission spectrum leads to keep a significant stimulated emission cross section at the depletion wavelength of 590 nm.

2.5.1.2 Fluorescence lifetime:

In order to obtain the fluorescence lifetime distribution over a large number of particles we performed fluorescence lifetime imaging on gNDs dispersed on a glass slide (inset in Figure 2-20(a)). As presented in Figure 2-20 (a), we obtained a mean value of $\tau=27\text{ns}$ and a FWHM of 10.1ns . The fluorescence lifetime in the nanoparticles is significantly larger than the lifetime in the bulk crystal (16ns) and it is also larger than the lifetime of red fluorescent nanodiamonds (rNDs) [53]. The large lifetime dispersion has already been observed with rNDs. It has been explained by the change in the conformation of the particles (cluster or single particle) inducing variation in the refractive index around each particle and also by the different dipole orientation of the emitters at the glass-air interface [84].

In order to characterize the nature of the defect contained in the gNDs, we also recorded the fluorescence decay trace for each nanodiamond (Module PicoHarp 300 (PicoQuant) on SP8 microscope (Leica)). One example is presented in Figure 2-20(b). All the fluorescence time traces recorded exhibit a linear combination of two exponential decays with a fast component ($\tau<3\text{ns}$) and a slow component ($\tau\approx 27\text{ns}$). This double-exponential decay has been previously observed in rNDs [53,85,86]. The major slow component is characteristic from the luminescence of the NVN center and the fast component is attributed to surface effects [86].

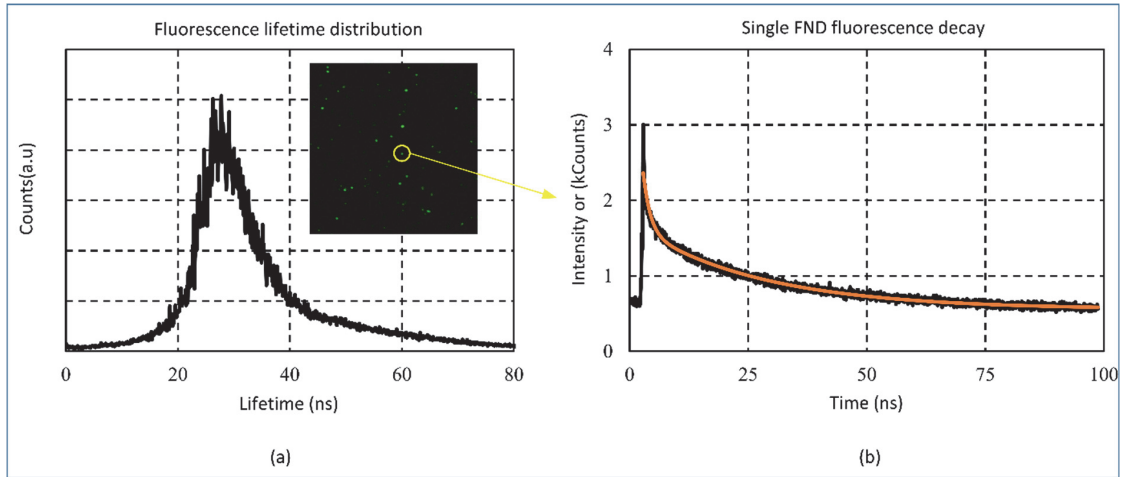


Figure 2-20 Fluorescence properties of green nanodiamonds. (a) Fluorescence lifetime distribution of gNDs immobilized on a glass slide (the inset shows the fluorescence image of the gNDs). (b) Fluorescence decay trace of a single nanodiamond situated into the yellow circle in the inset image. The best fit (red curve) is obtained with a two-exponential model.

2.5.1.3 Stimulated emission cross section:

The basis of the STED microscopy is to deplete the fluorescence by stimulated emission. The stimulated emission properties of NVN centers have been studied previously in macroscopic crystals for the production of a color center laser in diamonds. Laser action at 530 nm has been observed, confirming the potential use of NVN color centers with stimulated emission [87]. However, as we described in the lifetime measurement, in nanocrystals smaller than the excitation wavelength, the emission properties can be modified. The radiative transition in NVN crystal has been shown to occur with a high quantum yield of 0.95 [69]. Knowing the fluorescence decay time and the quantum yield of the transition, the stimulated emission cross section can be derived from the emission spectrum measurement [88]:

$$\sigma_s = \frac{\lambda^4 E(\lambda)}{(8\pi \cdot c \cdot n^2)} \quad \text{Equation 2-20}$$

where λ is the wavelength, E is the fluorescence intensity normalized to the quantum yield ($\int E(\lambda) d\lambda = 0.95$), c the speed of light and n the refractive index of the material. For different wavelengths, the result is displayed in the Figure 2-21 (b). At the wavelength used here for STED imaging (590 nm), we find $\sigma_s \approx 0.45 \cdot 10^{-17} \text{ cm}^2$.

The theoretical prediction is confirmed by measuring the depletion of the luminescence as a function of the depletion beam power. In continuous STED, both the excitation beam and the depletion beam are on, so the excited STED is constantly populated while the luminescence emission competes with the stimulated emission process. The luminescence rate is given by the inverse of the luminescence lifetime ($1/\tau_f$) while the stimulated emission rate is equal to $(\sigma_s I_{exc} \lambda / (hc))$ and scales with the excitation intensity. Under the assumption that the excitation saturation is low, the depletion intensity required to switch off half of luminescence signal is $I_s = hc / (\sigma_s \lambda \tau_f)$ and the depletion curve is described by a function of the form $1/(1 + I_{sted}/I_s)$ [89]. The luminescence inhibition curve presented in Figure 2-21(a) is an average over 18 measurements, taken from different individual nanodiamonds particles. As seen from the error bars, all individual curves are a bit different from each other's. This is a logical consequence of the luminescence decay time inhomogeneity mentioned in the previous paragraph. From the curve in Figure 2-21(a), the cross section of luminescence inhibition is found to be $\sigma_s \approx 0.49 \cdot 10^{-17} \text{ cm}^2$ in good agreement with the value determined from the emission spectrum. The consistency in between the two values confirms that the mechanism for fluorescence quenching is stimulated emission.

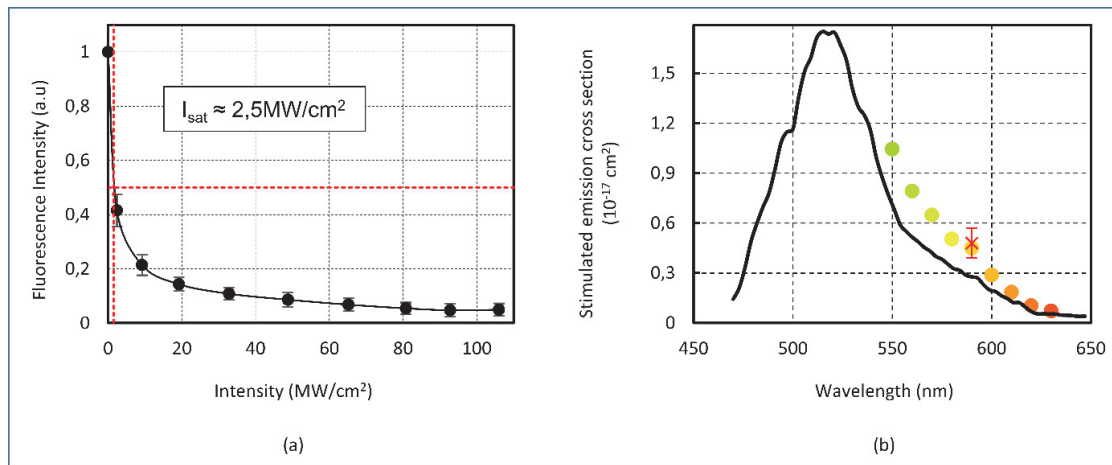


Figure 2-21 Depletion efficiency with green nanodiamonds. (a) Fluorescence inhibition curve of single gND as a function of the depletion CW beam intensity. The depletion intensity necessary to switch-off half of the luminescence characterizes the steepness of the curve and is directly related to the stimulated emission cross section. (b) Stimulated emission cross section values in function of the wavelength (color dots) derived from the emission spectrum measurement (black line). The value at 590 nm is in good agreement with the one derived from the depletion curve (red cross).

An ideal emitter for STED microscopy should possess altogether: high quantum yield and photostability, an emission spectra that match the STED wavelength, a long fluorescence lifetime and a low cross-section for multiphoton absorption and for absorption by the excited states. Roughly, gNDs exhibit similar parameters as the rNDs. The stimulated emission cross section of the NVN center is low (Figure 2-21 (b)) (about one order of magnitude lower than Atto 495 [90]). However, the long luminescence lifetime compensates for the limited emission cross section and results in a steep decrease of the luminescence with the depletion beam intensity (Figure 2-21 (a)). In addition, in contrast with organic dyes, the gNDs are especially suitable for continuous STED. As the decay time is longer than typical the pulse interval in pulsed mode locked lasers, the average power needed to achieve efficient emission depletion is similar in the continuous STED mode and in the more complex pulsed implementation. Furthermore, with only the depletion beam on, we did not observe any signal from the NDs, which indicates a very limited cross section for multiphoton absorption around 600nm. We also observed an excellent photostability, which indicates no photochemical alteration of the crystal but also no absorption by the excited states. All those parameters make gNDs well suited for STED nanoscopy.

Although gNDs share the advantages of the rNDs, they also share and even accentuate the main limitation of rNDs, which is the low emission brightness. A small absorption cross section (Figure 2-19, about one order of magnitude less than organic dyes) and the very large lifetime (Figure 2-21, one order of magnitude longer than organic dyes) result in a dim fluorescence. Indeed, the NVN center absorption cross section is half that of the NV centers [83] (at the absorption peaks), and the radiative lifetime is about 1.5 times longer [53]. So the signal emitted by a NVN center is about 3-times less bright (assuming same quantum yield) than the NV center. In order, to overcome this deficiency a large number of color center is needed inside each nanoparticle [91]. We work here with 70 nm commercially available gNDs (Adamas-Nano) specified to contain on average about 60 color centers that should deliver a luminescence intensity equivalent to a few organic dye molecules. Increasing the density of the color center in nanodiamonds would allow the use of smaller particle as biolabels and is an active research area [91].

2.5.2 STED imaging

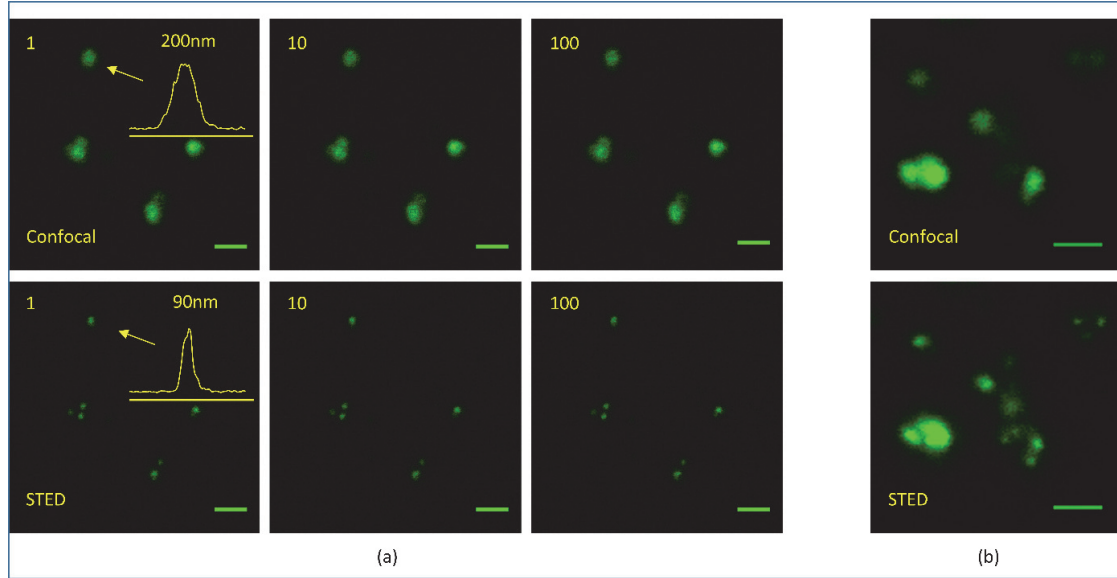


Figure 2-22 STED imaging of green nanodiamonds. (a) Consecutive confocal and continuous STED imaging of 70 nm sized nanodiamonds immobilized on a glass slide. The increase in resolution reveals details that are blurred in the confocal image. The inset on the first images is the profile along the particle indicated with an arrow. It allows to estimate the gain in resolution given by STED to be at least 70 nm for a particle bigger than 50 nm. The multiple scans illustrate the perfect photostability. Even if for the STED scan images, high depletion power is used ($P=150$ mW, 256×256 pixels with 3 ms dwell time), no change in the recorded signal level is observed after 100 scans. (b) Confocal and STED image revealing the inhomogeneity of the nanoparticles and their tendency to aggregate. Scale bars are 500 nm.

We have prepared samples composed of 70 nm nanodiamonds containing about 60 NVN centers dried on a glass coverslip. We used a Leica STED-SP5 with 488 nm pulsed excitation and 590 nm CW depletion. As illustrated in Figure 2-22 (a) the STED image improves the resolution compared to the confocal scan and reveals subwavelength details. The resolution obtained is evaluated by measuring the full width half maximum of a single nanocrystal, we measured the STED resolution to be about 70 nm (measuring a 90 nm FWHM profile in Figure 2-22(a) and assuming 50 nm particle, the resolution is even better if the size of the particle is bigger), which is consistent with the specification of the machine. Moreover, the green luminescence from the nanodiamonds remains perfectly stable under STED illumination as depicted in Figure 2-22(a): after 100 scans, no sign of photobleaching is detected. This excellent photostability is ideal for long-term high resolution observations.

The Figure 2-22(b) illustrates the gNDs properties that can complicate their use as biomarkers. First, they are prone to aggregation. It makes cellular labelling difficult and creates thicker structures that are more difficult to resolve with STED microscope (Figure 2-22(b)). So, in order to obtain homogenous [92] or targeted [78] labelling additional surface treatment is required. Second, the number of defect inside gNDs is not homogeneous. So even if the absence of bleaching allows the collection of more photons by increasing the acquisition time to resolve finer details, the brightest particle lead to saturation of the detector. This color center density inhomogeneity is to our opinion the main limitation that needs to be improved for better biological labelling.

2.5.3 Cell imaging

STED gain in resolution happens by quenching the fluorescent centers that are around the excitation peak center, so at the same time that the resolution is improved it degrades the fluorescence signal strength. To investigate if the green nanodiamonds can be imaged better than the diffraction-limited resolution in a biological sample, we demonstrated STED images of gNDs particles inside HeLa cells.

HeLa cells were grown in standard conditions on glass coverslips in Dulbecco's modified eagle medium glutamax medium. The cells were seeded at a density of $8 \cdot 10^4 \text{ cm}^{-2}$ and grown in an incubator at 37°C for one day. The cells were incubated for 2h with gNDs at a concentration of $10 \mu\text{g/mL}$ and then incubated for 30min also with WGA Alexa Fluor 680 (life technologies) at $2.5 \mu\text{g/mL}$. After incubation, the excess of dye and gNDs was washed three times with phosphate buffer saline solution. The cells were then fixed with 3.5% paraformaldehyde in citrate buffer saline solution and mounted on microscope slides for observation.

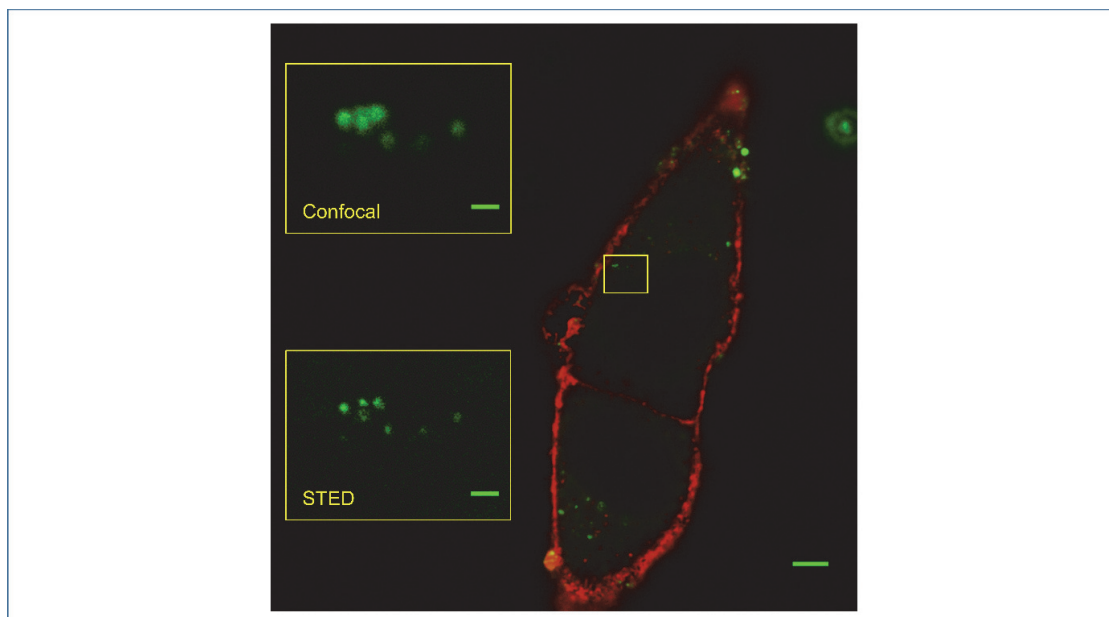


Figure 2-23 Superresolution imaging of gNDs uptake into HeLa cell. The cell membrane is labelled in red with an organic dye (WGA, Alexa Fluor 680, Invitrogen) and confocal imaging is used to evidence the presence of the nanodiamonds inside the cell. The two insets are zoomed images of the highlighted part of the cell. The STED imaging reveals more details about the conformation of the nanocrystals. Scale bars are 5 μm in the main image and 500 nm in the insets.

The cellular uptake was confirmed with two color confocal imaging. The cell membrane is labelled with the red dye (WGA), proving that the confocal section plane is situated inside the cell (Figure 2-23). The nanodiamonds appear on the green fluorescence channel. As in the previous reports, nanodiamonds tend to form aggregates in the cytoplasm and do not enter the cell nucleus [64,83]. The presence of green cell autofluorescence is visible in Figure 2-23, however the level of the autofluorescence signal is kept low by detecting the fluorescence only 4ns after the excitation. As the gNDs radiative lifetime is much longer than the autofluorescence decay it improves the signal to background ratio [64]. Some isolated gNDs internalized in the cytoplasm are imaged in the confocal mode and STED mode (Insets in Figure 2-23). It can be observed that the SNR is degraded because some part of the fluorescence signal is depleted but enough SNR can be maintained to isolate the single particles that were blurred in the confocal image.

As the rNDs, gNDs thanks to their high photostability can be an interesting probe when long acquisition with high resolution is required. In cellular environment they are prone to aggregation, however this can be overcome by surface treatment and specific labelling [78,92]. Owing to their photophysical properties, gNDs are promising candidates as a second color nonbleaching probe for long term nanosensing or nanoimaging application, however two main factors can still be improved for their use as specific marker in superresolved life-science experiment. First the limited density of NVN color center inside the nanocrystals limits the brightness or equivalently the minimal size of particles that can be resolved in cellular environment. For 10 nm crystal to be equivalent with other labels like quantum dots or fluorescent proteins the color center density of our probe should be increased by about two orders of magnitude [91]. Second, the inhomogeneity of the size of the particle (Figure 2-17 (b)) and of the color center density complicates quantitative studies.

2.5.4 Conclusion:

We have demonstrated that the photophysical properties of gNDs allow their efficient use in STED microscopy. Thanks to their long fluorescence lifetime, gNDs are especially suitable for CW STED implementation. The long lifetime also benefits from time gated detection STED, since it leads to the differentiation of the gND fluorescence from other signals like autofluorescence. However, their long lifetime and low absorption cross section also lead to a low signal brightness. Under our experimental conditions, gNDs do not exhibit any photobleaching and despite their limited brightness could still be observed with STED microscopy when internalized into a cell. Because of these characteristics, green nanodiamonds can be used as a second color biocompatible nonbleaching

probe for STED microscopy. Many other color centers could be tested to complete the spectrum of the available non bleaching marker for STED nanoscopy, for instance silicon vacancy that exhibit a far red emission [93].

2.6 Conclusion:

Thanks to its very high resolution, STED microscopy has become the gold standard of superresolution microscopy. It has already been used in numerous biological studies [94,95] and it has been turned in a commercial product (Leica-SP5-STED). However, some limitations remain and the research for improvement of STED imaging and for novel nonlinear fluorescence scanning microscopy techniques has been an active field during the period of this PhD.

In this chapter we focused on one solution to improve the photobleaching limitation: the use nanodiamonds crystal. We demonstrated both with a home built setup and with a commercial STED microscope that a resolution of 70 nm can be obtained with long term observation STED thanks to the nonbleaching color centers embedded in nanodiamonds. We have shown for the first time that different types of defect in diamond can be used in STED microscopy. This is the first step towards long term multi-color optical superresolution studies, like co-localization observation with nanometric resolution on long time scale. Numerous defects are present in diamonds and their properties are still to be explored to obtain a full color palette of nonbleaching probe available in STED microscopy. Near infra-red probes could be of particular interest because of the very low scattering and the limited absorption in tissues (the absorption in tissues increases dramatically above $1\mu\text{m}$ illumination wavelength). Moreover, depletion laser are already available in IR, for instance several recent implementation of STED utilize a single super-continuum laser that cover the full visible and IR spectrum. However, even if numerous color center have been identified in diamond, the more complex is the defect the more complicated is the synthesis, that's why up to now the NV and NVN defects have been mostly implanted into nanocrystals.

Here, we focused our attention on the nonbleaching nanodiamonds and we make the bet that they will become a viable bio-label. However, for other dyes, like fluorescent proteins the photobleaching induced by the high power depletion beam remains a major limitation. Different trails have been explored in the literature to reduce the amount of power necessary for an efficient depletion. Plasmonic enhancement of the depletion field in gold coated probes has been demonstrated to decrease by a factor of 4 the depletion beam power required [96]. Photo-switchable protein have also been synthesized and superresolution imaging has been demonstrated requiring three orders of magnitude lower depletion intensity [97,98].

Another subject of development for STED microscopy is the imaging speed. Since it is a scanning technique, STED microscopy is relatively slow, especially for three dimensional imaging (it requires multiple lateral scans at different depth to create a three dimensional picture). To accelerate the imaging process, remarkable work has been done to parallelize STED microscopy [99,100]. It is within this framework that we worked in this thesis on novel superresolution methods. We present in the next chapter a method based on STED microscopy that provides three dimensional localization in a single scan.

Chapter 3 Double Helix axial localization in STED microscopy.

We present here a new superresolution technique that leads to nanometric localization of single emitters in three dimensions. This novel method, that we name double-helix STED (DH-STED), combines STED microscopy for improvement in lateral resolution and the use of double-helix point spread function for axial localization. By recording a single STED scan with camera detection and modifying the fluorescent wavefront in the detection path, we obtain precise axial localization of superresolved sample.

3.1 Introduction

We have shown in Chapter 2 that scanning laser microscopy is a powerful tool for non-invasive observation and that the resolution can be improved through nonlinear fluorescence responses. After our first implementation of STED microscopy (Chapter 2), the idea of the DH-STED method came from noticing that STED is a popular method despite its relatively low axial resolution. Indeed, the discrepancy between the lateral and axial information in conventional STED images is one of the main weakness of the method. In typical STED implementation, the axial resolution is brought by the use of a confocal pinhole. A single lateral scan identifies the axial position of the resolved emitter within a $\sim 0.5 \mu\text{m}$ thick section (Figure 3-1 (a)), that is to say one order of magnitude less precisely than the lateral resolution. This leads to a very elongated PSF, which yields to an obvious lack of information in the axial direction (Figure 3-1 (a)).

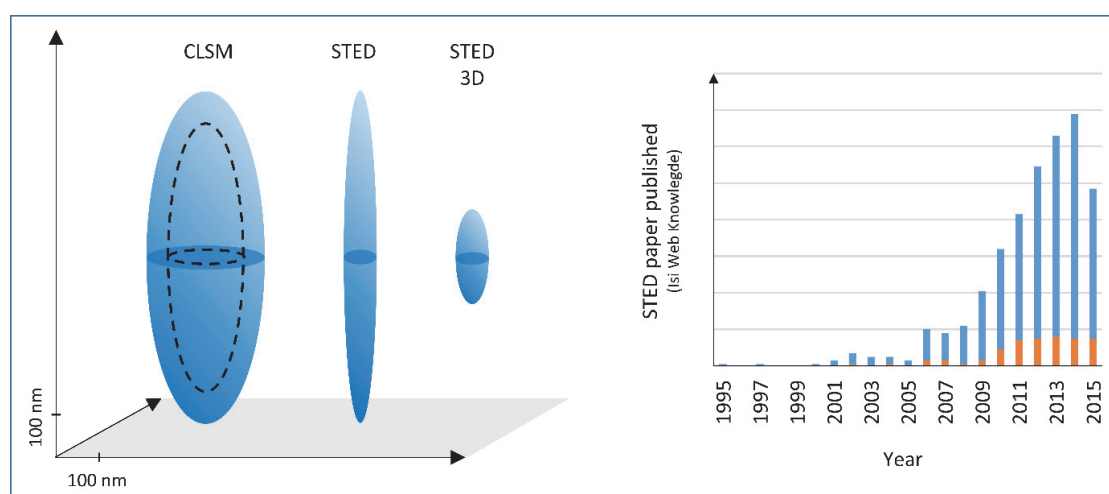


Figure 3-1 Conventional STED vs 3D STED. (a) Schematic of PSFs in different modes of scanning microscopy. In confocal laser scanning microscopy, the lateral resolution is typically 200 nm with high NA objectives (cf. Chapter 2), the axial resolution is $2n\lambda/NA^2 \sim 0.8 \mu\text{m}$ for large pinhole and can be reduced to typically 0.5 μm with small pinhole. Those values are FWHM and are represented with dashed lines on the picture. In conventional STED, the lateral resolution is reduced to $\sim 50\text{nm}$ and the axial resolution is unchanged. In STED-3D, a second depletion beam shrinks the PSF also in the axial dimension, typical obtained depth resolution is 100nm. (b) Number of paper referenced each year by Isi Web of Knowledge with STED microscopy (blue) and STED-3D (orange). It can be observed that despite its improved resolution, the STED-3D is use is not increasing as much as the conventional STED one.

On the other hand, even though it is possible to gain in axial resolution with the addition of a second depletion beam [101,102] (Figure 3-1 (a)), the majority of the published studies with STED microscopy have used lateral improvement only (Figure 3-1 (b)). This low use of 3D STED compared with the 2D version can be partially explained by the implementation complexity but more likely it is due to the longer acquisition time and the resulting phototoxic effects. Indeed, in numerous cases [94,95], the structure of interest can be resolved with two dimensional STED. In other word, lateral improvement in resolution is often sufficient to resolve the sample and there is no direct need for depth resolution to discriminate the feature; however, there is a need for depth localiza-

tion to gain information. This is especially true for imaging emitters situated at a well-defined interface. For example, two dimensional STED has recently revealed the octameric arrangement of *Xenopus* nuclear pores complexes [94]. The lateral resolution gain allowed for the observation of the emitter situated on the nucleus membrane but axial localization could have provided additional information about the protein arrangement. Another recent successful two dimensional STED experiment is the observation of a striking ring-like actin organization in axons of cultured hippocampal neurons [95], but no information was collected in depth to understand the structure better. As in these examples, researchers often prepare *in vitro* samples with a well-defined plane of interest, consequently two dimensional STED is sufficient to resolve the structure of interest. Although, precise axial localization could bring additional information, it is not used, because when brought with axial resolution improvement, it requires a long 3D scan. For this reason, we created a method that associates nanometric axial localization and lateral superresolution. It results in an imaging mode that provides three dimensional sample information in a single lateral scan, i.e. without the limitation of three dimensional scanning: slow data acquisition and potentially phototoxic effects.

The design of this method falls within a broader investigation about the use of a camera detector in scanning microscopy that is discussed in Chapter 4. Indeed, the standard configuration in scanning microscopy is to use a single pixel detector like photomultiplier tubes (PMT) or avalanche photodiodes (APD) and to integrate the signal at every scanning position. Nevertheless, the potential of using the information available on a 2D sensor in terms of resolution gain and improved signal level has been pointed out by Prof. Colin Sheppard since 1988 [103]. Several factors convinced us that the time has come to explore the possible gains of using a pixelated detector. First, the latest camera characteristics in terms of frame rate and noise level have begun to make them suitable for fluorescence laser scanning applications [104–107]. Second, as detailed in Chapter 2, nanodiamonds are perfectly photostable probes that allow for a proof of principle demonstration at low frame rate with a low noise cameras. Finally, during the time of this thesis, several noteworthy developments in the parallelization of superresolution scanning microscopy have been reported [97,99,100,108,109]. So, scanning methods based on the use of a camera detector (including the one we present in Chapter 3 and Chapter 4) can, in theory, be directly parallelized and have the potential for high frame rate.

Hence, the use of a camera detector in scanning microscopy opens the door for harnessing any wide-field imaging technique to scanning microscopy. The next chapter (Chapter 4) explores the possibility of obtaining a high resolution in nonlinear scanning microscopy with a method typically used in wide field imaging: structured illumination. In the present chapter (Chapter 3), we combine axial localization by the use of wavefront engineering, a method used previously in wide field microscopy [110–112], with STED microscopy. In the first part, we detail the principle of the method: after a section recalling the Laguerre Gaussian beams properties, we detail the generation of the three dimensional PSF with a double helix shape and its optimization for our specific application. Then, a high efficiency DH PSF is experimentally generated with a spatial light modulator (SLM) and isolated particles are localized with a precision better than 20 nm in every direction. In the second part, CW-STED microscopy is combined with DH for three dimensional localization of clusters of nanodiamonds crystals closer than the diffraction limit. In the third part, we apply the DH-STED method with pulsed laser STED to image organic dyes samples and investigate the limitation induced by photobleaching.

3.2 Principle

The resolution gain in STED microscopy originates from the engineering of the excitation PSF via the depletion beam. The collection PSF is usually identical to the linear excitation PSF or limited to a fixed pinhole in the confocal mode. The idea here is to modify the collection PSF in order to achieve precise localization in each scanning position by using an imaging detector. We detailed in the previous chapter (Chapter 2) the mechanism of STED microscopy, in consequence we focus in this section on the principle of DH PSF axial localization.

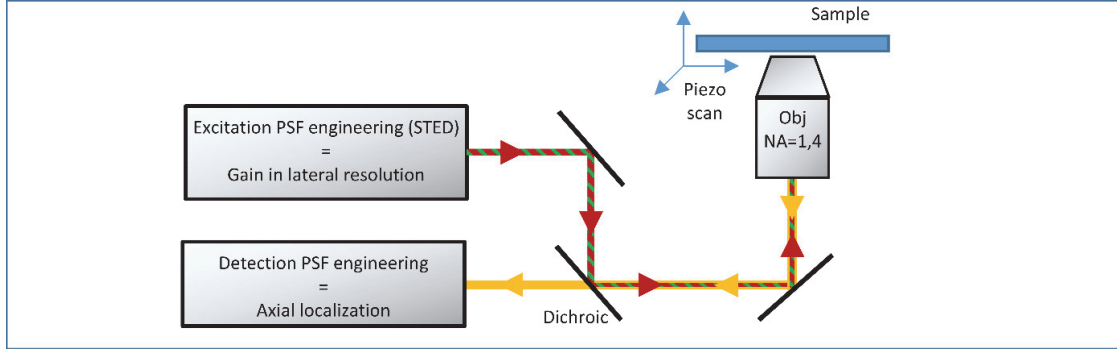


Figure 3-2 Principle of DH-STED. The Figure 3-2 illustrates the principle of the method, while STED results in a strong gain in lateral resolution the collection path which is usually not exploited in scanning fluorescence microscopy is modified to achieve localization. The localization is fundamentally a wide field method, in each scanning position a WF fluorescence image with a modified PSF is acquired in order to localize the emitters within the excitation volume.

3.2.1 Rotating beam

The DH PSF is made of two lobes that rotate continuously around the optical axis as the beam propagates, thereby forming a 3D double-helical shape. This PSF has been specifically designed by Prof. Piestun group for three dimensional localization. In order to understand how the PSF has been engineered and how it can be adapted to match our specific need, we present here the underlying background. The DH beam belongs to a more general family of “rotating beams”. We summarize the main properties of rotating beams and relate them to axial localization. (The theoretical background presented here are directly taken from Prof. Piestun publications and more details about rotating beams can be found in [113–115]).

3.2.1.1 Gauss Laguerre basis

There are numerous solutions to the paraxial wave equation (Gaussian, Bessel...). In cylindrical coordinates the set of solution is called the Gauss-Laguerre modes. The Gauss-Laguerre (GL) modes form a complete orthogonal basis of solutions of the paraxial wave equation, i.e. any paraxial wave can be decomposed in Gauss-Laguerre modes and this decomposition is unique [116].

Each GL mode in the cylindrical coordinates (ρ, φ, z) , can be expressed as [114,115]:

$$U_{n,m} = G(\rho, z) R_{n,m}(\rho) \Phi_m(\varphi) Z_n(z) \quad \text{Equation 3-1}$$

$$\text{where } \begin{cases} G(\rho, z) \text{ is composed of the Gaussian envelope and a radial quadratic phase factor.} \\ R_{n,m}(\rho) = (\sqrt{2}\rho)^{|m|} L_{(n-|m|)/2}^{|m|}(2\rho^2) \text{ with } L_{(n-|m|)/2}^{|m|} \text{ generalized Laguerre polynomial.} \\ \Phi_m(\varphi) \text{ is a phase factor dependant on } m \text{ and } \varphi \\ Z_n(z) \text{ is a phase factor dependant on } n \text{ and } z \end{cases}$$

Where m and n are the indices related to the Laguerre polynomial. The complete expression can be found in Appendix C

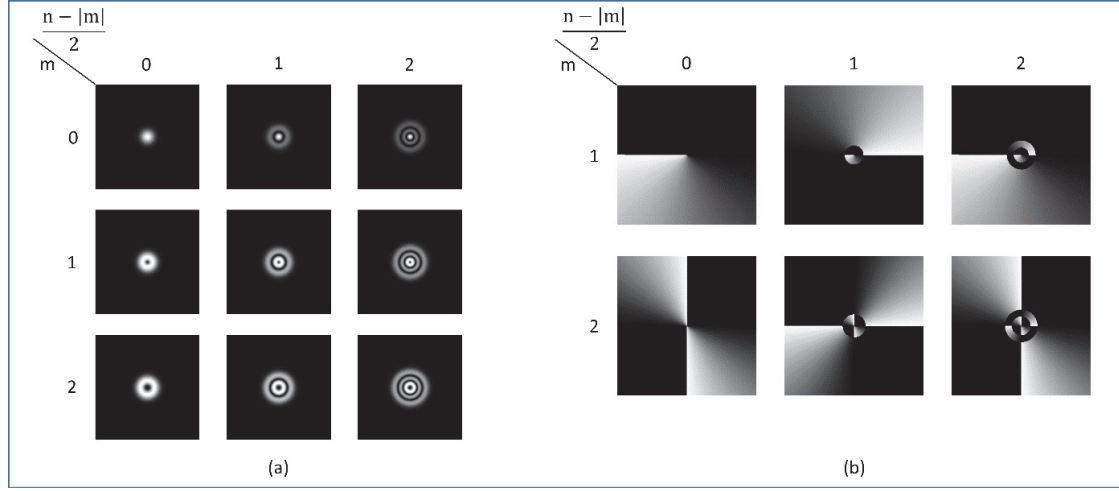


Figure 3-3 The GL basis. Every paraxial wavefront can be decomposed in a weighted sum of GL modes. Each mode is identified by two indices n and m (related to the indices of GL polynomial). The pictures represent the amplitude (a) and the phase (b) of the low indices GL modes. It can be noticed that some of those beam are used in STED microscopy and have been presented in chapter1. The mode $GL_{0,0}$ is a Gaussian beam it corresponds to the paraxial approximation of the intensity distribution at the lens focus (given in Figure 2-1). The mode $GL_{0,1}$ is the vortex beam with a donut profile that is used as depletion beam in STED microscopy.

Figure 3-3 represents the amplitude and phase profiles of the GL modes for the low (n, m) indices. As n increases the width of the beam grows and as $\frac{n-|m|}{2}$ increases the number of bright lobes grows (equal to $1 + \frac{n-|m|}{2}$). Each mode is both propagation invariant along the z axis (except for scale) and presents a cylindrical symmetry, i.e. it is an eigen mode for rotation along the z axis. By performing a decomposition of a wavefront in the GL basis, it is possible to analyze its properties. We summarize in the next section the propagation characteristics of rotating beams via GL decomposition analysis.

3.2.1.2 Rotating beam properties

A rotating beam is, by definition, a beam with a transverse intensity distribution that the only variation upon propagation is rotation along the optical axis and scaling. It can be shown [114,115], that if we consider a beam as a sum of GL modes:

$$E = \sum_i U_{n_i, m_i} \quad \text{Equation 3-2}$$

The necessary and sufficient condition for rigid rotation along the z axis is [114,115]:

$$\frac{n_{i+1} - n_i}{m_{i+1} - m_i} = \frac{\Delta n}{\Delta m} = \text{ctste} = V, \text{ where } V \text{ is an integer} \quad \text{Equation 3-3}$$

This condition can be easily visualized in the Gauss-Laguerre modal plane: a rotating beam is represented by a single line (Figure 3-4(a)). The evolution of the rate during the propagation is also well defined. The rotation rate is maximal at the waist and decreases during the propagation such as half of the total rotation (to go until far field) is performed at the Rayleigh distance. At the waist the rotation rate is equal to:

$$\frac{d\varphi}{dz} = V \cdot \frac{\lambda}{\pi \omega_0^2} \quad (\text{with } \omega_0 \text{ the waist of the Gaussian beam at } z=0 \text{ and } \lambda \text{ the wavelength}).$$

$$\text{And the total rotation (to far field) is: } \Delta\varphi_{\text{tot}} = V \cdot \frac{\pi}{2}$$

All those information are summarized in Figure 3-4. Thus, by choosing different combinations of GL modes to compose the rotation beam, it is possible to tune the width and the shape of the beam as well as its rotation speed. This is exemplified in Figure 3-4 (c) with three different rotating beams, with different shapes (“button beam”, “trefoil beam” and “cross beam”) and rotating speeds.

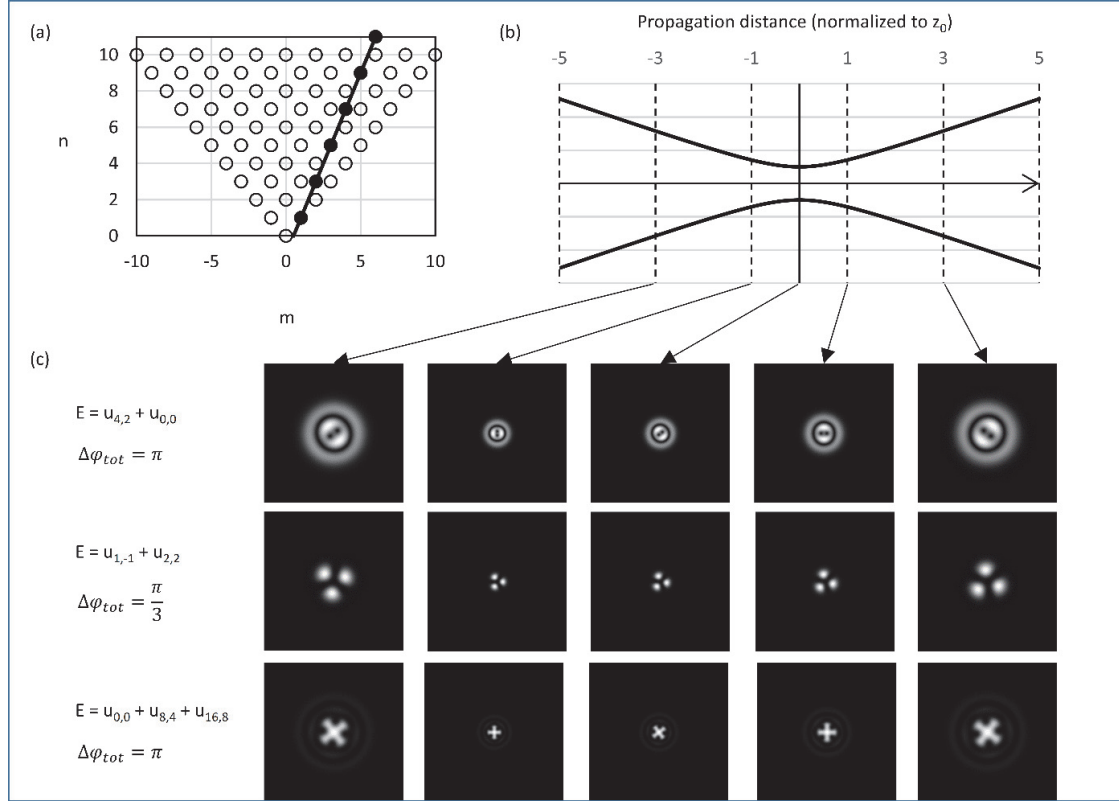


Figure 3-4 Rotating beam properties (adapted from [114,115]) (a) Decomposition of a rotating beam in Gauss-Laguerre modal plane, rotating beam composed of modes lying along a single line, and the speed of rotation is proportional to the slope of this line. (b) Rotation rate along the propagation. (c) Examples of rotating beams, with different modes composition which lead to different shapes and different rotational speed: the button beam ($u_{4,2} + u_{0,0}$), the trefoil beam ($u_{1,-1} + u_{2,2}$) and the cross beam ($u_{0,0} + u_{8,4} + u_{16,8}$).

3.2.2 Detection Point spread function

The same wavefront that is used to generate a rotating beam can be used to modify the imaging point spread function and make it rotate with defocus (Figure 3-5). The controlled rotation of the imaging PSF can thus be utilized for depth estimation, this concept is named “depth from diffracted rotation” [113]. In order to have equal access to all the spatial frequencies, it is convenient to modulate the wavefront in the Fourier plane (pupil plane) of the microscope imaging plane (pupil plane, cf. Figure 3-5). The rotating beams have the interesting property of being Eigen-Fourier function [114,115]. So in order, to obtain the desired rotating beam shape PSF the modulation to be applied, i.e. the transfer function, is the Gauss-Laguerre combination itself.

Even if they are designed to image one plane perpendicular to the optical axis, traditional imaging systems are conveying depth information through defocus blur. Indeed, the traditional PSF of an imaging system is varying in depth, so the axial position of an emitter can be measured by estimating the amount of defocus. However, this variation is minimal along the depth of field, so it does not lead to precise axial localization (with a single acquisition). Moreover, the conventional PSF is symmetric with respect to the focal plane so it does not allow for localization over the full depth of field. Other three-dimensional localization techniques have been demonstrated. For instance, the introduction of astigmatism in the detection PSF results in asymmetrical variation with depth [9]. Digital holography have also been used [117], but those methods do not provide a uniform accuracy over the entire depth of field [118]. We focused on the rotating-PSFs for their combination of high accuracy, high efficiency and above all the design flexibility that makes it easily adaptable to the specific need.

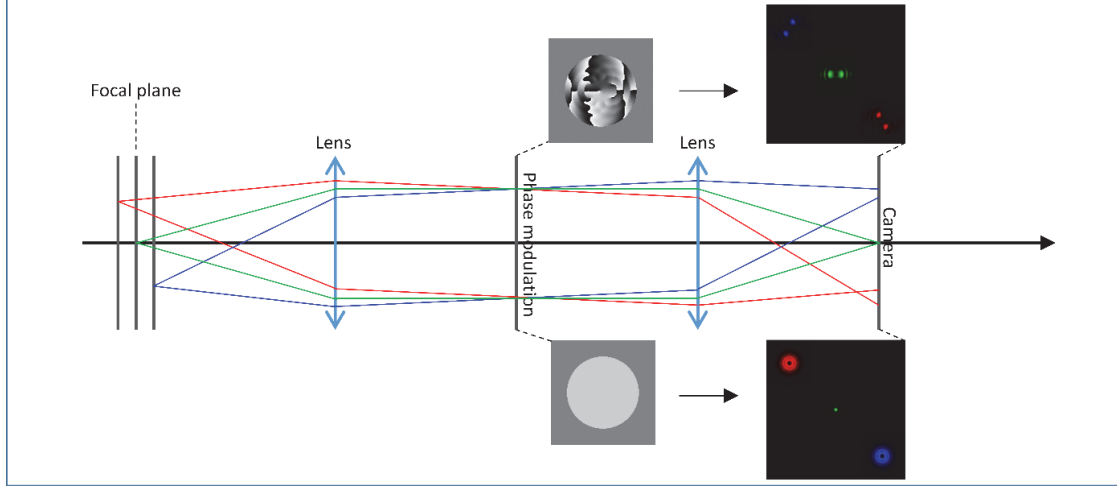


Figure 3-5 Axial localization with rotating PSF based microscope. In the absence of modulation the image of a single emitter is blurred depending on the position. The wavefront is modulated in pupil plane (Fourier plane of the imaging plane) in order to obtain a DH-PSF. Depending on the position the image rotate with minimal blur resulting in precise axial localization.

3.2.2.1 Double Helix PSF

Every point of any rotating PSF exhibits a helical trajectory with defocus. For depth localization it is desirable to have a pattern that allow the precise measurement of the rotational angle. The combination of the modes $u_{1,1}+u_{5,3}+u_{9,5}+u_{13,7}+u_{17,9}$ creates a pattern with all the light concentrated into two lobes of equal energy (Figure 3-6). Thus, each lobe can be localized precisely and their respective position related to the rotational angle and then to the emitter axial position.

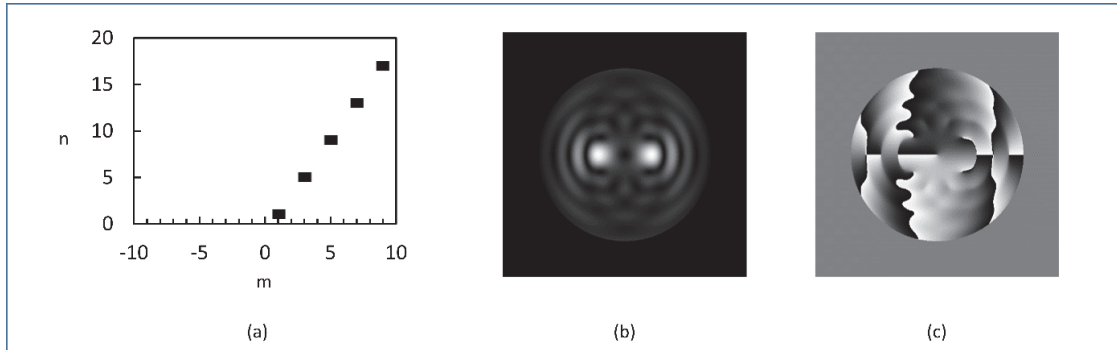


Figure 3-6 DH transfer function. (a) Modal decomposition in the GL modal plane. (b) Amplitude (c) Phase.

The exact rotating DH-PSF, obtained by modulation with the DH transfer function is estimated with the scalar paraxial approximation. We consider the imaging of isotropic fluorescent emitters with randomly rotating dipole, so that the paraxial model is still a valid approximation even with high NA objective [119]. The insertion in the pupil plane (Figure 3-5) of the modulation transfer function $H(u,v)$ results in a three-dimensional incoherent intensity PSF [119]:

$$PSF(x, y, z) = \left| TF^{-1} \left\{ H(u, v) \exp \left(-i \frac{\pi}{\lambda n} NA^2 dz (u^2 + v^2) \right) \right\} \right|^2 \quad \text{Equation 3-4}$$

with n the mounting medium refractive index, λ the wavelength, dz the distance to the focal plane (defocus), (u, v) the normalized frequency coordinates in the pupil plane and $H(u, v)$ the pupil transfer function (and TF^{-1} the inverse Fourier Transform).

The resulting PSF for an imaging system with a 1.4 NA and a 650 nm wavelength is represented in Figure 3-7. The exact double helix point spread function exhibits two lobes that rotate by about $\pm 40^\circ$ within the ± 500 nm.

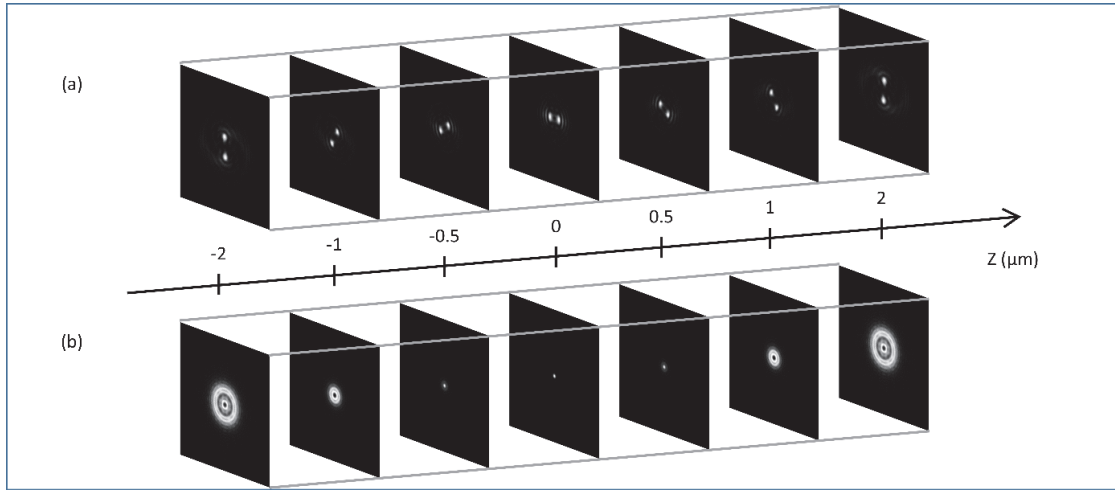


Figure 3-7 DH and conventional point spread functions around the focal plane. (a) The DH PSF exhibits a two lobes profile that only rotates with defocus. It leads to efficient axial localization. (b) In contrast, the standard microscope PSF does not exhibit a change in its orientation and quickly expands with defocus.

So, in the chosen experimental conditions ($\text{NA}=1.4$, $\lambda=650\text{ nm}$), the DH-PSF exhibits a significant change in orientation within the depth of field. Moreover, in contrast with the standard PSF, the light remains concentrated in the lobes throughout the entire axial range. In the focal plane, the DH lobes are about 2 times larger compared with the standard PSF spot and they are separated by about 3 times the Airy diameter. The DH-PSF expands about 1.6 times within the calculated range ($\pm 2\text{ }\mu\text{m}$) while the standard PSF expands about 12 times. Hence, the DH pattern keeps the light concentrated in the lobes during propagation and the rotation is not symmetric with respect to the focal plane, so it leads to a precise localization on the whole range.

Using the rotating beam properties, the PSF can be adapted for the experiment. The rotation speed can be tuned by choosing a different combinations of GL modes lying around a steeper line in the modal plane (Figure 3-4). The pattern size can also be tuned by choosing the waist of the pattern with respect to the pupil aperture. As the waist increases the two lobes of the PSF become brighter and closer as a result of wave propagation (Figure 3-8).

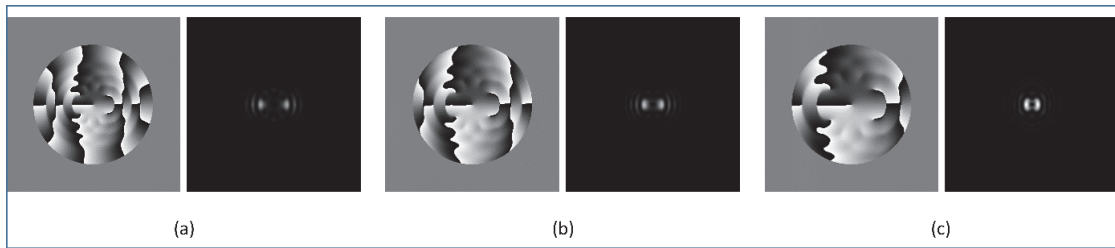


Figure 3-8 Influence of the mode waist size (with respect to the pupil diameter) on the PSF width. Each panel represents on the left the phase map of the transfer function and on the right its corresponding PSF. (a) The transfer function is the sum of GL modes with a waist equal to 0.2 times the pupil diameter. (b) The same with a waist equal to 0.3 times the pupil diameter (c) The same with a waist equal to 0.4 times the pupil diameter

3.2.2.2 Transfer function Efficiency

In contrast with the standard PSF, the DH-PSF changes its orientation with defocus and leads to a more precise axial localization. Intuitively, this is true because the faster the PSF varies in one dimension the more accurate is the localization in this dimension (that's why the standard PSF which exhibits a small lateral pattern results in precise lateral localization). However, this does not take into account the major limitation of the rotating PSFs: their low transfer function efficiency. Indeed, the exact GL mode solution of the DH-PSF has a function transfer efficiency below 2%.

As, we aim to image fluorescence sample with small emitters (below the diffraction limit), so with a limited brightness, the efficiency of the wavefront modulation needs to be significantly improved. Professor Piestun group has worked extensively on different strategies to maintain the DH-PSF advantages (extended depth of field, high precision axial localization and adaptable design) while improving the transfer function efficiency. We summarized quickly here the main results that we used to design our PSF.

The limited total light efficiency of the exact GL solution is primarily due to the amplitude modulation (the exact amplitude modulation in the pupil plane consists roughly in absorbing the light everywhere except in the lobes). However, it has been demonstrated that the phase modulation is predominant [120]. Indeed, if only the phase of the GL pattern is applied as pupil function, the PSF still resembles to a DH and maintains its rotational properties. This can be explained by observing the modal decomposition of the field with constant amplitude and with the DH phase. It is formed with a cloud of modes lying around the exact solution: the line direction responsible for the rotational properties of the PSF still rules the PSF behavior. From this observation, it has been shown that optimization algorithm can be run to further enhanced the transfer function efficiency [112,120]. By keeping a modal distribution close to the original line and maximizing the light into the lobes only for the axial range of interest, the transfer function efficiency can be improved about 30 times compared to the exact solution [120]. The phase pattern resulting from the optimization process and the corresponding generated PSF are displayed in Figure 3-9. An elegant way to analytically describe the result of the optimization has been proposed in [119,121]. The phase mask can be seen as a sum of vortices equally spaced and aligned along a horizontal line and this exact expression exhibits in fact slightly better performance.

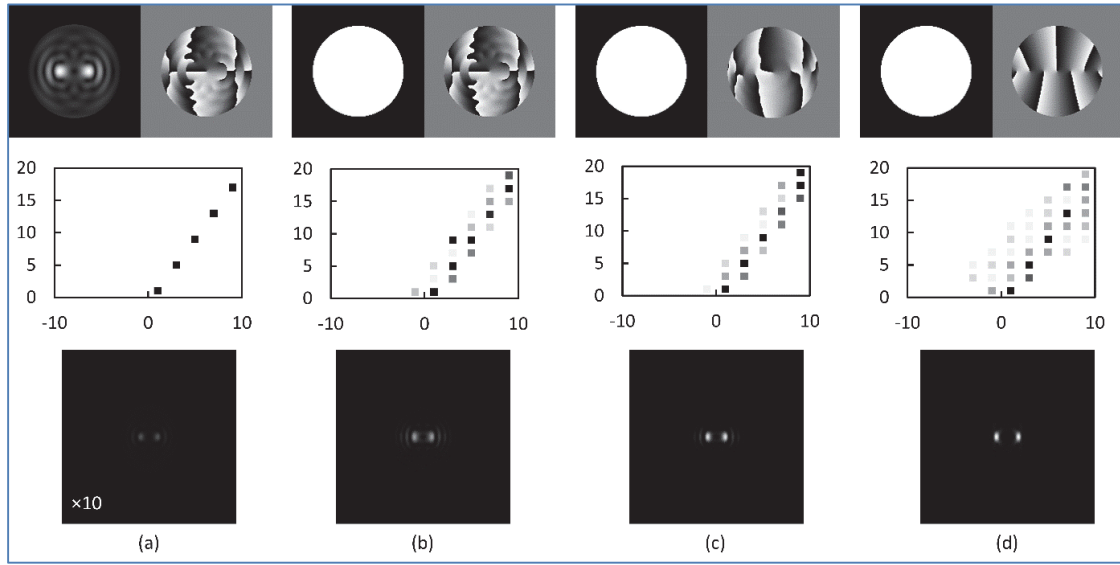


Figure 3-9 DH transfer function optimization. First row: Double-Helix Transfer functions, amplitudes (left) and phases (right). Second row: corresponding decompositions in Gauss Laguerre modal plane. Third row: resulting intensity PSFs. (a) The exact solution $u_{1,1}+u_{5,3}+u_{9,5}+u_{13,7}+u_{17,9}$, it leads to a 2% efficiency (the intensity PSF is multiplied by 10 to be visible). (b) The phase only modulation (of $u_{1,1}+u_{5,3}+u_{9,5}+u_{13,7}+u_{17,9}$), it leads to a 38% efficiency. (c) The optimized phase only modulation (of $u_{1,1}+u_{5,3}+u_{9,5}+u_{13,7}+u_{17,9}$), it leads to a 57% efficiency. (d) DH transfer function, mimicking the optimized transfer function with a line of vortices leads to a 63% efficiency.

The generated optimized DH phase only modulation is now suitable to be used in our experiment. Indeed, it can be implemented with a phase-only SLM and the transfer function efficiency is compatible with photon-limited microscopy observation [111,112,119]. The experimental efficiency improvement is illustrated in Figure 3-10. Fluorescent beads are imaged with different PSF modulations: with the optimized phase mask, the axial range where the light is concentrated within the lobes is reduced but close to the focus, the signal is much higher.

The performance of the localization with optimized DH has been evaluated with information theory calculation [112,118,122]. In broad lines, as the energy is distributed within the two lobes of the DH, for a given total energy, the peak intensity in the DH-PSF is lower than the one in the normal PSF. This transversal spread compared with the standard PSF degrades the achievable precision. However, unlike standard or astigmatic PSFs, the DH concentrates the light in the lobes throughout the entire axial range. So the larger is the axial range of operation, the more competitive is the DH-PSF localization. For our specific application, we are in the range where the precision of different techniques are equivalent [118]. As the idea is to tend towards a larger depth of focus, (an increased section thickness could be envisaged for instance with the use of Bessel beam STED [123]), and because of its design flexibility the DH-PSF seemed to be the appropriate choice. Experimentally, the lateral size of the PSF is also adapted, as the two lobes become closer they also become brighter, so if the case of limited photon budget, the two lobes can be brought closer (at the cost of a more challenging detection [119]).

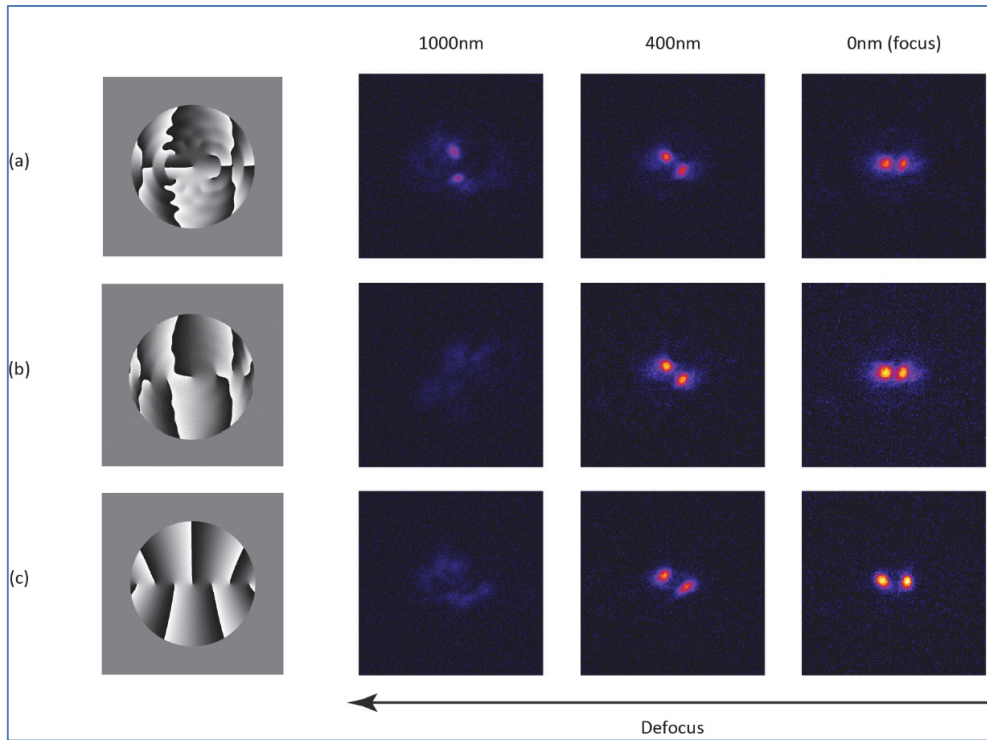


Figure 3-10 Transfer function efficiency. First column: different phase mask used as transfer function. From top to bottom: Exact GL $U_{1,1}+U_{5,3}+U_{9,5}+U_{13,7}+U_{17,9}$ solution, iteratively optimized modulation, sum of vortices solution. Other columns: Fluorescence image of a 70nm FND at different depth position, with the modified detection PSF corresponding to the transfer function. Each image has been taken with the same camera parameters. (a) With the phase only exact solution, the range is longer but the intensity of the lobes at the focus are dimmer compared with the other transfer function. (b) and (c) The iteratively optimized solution exhibits a slightly lower intensity at the focus compared with the sum of vortices but a faster rotation and slightly stronger intensity at 400nm.

3.2.2.3 Axial localization: experimental demonstration

In order to exemplify the axial localization of fluorescent emitters with DH-PSF, we imaged fixed fluorescent beads immobilized on the surface of a metallic target. The target thickness is known to be 200 nm (fabricated by chemical vapor deposition). Thus, we have a well specified sample with two planar surfaces with different depths. The result are presented in Figure 3-11. While the standard PSF image (Figure 3-11b) does not allow for precise axial localization (the depth difference is not enough so that one plane is outside the focal region and clearly blurred), the DH-PSF image exhibits a clear visual difference (Figure 3-11 (c)). The axial position is encoded in the PSF's rotational angle: the beads within the blue line shapes (indicating the target position) are rotated compared to the other because of the depth difference. Hence, the DH-PSF allows for fast and precise three dimensional localization of the emitters and has been applied for particle tracking [112,124] and superresolution imaging [111,119]. To estimate the depth with the double helix PSF, the respective position of the lobes can be estimated by particle detection and centroid calculation (we will detail the localization procedure in the section 3.3.2.1).

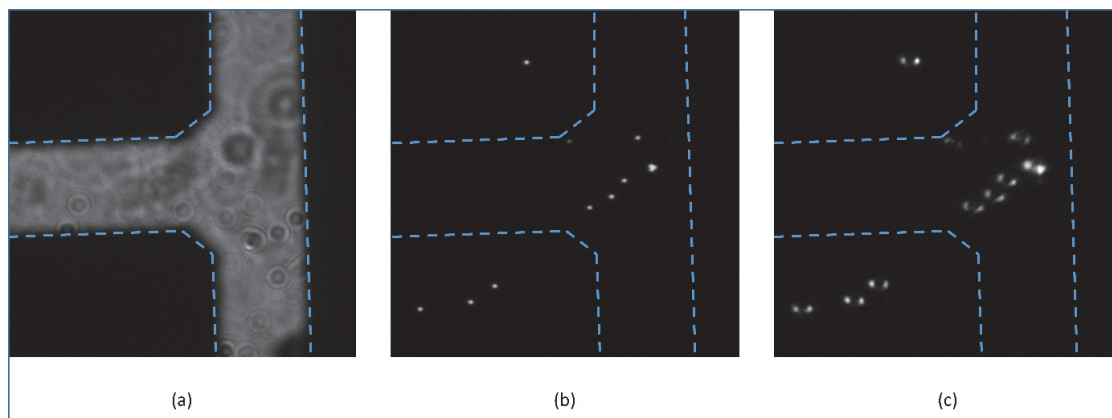


Figure 3-11 Three dimensional localization of fluorescent beads, immobilized on a two level planar surface. (a) Bright field image of the metallic target, the edges are represented with dashed blue lines and reported on the other pictures. The target has been created in clean room by chemical vapour deposition and the thickness is known to be 200nm. (b) Fluorescence images with non modified PSF, the depth difference is not visible. (c) On the contrary with the standard PSF, in the image taken with the DH-PSF we can see the difference in orientation of the particle sitting on the metallic layer. (And the 13° difference in between the two rotational angles in the two planes match the 200 nm expectation as we will detail in section 3.3.2.1).

3.2.3 PSF-design for axial localization in fluorescence scanning microscopy

The microscope technique that we present in this chapter combines DH-PSF localization and STED scanning microscopy. In each scanning step, the region around the excitation focus is imaged on a CCD camera. The useful range of depth localization is determined by the axial widths of the excitation focus. In consequence we design a DH-PSF for localization within about 0.5 μm depth range and with maximum efficiency and localization precision.

3.2.3.1 Fluorescence microscopy

The STED improvement in resolution is based on the depletion of fluorescent emitters and typical fluorescent molecules exhibit a wide emission spectrum. However, the simulations presented in the previous figures for the rotating PSFs have been generated for single light wavelength. We consider here the impact of the wavelength change on the resulting PSF.

Two factors are affected by the modification of the wavelength. First, the phase modulation encrypted on the SLM is designed for one wavelength, therefore a different wavelength leads to a modified phase retardation and to a change in the PSF shape. Second, as a result of diffraction upon wave propagation, the rotational rate varies with the wavelength.

The effect of different fluorescence wavelengths is shown in Figure 3-12 for a 1.4 NA imaging system. It can be observed in Figure 3-12 (a) that the modification of the phase modulation has a very limited impact. Indeed, the calculated PSF at 600 and 700nm for a phase mask designed for 650nm exhibits minimal changes in the lobes shape (minimal changes are visible especially in the light lines in between the lobes). The main double helix shape with two clearly identified lobes is still present and can be used for localization. However, as illustrated in Figure 3-12 (b), different wavelengths result in different rotational rates and could affect the localization precision. In Figure 3-12 (b), it can be observed that a smaller wavelength increases the rotational rate [120]. In the experiments presented in the next section, we use 50 nm large detection bandpass filter and consider a limited axial range (below ± 500 nm), thus the bandwidth of the fluorescence spectrum has a minimal impact on the localization measurement precision.

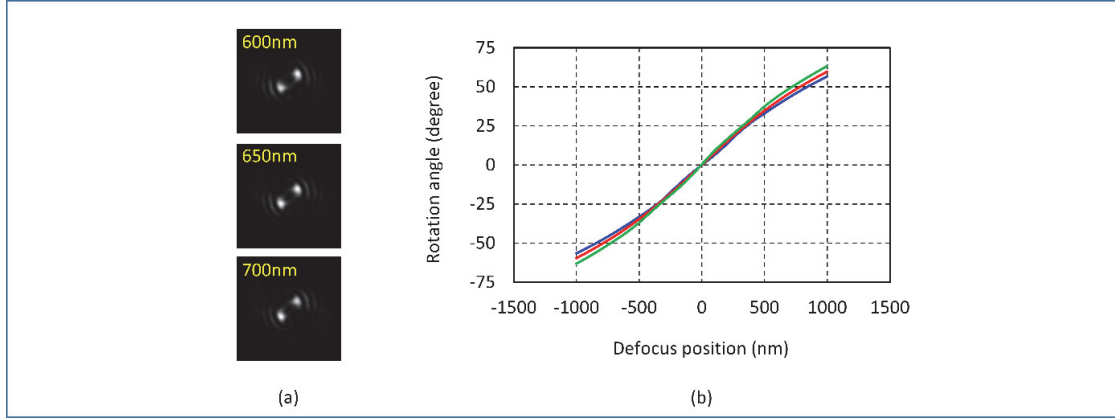


Figure 3-12 Effect of wavelength on DH modulation. (a) Resulting PSF at different emission wavelength for a defocused position of 500nm with a phase modulation designed for 650nm. (b) Rotation angle of the resulting PSF after phase modulation designed for 650nm in function of the defocus position, when used with 600nm (green), 650nm (red) and 700nm (blue).

3.2.3.2 Scanning microscopy: sectioning

We present here the combination of a wide field imaging localization technique with a scanning fluorescence microscopy. The use of scanning microscopy has been primarily motivated by the fast high resolution imaging available with STED compared with stochastic wide field superresolution techniques [8,125]. However, it is important to investigate whether our technique retains one of the most important feature of scanning microscopy: the depth discrimination by confocal sectioning. The camera detector allows for the use of a digital pinhole. Indeed, with a non-modified detection PSF, the confocal filtering can be applied digitally directly by recording on the camera only the area that corresponds to the image of the excitation spot (i.e. the Airy disc). The depth discrimination property (equivalent to the axial resolution in the case of small pinhole) can be quantified by considering the total response of a fluorescent plane as it is scanned through the excitation focus [126]. For traditional confocal microscope, it results in a Gaussian curve (Figure 3-13) (under paraxial approximation) indicating the optical section thickness (for small pinhole, it tends towards

the confocal PSF profile with $\text{FWHM} \approx \frac{1.4\lambda_{em}n}{NA^2}$).

In the case of DH-PSF, we can apply a digital pinhole in the form of two discs (of the same diameter as the confocal pinhole) matching the lobes positions (Figure 3-13 (i)). The red curve of Figure 3-13 represents the simulated sectioning performance with this digital aperture. It can be observed that with a fixed position, the sectioning performance is comparable to confocal microscopy. However, this does not allow for tracking the position of the DH-lobes along the full depth of field. An enlarged “double bean” shape aperture allows for the localization on the full range but results in a larger optical section (green curve Figure 3-13). It can be noticed that if we choose a different position for the digital pinhole, corresponding to a different axial plane localization with the DH lobes, the optical slice is shifted axially (dashed yellow curve Figure 3-13). This has been used very recently to demonstrate refocusing ability after a single scan in scanning microscopy with DH read-out [104]. Also, we did not verify it experimentally but our simulations indicate that with a different rotating PSFs with a faster rotational rate, it should be possible to surpass the sectioning obtained for confocal (even the theoretical one with an infinitely small pinhole).

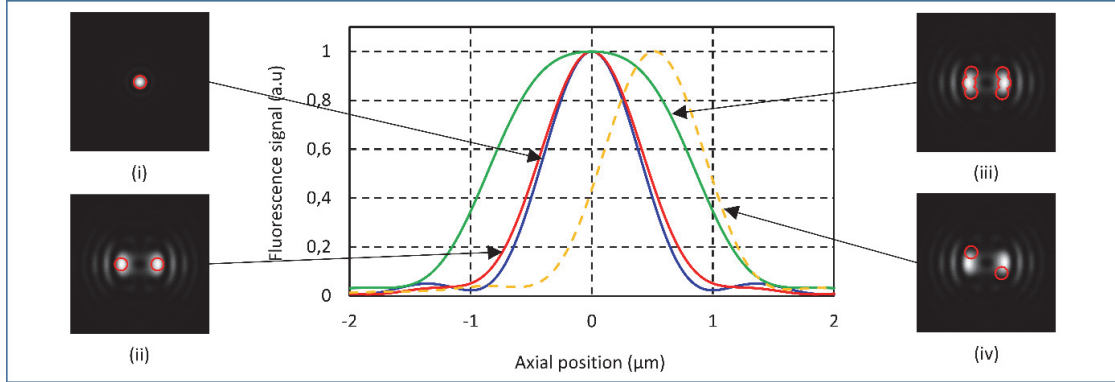


Figure 3-13 Sectioning ability of scanning microscopes with DH localization. The curves represent the fluorescence intensity detected through different type of confocal pinholes (red circles in the images) as a fluorescent plane as it is scanned axially through the excitation focus. Blue curve: Characteristic profile obtained with a normal PSF and a one Airy unit pinhole (image (i)) [126]. Red Curve: The profile obtained with a DH-PSF and a two discs aperture (image (ii)). Green curve: The profile obtained with a double beam shape aperture that covers all the axial range of interest (image (iii)). Yellow dashed curve: The profile obtained with a DH-PSF and a two discs aperture rotated by 40° (image (iv)).

Thus, two types of post-processing can be envisaged with our technique, either we systematically apply the double beams shape pinhole that allow for an optical section of about two times the standard confocal section. It allows to isolate the plane to be imaged from the majority of out of focus background light. However, if a thinner optical section is required, a double digital pinhole that tracks the lobes position could be used.

3.3 DH-STED of red nanodiamonds

In this section we demonstrate, within a single DH-STED scan, 20 nm axial localization of superresolved fluorescent nanodiamonds emitters.

3.3.1 Setup

We describe here the DH-STED setup designed to obtain superresolution image of particles and at the same time three dimensional localization.

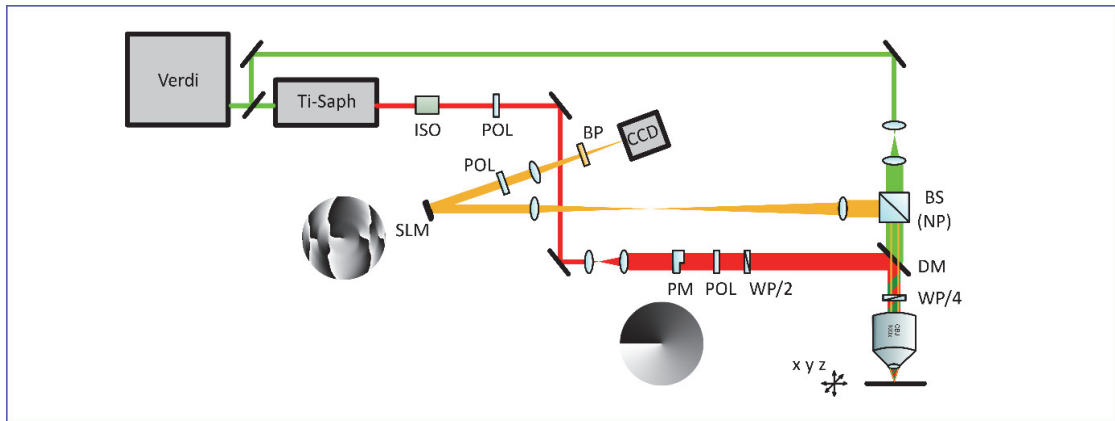


Figure 3-14 Schematic of the DH CW-STED setup. ISO-Faraday isolator; POL-polarizer; SLM-spatial light modulator; BP-band pass fluorescence filter; WP/2-half wave plate; PM-helical phase mask; BS(NP)-non polarizing beam splitter; DM-dichroic mirror; WP/4-quarter wave plate. Inserted pictures show the double helix and donut phase fronts assigned respectively by the SLM and the phase plate, scaled from 0 (white) to 2π (black). A small portion of the Verdi (532nm) is used for fluorescence excitation and the rest is used to pump the Ti-Saph depletion laser (770nm).

The basis of the setup is the home built STED microscope setup described in section 2.4.1. The modification consists in the addition of a spatial light modulator and a camera detector. A 4-f imaging system creates a wide field image on the CCD camera and the SLM is placed in the Fourier plane of the image plane in order to modulate the PSF. A polarizer is also placed after the SLM, in order to

select only the portion of fluorescence signal that is modulated. (In order to remove completely the signal that is not modulated a grating is applied on the SLM and an aperture blocks the DC signal).

3.3.2 Three dimensional imaging of superresolved nanodiamonds

3.3.2.1 Calibration localization precision:

In order to relate the angular rotation of the DH lobes to the axial position we need to measure precisely the respective position of the lobes. This is done by applying a threshold to the picture so that the (10 pixel²) brighter area of the lobes are isolated. Then, the position is evaluated by calculating the centroid of the each lobe. Best results have been shown to be obtained by two dimensional Gaussian fitting [111], however the accuracy gain is limited (about 10%) and the method is less robust to aberration (the performance drops if the PSF is not well symmetric).

Axial localization is calibrated by recording wide field images of a single FND immobilized on a glass slide at different depths. As illustrated in Figure 3-15, the rotation angle of the lobes is recorded for each depth position. The calibration curve indicates a rotation of about $\pm 40^\circ$ in the range $\pm 500\text{nm}$, which is in good agreement with the theoretical prediction (cf. Figure 3-7). The measurement precision depends on the localization repeatability from the lobes, which is dependent on the signal to noise ratio (SNR) [122]. During the acquisition, the presence of the depletion beam in addition to the excitation lowers the photon budget and therefore the precision of the z-localization. Consequently, to evaluate the accuracy of the axial localization in our system, immobilized single NDs are illuminated with focused excitation and depletion beams, and the z-localization measurement is repeated several times. The standard deviations of the measured rotational angle over 100 successive measurements are displayed in the table in Figure 3-15 (c) and do not exceed 20nm. It can be observed, that even if more light is concentrated at the focus, the measurement precision is not the best at the focus but 100nm above and below. This is probably due to the shape of the lobes more circular and consequently more accurate with the centroid estimator. Thus, over the range of interest the axial localization precision is below 20nm (which corresponds to an angular variation of 1.7°). Equivalently, the axial localization precision for single DH-STED image is below 20 nm. It must be noticed that those position accuracies are not the fundamental limits for single image DH-PSF detection. It could be potentially improved by the use of a more complex localization emitter estimator and more stable optical setup. With typical noise conditions, the theoretical limit of the localization accuracy has been shown to be below 1nm [111]. The precision we obtain here is comparable to other publications, it means that there is room for an estimator that would improve localization precision specifically with DH-PSF. Also, as we have nonbleaching emitters, if we consider the camera is noise free, we could also theoretically improve the axial resolution at the cost of a longer integration time.

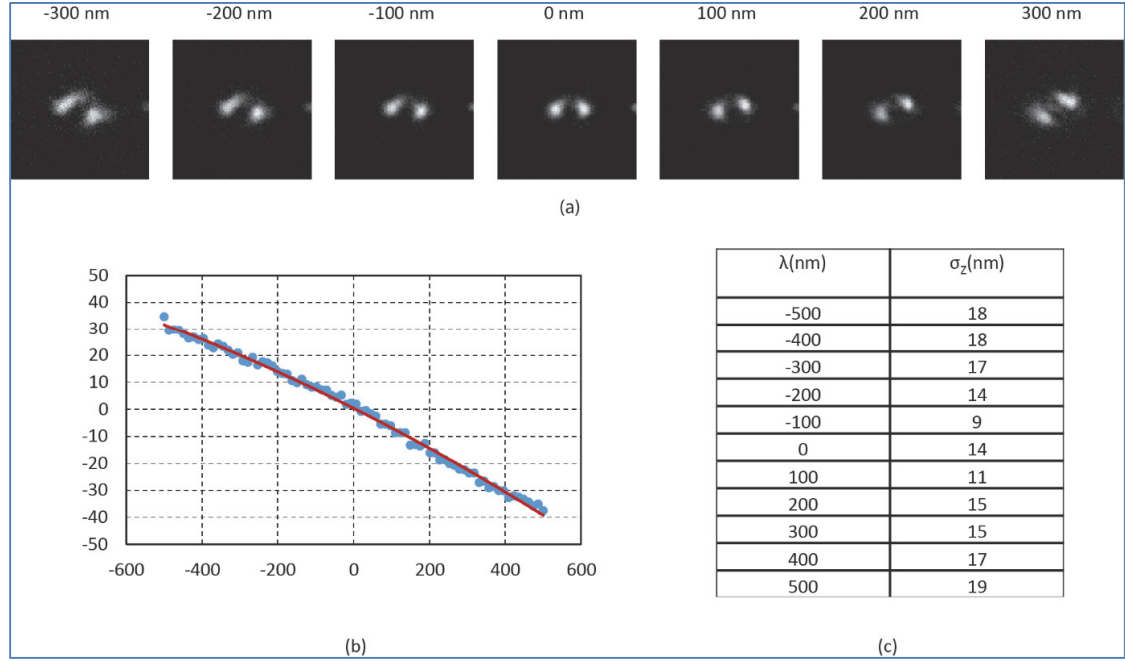


Figure 3-15 Axial localization calibration with DH. (a) Images of a fluorescent nanodiamond at different axial positions (100×100 pixels). (b) Corresponding calibration curve of the inclination of the lobes with respect to the bead axial position. (c) The \pm standard deviation of the measured angle over 100 images of fixed NDs at each axial position. To obtain the calibration curve, a single bead image is recorded at every axial position, and the lobes rotational angle is determined on each image. The accuracy of the measurement is evaluated by repeating several times the same localization event with the depletion beam on and calculating the standard deviation.

3.3.2.2 Three dimensional imaging

In order to generate a three dimensional sample with fluorescent nanodiamonds, we incorporate them in PDMS and spincoat the solution to the desired thickness. After curing, we image them with the DH-STED method. Figure 3-16 demonstrates the gain of information in every direction with a single scanning image. As a reference, a confocal scanning image with a camera detector is recorded (Figure 3-16 (a)). (The phase on the SLM is kept flat and the confocal sectioning is obtained by integrating the signal only from the pixel matching the focus position). The DH phase is then assigned to the SLM, the depletion beam is turned on and the camera image for each scanning position is recorded. Figure 3-16 (b), shows the image obtained by integrating the signal from the two lobes (double beam aperture image (iii), Figure 3-13). Individual NDs, hidden in the linear confocal image, are clearly resolved thanks to the STED improvement in resolution. To extract the three dimensional image, the axial localization is measured with the DH lobes positions. The result is presented in Figure 3-16 (d), a colormap encodes for the axial position. The depth positions of particles that were localized within the confocal depth of field are revealed. The final image is a three dimensional map of the sample and this result is obtained after a single scan acquisition. The DH axial localization needs a minimal SNR to be practical, in the final picture only the pixel with two lobes detected (with the particles detection function of ImageJ) are presented. It is equivalent to threshold the picture before axial localization readout (Figure 3-16 (c)).

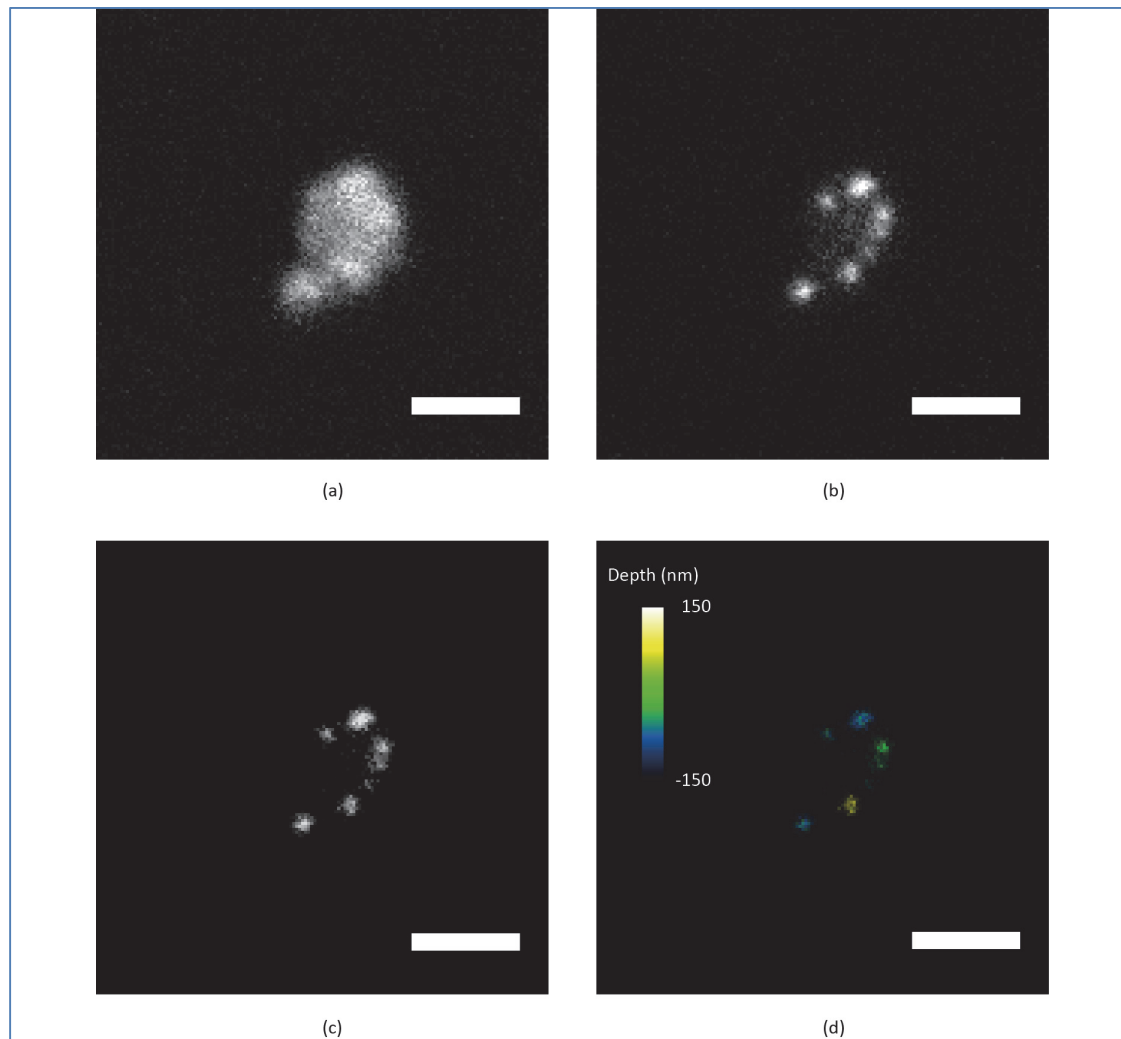


Figure 3-16 Three dimensional imaging with DH-STED. Scale bars are $1\mu\text{m}$. (a) Confocal image. (b) STED image. As the STED scanning image is recorded with a modified detection and a camera sensor, the DH-STED image is obtained by post-processing the same acquisition. (c) A threshold is applied in order to keep only the pixel with sufficient signal for DH read-out. (d) DH three dimensional image (the depth localization for each pixel is encoded with the colormap).

Figure 3-17 presents different scans with similar results. Hence, in those pictures we achieved three dimensional localization below 20 nm of superresolved fluorescent nanocrystals within a single scan acquisition. (We did not quantified here the lateral localization precision, but a precise axial localization implies a precise lateral localization of the DH lobes and consequently of the particle).

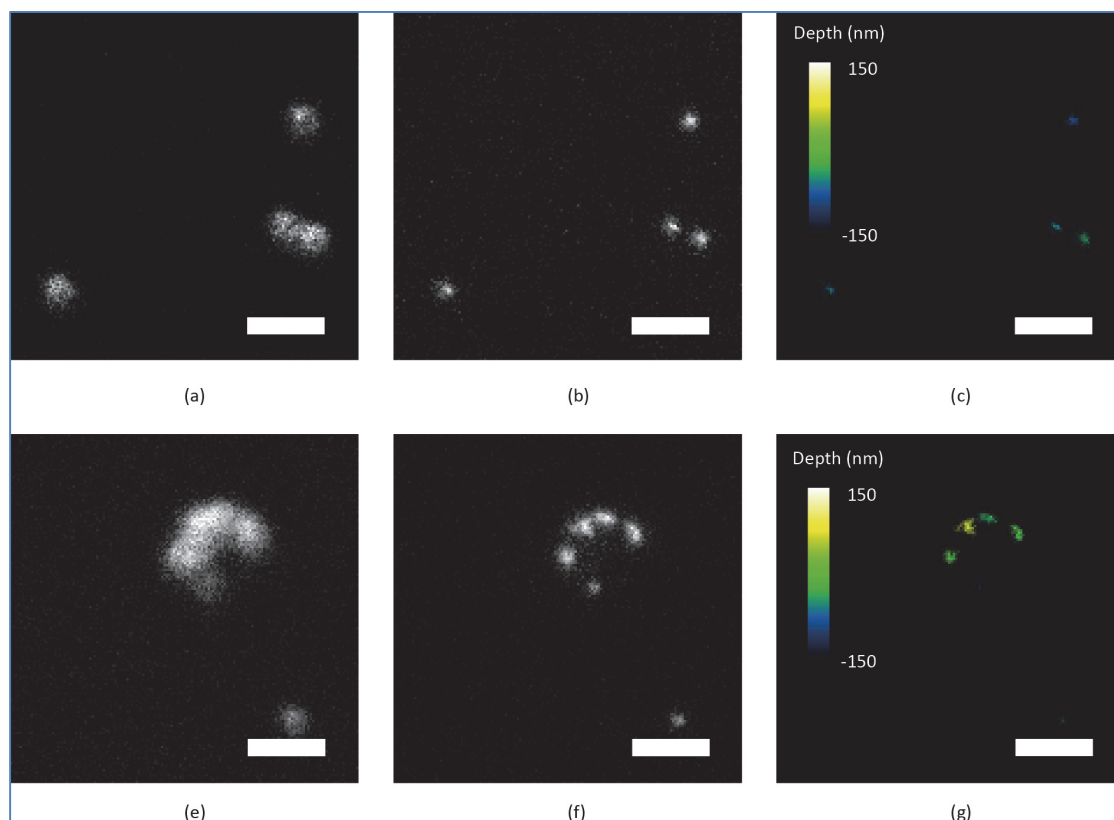


Figure 3-17 Immobilized NDs DH-STED three dimensional imaging. Scale bars are $1\mu\text{m}$ (a) and (e) Confocal scans. (b) and (f) STED scans. (c) and (g) DH-STED scan.

3.4 DH-STED with organic dye emitters

We proposed a method based on the combination of lateral superresolution microscopy and DH wavefront for localizing fluorescent labels with a very high precision. We demonstrated below 20 nm axial localization of superresolved nanodiamonds. We investigate in this section whether the method can be applied with organic dyes molecules that are subject to photobleaching. (In this thesis, we re-organized all the particular experiments to make a coherent story. In fact, this section is the first STED images that were acquired, that's how we realized how severe was that photobleaching with organic dyes in STED and why we get interested in diamonds containing vacancies).

3.4.1 Photobleaching limitation in STED microscopy.

Photobleaching was one of the early problem in STED microscopy and has been studied in the literature [127,128]. We aggravate the difficulty with the use of a camera detector since the frame rate is low compared with single pixel detector.

In the Chapter 2, we have presented the continuous wave version of STED where the excitation and depletion lasers are continuously illuminating the sample. As we detailed previously, it means that the excitation and the depletion process are competing constantly and it implies that the depletion beam power has to be high enough for the fluorescence quenching to be effective. A more complex but more efficient version of STED microscopy consists in using pulsed laser. In this case, the depletion pulse is launched immediately after the excitation pulse so that the two processes do not compete and the depletion is more efficient. A more efficient depletion process leads to a lower depletion power needed for a given resolution and leads to a reduced photobleaching [129].

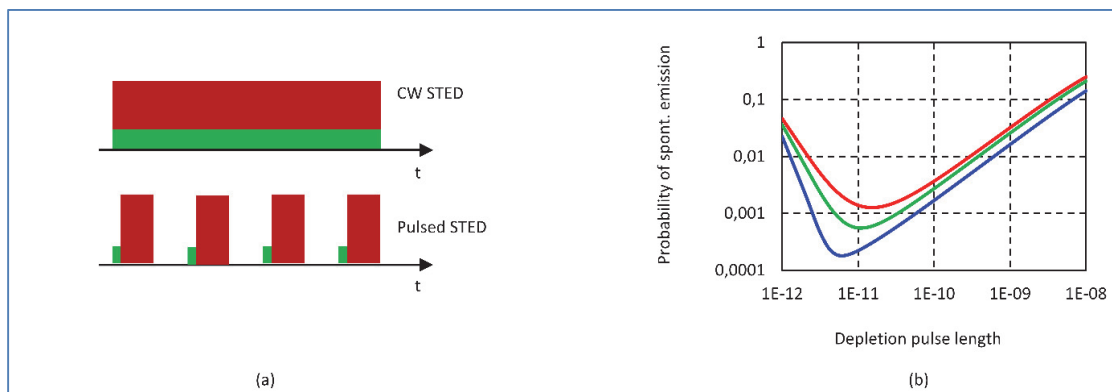


Figure 3-18 Depletion efficiency with pulsed STED (a) Schematic of the two methods, in CW STED both the excitation beam and the depletion beams are ON. In pulsed STED the depletion pulse is brought right after the excitation pulse so that the spontaneous decay did not happen yet but the excitation is finished and so do not compete with the depletion. (b) Extinction ratio (i.e. probability of spontaneous decay) in function of the depletion pulse length for a constant pulse energy. The parameter used for this calculation are fluorescence life time $\tau_{\text{fluor}} = 4$ ns, interpulse time $\tau_{\text{rep}} = 12$ ns and vibrational transition rate 5 ps^{-1} . Each plot corresponds to a fixed pulse energy and exhibits a minimum (ie a depletion efficiency) in the range 8-40 ps. The pulse energy is quantified in term of number of potential de-excitation events [130], here we represent 8 (red), 10 (green) and 16 (blue).

In order to achieve the most efficient depletion and so the more reduced photobleaching, the pulse length can be optimized. In a nutshell, for a constant pulse energy, if the depletion pulse is too long the spontaneous emission decay is not efficiently quenched (the excited molecule have enough time to emit photon), if the depletion pulse is too short the vibrational de-excitation limits the efficiency (the excited molecule do not have enough time to relax to the base level of the excited state). Depending of the dye photophysical characteristic, a pulse length of about 10-100 ps exploits the depletion power maximally. Following the same type of derivation presented in the Chapter 2 for the CW case, the influence of pulse length on depletion efficiency can be quantified [130] (details in Appendix D). The Figure 3-18 represents the extinction ratio in function of the depletion pulse length. It shows that for a fluorophore with a typical 4 ns lifetime and 0.2 ps vibrational relaxation time, the optimal depletion theoretical pulse length is 8-40 ps, depending on the pulse energy. (It must be noticed that several reports indicate better experimental results in term of signal strength for a pulse length larger than the theoretical optimal, this has been attributed to a nonlinear influence of pulse peak intensity on photodamage mechanisms [127]).

Moreover, a significant portion of photobleaching in STED has been shown to be due to triplet state build-up, i.e. caused by depletion light acting on intermediate excited state with lower energy. Consequently, the solution to reduce further photobleaching is to stop illuminating the molecule which is in its triplet state to allow relaxation to the ground state. Triplet states have typical decay time $\geq \mu\text{s}$, so two solutions have been demonstrated to reduce the photobleaching [128,131]. First, the implementation of very fast scan leads to a dwell time short enough (μs) to minimize the interaction of the depletion beam with the longer triplet state [131]. This was not a viable option for our experiment since it relies on the use of a camera detector that cannot reach million fps rate. Second, the use of low repetition rate (kHz) laser with ms interpulse: this delay is sufficient to let the molecule quit its triplet state between each pulse and has been shown to limit photobleaching [128]. This solution could have been envisaged but such a laser was not available in our lab. So, in order to demonstrate DH-STED, we built a pulsed laser STED system with 76MHz repetition rate laser with optimized depletion beam pulse length. High repetition rate laser are not ideal but it already represents an improvement compared with CW-STED, because of the optimal use of the depletion power (and so lower average power) and because the depletion sample is illuminated $\tau_{\text{pulse,depletion}}/\tau_{\text{rep}} \approx 1\%$ of the time (and so partial triplet relaxation occurs during the interpulse time).

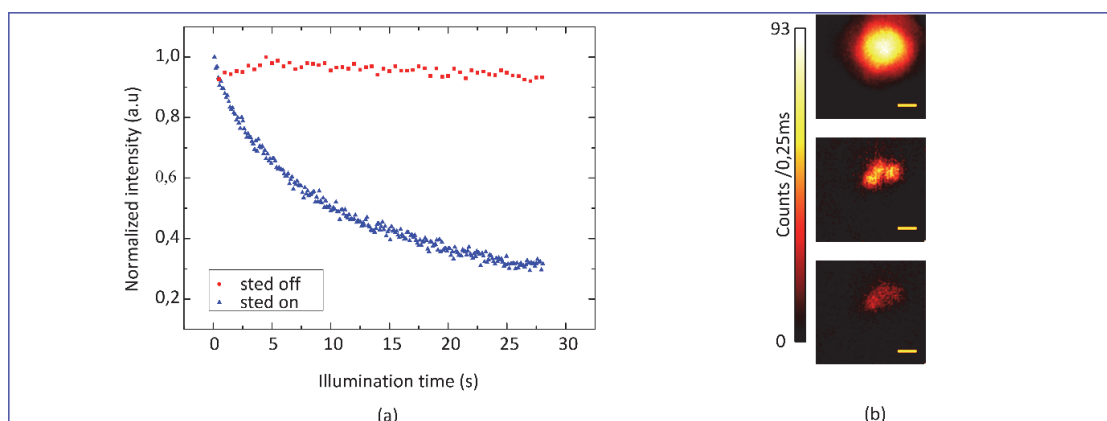


Figure 3-20 Photobleaching induced by depletion beam. (a) Images of three fluorescent beads represented with the same intensity scaling. From top to bottom: initial confocal scan, consecutive STED image before and after DH localization (around 2s illumination on each bead). (b) Fluorescence photoresistance of 100nm beads under focused light excitation and depletion beam off (red), and on (blue). Each curve on (b) is averaged out of 10 single beads. The three scanning images show depletion beam induces strong photobleaching during prolonged excitation for the DH axial localization.

As we were not able to make an entire scan with the camera as with the nanodiamonds, we proposed an alternative two steps procedure for a proof of concept experiment. The sample is placed on the focal plane of the objective. It is first scanned and a fast standard STED image is recorded with the avalanche photodiode, resolving details below the diffraction limit laterally. As a second step, the focused illumination is brought onto the spots of interest (where some fluorescent molecules are detected) and a DH image is recorded on the CCD, which is then processed to obtain the axial localization of the excited spot. During this second step the depletion beam remains on in order to maintain sub-diffraction confinement of the excited area. To perform the axial localization DH read-out the beams are immobilized 2s on each bead, as shown in Figure 3-20 (b), it leads to significant photobleaching but a limited number of points can be localized. The final image is then reconstructed with the collected lateral and axial information. This method necessitates two consecutive acquisitions but as it reduces the use of the low rate sensor (the camera) only to the points of interest, it has the potential to accelerate the process in sparse sample.

3.4.4 Three dimensional imaging of fluorescent beads (containing organic dyes)

3.4.4.1 Localization precision.

We reproduce here the same measurement that in Figure 3-15 but with fluorescent beads containing organic dye (crimson, Invitrogen): we record wide field images of the emitter immobilized on a glass slide at different depths. The bead of interest is first localized under wide field illumination, and brought at the excitation focus position. Then, for each picture, the excitation and depletion beams are switched on during the acquisition. Within the exposure time used to take the picture (100 ms), the photobleaching does not affect significantly the fluorescence level. In consequence, the localization accuracy is comparable with the one obtained with NDs. This accuracy measurement is represented with the error bars on the calibration curve, the standard deviation of the rotational angle was measured to vary between 0.9 and 1.9° corresponding to a precision between 9 and 22nm, depending on the chosen position.

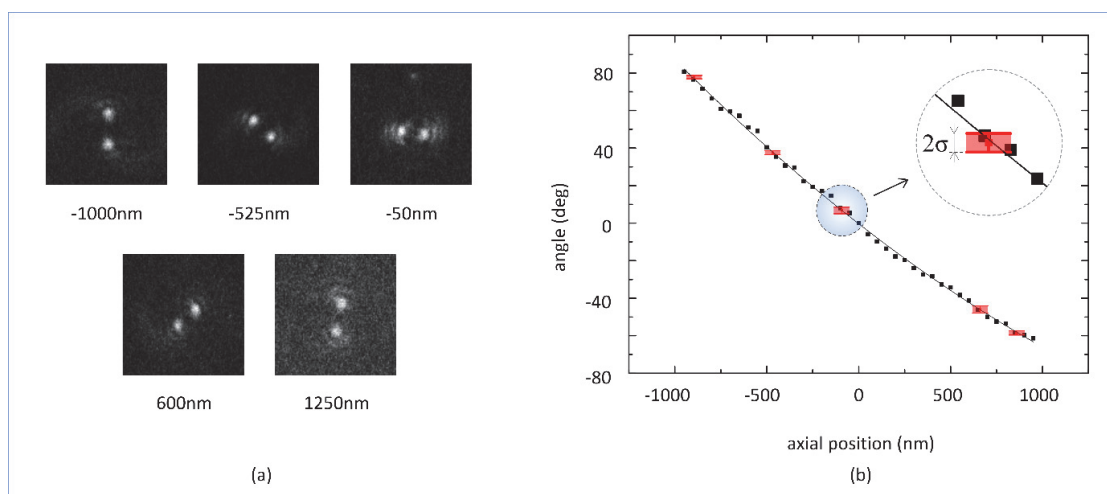


Figure 3-21 Axial localization calibration of organic label with DH. (a) Images of a fluorescent bead at different axial positions. (b) Corresponding calibration curve of the inclination of the lobes with respect to the bead axial position. Error bars represent the \pm standard deviation of the measured angle over 100 images of fixed beads. (For better visualization of those small intervals error bars are represented by lines filled with 2σ height red transparent rectangles centered on the average position. On the upper right hand corner, the area around the third error bar is magnified). To obtain the calibration curve, a single bead image is recorded at every axial position, and the lobes rotational angle is determined on each image. The accuracy of the measurement is evaluated by repeating several times the same localization event with the depletion beam on and calculating the standard deviation

3.4.4.2 Two-steps, three dimensional imaging:

To demonstrate the feasibility of the method, we imaged 100nm diameter fluorescent beads. To obtain a three dimensional sample, beads are embedded in PDMS and spin-coated on a glass slide. Figure 3-22 shows a group of nanospheres imaged by the confocal microscope, with a resolution of 250nm in Figure 3-22 (a) and resolved in Figure 3-22 (b) with DH assisted STED. Figure 3-22 (c) indicates the lateral position of each bead on the STED resolved image where beams are focused for DH readout as shown in Figure 3-22 (d). This position is determined by centroid localization onto each spot after deconvolution with the Richardson-Lucy Matlab function with a 95nm FWHM Lorentzian PSF for better bead discrimination. Thanks to the superior DH precision, the sample map is reconstructed with the bead positions in three dimensions in Figure 3-22 (e). For instance, adjacent beads "I" and "II" are resolved. They are measured to be separated by 100nm, 90nm, and 110nm, respectively in the x, y, and z directions. Thus, these two beads with a total separation distance of 173nm are resolved and localized within the accuracy range defined above in a field of view of $3\mu\text{m}$ by $3\mu\text{m}$. Without the DH localization, the beads would have appeared to be in the same axial plane.

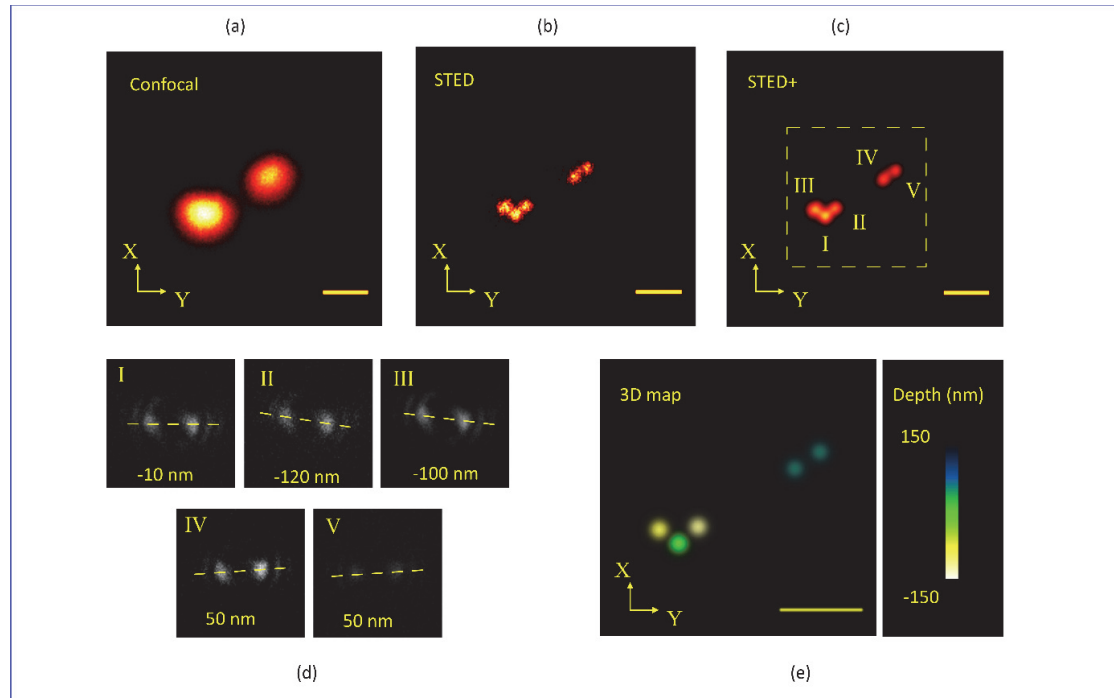


Figure 3-22 Three dimensional imaging of a group of 100nm beads immobilized in a PDMS matrix. (a) Confocal image (b) Corresponding STED image reveals five individual beads (c) Deconvolved STED with numbered cursors on the bead locations and (d) corresponding DH images recorded at these points. (e) 3D representation of the beads position into the dashed boxed delimited on (c) within the focal plane. Scale bars are 500nm. Successive use of STED resolution and DH localization, reveal the three dimensional position of each bead. Although, they appear as a large cluster merged in the focal plane on the confocal image.

3.5 Discussion

As demonstrated above, DH-STED allows for the discrimination of fluorescent emitters spaced closer than the diffraction limit and the precise localization of individual emitters in the axial dimension. However, as we mentioned in the introduction the technique relies on the fact that, STED lateral confinement and confocal sectioning are sufficient to isolate every single emitter. In other words, if the sample is so highly concentrated such that two separate fluorescence sources strictly overlap transversely and are closer than confocal axial resolution in depth, they cannot be directly resolved within a single scan. In such case, multi-scan acquisition have demonstrated good results with resolution improvement in every dimension [102], but at the cost of more phototoxic effect. However, recent work has demonstrated progress towards resolving overlapping PSFs through further data post-processing via a PSF fitting algorithm [132]. Additional work addressing this limitation to resolve a cluster of overlapping emitters with a high three dimensional localization precision is ongoing. In this case the STED depth of field could be further enhanced by the use of Bessel beams [123].

The fact that from a single lateral scan, we can extract three dimensional information (which is otherwise not possible with three dimensional STED imaging) means that the total light efficiency is better compared with three dimensional scans. In axially sparse enough sample (several examples of potential applications have been given in the introduction), DH-STED enables depth localization of a superresolved object with high, uniform precision through an extended depth of field. However, the interest of the method resides also in its flexibility. Indeed, as the pinhole is placed in the digital domain, its size can be chosen after the acquisition to optimize the image. Moreover, thanks the placement of an SLM in the imaging path, any type of Fourier filtering can be envisaged [133]. In particular, the importance of wide field imaging and a phase contrast mode in addition to STED, for overall context understanding of transparent samples, has been recently highlighted [134]. As demonstrated in the Figure 3-23, the SLM can allow for dynamically switching to phase contrast wide field imaging before scanning the region of interest. As STED imaging is entirely dependent on the fluorescent staining, the ability to reveal surrounding non-stained structures should also facilitate the use of DH-STED method with biological sample.

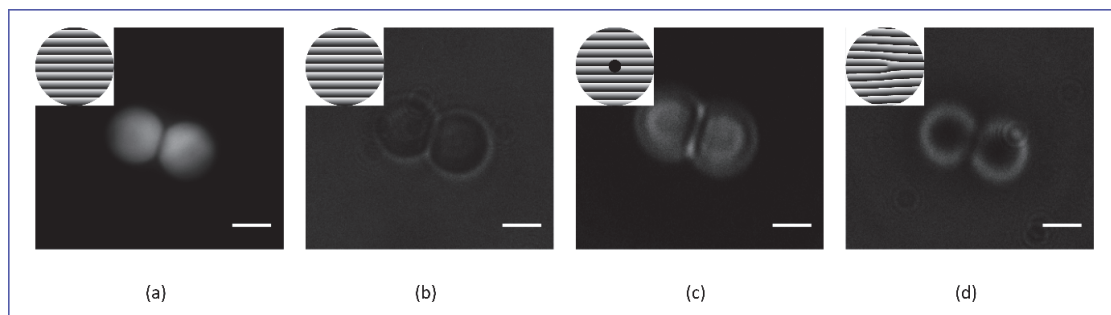


Figure 3-23 Phase contrast imaging with DH-STED setup. Images of two $1.5\mu\text{m}$ fluorescent beads immobilized on a glass slide. (a) Wide field fluorescence image. (b) White light illumination image. (c) and (d) Examples of filtering in the Fourier domain: dark field (c) and spiral contrast (d). Insets on the left hand corners represent corresponding phase pattern projected onto the SLM. Scale bars are $1\mu\text{m}$.

The major advantage of STED over stochastic methods is the acquisition time. In STED microscopy, fast scanning mechanisms lead to several frames per second acquisition within a reasonable field of view [135]. In this chapter, in the experiments we presented, the time length of the scan is still limited by the camera. We showed that the full scanning image can be recorded point by points entirely with the CCD only with nonbleaching NDs probes. In the case of organic dye, with our arrangement, we had to run the DH axial localization consecutively to the STED image and only on the points of interest. The Figure 3-20 clearly indicates that with our experimental conditions, multiple DH-STED scans with organic dyes sample would be challenging. However, those limitations are not fundamental and the recent advances in CMOS sensors make cameras more adapted for this kind of scanning microscopy experiments with low noise and high frame rate [104]. Also, as the DH detection requires a very limited number of pixel, the camera performance are now matching the required performance in term of frame rate (a camera capable of 10^4fps for $500\times 500\text{ pixel}^2$ images was recently acquired in the lab) but not yet in term of sensitivity (also some loss of collection is due to the DH phase mask itself). Otherwise, the use of a sensitive multiple point detector, like an APD array (installed recently in the latest Airyscan Zeiss commercial microscope), as a single sensor would allow a decrease in the time the laser beams dwell on a single emitter by several orders of magnitude (typical dwell time for STED is $10\mu\text{s}$ - 1ms compared with ms camera exposure). This could dramatically decrease acquisition time and improve fluorescence degradation by photobleaching and allow fast multiple 3D imaging with DH-STED.

In a more general perspective, during the time of this thesis numerous publications have involved camera detector in scanning microscopy [104–107] and the continuous improvement of the fluorescent dyes and camera sensor make those techniques more and more attractive. Finally, as we already mentioned in section 2.6, recent advances in STED microscopy have been obtained with large parallelization [99,100]. As this method is based on the wide field detection PSF modulation, it is directly compatible with STED parallelization that leads to high frame rate [99,100]. This would allow for instance to track superresolved particle position in denser environment.

3.6 Conclusion

We demonstrated the first realization of STED microscopy assisted with DH axial localization. We quantified the performance of the system by imaging single immobilized emitters on a surface. We were able to make 3D images of nanodiamonds located within a single confocal scanning plane. Following this, we applied a similar method to fluorescent beads subject to photobleaching. We first superresolved an assembly of subdiffraction beads which were axially located within a single confocal imaging plane and second localized those in depth with 25 nm precision.

The method combines the advantages of STED and DH localization, a large depth of field, fast acquisition time, and nanometric accuracy in three dimensions. We demonstrated here the feasibility of the method with nonbleaching emitters and discussed the current limitations with standard fluorophores. The potential long term significance of this work lies in the fact it combines two methods for which there is a reasonable expectation that future improvement on the emitter brightness and the detector sensitivity and speed can lead to increased performance. We expect that this technique can find use in applications requiring dynamic three dimensional far field imaging with high precision, such as protein tracking along immobilized DNA [136] or topographic measurements of cellular structures.

We have explored here one possibility of modified detection in scanning microscopy equipped with camera detector that in our opinion can have interesting application. In the next chapter we pursue our thought on scanning microscopy with a camera detector, at a bit more fundamental level. We investigate to what extent it is possible to improve the resolution of a scanning microscope only by the addition of a camera detector without direct modulation of the excitation or detection PSF.

Chapter 4 Computational nonlinear scanning microscopy.

4.1 Introduction

As we described in the previous chapter, placing a two dimensional sensor into a scanning microscope gives additional information about the collected field. After exploiting it to obtain axial information in the DH-STED technique, we propose here to investigate the possibility to gain in lateral resolution. Indeed, in an intuitive picture, it is known that a confocal microscope with an infinitely small pinhole provides not only an increase in axial resolution but also an enhancement in the lateral resolution (compared with a conventional scanning microscope). However, experimentally, a pinhole size below one Airy unit is rarely used in fluorescence microscopy because of the limited signal strength. Now, if the pinhole is replaced by a camera, each pixel of the camera can be used as a very small pinhole. Then, it is possible to recombine the information contained in each pixel of the array to obtain high enough signal and retain the resolution enhancement. This statement was made first by Prof. Sheppard [30] and later used in a different manners [106,108,109,137].

In this chapter, we first analyze the problem in a more general sense, in terms of spatial frequency filtering and structured illumination. We then examine the existing techniques to retrieve the information offered by the imaging of the excitation focal spot in a scanning system. All the existing methods are linear and are subject to a common limit: they are constrained to a factor of at most 2 in the lateral resolution improvement. We describe here how those method can be adapted to harness nonlinear optical response to further improve the resolution in a standard scanning microscope using a camera detector. We name this method Computational Nonlinear Scanning (CNS) microscopy. We experimentally demonstrate an improvement in resolution by a factor of 2.6 compared with wide field imaging by only increasing the excitation power and performing acquisition post-processing. This factor surpasses the theoretical limit in resolution that can be obtained with any linear optical technique (like SIM microscopy). It validates our approach, however this resolution gain is clearly less than what has been reported with nonlinear wide field SIM. In order to find the origin of this discrepancy, we carried out simulations on the performance of our imaging method under noisy condition compared with other imaging techniques especially WF-SIM. From the simulation results, we underline the limitation of scanning microscopy in terms of SNR performance. Finally, we propose alternative solutions, analyze their consequence in terms of sectioning and briefly investigate their feasibility.

4.2 Underlying principle

4.2.1 Structured Illumination Microscopy

The diffraction limit defines the range of spatial frequencies that can be transmitted through an imaging system. An imaging system can be seen as a low pass filter with a certain cutoff frequency. However, this statement is true only when the system is space invariant. To break this limit, SIM exploits the interaction between a patterned illumination excitation and the object. For simplicity, we assume that excitation and collection imaging systems have the same resolution limit, i.e. the same cutoff frequency equal to k_c . A sinusoidal illumination intensity pattern has a spectrum consisting of three peaks, two given by the modulation centered at $\pm k_c$, and a central peak given by the mean intensity of the pattern. In the Fourier domain, the convolution between this peaked spectrum and the sample's frequency content yields the superposition of three shifted versions of the sample's Fourier transform (Figure 4-1). Thus, frequencies higher than k_c can be collected and imaged. By recording images generated by different illumination patterns, it is possible to separate the three information components and digitally shift them back to their original position. Hence, a super-resolved image is synthesized (Figure 4-1). This is the original principle of SIM described in [138]. The sinusoidal pattern is also diffraction limited, so the maximum achievable spectral shift is equal to k_c , meaning that the maximum frequency that can be collected is $2k_c$. Thereby, the diffraction limit is increased by a factor of 2. A larger increase in resolution is possible if the object response depends non-linearly on the excitation intensity. In this case the response of the sample will contain harmonics of the spatial frequency of the illumination pattern and the resolution is then limited by the higher harmonic that can be detected.

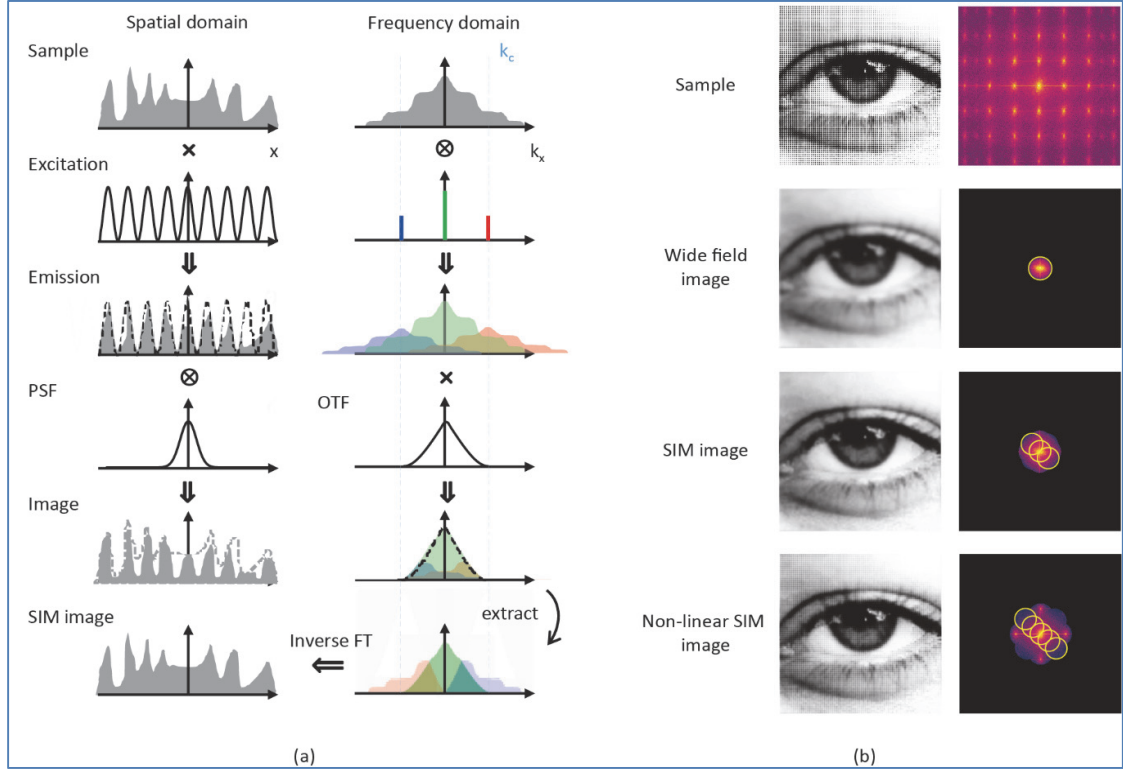


Figure 4-1 Principle of structured illumination microscopy (a) Sinusoidal illumination shift high frequency components present in the sample inside the collection band ($\pm k_c$, blue dashed lines). However, they are overlapped with lower frequency image components. The three components are extracted after multiple image acquisition and reassembled in the frequency domain to reconstruct the superresolved image. (b) Illustration of the gain in resolution with SIM. An example of sample, a picture of one eye with a high frequency grid pattern (left) and its Fourier transform (right). Different levels of detail can be observed when the spatial spectrum is limited by the cut off frequency dictated by the diffraction limit (wide field image), extended by one times the cut off frequency (linear SIM image) or extended by two times the cut off frequency (non-linear SIM). As a consequence, the grid on the sample is observed in the nonlinear SIM image demonstrating the bandwidth extension.

To be self-consistent, we recall here the basic equations of SIM [32,138]. All the formulas are based on 1D case without loss of generality. We consider a microscope with an excitation PSF (PSF_{exc}) and a collection PSF (PSF_{det}) with the same cut-off frequency k_c . Because of the incoherent nature of fluorescent imaging, the PSFs and the Optical Transfer Functions (OTF) are considered in intensity. The fluorescence intensity emitted is given by the product of the illumination intensity ($I_{exc}(r)$) and the fluorophore concentration ($S(r)$), where r indicates the position on the sample plane. In a wide field fluorescence microscope the acquired image in the imaging plane is defined as:

$$I_{camera,WF}(x) = \int I_{exc}(r)S(r)PSF_{det}(x-r) = [I_{exc}(x)S(x)] \otimes PSF_{det}(x) \quad \text{Equation 4-1}$$

Where x stands for the coordinates in the camera plane and r in the sample plane. In Fourier space it is equivalent to:

$$\tilde{I}_{camera,WF}(k) = \{ \tilde{I}_{exc}(k) \otimes \tilde{S}(k) \} OTF_{det}(k) \quad \text{Equation 4-2}$$

Where k the spatial frequency. In conventional WF-SIM, the illumination pattern is a sinusoid created by the interference of 2 beams:

$$I_{exc}(r) = 0.5 \{ 1 + \cos(k_c \cdot r + \phi) \} \Rightarrow \tilde{I}_{exc}(k) = \delta(k) + 0.5\delta(k-k_c) + 0.5\delta(k+k_c) \quad \text{Equation 4-3}$$

Which, by applying Equation 4-3 in Equation 4-2 leads to the picture acquired on the CCD:

$$\tilde{I}_{\text{camera,WF}}(k) = \left\{ \tilde{S}(k) + 0.5\tilde{S}(k-k_c)e^{-i\phi} + 0.5\tilde{S}(k+k_c)e^{+i\phi} \right\} \cdot \text{OTF}_{\text{det}}(k) \quad \text{Equation 4-4}$$

With three different excitation pattern positions (different value of Φ), the three components $S(k)\text{OTF}_{\text{det}}(k)$, $S(k+k_c)\text{OTF}_{\text{det}}(k)$, $S(k-k_c)\text{OTF}_{\text{det}}(k)$ can be calculated. The next step of the reconstruction is to shift them back to their position in the Fourier domain and sum them via a generalized Wiener filter:

$$\tilde{S}_{\text{tot}}(k) = \frac{\sum_{i=k, k+k_c, k-k_c} \tilde{S}(k)\text{OTF}_{\text{det}}(k)}{\sum_{i=k, k+k_c, k-k_c} \text{OTF}_{\text{det}}(k) + w} \cdot \tilde{a}(k) \quad \text{Equation 4-5}$$

The final image is obtained by taking the inverse Fourier transform of \tilde{S}_{tot} . The sum with the generalized Wiener filter leads both to boost spatial frequencies that lie far from the origin attenuated by the collection OTF and to prevent increasing very weak signal induced by noise (by adjusting the parameter w). Because the simple Wiener filter can cause ringing artifacts in the reconstructed image, a triangle function is used as an apodization function before the resultant spectrum becomes retransformed. This filter is by definition a deconvolution since we divide by the calculated OTF. Even if better results can be obtained with more sophisticated deconvolution (especially iterative like Richardson Lucy), we use this simple reconstruction in all the experiments in which the influence on the resolution enhancement is well defined. As the sinusoidal pattern results in the shift in one direction, the same process is repeated with different orientation to obtain isotropic resolution enhancement.

In the nonlinear case the sinusoidal excitation includes some harmonics given by fluorescence saturation:

$$\tilde{I}_{\text{exc}}(k) = \delta(k) + \alpha \cdot \delta(k-k_c) + \alpha \cdot \delta(k+k_c) + \beta \cdot \delta(k-2k_c) + \beta \cdot \delta(k+2k_c) + \dots \quad \text{Equation 4-6}$$

Where α and β are constant coefficients that depend of the nonlinearity. So the Equation 4-4 becomes:

$$\tilde{I}_{\text{camera,WF}}(k) = \left\{ \tilde{S}(k) + \alpha \cdot \tilde{S}(k-k_c)e^{-i\phi} + \alpha \cdot \tilde{S}(k+k_c)e^{+i\phi} + \beta \cdot \tilde{S}(k-2k_c)e^{-i\phi} + \beta \cdot \tilde{S}(k+2k_c)e^{+i\phi} + \dots \right\} \cdot \text{OTF}_{\text{det}}(k) \quad \text{Equation 4-7}$$

Meaning that two more acquisition per harmonics are needed to resolve the system. Then, the image reconstruction follows the linear one.

4.2.2 Structured Illumination in Scanning microscopy

The spot obtained at the focus of a microscope objective has a non-uniform intensity spatial profile, the Airy pattern described (Chapter 2) as:

$$I_{\text{exc}}(r) = \text{PSF}_{\text{exc}}(r) = \left(\frac{2 \cdot J_1(r)}{r} \right)^2 \quad \text{Equation 4-8}$$

So a focused spot is not space invariant and in this sense it is a special type of structured illumination pattern. In traditional scanning microscope, the signal collected for each scanning position is integrated on a detector, losing the spatial information. This information loss is illustrated in Figure 4-2. If a grating of a spatial frequency above the cutoff frequency of the objective is imaged (Figure 4-2 (a)), both the scanned and the wide field images are flat: no information about the sample is collected. Now, during the scan, if the spot of the sample excited by the scanning laser focused is spatially resolved with a multi-pixel detector array, i.e. a camera (Figure 4-2 (b)), it makes a difference: some variations in the detected profile depending on the position of the focused spot on the sample can be registered. In consequence, some information provided by the interaction between the sample and the focused spot pattern is collected. Thus, by imaging the diffraction limited focused excitation pattern in each point of a scanning mi-

croscope it is possible to retrieve some information as in SIM. This is the underlying idea to all those methods. However, as opposed to a wide field sinusoidal pattern that contains only one frequency, a focused spot is a pattern that contains all the frequencies possibly supported by the objective. As a focused spot holds a continuous spectrum of frequencies, the information brought in the collection band by each of these frequencies overlap. The techniques presented in the next paragraph allow for the isolation of the contribution from one single frequency, and thus lead to a final image as it would be obtained with a wide field SIM setup.

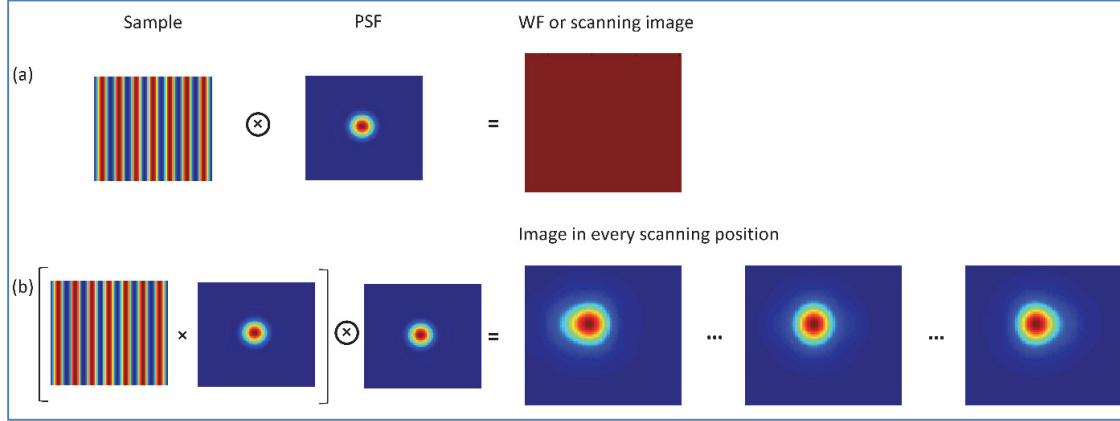


Figure 4-2 Information loss during scanning imaging. (a) The scanning (or a wide-field) image of a sinusoidal pattern is given by the convolution of the PSF by the sample. In the present case, the sample spatial frequency is above the OTF cut-off frequency so the resulting image is flat. (b) The image of the excitation spot during the scan. Due to the frequency mixing in between the sample and the excitation focus some variation can be observed in the images. Those variations hold the high frequency information that can be extracted to gain in resolution.

4.3 Method

4.3.1 Setup

As illustrated in Figure 4-3, the beauty of the method lies in its simplicity. The image are acquired with a standard scanning microscope where the point detector has been replaced by a camera in the conjugate plane of the sample. While the sample is scanned, individual patterns are recorded for each scanning position. The final dataset of images includes the full scan dependency on both the focus scan position and the position on the detector. As we explained in the previous paragraph, this four dimensional acquisition dataset contains additional information that leads to resolution enhancement.

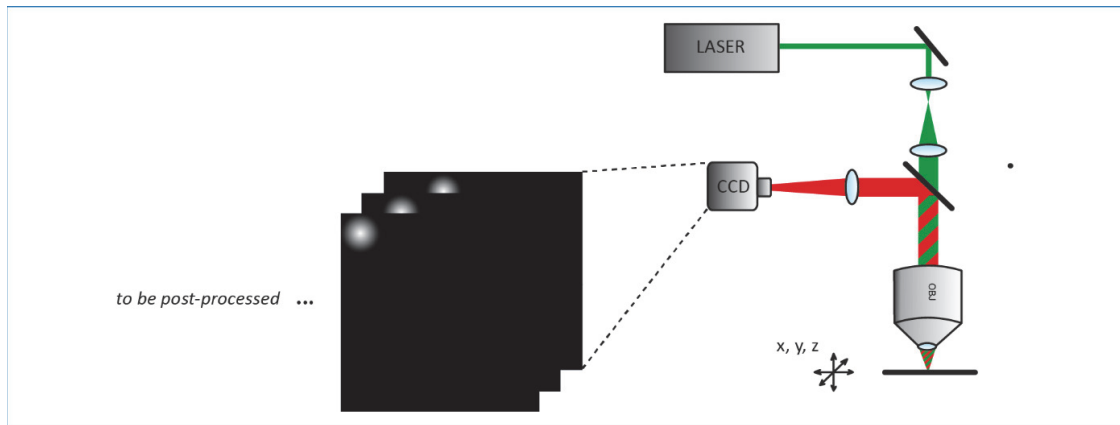


Figure 4-3 CNS microscopy setup. A standard scanning microscope with a camera detector.

Here, we give more details about the experimental setup. A 532 nm excitation laser (Verdi V10 Coherent) is used for the excitation. The incident power on the setup is controlled with a half wave plate (WPH05M-532 -Thorlabs) and a cube beam splitter (PBS251-Thorlabs). The quality of the focus spot is critical for 2 reasons. First, since the method relies on the change in shape induced by the sample on the excitation pattern, the closer the spot is from the theoretical pattern the more isotropic will be the gain in resolu-

tion. Second when the fluorescence saturation will be involved to create an equivalent PSF with an extended frequency the lack of aberration is crucial. Especially the quality of the first zero of the Airy pattern determines how steep the slope is in the saturated PSF, i.e. how large the equivalent OTF is. Therefore, in order to obtain the best focus quality, the beam is spatially filtered and expanded to largely overfill the microscope objective (60X Newport). The beam is reflected on a beam splitter (Lasermux 514-543 Semrock) and the fluorescence is collected in reflection through a fluorescence filter (670/30ET Chroma). The sample is moved with a piezoelectric stage (P733.3 PI) and the images are acquired with a standard CCD camera (Scion corporation CFW-1312M). The camera and the stage are controlled with a home written program in Labview.

4.3.2 Post-processing algorithms

The three post processing algorithms presented here have been proposed in [30,32,139]. Two of them were demonstrated (namely structured detection [140] and pixel reassignment [106,137]) before our work and the third one, the temporally modulated excitation [141], after our work. Each of those methods can be implemented entirely optically which allow faster imaging. We show here how they can be applied entirely digitally. It is obviously slower but it allows us to compare their performance (by post processing differently the same acquisition scan) in term of lateral resolution.

In a scanning microscope, at every scan position, at time t , the fluorophores in the sample are excited by the focused beam PSF_{exc} , and the image created on the camera (for a non-descanned setup) is obtained as:

$$I_{\text{camera}}(x, t) = \int \text{PSF}_{\text{exc}}(r - t) S(r) \text{PSF}_{\text{det}}(x - r) dr \quad \text{Equation 4-9}$$

where t stands both for the scanning position and the time, assuming a constant scanning velocity equal to one (and x and r defined as above). It can be seen in Equation 4-9, that the signal collected is dependent on both the scan position (t) and on the position on the detector (x).

The OTF has a continuous spectrum up to k_c , all the frequencies of the sample lower than $2k_c$ are folded into the detection bandwidth. Thus, the three methods described below can be seen as a way to extract the information of interest brought into the collection objective.

4.3.2.1 Pixel reassignment

The first and probably the most elegant way to treat it, is based on the fact that the most probable origin of the detected photons on the camera is half way (assuming identical PSF_{exc} and PSF_{det}) between the scan position and the detected position [139]. Mathematically, the signal from a point $x_d = t - x$ on the camera detector is reassigned to its most probable origin, the point $x_r = 0.5t + 0.5x$. After integration over the detector, it results in an image [109,137,139]:

$$I_{\text{scan}}(x_r) = \iint \text{PSF}_{\text{exc}}(r - x_r - 0.5x_d) \text{PSF}_{\text{det}}(r - x_r + 0.5x_d) S(r) dr dx_d \quad \text{Equation 4-10}$$

Leading to an effective optical transfer function [109,137,139]:

$$\text{OTF}_{\text{eff}}(k) = \text{OTF}_{\text{exc}}(0.5k) \cdot \text{OTF}_{\text{det}}(0.5k) \quad \text{Equation 4-11}$$

Therefore, improving the cut-off frequency and the equivalent resolution by a factor 2. The reassignment corresponds to a two times magnification of the image before being integrated on the non-descanned camera. Thus, it has been implemented optically by descanning the collected signal, magnifying by a factor two and rescanning it [107].

4.3.2.2 Structured detection

As proposed in [32], the recorded image at each time t (i.e. each scan position) can be multiplied by a transmittance grating mask, as if a transmission mask would be placed onto the camera sensor. Then, the image recorded on the camera for each scanning point is:

$$I_{\text{scan,mod}}(x, t) = \int M(x) \text{PSF}_{\text{exc}}(r - t) S(r) \text{PSF}_{\text{det}}(x - r) dr, \text{ with } M(x) = \cos(k_{\text{mod}} x + \phi) \quad \text{Equation 4-12}$$

Following this, the total signal on the camera is integrated and assigned to the current scanning position, like in scanning microscopy with a point detector:

$$I_{\text{scan,mod}}(x) = \iint \text{PSF}_{\text{exc}}(r - t) S(r) \{M(x) \text{PSF}_{\text{det}}(x - r) dx\} dr \quad \text{Equation 4-13}$$

Which can be written in the Fourier domain:

$$\begin{aligned} \tilde{I}_{\text{scan,mod}}(k) &= \text{OTF}_{\text{exc}}(k) \left\{ \tilde{S}(k) \otimes [\text{OTF}_{\text{det}}(k) \tilde{M}(k)] \right\} \\ &= \text{OTF}_{\text{exc}}(k) \left\{ \text{OTF}_{\text{det}}(k_{\text{mod}}) \tilde{S}(k - k_{\text{mod}}) e^{-i\phi} + \text{OTF}_{\text{det}}(-k_{\text{mod}}) \tilde{S}(k + k_{\text{mod}}) e^{i\phi} \right\} \end{aligned} \quad \text{Equation 4-14}$$

If $\text{OTF}_{\text{exc}} = \text{OTF}_{\text{det}}$, the $\tilde{I}_{\text{scan,mod}}$ image is analogous to the image recorded in wide field SIM presented in Equation 4-4. The operation is repeated for different orientations and different phase shifts and the algorithm detailed for WF-SIM can be applied to reconstruct the final image with a twice better resolution. Here, two comments can be made. First, the modulation is digital, so it can be negative, and the zero order can be removed improving the out of focus light rejection [140]. Second, the constant factors $\text{OTF}_{\text{det}}(\pm k_{\text{mod}})$, are different from the 0.5 in WF-SIM it does not change the theoretical resolution but their value will have a strong influence on our final results as we will explain later.

4.3.2.3 Temporal modulation:

Alternatively, as proposed in [32], the recorded image at each time t (i.e. each scan position) can be multiplied by a constant factor, just as if the excitation laser intensity would be modulated in time:

$$I_{\text{scan,mod}}(x) = \iint M(t) \text{PSF}_{\text{exc}}(r - t) S(r) \text{PSF}_{\text{det}}(x - r) dr dt, \text{ with } M(t) = \cos(k_{\text{mod}} t) \quad \text{Equation 4-15}$$

Or equivalently, in the Fourier domain:

$$\begin{aligned} \tilde{I}_{\text{scan,mod}}(k) &= \left\{ [\tilde{M}(k) \text{OTF}_{\text{exc}}(k)] \otimes \tilde{S}(k) \right\} \text{OTF}_{\text{det}}(k) \\ &= \left\{ \text{OTF}_{\text{exc}}(k_{\text{mod}}) \tilde{S}(k - k_{\text{mod}}) + \text{OTF}_{\text{exc}}(-k_{\text{mod}}) \tilde{S}(k + k_{\text{mod}}) \right\} \text{OTF}_{\text{det}}(k) \end{aligned} \quad \text{Equation 4-16}$$

The $\tilde{I}_{\text{scan,mod}}$ image is this time fully analogous to Equation 4-4 (as opposed to the spatial modulation case the excitation and detection OTF don't need to be swapped). The WF SIM reconstruction can be directly applied, leading to doubling in resolution. As for Equation 4-14 the digital modulation removes the DC term, and again we note that the constant coefficients $\text{OTF}_{\text{exc}}(\pm k_{\text{mod}})$ in front of the different spectrum components differ from the WF SIM case.

4.3.3 Digital post-processing implementation with sample scan:

In our implementation we move the sample instead of the beam for scanning. Thanks to the nanometric precision of the piezo-electric stage, we have a very precise knowledge of the respective beam and sample positions. This precision is necessary to guarantee the uniformity of the modulation, however, as we move the sample (and not the beam), it obliges us to reassign each picture to the scanning position. Thus, we recreate a set of data as in a non descanned setup before applying the actual post processing reconstruction. Figure 4-4 summarizes the full reconstruction procedure.

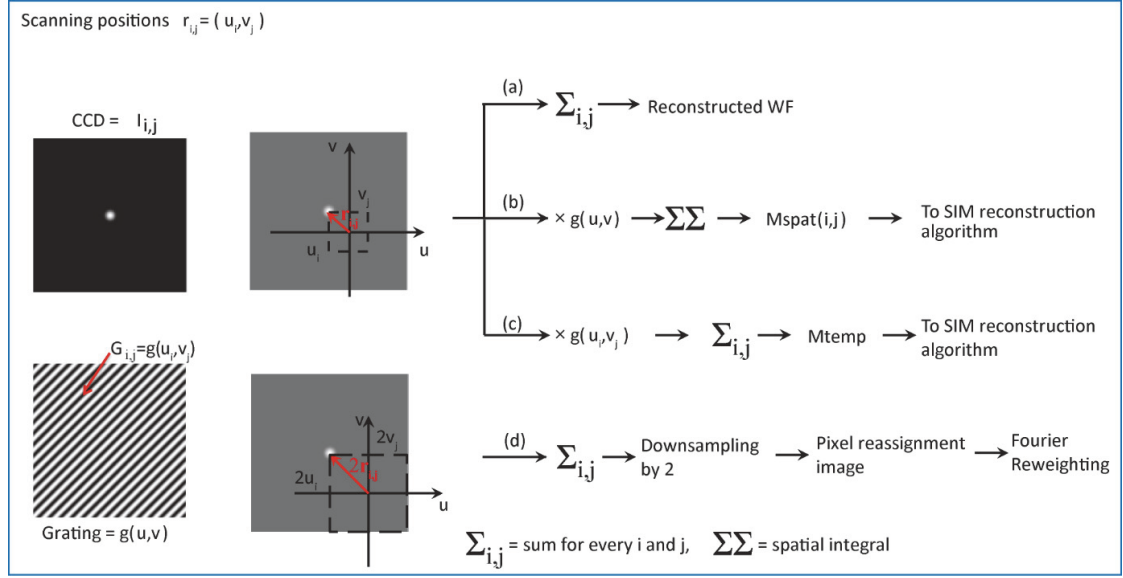


Figure 4-4 Reconstruction steps to recreate a non-descanned modulated illumination. As in our experimental apparatus the sample is moved (and not the beam), the relative position of the excitation beam compared to the camera sensor will remain the same for the whole experiment. We note the sample shift r . A confocal image can be formed by summing all the pixels of the image (integrating the image in space) and assigning the obtained value to the position $-r$. The pictures acquired can also be processed, yielding to four possible kinds of reconstructed images: (a) *Wide field reconstruction*: for each scanning position r_{ij} , the CCD image I_{ij} is shifted over a distance $-r_{ij}$ and summed to the images acquired in every i and j position. (b) *Temporal point scanning SIM*: for each scanning position r_{ij} , the CCD image I_{ij} is shifted over a distance $-r_{ij}$ and multiplied by a coefficient G_{ij} . Summing all the images acquired in every i and j position, it is possible to obtain a digital temporal sinusoidal modulation (Mtemp). Same procedure is applied for all the orientation and phase shifts needed for SIM. At the end SIM reconstruction algorithm as in [138] is used. (c) *Spatial point scanning SIM*: for each scanning position r_{ij} , the CCD image I_{ij} is shifted over a distance $-r_{ij}$ and multiplied by a grating function g . Integrating the modulated images in space and assigning the obtained values to the position $-r_{ij}$, a spatial sinusoidal modulation is obtained (Mspat). At the end SIM reconstruction algorithm as in [138] is used. (d) *Pixel reassignment*: for each scanning position r_{ij} , the CCD image I_{ij} is shifted over a distance $-2r_{ij}$ and summed to the images acquired in every i and j position. The superresolved image is obtained downsampling the final image by a factor of 2 and applying Fourier reweighting as in [109].

4.4 Comparison of the linear algorithms:

As described above, the three methods (pixel reassignment, temporal modulation and spatial modulation) adapt the SIM principle to scanning microscopy and in theory provide the same resolution improvement. To verify this experimentally, we imaged 40 nm fluorescent nanodiamonds immobilized on a glass slide. We used red NDs with the emission peak centered at 670 nm and a 0.8 NA objective, so that the theoretical Full Width at Half Maximum (FWHM) of the image spots is 430 nm. Figure 4-5 illustrates the effect of the different post processing techniques. The images were reconstructed through digital temporal modulation SIM, as shown in Figure 4-5 (b). Digital spatial modulation SIM, shown in Figure 4-5 (c) and pixel reassignment method, in Figure 4-5 (d), are also demonstrated using the same set of data. As indicated in Figure 4-5 (e), the three methods enhanced the lateral resolution nearly identically by a factor of 1.75. To obtain comparable resolution improvement in Figure 4-5 (d), Fourier reweighting is applied on the processed image with pixel reassignment [109], while Fourier reweighting is included in the last inversion step of conventional structured illumination (cf Equation 4-5) used with the spatial and temporal techniques.

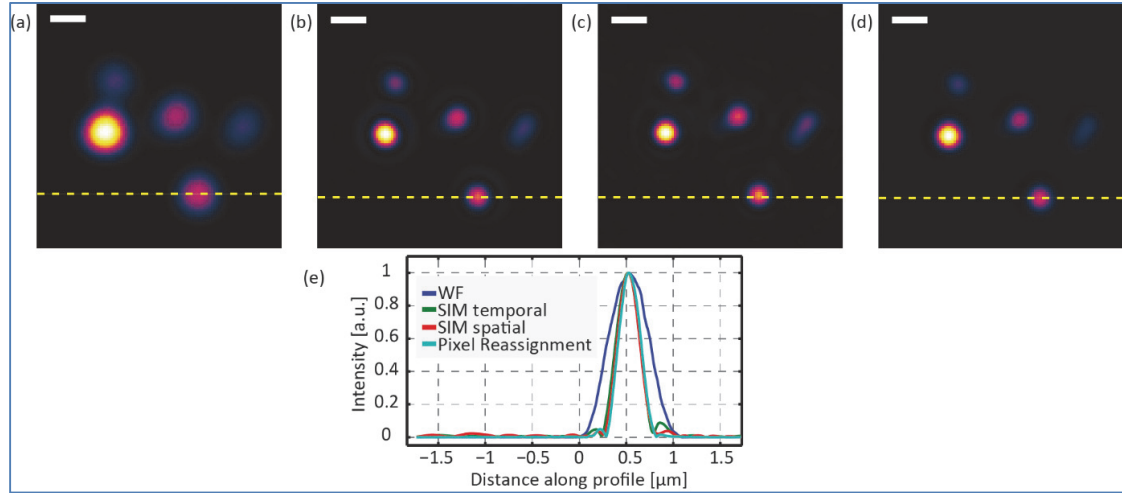


Figure 4-5 Linear imaging of FNDs with an 0.8 NA objective. (a) wide field image, (b) digital temporal scanning SIM image, (c) digital spatial scanning SIM image, (d) pixel reassignment image. (e) Intensity profiles along the yellow dashed line for the different techniques. The signal from a single subdiffraction FND gives an estimation of the lateral resolution improvement. The FWHM is 500 nm in the wide field image and 285 nm with the linear processing techniques. It corresponds to a 1.75 times improvement in lateral resolution. Scale bars are 500 nm

Thus, we digitally implemented the methods proposed in [139] and [32], and observed that the temporal point scanning SIM leads to a similar gain in resolution compared to the other methods. However, it can be noticed that, as in [106,107,109,137], we did not reach the theoretical factor 2 of improvement, while in linear wide field structured illumination, a true doubling in resolution is usually observed [108,142]. We will come back to the cause of this observation later since the effect will be critical in the nonlinear case.

Hence, as previously demonstrated, these techniques provide a resolution that slightly surpasses the theoretical resolution limit of a confocal microscope with an infinitely small pinhole, with a much stronger signal, while retaining the confocal sectioning ability (by the placement of a digital pinhole). This hybrid method can improve considerably the imaging quality of a large variety of biological samples [108,109], but the improvement in lateral resolution is inherently limited to less than 2 fold.

4.5 Non-linear resolution enhancement method:

As stated by Heintzmann et al. [143] (and also in Chapter 2), to increase the resolution above the doubling provided by SIM, the system should be both space variant and nonlinear, it is the case for instance in STED microscopy where the fluorescence is depleted with a donut profile and by stimulated emission which is a nonlinear mechanism. Fluorescence saturation was proposed as a nonlinear mechanism susceptible to improve the resolution of wide-field patterned illumination [144] and Gustafsson et al. demonstrated a lateral improvement in resolution by 5.5 times [28] with saturated SIM (method detailed in section 4.2.1). We show now how the fluorescence saturation phenomenon can be harnessed to the point scanning configuration to provide similar improvement in resolution.

4.5.1 OTF spectrum elongation with fluorescence saturation

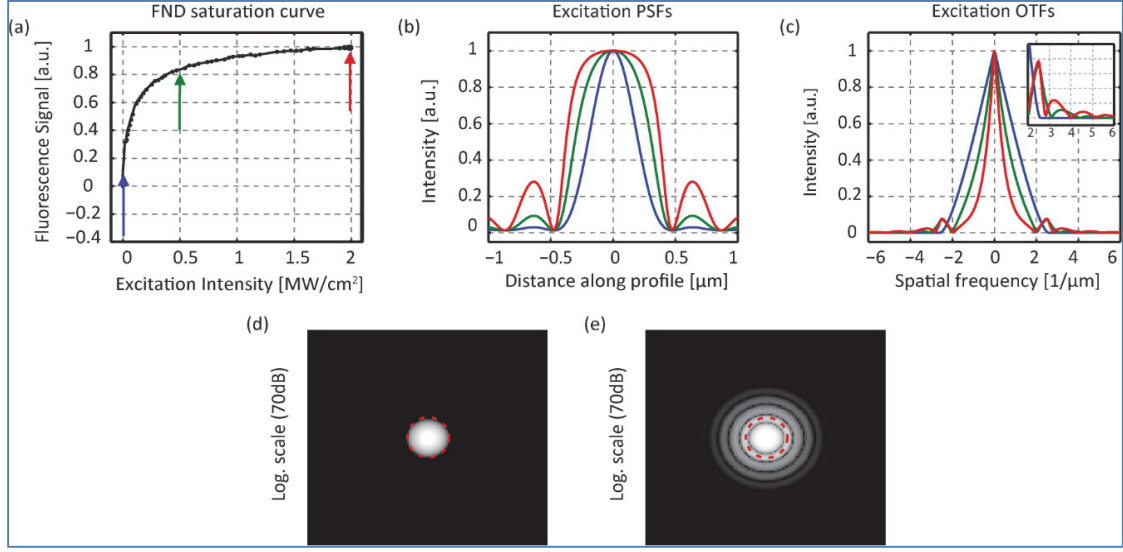


Figure 4-6 Saturation of FNDs and corresponding saturated PSFs. (a) Fluorescence signal from a single ND as a function of laser excitation intensity. (b) Equivalent PSFs corresponding for different excitation intensities indicated by the arrows on the curve in (a). (c) Fourier transforms of the PSFs in (b). The inset shows a close-up of the profiles for spatial frequencies above $0.8 k_c$ highlighting the higher frequency content introduced by the nonlinearity. In (a), (b) and (c) red color stands for 2 MW/cm^2 excitation intensity, green stands for 0.5 MW/cm^2 and blue for 0.02 MW/cm^2 . (d) Linear PSF and (e) saturated PSF (2 MW/cm^2) plotted in logarithmic scale with a dark to white range of 70dB.

Figure 4-6, illustrates the saturation of the NDs fluorescence. In Figure 4-6 (a), we show the fluorescence signal emitted by a single FND with respect to applied laser intensity. For illumination intensities above one photon per absorption cross-section per lifetime rate, the fluorescence emission rate of the NDs depends nonlinearly on the illumination. The fluorescence saturation phenomenon can be described by the model presented in Appendix B [144]:

$$I_{\text{em,sat}}(r) = \frac{a \cdot I_{\text{exc}}(r)}{1 + b \cdot I_{\text{exc}}(r)} S(r) \quad \text{Equation 4-17}$$

Where I_{em} is the fluorescence intensity and a and b are constant factors.

The fluorescence response, $I_{\text{em,sat}}$, is consequently non-linear to the excitation intensity I_{exc} , but remains proportional to the fluorophores density $S(r)$ even under saturation. Therefore, the excitation PSF is:

$$\text{PSF}_{\text{exc,sat}}(r) = \frac{a \cdot \text{PSF}_{\text{exc}}(r)}{1 + b \cdot \text{PSF}_{\text{exc}}(r)} \quad \text{Equation 4-18}$$

The induced excitation PSFs for different saturation levels are plotted on Figure 4-6(b). It can be observed that the bandwidths of the absolute value of the corresponding OTFs increase with the excitation power (Figure 4-6(c)). The widening of the OTFs is illustrated in Figure 4-6 (d) and (e), the absolute value linear and saturated OTFs are plotted with logarithmic scale. The saturated OTF clearly expands above the cut-off frequency (red dashed circle). In theory, as saturation increases, the gain in resolution is unlimited; however, the noise in the image acquisition will limit the technique and with standard fluorophores photobleaching would be a major limitation. Furthermore, special care has to be taken with the sample preparation to limit background emission when using high power excitation. In our experiments, in order to minimize fluorescent background, low fluorescence glass slides and immersion oil were used. It can also be noticed that we consider here the absolute value of the OTF (commonly referred to as the modulation transfer function). Depending on the saturation level the real part of the OTF can exhibit negative ripples, however, it does not influence the final image since it is compensated for in the final deconvolution of the SIM reconstruction (as described in paragraph 4.2.1).

4.5.2 CNS reconstruction

In the non-linear case, a constant high power is used for the excitation beam in order to obtain a non-linear response in fluorescence from the sample. It results in an equivalent non-linear excitation PSF that retains higher spatial frequencies up to $k_{\max\{exc,NL\}} \gg k_c$ (Figure 4-6(e)). Consequently the maximum frequency that can be collected through the objective ($k_{\max\{sample\}}$) is given by:

$$k_{\max\{sample\}} - k_{\max\{exc,NL\}} \leq k_c \quad \text{Equation 4-19}$$

So the maximum gain in resolution is more than 2 fold. As the modulation is produced in the digital domain, we can generate a pattern with all the desired frequencies. We chose it to be:

$$M(t) = 0.5[\cos(k_{mod}t) + \cos(2k_{mod}t + \pi)] \quad \text{Equation 4-20}$$

In order to isolate the frequency of interest from saturated OTF we use the temporal modulation reconstruction. Thus, the modulation filters out the Fourier transform of the sample shifted by the $\pm k_{mod}$ and $\pm 2k_{mod}$ components of the excitation OTF. By plugging Equation 4-20 into Equation 4-16 we obtain:

$$\begin{aligned} \tilde{I}_{scan,mod}(k) &= \left\{ \left[\tilde{M}(k) \text{OTF}_{exc,NL}(k) \right] \otimes \tilde{S}(k) \right\} \text{OTF}_{det}(k) \\ &= \left\{ \begin{aligned} &\text{OTF}_{exc,NL}(k_{mod}) \tilde{S}(k - k_{mod}) + \text{OTF}_{exc,NL}(-k_{mod}) \tilde{S}(k + k_{mod}) \\ &+ \text{OTF}_{exc,NL}(2k_{mod}) \tilde{S}(k - 2k_{mod}) + \text{OTF}_{exc,NL}(-2k_{mod}) \tilde{S}(k + 2k_{mod}) \end{aligned} \right\} \text{OTF}_{det}(k) \end{aligned} \quad \text{Equation 4-21}$$

This equation is equivalent to Equation 4-7 in nonlinear WF SIM. So, sample frequencies up to $3k_c$ can be extracted and used to recompose a super-resolved image (if $k_{\max\{exc,NL\}} > 2k_c$). The number of modulation phase shifts necessary to recompose the final image is proportional to the number of components used. An important comment is that only the specific combination of digital and temporal modulation makes the nonlinear resolution improvement feasible. We thus name our method computational nonlinear scanning (CNS) microscopy. Indeed, as shown in Figure 4-6 (b), the saturation modifies the shape of the excitation PSF ($\text{PSF}_{exc,sat}$) while the detection PSF remains unchanged. Below, we explain why this dictates the way the method can be implemented.

We explained above that the structured detection method relies on the fact that PSF_{exc} and PSF_{det} are the same (Equation 4-14 equivalent to Equation 4-4 only if OTF_{exc} and OTF_{det}). This approximation does not hold in the non-linear case, so structured detection cannot be used. For the pixel reassignment technique, the fact that PSF_{exc} and PSF_{det} do not have the same frequency content can be taken into account by adapting the magnification factor applied to the image during the post processing [139]. However, the technique relies on the fact that PSF_{exc} and PSF_{det} are scaled version of each other, which is not the case with fluorescence saturation. So only the temporal modulation allows to filter out spectral components of interest from the excitation OTF irrespectively of its shape. Intuitively, this is true because the temporal modulation happens before the objective, thus it modulates the signal before it is collected by the imaging system. To illustrate the fact that the temporal modulation makes the reconstruction insensitive in shape we ran a simulation of the reconstruction both with a standard focus and with a cross shaped beam with the same maximum frequency. As it can be observed in Figure 4-7, even if the scanned image is distorted because of the shape of a different excitation beam, the reconstructed image looks identical to the standard case.

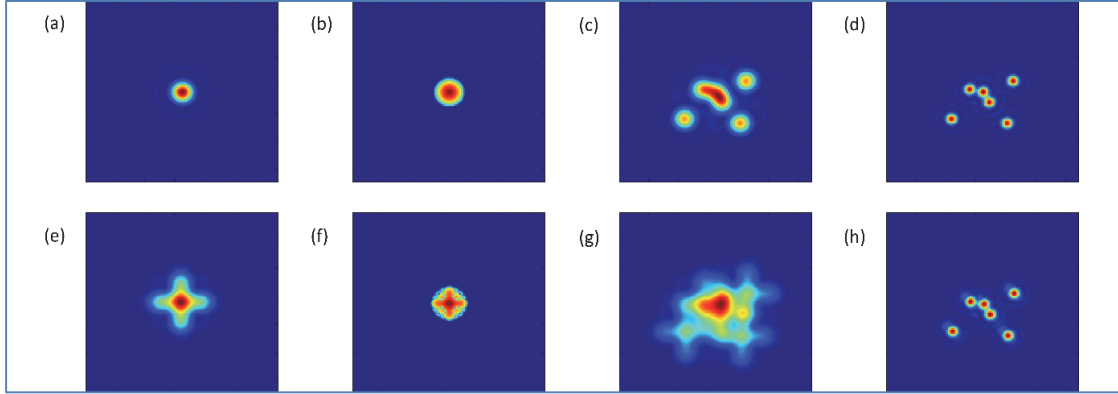


Figure 4-7 Insensitivity of the temporal modulation algorithm to the beam shape. (a) Standard excitation focus. (b) Corresponding OTF. (c) Simulated scanning image of a few particles. (d) Reconstructed image with a factor 2 improvement in resolution. (e) Excitation focus with a modified cross shape. (f) Corresponding OTF, the maximum frequency is the same. (g) Simulated scanning image of a few particles, because of the shape of the excitation beam, the image looks distorted. (h) Reconstructed image with a factor 2 improvement in resolution. As the two PSFs have the same frequency content and the temporal modulation algorithm is insensitive to the excitation pattern shape, the reconstructed images is identical to the standard case.

The temporal modulation leads to a correct reconstruction with any excitation beam shape including the “bell shape” saturated PSF (Figure 4-6 (b)). However, it is not possible to use the physical temporal modulation filtering. Only the equivalent digital post treatment can be applied. Indeed, any excitation PSF shape can be used but it needs to remain constant during the scan. Now, if the beam is physically modulated temporally, it means that the level of saturation and thus the excitation PSF shape changes with time (and equivalently with scanning position). In such a case, the coefficient $OTF_{exc,NL}(\pm k_{mod})$ would vary during the scan, making the Equation 4-21 unsolvable. Therefore, keeping the intensity constant over the scan allows to keep the shape of the PSF unchanged, but it necessitates the digital implementation, i.e. the complete record of a camera image for each scanning position, to extract the high frequencies contained in the saturated OTF.

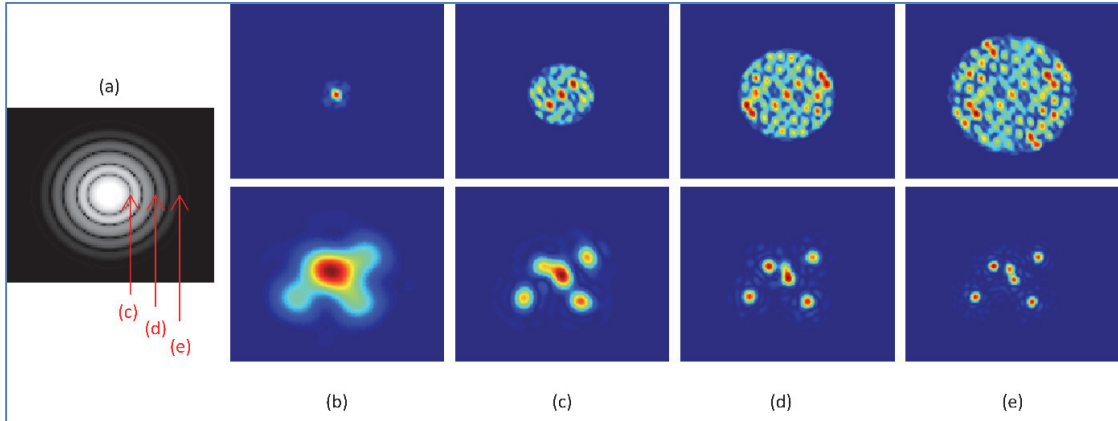


Figure 4-8 Resolution improvement with CNS microscopy. (a) Saturated excitation OTF. (b) Simulated linear scanning image (down) of a few particles and the corresponding Fourier Transform (up). (c-e) Reconstruction with temporal modulation at k_c (c), at k_c and $2k_c$ (d) at k_c , $2k_c$ and $3k_c$. The higher is the excitation OTF frequency included in the reconstruction, the wider part of the sample Fourier Transform is revealed, the better is the resolution.

The unique combination of fluorescence saturation, and digital temporal modulation post processing leads to an improvement of the resolution above the factor two. With CNS microscopy, we were able to translate the principle of saturated SIM to scanning microscopy. As described by Gustafsson, the achievable resolution is then theoretically infinite. As the saturation is a non-polynomial transition, it makes the saturated OTF infinitely large and the higher are the frequencies used in the reconstruction the better is the resolution. This is illustrated in Figure 4-8, which shows the simulation of the reconstruction with saturated OTF frequency extraction up to $3k_c$. Experimentally, the available SNR practically limits the extraction of the highest frequencies and in consequence the resolution.

4.6 CNS microscopy

We present here the experimental demonstration of CNS microscopy. As detailed above, to improve the resolution beyond a factor of 2, we combined the digital temporal modulation point scanning illumination method with the non-linear mechanism of fluorescence saturation. By choosing fluorescence saturation, no modification of the setup is required: the same acquisition as in the linear case was used, but with higher excitation power and the resolution improvement is obtained entirely with post-processing. The excitation intensity was set to 1 MW/cm^2 so that the Fourier spectrum of the saturated point spread function is at least twice larger (see Figure 4-6 (b)). The spectrum of the digital temporal modulation is selected to introduce four Dirac delta functions in the frequency domain centered at $\pm k_c$ and $\pm 2k_c$, where k_c is the cut-off frequency of the collection incoherent OTF. We reconstructed the final image with the same algorithm as used for wide field saturated SIM [28].

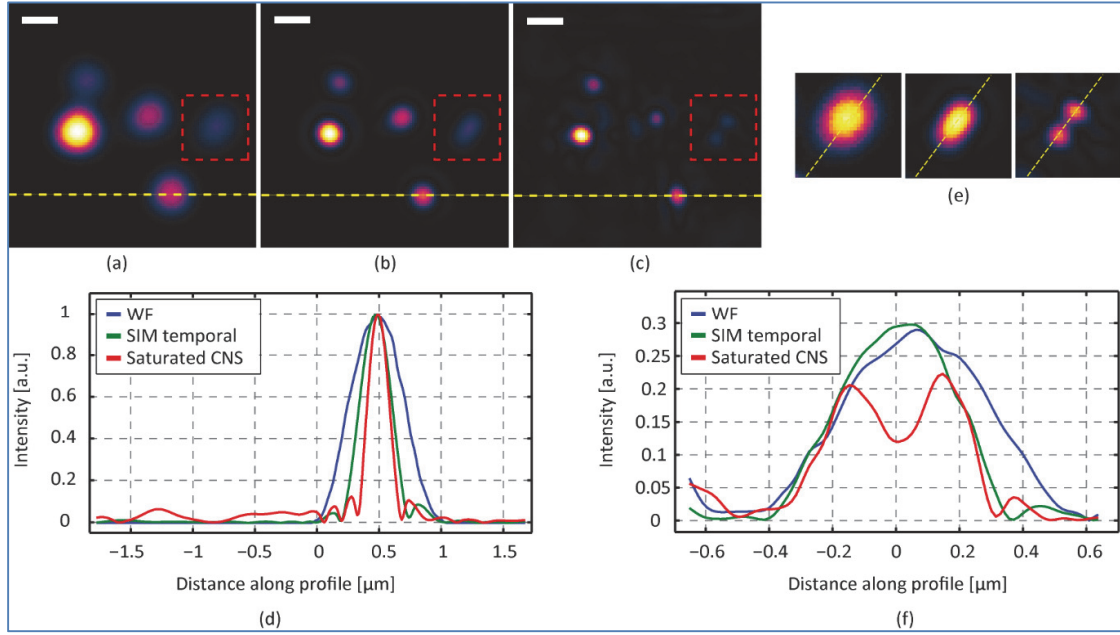


Figure 4-9 Experimental demonstration of CNS microscopy on fluorescent NDs with a 0.8NA objective. (a) wide field image, (b) linear digital temporal scanning SIM image, (c) saturated CNS image. Scale bars are 500 nm. (d) As in the previous figure, intensity profile along the yellow dashed line to measure the lateral resolution. The FWHM is 500nm in the wide field image, 285nm with the linear processing and 195 nm in the non linear image. Consequently, saturated scanning SIM enhances the resolution by a factor 2.6 compared to a wide field microscope. (e) Zoomed and normalized images on the red dashed area in (a-c), showing that two fluorescent NDs separated by 300 nm are resolved. (f) The intensity profile along the yellow dashed line proves they are resolved.

Figure 4-9 illustrates the resolution improvement with CNS microscopy. Conventional point scanning structured illumination improved the resolution by a factor 1.75, while the profile in Figure 4-9 (d) shows a 195 nm FWHM. This corresponds to an improvement of 2.6 fold for the saturated image versus linear wide field. Figure 4-9 (e) shows the region of the sample highlighted by dashed red squares (in the images Figure 4-9 (a-c)) and the corresponding profiles: the saturation of nanodiamond fluorescence allows for the inclusion of higher spatial frequencies in the computational reconstruction, and reveals the presence of two nanocrystals that could not be separated with conventional structured illumination. Hence, simply by increasing the laser power of the scanning microscope we were able to demonstrate, for the first time in our knowledge, an improvement in the resolution by a factor superior to 2 with post detection digital signal processing.

At first glance, since focused illumination can easily provide high peak excitation intensity, it would appear that for the nonlinear case, it can bring better results than WF-SIM. However increasing the excitation intensity above 1 MW/cm^2 did not result in higher resolution gain. Higher excitation OTF frequencies were too weak to be extracted, so we could only achieve a resolution gain of approximately 2.6 times which is much lower than the 5.5 improvement previously demonstrated with nonlinear WF SIM [28]. The rest of this chapter aims at understanding the physical origin of the discrepancy in the enhancement obtained with nonlinear WF-SIM versus CNS and at considering possible solutions.

4.7 SNR performance compared to wide field

We studied the different methods of adapting structured illumination principle to scanning microscopy and we showed how entirely digital post processing combined with temporal modulation allows us to harness nonlinear fluorescence response for higher imaging resolution. We experimentally verified in the linear case that the resolution of a wide field image can be significantly improved with the different algorithms. In the non-linear case we demonstrated a resolution improvement by a factor above 2, meaning that the technique is not limited by diffraction. However, for both linear and non-linear implementation we obtained resolution performance below the one demonstrated with WF-SIM.

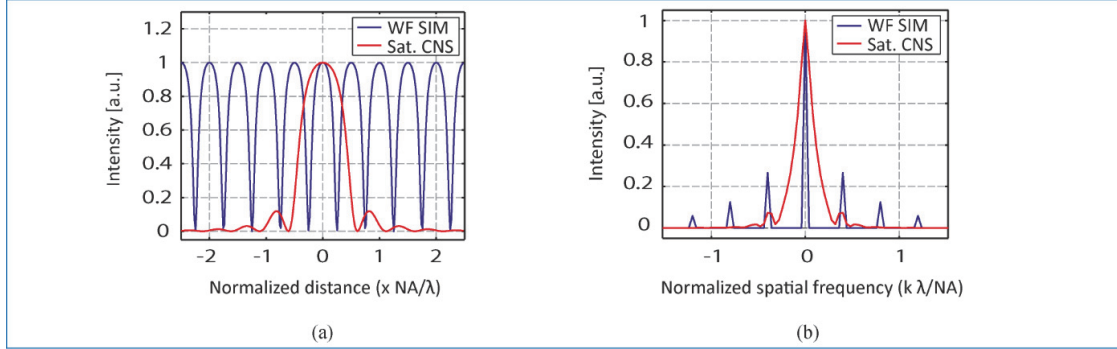


Figure 4-10 Equivalent focused and sinusoidal illumination under saturated absorption. (a) The equivalent excitation intensity patterns obtained with saturation of fluorescent nanodiamonds with a peak intensity of $2\text{MW}/\text{cm}^2$. The blue curve is the WF structured illumination and the red curve is the focused one. (b) The corresponding Fourier transforms.

To understand this, we note that while the information is transferred through a microscope, the high frequencies into the bandwidth are attenuated (see the optical transfer function in Figure 4-6). In an analogy, the modulation is like drawing a sinusoidal pattern with a pen of the focused spot. Now, if the sinus frequency is close to the cut-off (held by the spot) it can only be generated with a limited contrast. Consequently, when a focused laser beam is used as an excitation pattern, the higher frequencies that shift sample information into the collection bandwidth are much weaker than the low frequencies and therefore they can be obscured by noise. On the contrary, in WF-SIM, the entire excitation signal is concentrated into the highest possible frequency. For this reason, WF-SIM shows a better SNR performance than the point scanning technique. This SNR deterioration induced by the point scanning illumination becomes dramatic for the higher orders in the nonlinear implementation. The comparison of the Fourier transforms of the saturated excitation patterns in Figure 4-10 shows that the harmonics of the WF illumination generate much stronger high frequencies than the focused spot whereas at low frequencies both excitation patterns are strong.

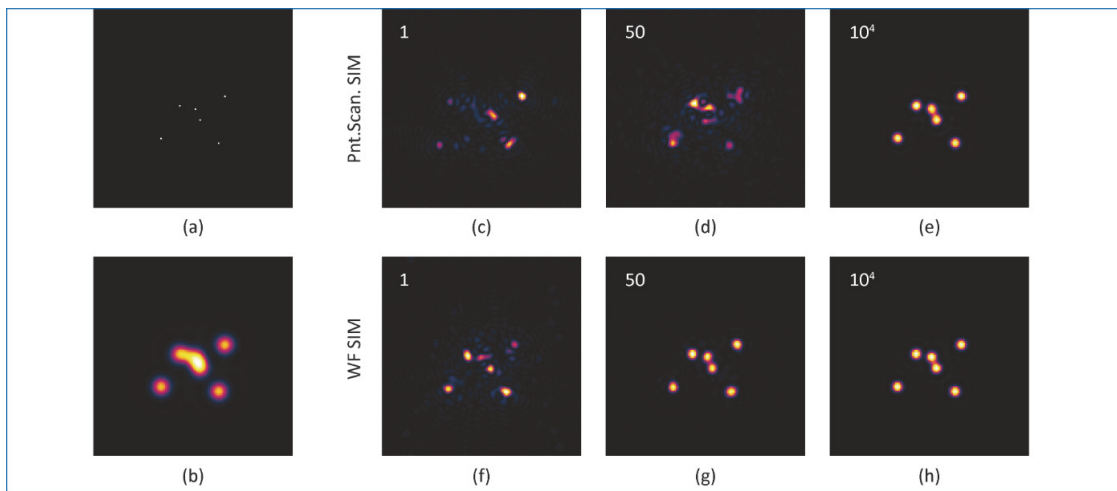


Figure 4-11 Simulated data on photon budget influence on linear imaging of fluorescent nanoparticles. (a) $3.2 \times 3.2 \mu\text{m}$ sample composed of 5 25nm particles. The number on each picture indicates total number of excitation photons incident on the sample during the acquisition (excitation dose) relatively to the weaker one (b) WF image (c), (d) and (e) Point scanning SIM with increasing excitation doses. (d) (f) and (h) Wide field SIM with the

same respective doses. The comparison of image (d) and (g) indicates that the WF method is clearly superior in term of signal to noise ratio. The images (e) and (h) show that the two methods are equivalent with a bright enough sample.

In order to analyze the deterioration in signal to noise ratio of point-scanning SIM compared to the WF case, we carried out numerical simulations. In the simulations presented in Figure 4-11 and Figure 4-12 only photon shot noise is considered and fluorescent particles are imaged with a 0.8 NA objective and resolved both by point scanning and WF SIM.

In the simulation in Figure 4-11, the WF-and point scanning SIM images are calculated in the linear case and for the same excitation dose. That is to say that we set the total number of excitation photons incident on an individual nanoparticle during the acquisition process to be the same for both cases. Comparison of Figure 4-11 (g) and Figure 4-11 (d) shows that better image quality is obtained with WF-SIM. The high frequency components contained in the excitation beam used to retrieve the high frequencies from the object, represent a very small portion of the energy contained in the beam. As a result, the signal that accumulates on the detector contains a strong low frequency component (and corresponding strong shot noise) whereas the higher frequency components are suppressed. Thus, with the same excitation dose, the WF-SIM exhibits better performance under noisy environment compared with the scanning microscopy method.

In general, the physical limitation originates from the total number of photons that a fluorophore can emit. So, the comparison of the methods for the same illumination dose is usually the most appropriate [108,145]. However, in our case we use NDs that do not bleach (and can in theory deliver an infinite number of photon for an infinitely long acquisition). We thus performed the same simulation as in Figure 4-11 for both linear and nonlinear case but with the same excitation peak intensity (Figure 4-12). This implies that the total light dose is much higher for the focused case since each ND is exposed more than 100 times by the scanning beam.

In this case, due to the much larger number of photons that are used to form the image, in the linear case the focused illumination image has a better SNR than the WF version. However for the nonlinear case, the higher frequencies above the cut-off are strongly attenuated and Figure 4-12, clearly shows the fast degradation of the SNR, performance in saturated point scanning structured illumination compared to WF. For instance, the comparison of the reconstruction for the third order shows that similar image quality is obtained with linear WF-SIM with a sample 100 times less bright (and an illumination dose 100 times weaker).

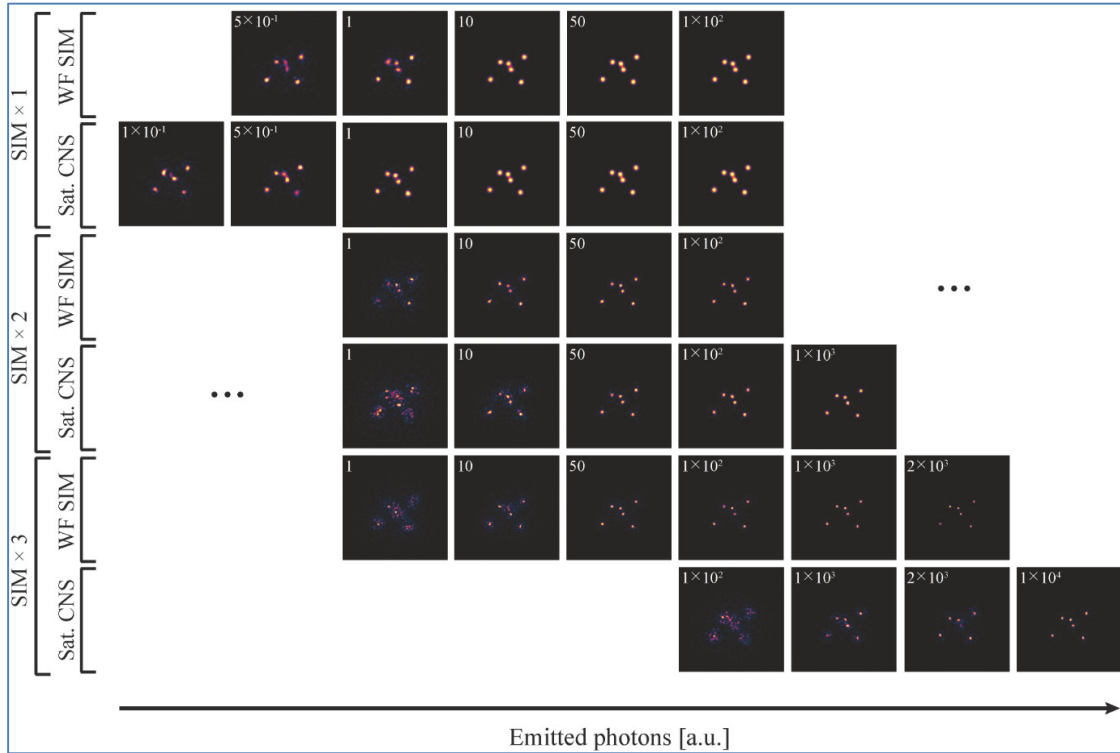


Figure 4-12 Simulated data on photon budget influence on wide field and point scanning nonlinear imaging of fluorescent nanoparticles. The peak excitation intensity is the same both for point scanning and WF structured illumination ($2\text{MW}/\text{cm}^2$). The numbers in the upper left corners give the

fluorescence quantum yield respectively to the one for which point scanning linear reconstruction is successful. (a) The two first rows simulate imaging with linear SIM. It can be seen that for the same peak excitation intensity (i.e. with a lower excitation dose for the WF), the point scanning technique gives slightly better results. The same reconstruction is achieved with WF SIM with 10 times more photons. (b) The third and fourth rows simulate imaging with the first order nonlinear SIM. The point scanning SNR performance deteriorates faster: to achieve a good reconstruction point scanning SIM requires 5 times more photon than in the linear case while WF SIM requires 100 times more photon than in the linear case. (c) The last two rows simulate imaging with the second order nonlinear imaging. The effect become dramatic, the point scanning SIM requires 10000 more photon than in the linear case to provide a good reconstruction while the WF requires 100 times more photon

Thus, in WF-SIM all the excitation intensity is modulated with the same frequency while in point scanning technique it is spread over the whole spectrum and the highest frequency are underweighted. In linear acquisition, the poor SNR performance compared with WF-SIM does not prevent us from recording fluorescent images. However, in the nonlinear case this effect becomes dramatic, and the high frequencies created by the saturation are quickly buried into the noise and cannot be extracted. In conclusion, CNS is particularly inefficient in preserving the SNR of the high frequency components of the image when compared to nonlinear WF-SIM.

4.8 Sectioning

The acquisition with the camera allows us to apply a digital pinhole i.e. to restrict the recorded area to a limited number of pixels. This is strictly equivalent to use a physical pinhole and it results in confocal sectioning ability. However, by restricting the sensing surface to only a small part of the excitation spot and discarding its entire spatial profile, certain information is lost. To analyze the influence of the pinhole size on the quality of the reconstruction we simulated a CNS reconstruction with different pinhole sizes. As a metric to characterize the quality of the reconstruction, we plot the lateral resolution measured as the FWHM of the reconstructed impulse response versus the digital pinhole size in Figure 4-13 (a).

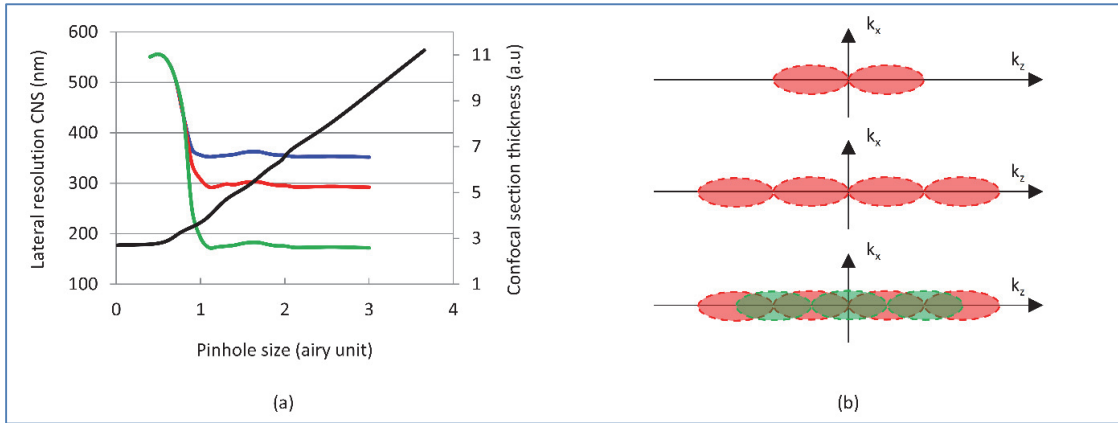


Figure 4-13 Sectioning in CNS microscopy. (a) Color curves: simulated lateral resolution in CNS in function of the digital pinhole size. The blue curve is linear CNS, red nonlinear with second harmonic reconstruction and green fourth harmonic reconstruction. Black curve: section thickness versus pinhole size in confocal microscopy [46] (b) Schematic of the OTF in microscopy. From top to bottom: wide-field (or scanning non confocal), SIM with the usual sinusoidal illumination at the cut-off frequency k_c (or CNS), SIM with illumination at k_c and $0.5 k_c$ the missing cone is filled (or equivalently CNS).

As shown in Figure 4-13, the obtained resolution is unaffected for pinhole larger than 2 Airy units. Such a pinhole size does not give the best axial resolution but would remove most of the out of focus light in thick samples. The reconstruction is marginally affected for pinhole sizes between one and two Airy units. Finally, below 1 Airy unit, the digital pinhole filtering strongly affects the reconstruction and the resolution dramatically deteriorates. Intuitively, it means that the main information about the spatial profile of the focus spot resides in its central lobe, i.e. the tail of the focus profile does not provide much information about the interaction between the excitation pattern and the sample. Interestingly the curves are similar in the linear and nonlinear cases, which can also be understood since the saturation occurs where the intensity is the highest, in the central lobe part of the beam. In our experimental measurements, we have focused on the lateral resolution improvement. The particles were immobilized on a glass surface, therefore no out of focus light was present and the sectioning influence was not observed. We still used windows of two Airy units, which is enough to obtain a good reconstruction and would potentially lead to the same sectioning thickness than the one obtained in two photon microscopy. In each case, as it is a post processing method, the size can be adapted afterwards to match the best compromise in between sectioning enhancement and resolution enhancement.

Sectioning can be obtained with not only the adjunction of a pinhole but also with a structured illumination approach [146,147]. This can be visualized in the Fourier domain (Figure 4-13 (b)). The origin of the lack of sectioning in conventional microscope is the

so-called missing cone: the cross section of the conventional microscope OTF presents an area of missing frequencies. Conventional SIM expands the OTF (and improves the resolution) by exploiting the shift given by sinusoidal illumination, but as it uses a modulation at the cut-off frequency, the missing cone is not filled. However, by illuminating the sample with intermediate frequencies the missing cone can be filled and samples can be resolved in depth. This can be directly translated to CNS microscopy, as the focused spot contains all the spatial frequencies it does not require additional acquisition. Hence, it is possible to include intermediate frequencies in the reconstruction to obtain depth sectioning (without any k_x components owing to the digital nature of our modulation). However this type of post-processing relies again on SNR considerations so will not be applicable as deep as confocal [148].

The focused beam also has a spatial profile in the axial dimension, so CNS microscopy could be adapted in three dimensions to obtain not only depth sectioning but also an enhancement in axial resolution. To improve the axial resolution, the beam position has to be moved axially relative to the sample, in addition to the lateral scan. It means that an entire three dimensional scan of the beam is required to reconstruct a two dimensional image with enhanced axial resolution at the center plane of the scanned volume. In consequence to obtain a three dimensional CNS image of the sample, 3D acquisitions must be repeated for each sample plane. In other words, to make a CNS image with 3 dimensional improvement in resolution it would require N^2 scans compared to for instance 3D STED that would need N scans. Such a 3D CNS scan would be thus impractical in terms of acquisition speed.

4.9 Alternative Illumination patterns

We saw earlier that the digital temporal modulation can be used with any excitation pattern. So, one solution to prevent the degradation of the SNR performance in CNS microscopy is to modify the excitation pattern. Here we propose two alternative beams (insets in Figure 4-14) that could give better results when fluorescence saturation is used to improve the resolution in CNS microscopy: first the Bessel beam, and second, the hexagonal beam pattern obtained with the interference of 3 plane waves [100]. In Figure 4-14, the Fourier transform of the 3 saturated beams with the same peak excitation intensity are represented with the same scale. Both for the Bessel beam and the hexagonal pattern, high frequencies far from the center can be distinguished while for the focused spot it disappears around $2 k_c$. The reason is illustrated on the curve in Figure 4-14 (d), the profiles of the OTFs are drawn together. It can be seen that for the Bessel beam and the 3 beam interference pattern the energy is concentrated into a peak close to the cut-off frequency. In consequence, the harmonics remain visible up to $3 k_c$ while the Fourier transform of the focused spot drops faster.

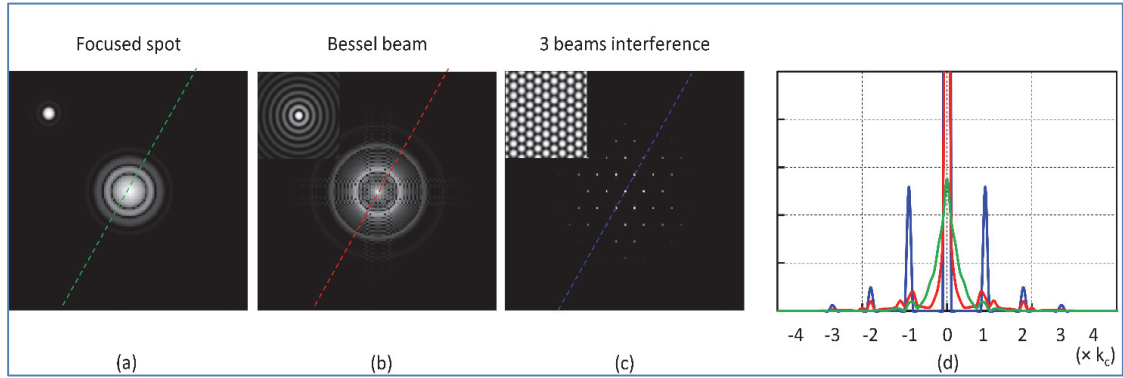


Figure 4-14 Alternative illumination patterns for CNS microscopy. (a-c) The equivalent (saturated) excitation beam in the insets and their corresponding OTF in the main picture. (a) Conventional focused illumination. (b) Bessel beam (c) Three beam interference pattern. Logarithmic scale: black to white 50 dB. (d) The section intensity profiles along the dashed lines in the three OTFs (linear scale). The colors are corresponding. As (b) and (c) concentrates the energy into a narrow frequency domain, some lobes well above the cut-off frequency are visible in the profile (d) as opposed to the standard focused spot.

In order to quantify the improvement brought by the Bessel beam and the hexagonal pattern illuminations compared with the focused spot, we perform the same simulation as in Figure 4-12 for each pattern. In this case we also used a peak intensity of 2 MW/cm^2 as excitation and the results for the second order nonlinear imaging are displayed in Figure 4-15. For the reconstruction with the third harmonics (second order nonlinear) it can be seen that similar quality is obtained with the modified illuminations with a sample 10 times less bright. In consequence, the use of those patterns improve significantly the SNR performance of CNS microscopy and should result in an important improvement in resolution.

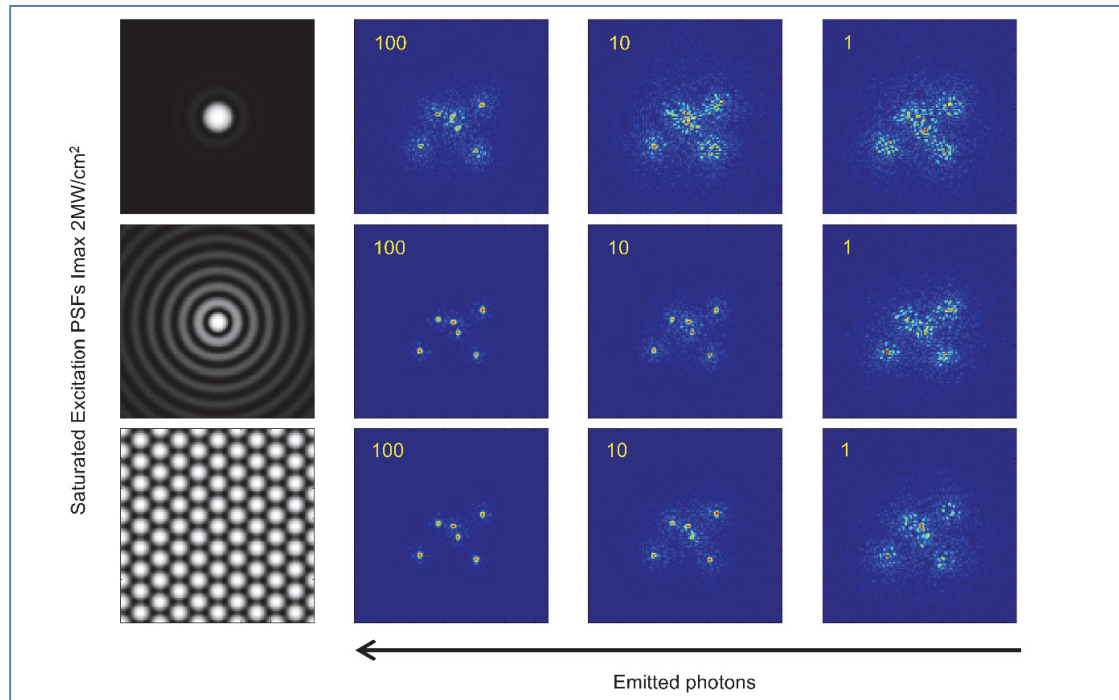


Figure 4-15 Simulated data on photon budget influence on point scanning third harmonic nonlinear imaging of fluorescent nanoparticles with standard focus, Bessel beam and hexagonal pattern illuminations. The peak excitation intensity is the same for the three type of illumination patterns ($2\text{MW}/\text{cm}^2$) and the images are reconstructed with the second order nonlinear imaging. The numbers in the upper left corners give the fluorescence quantum yield respectively to the lower one. In this case of the second nonlinear order (that corresponds to a resolution improvement by a factor 4), both Bessel beam and hexagonal pattern illuminations require 10 times less photon than standard focus illumination to achieve similar reconstruction.

In order to verify experimentally the potential gain in resolution brought by those alternative patterns we measured the saturated PSF by scanning a single 40 nm nanodiamonds and recording the signal with a point detector (avalanche photodiode). In the scanned image, the influence of the detection PSF is eliminated, and we consider the nanodiamond infinitely small so we visualize directly the excitation PSF. In order to generate each of the three patterns successively, a spatial light modulator is placed in the excitation line. We measured the peak intensity through backscattered light from a single 80 nm gold particle relatively to the value we estimated for the focused spot. We set the maximum intensity to be the same ($2\text{MW}/\text{cm}^2$), for each pattern. It can be seen in Figure 4-16 that in the measured hexagonal pattern excitation OTF, high frequencies at $3k_c$ are visible above the background while we are not able to detect them on the saturated focused spot OTF. It confirms that with a modified pattern CNS microscopy resolution can be improved. For the Bessel beam, the improvement is more limited than expected. Indeed, compared with the theoretical OTF profile we could not detect the $3k_c$ component but only the $2k_c$ one. It results from the imperfect zeros in between the lobes in the experimental Bessel PSF. The residual light in the dark rings of the Bessel profile leads to spread of the energy in the whole spectrum and creates smaller high frequency peaks. We attributed the limited contrast in our beam to the imperfection in the radial polarization generation and to the presence of astigmatism.

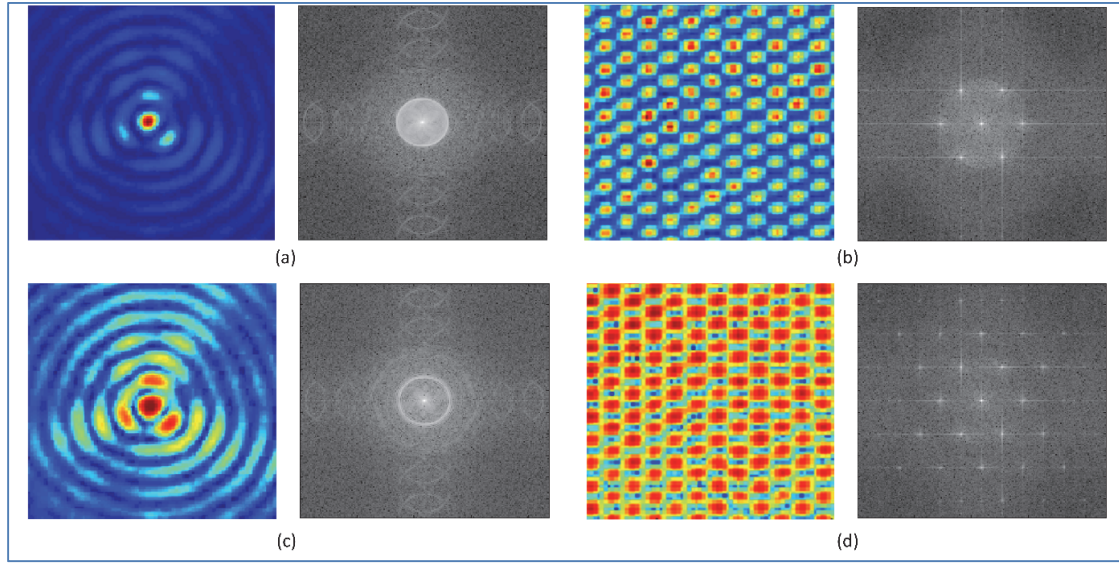


Figure 4-16 Experimental alternative patterns for CNS microscopy. Each acquisition is a scanning image of the illumination pattern (recorded with a nonbleaching subdiffraction fluorescent emitters) on the left and its corresponding Fourier transform on the right. (a) and (b) Linear scan (low excitation power, with respectively Bessel beam and hexagonal pattern illumination. No nonlinear signal (above the cut-off frequency) rise up above the noise floor. (c) and (d) Nonlinear scans (at $2\text{MW}/\text{cm}^2$) for the same excitation pattern. In (c), in the Bessel beam OTF, some signal is present at twice the cut-off frequency, while with the hexagonal pattern some signal is detected up to 3 times the cut-off frequency.

The aberrations in the experimental Bessel beam prevent us from recording a saturated CNS image and observing a larger improvement in resolution. However the benefit of using such a beam can already be observed in the linear case. Figure 4-17 displays a scanning image acquired with a Bessel beam excitation and post-treated with temporal digital modulation. On the contrary to the image acquired with the standard focus spot, the resolution gain reached the theoretical improvement 2 in resolution (to be compared with the factor 1.75 obtain with the standard focus in Figure 4-17(b) and Figure 4-5). The Bessel beam concentrates the excitation light exactly into the cut off frequency, in consequence the signal is strong enough to be extracted exactly at the cut off frequency. Thus, the use of the Bessel beam allows us to maximize the resolution improvement in the linear case (i.e. to reach a factor 2 as in WF SIM) and it also gives another experimental proof that any excitation beam shape can be used with the temporal modulation.

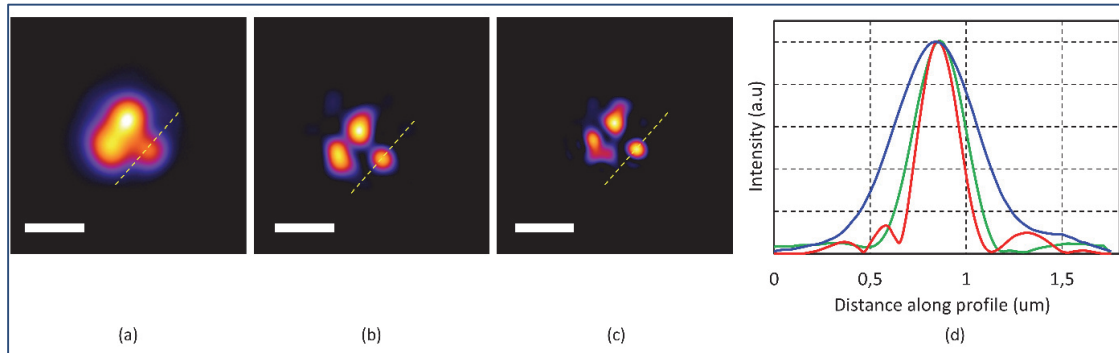


Figure 4-17 Linear imaging of FNDs with Bessel beam illumination and with an 0.8 NA objective. (a) wide field image, (b) digital temporal scanning SIM image with standard illumination (c) digital temporal scanning SIM image with Bessel illumination (d) Intensity profiles along the yellow dashed line for the different cases. The signal from a single subdiffraction FND gives an estimation of the lateral resolution improvement. The FWHM is 500 nm in the wide field image. The FWHM is 295 nm in the post-processed image with the standard focus, it corresponds to a 1.7 times improvement in lateral resolution, in good agreement with the 1.75 times measured in Figure 4-5. The FWHM is 250 nm in the post-processed image with the Bessel beam, it corresponds to the optimal 2 times improvement in lateral resolution that can be achieved with linear imaging. Scale bars are 1 μm .

We experimentally verified that a hexagonal pattern conveys more energy in the frequencies close to the cut off and should lead to a one order of magnitude improvement in term of SNR performance compared to the focused spot. However, the concentration of the energy to a limited part of the excitation spectrum implies a broadening the pattern, and both Bessel and hexagonal patterns

are very large compared with the focused spot. Thus, by making the excitation beam wider to improve the SNR performance, we get closer to the conventional WF-SIM implementation and we can wonder if using it with scanning microscopy still makes sense. Indeed, if we take the extreme case of the hexagonal pattern obtained with 3 beam interference, as it covers entirely the sample only $(2n+1) \times 3$ pictures, as in WF-SIM, are needed in theory to reconstruct a nonlinear image to the n^{th} order. So, recording all the pictures as in scanning microscopy is a huge loss of time in this case and is far from being optimal.

Hence, the choice of the more adapted pattern is really a trade-off. In one extreme, the hexagonal illumination pattern is fundamentally a wide field illumination pattern with a very limited deterioration compared to WF SIM (the energy is only spread in specific spatial frequencies in three specific directions). It can be used with the scanning technique we described in this chapter and it should lead to resolution close to saturated WF SIM. However, in presence of out of focus background, digital pinhole should be applied and the part of the pattern used limited, which would again degrade the SNR performance. In the other extreme, in order to retain the true confocal ability, scanning microscopy should be used with standard focused spot. However, this implies a limited energy conveyed in the highest frequency and so a limited resolution improvement even by harnessing nonlinear photoresponse.

In conclusion, changing the illumination pattern in SIM techniques results in a degradation of the SNR performance compared with WF but can bring other advantages especially sectioning and depth of imaging. The intermediate patterns we described in this section can lead to improvements in certain aspects while compromising others.

4.10 Another nonlinear mechanism: stimulated emission depletion

CNS microscopy is not restricted to one type of nonlinearity. Indeed, it can be seen as a way to extract the high frequency components brought in the equivalent excitation PSF by the nonlinear photoresponse. Several possible nonlinear response mechanisms could have been used for resolution enhancement (saturation [28], blinking [149], photoactivation [54]...). In order to illustrate this flexibility, we performed experiments with another nonlinearity that can only be implemented in point-scan mode because it requires high intensity: stimulated emission depletion.

4.10.1 CNS STED

To show point scanning SIM with STED non-linearity, we added a standard depletion beam with a doughnut-shape that inhibits the fluorescence of the emitters around the excitation beam (Chapter 2). Comparison with the wide field image (Figure 4-18 (a)) shows a clear improvement in resolution with STED CNS microscopy. Indeed, in the STED CNS image (Figure 4-18(c)), NDs conformations, which are invisible on the wide field image, are resolved. The profile in Figure 4-18 (d) indicates that the resolution is increased by a factor of about 3 compared to wide field image.

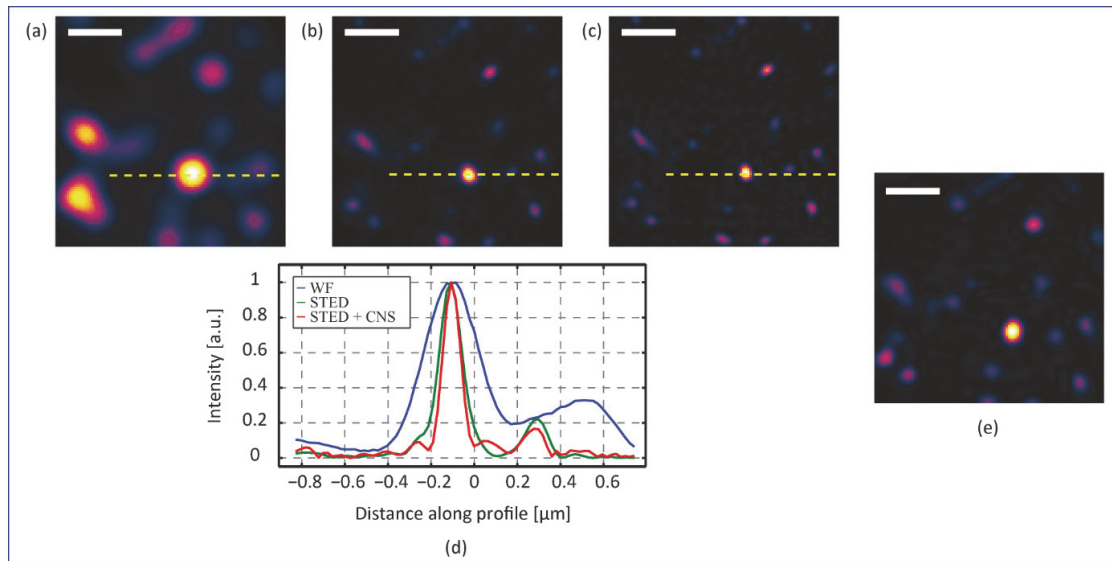


Figure 4-18 Non-linear imaging of fluorescent NDs with a 1.4NA objective. (a) Wide field image, (b) STED image, (c) STED CNS image. Scale bars are 500nm (d) Intensity profile along a single fluorescent ND showing the improvement in resolution. The measured FWHM is 280 nm for wide field,

125 nm for STED and 98 nm for STED scanning SIM. (e) Linear point scanning structured illumination image (the details hidden by diffraction limit in (a) are resolved both with linear point scanning structured illumination and STED).

As in the previous example with saturation, the gain in resolution with the depletion beam is the result of both the non-linearity and the digital computation. Similarly, the higher the power of the beam inducing the nonlinearity, the more spatial frequencies are carried in the excitation PSF. Here we set the depletion power, such that the FWHM of the STED excitation PSF is about half that of the linear one. Post detection digital signal processing allows a gain in resolution equivalent to one cut-off frequency k_c on top of the highest frequency generated by the illumination pattern. Hence, in our case, the expected gain in resolution compared to the excitation PSF cannot exceed 1.5. On the profile on Figure 4-18 (d), the measured PSF is 98 nm, which corresponds to a gain of 1.27 times in resolution compared to STED, and thus is in good agreement with the expectation.

Saturation and STED implementations of nonlinear point scanning SIM greatly improve the resolution compared to a wide field microscope. However, a standalone STED microscope already provides a high gain in resolution and only profits marginally from the additional enhancement due to structured illumination. Thus, the STED implementation of point scanning SIM is not presented as a competitive imaging technique, but rather to show the possibility for point scanning microscopy to be combined with various types of nonlinearity.

4.10.2 STED as a ground truth for CNS microscopy

As the whole method is based on post processing, it is always interesting to obtain an all optical verification of the images obtained with the method. As we built a STED microscope to illustrate the possibility to apply CNS reconstruction with different type of nonlinearity we can compare the images obtained with linear digital point scanning structured illumination and with STED. We chose the depletion power to reach a gain in resolution by a factor 2 with the STED microscope, so that it is easy to verify that the digital point scanning structured illumination (Figure 4-18 (e)) is similar to the STED image. The details hidden in the wide field image (Figure 4-18 (a)) and superresolved both with STED (Figure 4-18 (b)) and point scanning illumination technique (Figure 4-18 (e)) are identical.

4.11 Conclusion

We have demonstrated how the resolution of a confocal microscope can be enhanced only by increasing the power of the excitation laser and by using an array detector (i.e camera). The beauty of the method is that it gives a theoretical unlimited resolution without any change on existing equipment, only by digitally post processing the acquired data. However, the signal to noise ratio is never infinite and experimentally the achievable resolution is bound to the fluorophores brightness. This inspires two considerations. First, it is not a physical limit, and the synthesis of new dyes is an active research field, especially because the very popular STED nanoscopy requires high brightness and good photoresistance at a few hundred MW/cm² power level. In nanodiamonds, for example, the vacancy density has been drastically improved over the last few years [68] and nanocrystals with 10 times more concentrated NV-center might be possible. At this level, the predictable resolution would make CNS competitive with other superresolution techniques. Second, as it was described, the modification of the illumination pattern can bring an important improvement in term of SNR and result in enhanced resolution. However, this modification would come with enlargement of the pattern, i.e. without retaining the physical out of focus light rejection given by a pinhole. Finally, the trend in the latest research in scanning nanoscopy is to use multi-pixel detectors for either the parallelization [99] or the additional gain in resolution [108]. Thus the performance improvement could also come from the development of new type of detector like APD arrays, like Airyscan detectors, from Zeiss.

Chapter 5 Resolution enhancement in ultrathin endoscopy by saturated fluorescence excitation.

In the previous chapters, we explained that nonlinear sample photoresponse is a fundamental requirement for superresolution optical imaging methods. We presented three different techniques (STED, DH-STED and CNS) based on saturation mechanisms which expand the excitation optical transfer function and resulted in superresolved images. Unfortunately, scattering materials, such as biological tissue, deteriorate the focusing capability of an optical scanning imaging system as well as the collection of the generated signal (i.e. fluorescence), which restrict the imaging depth. Various techniques have recently been investigated to focus light [150–156] and image [33,34,157] through scattering media, but the depth limit remains a few mm at best. An alternative to these techniques is fiber-based endoscopy which bypasses completely the scatterer (Figure 5-1). During the period of this PhD, our lab [35] and other groups [158–160] have identified multimode fiber (MMF) as a potential candidate for ultrathin endoscopic imaging. A patent has been registered and several people are now working in our lab to create a commercial MMF based endoscope. In this chapter, we will show how we can translate a nonlinear scanning microscopy technique to improve the resolution and the image contrast of imaging through multimode fiber.

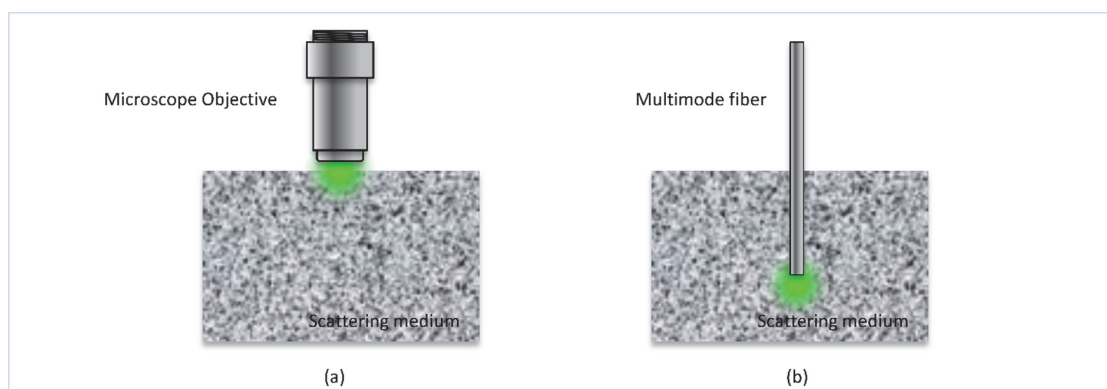


Figure 5-1 One solution to image deep into scattering materials (like biological tissues). While microscopy (a) is non-invasive but limited to a surface layer, endoscopy (b) is invasive but can access deep inside the sample. To tend towards minimally invasive endoscopy, multimode fiber provides ultrathin waveguiding and high resolution imaging.

5.1 Introduction

In this section, we quickly review the different types of existing fiber based endoscopes and explain the competitive advantage of the MMF based one. We will also detail the challenges that come with the use of MMF as an endoscope and explain our motivations to combine superresolution imaging technique with MMF imaging.

Fiber-based endoscopes are typically constructed with fiber bundles. Fiber bundles, also called multicore fibers, are cords made of a large number of single mode fiber cores in parallel, embedded in a cladding material. In bundle endoscopes, each single mode waveguide is excited successively and a scanning image is recorded. It means that each pixel of the final image corresponds to the position of one core. However, to guarantee independent propagation in each core (avoid inter-core coupling), the cores have to be spaced by a minimal distance (Figure 5-2(a)). No light propagates in the inter-core spacing, so in term of information transmission this space is lost. This is the reason why fiber bundles are suboptimal in term of confinement of the spatial information. On the contrary, in MMF the light propagates everywhere in the core and is guided with an external cladding. It means that the overall filling factor is much higher in MMF compared with fiber bundles (Figure 5-2(a)). Hence, the density of transmitted information is

higher in MMF and the resolution at the bundle output is poorer compared with MMF. The resolution can be increased with an additional imaging system [161], but at the cost of a limited field of view (or a bigger bundle). Alternatively, fiber based endoscopes consist of a single-mode fiber, a lens, and an actuation system to scan a focused spot. In this case, the loss in space is induced by the actuation system that is typically millimetre size in miniaturized system [162].

Thus, the interest of using MMF resides in the fact that it is optimal in term of spatial information transmission (see also Appendix G). Therefore, for a given resolution and field of view, MMF endoscope is fundamentally thinner compared with the existing techniques. This is obviously a desired feature to reduce the damage caused by the endoscope, especially when it is used in medical application. Once embedded into a needle, high resolution images have been recorded with 460 μm large MMF endoscope [163]. Some applications that take advantage of this minimal invasiveness are already investigated in our lab, like cochlea diagnosis or retinal imaging.

However, the use of MMF as a material for high performance endoscopy comes with some challenges. The resolution of the MMF image is limited by the relatively small numerical aperture of the fiber (NA typically between 0.2 and 0.5) [35,164]. The numerical aperture of the multimode fiber endoscope system can be increased by using a thin layer of scattering material [165,166], but at the cost of critical loss in the collection efficiency. The NA of the MMF can also be enhanced with dedicated micro-fabricated optics [167] in front of the fiber but creating side lobes and reducing the field of view. Thus, the first goal of this project was to use nonlinear sample photoreponse, as in microscopy, to improve the resolution in MMF fiber imaging, while keeping the thin diameter of the MMF waveguide.

The second goal was to provide depth sectioning. Indeed, to discriminate structural features in a thick sample, the ability to reject out of focus light is also important: if out of focus fluorescence signal is not filtered out during imaging it can severely degrade the image contrast. Fiber-based endoscopic sectioning has been demonstrated by using fiber bundles but is not available in conventional scanning imaging used with MMF. More precisely, sectioning by multiphoton imaging has been obtained using fiber bundles [168,169]. However, multi-photon excitation is challenging with MMFs since the focusing of femtosecond pulses through MMFs requires modal and chromatic dispersion compensation as demonstrated recently [170]. Endoscopic sectioning can also be obtained by implementing confocal filtering. Confocal microendoscopy using a fiber bundle was demonstrated in 1996 [171]. In the case of coherent imaging through MMFs, it has recently been demonstrated that modal scrambling can be compensated. A virtual pinhole was applied to obtain a digital confocal endoscope [172]. Nevertheless, this method relies on the coherence of light, and thus cannot be used in fluorescence endoscopy. Hence the challenge was to be able to exploit, in combination with MMF imaging, a nonlinear microscopy also capable of optical sectioning.

In this chapter, we use saturated excitation (SAX) [173], a nonlinear method that both improves spatial resolution and introduces optical sectioning. SAX is well matched to MMF imaging since it involves a continuous wave laser, thereby bypassing the problem of modal and chromatic dispersion existing with femtosecond pulses used for two-photon. In the next section, we will detail the principle of imaging through MMF by phase conjugation and the principle of SAX microscopy. Afterwards, we will present the improved images obtained by SAX imaging through multimode fiber. Finally, we will characterize the performance and discuss the limitations.

5.2 Principle of the method

5.2.1 Scanning fluorescent imaging through multimode fiber using phase conjugation.

When propagating in scattering material, the optical wavefront is distorted by random multiple scattering events. That's why the image of an object through the fog (composed of thousands of scattering droplets) is blurred. On the contrary, at first sight, a multimode fiber looks like a well define medium. It is a cylindrical waveguide, with a constant diameter. The propagating light is constrained in the guiding core and all the propagation solutions can be calculated. In a typical multimode fiber, hundreds to thousands of modes are guided. In theory, when propagating through a multimode fiber the optical wavefront is decomposed into the supported modes (proportionally to the spatial overlap of each mode and the incident wavefront) and reaches the output of the fiber with the same modal composition that it entered the fiber with. However, in a real MMF each tiny material defect during the propagation results in a non-perfect guiding condition and in the jumping of the light in between modes. This phenomenon is called mode mixing and leads to a random distribution of the light in between the supported modes at the output of the fiber (Figure 5-2(b)). Because of the large number of propagation modes, the MMF effect resembles a lot to the wavefront distortion induced by a random scattering material. So, a multimode fiber is guiding the light in a way the information is optimally confined, but to be able to use it as an endoscope the modal mixing must be compensated for.

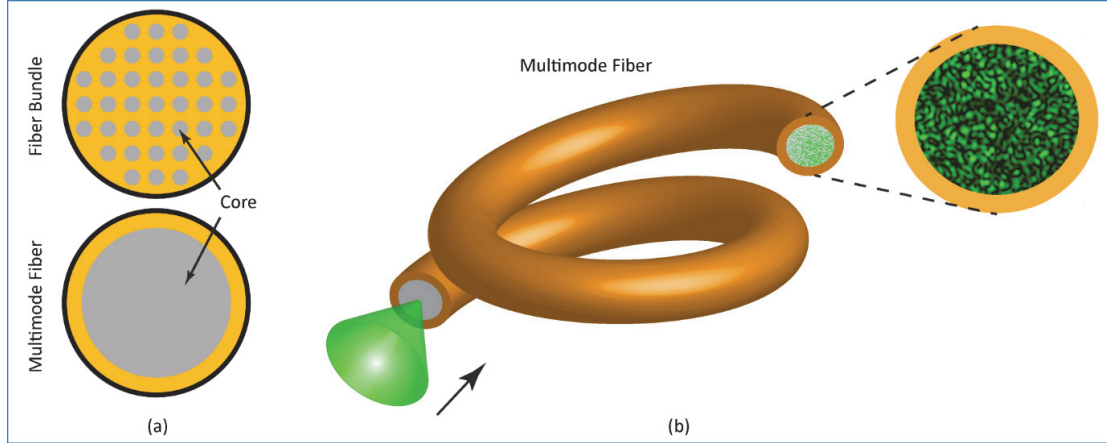


Figure 5-2 Fiber waveguides outlook. (a) Filling factor in fiber bundle (up) and MMF fiber (down). For typical value, the filling factor is much higher in MMF. MMF (Thorlabs, 0.39NA): core diameter 200 μm , core + cladding diameter 225 μm , so filling factor 80 %. Fiber bundle (Fujikura-10-350s): total diameter 450 μm , number core 10000 and core diameter 2 μm , so filling factor 20 %. (b) Modal mixing in multimode fiber. A well define wavefront enters the core of the fiber and the amount of energy coupled into each mode is well defined. However, during the propagation, due to imperfections in the waveguide, the light is randomly dispersed in the available propagation modes. The output is a speckle of light whom the grain size is related to the numerical aperture of the fiber.

5.2.1.1 Phase conjugation

The imaging method proposed by Papadopoulos and all. [35,165,174] in our group is a scanning method. So, in order to create an image, an excitation focused spot of light is generated at the distal end of the fiber. We made above the analogy between a MMF and a random scattering medium. Several routes to generate a focused spot through a scattering medium have been developed in the literature. A spot of light can be obtained with optimization algorithms. By iteratively changing the value of each pixel of a phase modulator, modulating the input wavefront, the value that maximizes the intensity of the output spot can be determined [150]. Another approach, is to represent the medium as a transmission matrix and acquire enough different inputs and corresponding outputs in order to gain the complete knowledge of the medium [152]. Once the matrix representing the medium is obtained, it is possible to calculate the incident input wavefront that will result in any desired output, including a focused spot in the desired position. The method we will use, on the contrary of the other approaches, is entirely optical and does not require any computation. This elegant way of focusing light through multimode fiber is based on phase conjugation [174,175]. The principle of phase conjugation is to transform the scattered field at the output of the medium so that it can back propagate to its original unaberrated state on the input side.

In order to explain the physical mechanism of phase conjugation, we come back to the postulate of wave optic. The propagation of an electromagnetic wave (complex field E) in an inhomogeneous nonmagnetic medium with a permittivity $\epsilon(r)$ is described by the wave equation [42] (p159):

$$\nabla^2 E - \frac{\epsilon(r)}{\epsilon_0 c^2} \frac{\partial^2 E}{\partial t^2} = 0 \quad \text{Equation 5-1}$$

If we consider a monochromatic optical wave, with a complex amplitude A , a wave-vector k and an angular frequency ω , $E(r) = A(r) e^{j(\omega t - k z)}$. Using Equation 5-1 leads to:

$$\nabla_r^2 A + \frac{\partial^2 A}{\partial z^2} - j 2k \frac{\partial A}{\partial z} + \left(\frac{\omega^2 \epsilon(r)}{\epsilon_0 c^2} - k^2 \right) A = 0 \quad \text{Equation 5-2}$$

Where $\nabla_r^2 = \partial^2 / \partial x^2 + \partial^2 / \partial y^2$ is the transverse Laplacian operator. Under paraxial approximation $\frac{\partial^2 A}{\partial z^2} \ll k A$, Equation 5-2 results in the paraxial wave equation:

$$\nabla_T^2 A - j2k \frac{\partial A}{\partial z} + \left(\frac{\omega^2 \varepsilon(\mathbf{r})}{\varepsilon_0 c^2} - k^2 \right) A = 0$$

Equation 5-3

Now, Equation 5-3 is equivalent to its complex conjugate:

$$\nabla_T^2 A - j2k \frac{\partial A}{\partial z} + \left(\frac{\omega^2 \varepsilon(\mathbf{r})}{\varepsilon_0 c^2} - k^2 \right) A = 0 \Leftrightarrow \nabla_T^2 A^* + j2k \frac{\partial A^*}{\partial z} + \left(\frac{\omega^2 \varepsilon(\mathbf{r})}{\varepsilon_0 c^2} - k^2 \right) A^* = 0$$

Equation 5-4

The two parts of Equation 5-4 are equivalent, so they describe the same propagation problem. This means that the original optical wave $E(\mathbf{r}) = A(\mathbf{r}) e^{j(\omega t - k z)}$ and the so-called phase conjugated wave $E(\mathbf{r}) = A^*(\mathbf{r}) e^{j(\omega t + k z)}$ satisfies the same propagation problem. Thus, a wave that propagates in the reverse direction with a complex amplitude which is everywhere the complex conjugate of the initial wave is equivalent to the original wave. Another common description of this phenomenon, is known as time reversal. The phase conjugated wave can be seen as the original wave that would turn back the clock and would back propagate to its original state.

From the above equations, we can conclude that the phase conjugated wave retraces the path of the incident radiation. This is illustrated in Figure 5-3. When an incident optical wave propagates through a disturbing medium, the output wave is distorted. If this wave is reflected by a conventional mirror, it is going to be distorted again and all the information about the spatial profile of the initial field is lost. On the contrary, if the light is reflected with a phase conjugation mirror, the backpropagating wave will built up in a reversed manner so that the field will be equal to the complex conjugate of the initial field at any point of the propagation. As a result, at the initial position, the distortion in the exiting field will have disappeared and the original wavefront can be recovered. Hence, if we focus the light at one end of the fiber, the wave re-emitted from the other end by a phase conjugation mirror will auto-compensate the phase distortion and auto-focus itself on its initial source. This is the beauty of the method, it does not need any previous knowledge about the scattering medium or any computation, it returns the initial input to the distal end of the fiber.

The initial implementation of a phase conjugation was done by holography [176,177] and then dynamically with $\chi^{(3)}$ medium or photorefractive material [178]. However, as we saw in Chapter 3, we have at our disposal spatial light modulators that are able to modulate the phase of a wavefront with a desired value in each pixel. So, the practical implementation proposed in [174] and that we will present here, consists in separating the recording of the complex field information and the creation of the phase conjugated wavefront with the SLM. We detail in the next section how we record the amplitude and phase profile at the output of the fiber in order to apply phase conjugation.

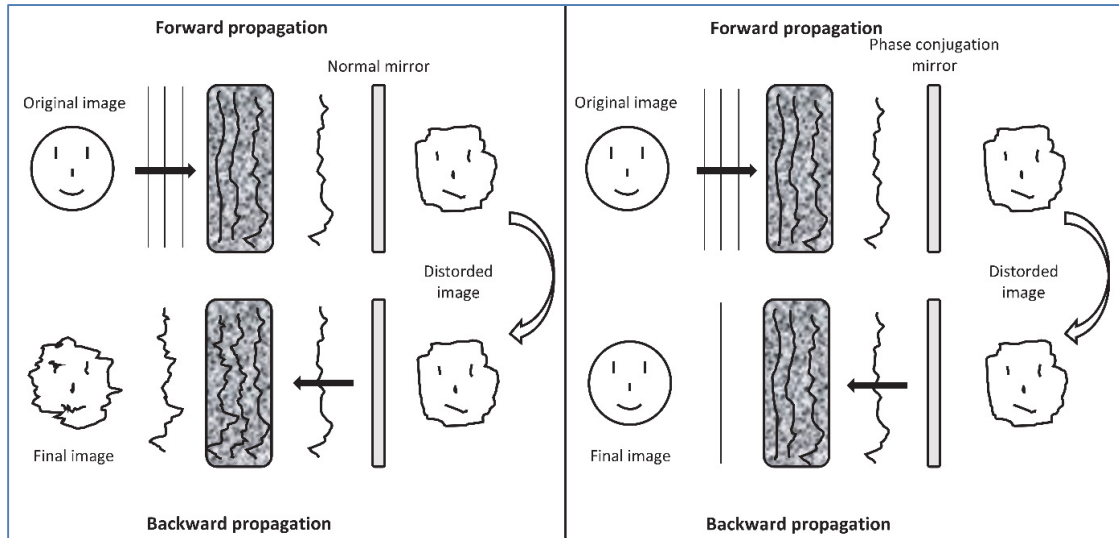


Figure 5-3 Principle of optical phase conjugation, comparison of a phase conjugated mirror with a conventional mirror. In the first row, a wavefront propagates through a scattering medium and gets distorted. It results in a blurred image. On the left, the field is reflected by a normal mirror it is scattered again in a random way and the resulting image is heavily distorted. On the right, on the contrary, it is reflected by a phase conjugated mirror. During the backpropagation, it retraces the exact same path in the opposite direction through the scattering medium. The effect of scattering during the forward propagation is cancelled and the original image is recovered.

It must be noticed that phase conjugation as the other possible approaches to generate a focused spot through a multimode fiber requires the access to the distal end of the fiber (to generate the excitation in phase conjugation technique or get a feedback with the iterative methods), i.e. where the sample is placed to be imaged. This was a major limitation for direct imaging through scattering media, but in the case of MMF endoscopy, as the turbid medium is the fiber itself, it is not a strong limitation. It means that the fiber system must be calibrated before placing the sample for the imaging step. We present in the next section how the phase information of the wave propagating after transmission through the fiber is collected.

5.2.1.2 Off axis digital holography

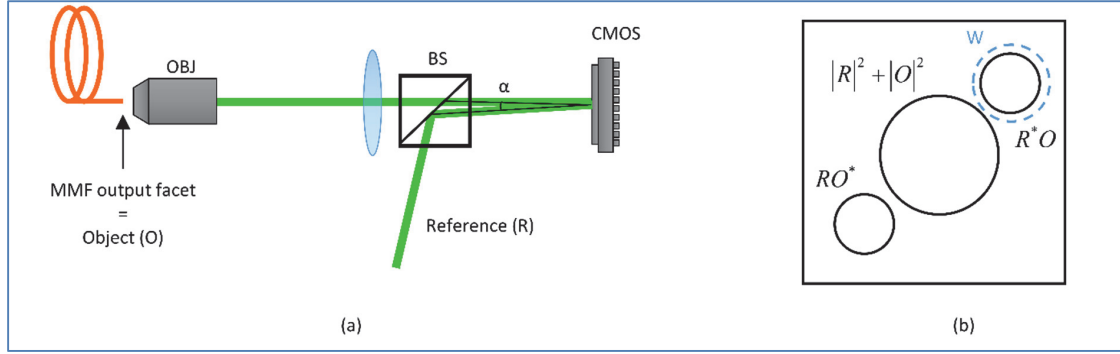


Figure 5-4 Off-axis digital holography setup and principle. (a) The output facet of the MMF is imaged onto a CCD camera sensor. The camera records only the intensity of the wavefront. In order to record the entire field information necessary for phase conjugation, it is combined with a reference beam. (b) The Fourier transform of the resulting interference pattern is composed of three parts, the DC part and the ± 1 diffraction orders which contain the phase information. The separation of those components due to the off-axis configuration allows for an easy extraction of the object phase.

As explained above, in order to implement phase conjugation through multimode fiber, we need to record the complex field after the propagation through the MMF. This is done by digital holography. In practice, the output facet of the fiber is imaged onto a CCD camera (Figure 5-4(a)). The interference pattern composed of the fiber output beam beating against a reference beam (which has not been disturbed by the propagation through the MMF) is recorded. The interference pattern onto the CCD can be expressed as:

$$I = |o + r|^2 = |r|^2 + |o|^2 + o^* r + r^* o \quad \text{Equation 5-5}$$

Where r stands for the reference field and o the object field, i.e. the output of the MMF. We work here in off-axis holography mode, i.e. the reference beam and the fiber beam are combined with a relative angle α , using a non-polarizing beam splitter. The off-axis angle results in the separation of the different terms of the Equation 5-5 in the spatial frequency domain. Indeed, taking the Fourier Transform of the Equation 5-5, we have:

$$\tilde{I}(k_x, k_y) = TF \left[|r|^2 + |o|^2 \right] + |r| \tilde{o}^*(k_x + k_{rx}, k_y + k_{ry}) + |r| \tilde{o}(k_x - k_{rx}, k_y - k_{ry}) \quad \text{Equation 5-6}$$

Where we have assumed that the reference is a plane wave (so with a constant amplitude) and k_r is the wave vector of the reference (and k_{rx}, k_{ry} its components projected in the camera plane). The two first terms of the Equation 5-6 correspond to the DC term which contains only the amplitude information. The two last terms are the ± 1 order diffraction terms. They are modulated at the carrier frequency (of the interference fringes) given by the off-axis angle. Consequently, they are shifted in the Fourier domain as illustrated in Figure 5-4(b). Thanks to this shift, the off-axis configuration makes it possible to filter out the $+1$ order in the Fourier domain. By applying a filtering window (W) in the frequency domain (Figure 5-4(b)) and taking the inverse Fourier Transform, we can isolate the field:

$$W(\tilde{I}(k_x, k_y)) = |r| \tilde{o}(k_x - k_{rx}, k_y - k_{ry}) \Rightarrow E_{recons.} = TF^{-1} \left[W(\tilde{I}(k_x, k_y)) \right] = |r| \cdot o \cdot e^{j(k_{rx} x + k_{ry} y)} \quad \text{Equation 5-7}$$

At this step, the reconstructed field amplitude is proportional to the object amplitude and the phase is the phase of the object in addition to a grating phase induced by the off-axis configuration. In order to apply phase conjugation, we need to recover the initial object phase. To do so, we digitally apply the inverse transformation in the frequency domain. We shift back the $+1$ diffraction order to the center of the Fourier domain.

$$E_{recons_final} = |r| \cdot o \cdot e^{j(k_x x + k_y y)} \cdot e^{-j(k_x x + k_y y)} = |r| \cdot o \propto |o| e^{j\phi} \quad \text{Equation 5-8}$$

The final reconstructed field is then proportional to the initial object field, the complex conjugate to create a phase conjugation mirror can be directly calculated. This digital shift procedure is analogous to the read out step by the reference beam in optical holography, except that the first diffraction order is already isolated.

In order to obtain a good quality reconstruction, a few practical criteria must be fulfilled. We list them briefly here. First, the numerical aperture of the 4f imaging system (Figure 5-4) is chosen with a higher NA than the MMF in order not to lose any information about the fiber output speckle field distribution. The imaging system magnification and the sensor are chosen so that the entire fiber is imaged onto the sensor and the pixel size allows for the sufficient sampling of the speckle pattern. Finally, the angle of reference is taken to be large enough so that the +1 diffraction order can be completely separated in the Fourier domain and small enough so that the interference pattern is sampled correctly by the CCD.

The Figure 5-5 shows the experimental implementation of the reconstruction of the fiber output field. The hologram resulting from the interference of the fiber output beam and the reference is acquired on the camera (Figure 5-5(a)). The fiber output beam is blocked so that the reference can be acquired (Figure 5-5(b)). We create a large beam so that the reference is pretty constant over the entire sensor (thereby, we don't have to compensate for the reference profile in the reconstruction). As expected in Equation 5-6, in the frequency domain, the hologram exhibits three components (Figure 5-5(c)). They do not overlap, so the +1 order can be digitally filtered out by directly cropping the Fourier transform image (Figure 5-5(d)). As explained above, to compensate for the effect of the reference, the +1 order is shifted in the center of the spatial frequency domain (Figure 5-5(e)). After an inverse Fourier transform, we recover the field amplitude (Figure 5-5(f)) and phase (Figure 5-5(g)) at the output of the fiber. We calculated the entire field information in one plane, by applying the complex conjugate and reversing the propagation direction we can implement phase conjugation.

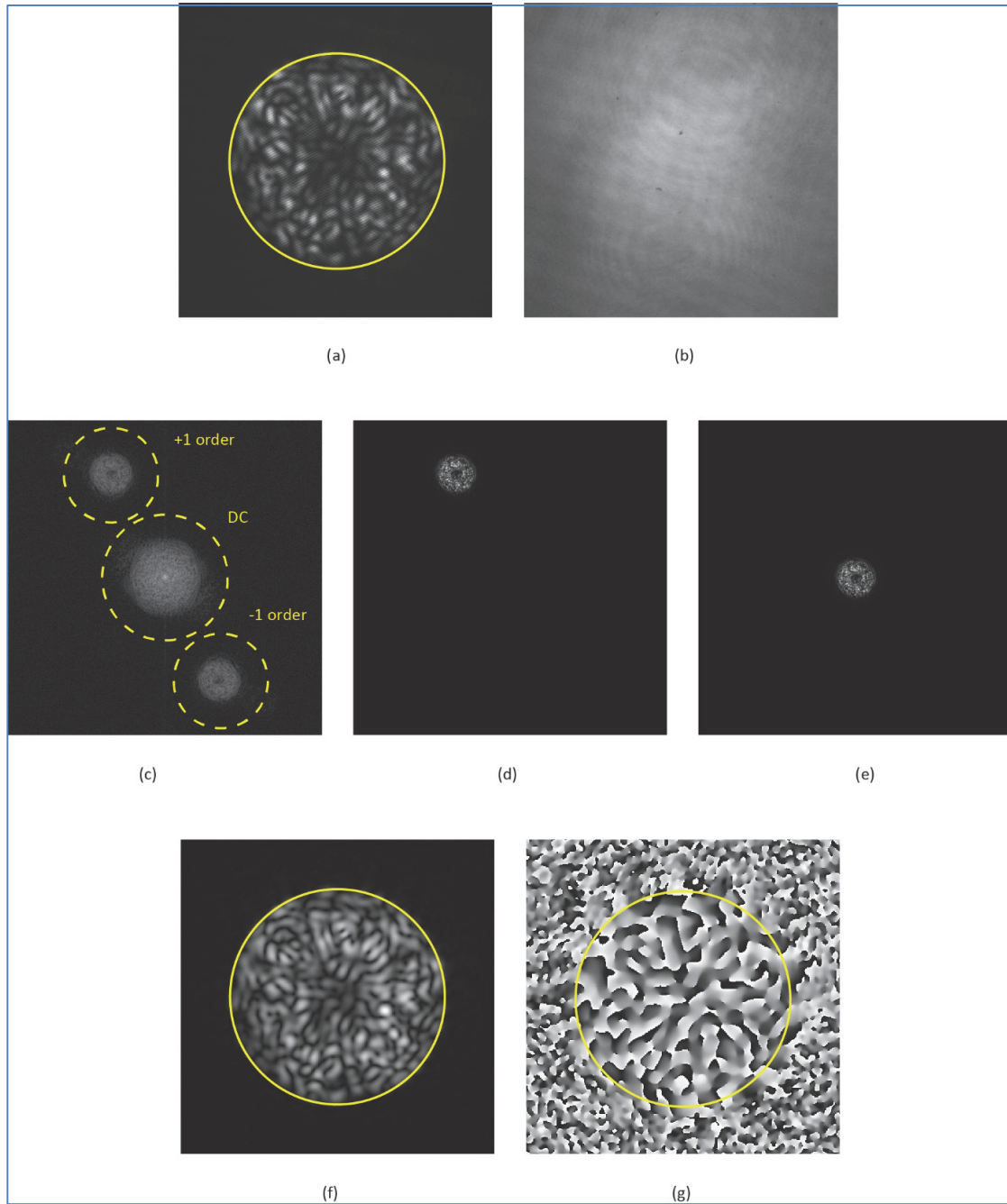


Figure 5-5 Reconstruction of the complex field at the output of the fiber. (a) Acquired hologram on the CCD (combination of reference and the object, in this case the output fiber beam). (b) The reference intensity. (c) Fourier transform of the hologram with the DC and ± 1 order. The space between the diffraction orders and the DC component and their positions are directly linked to the angle between the reference beam and the fiber output beam. (d) $+1$ diffraction order filtered out (e) $+1$ diffraction order shifted in the center of the Fourier domain (f) Reconstructed field amplitude, the speckle pattern partially visible in (a) is now entirely reconstructed. (g) Reconstructed phase. All the information about the complex field is extracted.

5.2.1.3 Phase conjugated focused spot through multimode fiber

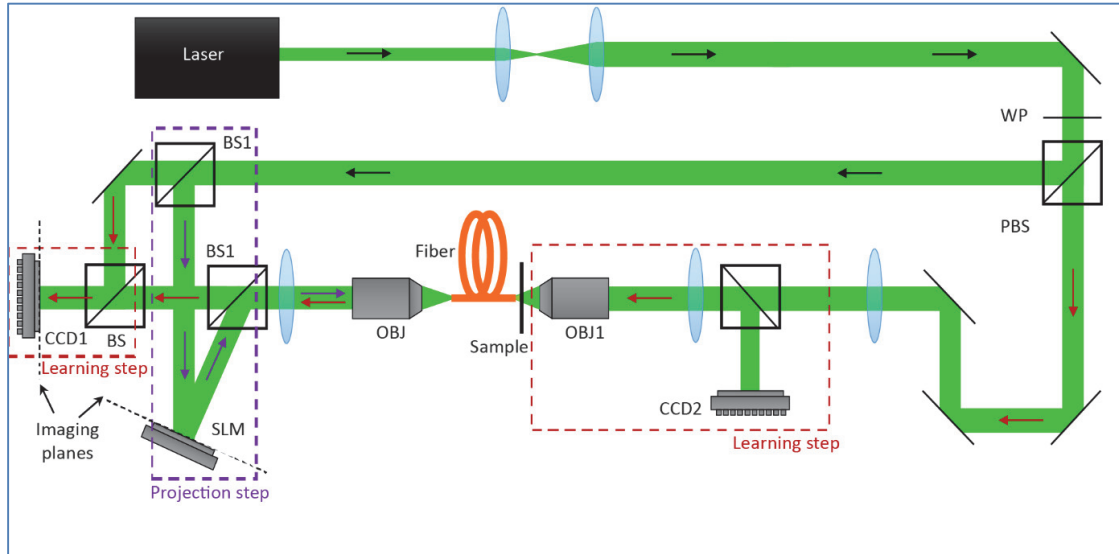


Figure 5-6 Optical setup for focus generation through fiber by phase conjugation. The procedure requires successive two steps, the calibration (learning step, red arrows) and the phase conjugation step (projection step, purple arrows). First step: Light is focused on the fiber facet by an objective (OBJ1) the speckled output interferes with the reference and the resulting interference pattern is digitally recorded onto the camera sensor (CCD1). Second step: The complex conjugate of the reconstructed phase of the hologram is assigned on the Spatial Light Modulator (SLM), which then modulates the high power arm of the reference beam. The phase conjugate beam propagates backwards recreating a focused spot in the initial position. This focused beam is used to excite the sample. (Other acronyms: WP: wave plate, PBS: Polarizing Beam Splitter, BS: 50/50 Beam Splitter, BS1: 90/10 Beam Splitter).

In the previous section, we detailed how the phase of the field at the fiber output is recorded by digital holography and how the phase conjugation field is calculated. To be able to back propagate the phase conjugated field we install the SLM in a different location but in the same imaging plane than the camera (Figure 5-6). Thus, we can use the SLM just as a phase conjugation mirror. In order to generate a focused excitation through the MMF the sequence is as follow. First, in a learning step (red arrow in Figure 5-6), we excite the fiber with a focused beam from the sample side on the distal end (right handed red dashed rectangle in Figure 5-6). This allows for the learning of the propagation information through the fiber. We record the off-axis hologram and calculate the phase from the recorded hologram (left handed red dashed rectangle in Figure 5-6). In a second step, we project the phase conjugated field pattern on the SLM (purple dashed rectangle). We let the phase conjugated field to back propagate through the multimode fiber and recreate a focus spot in the position of the original excitation.

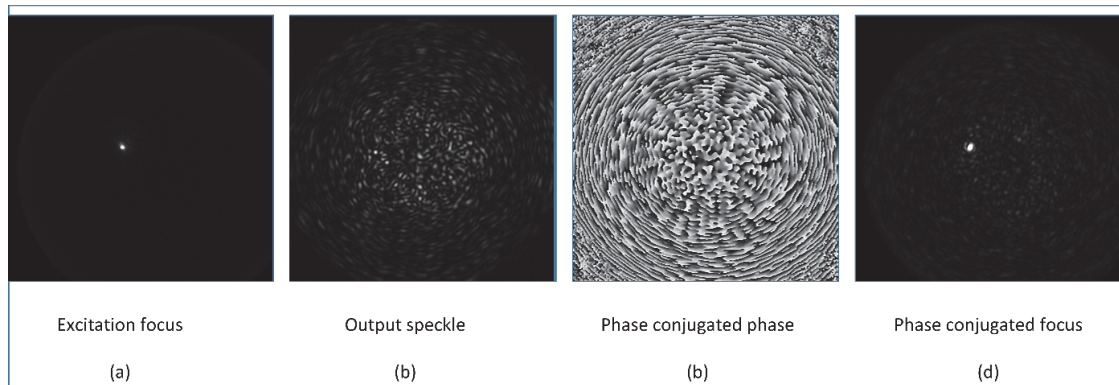


Figure 5-7 Focused excitation through multimode fiber by phase conjugation. (a) Excitation focus, imaged by reflection on the fiber facet. (white light is propagated through the fiber so that the edge is visible) (b) Output speckle after the propagation of the excitation focus through the fiber. (c) The phase projected on the SLM to create the phase conjugated spot. (d) Phase conjugated spot at the output of the fiber, in the exact same position as the excitation spot (the camera spot is strongly saturated so that the background is visible).

The Figure 5-7 (a) and (d) shows the images of the distal end of the fiber (CCD 2 in Figure 5-6) recorded at the different steps. It can be observed that after phase conjugation an intense focus is generated at the exact same location than the excitation beam. In order to evaluate the quality of the phase conjugated focus, we measure the enhancement defined as the ratio of the peak intensity to the average residual speckle background intensity. We obtain typical enhancement of 1000 that is compatible with fluorescence scanning microscopy. To be efficient the digital phase conjugation read out necessitates a very precise alignment of the SLM. Indeed, the SLM must act as a phase conjugated mirror. It means that, laterally, the position of each pixel of the SLM must correspond to the camera pixel used to record the hologram. It also means that the angle of the SLM must be chosen so that it reverts exactly the phase conjugated beam to the opposite direction of the original field. The details about the alignment procedure are given in Appendix E.

5.2.1.4 Fluorescence imaging

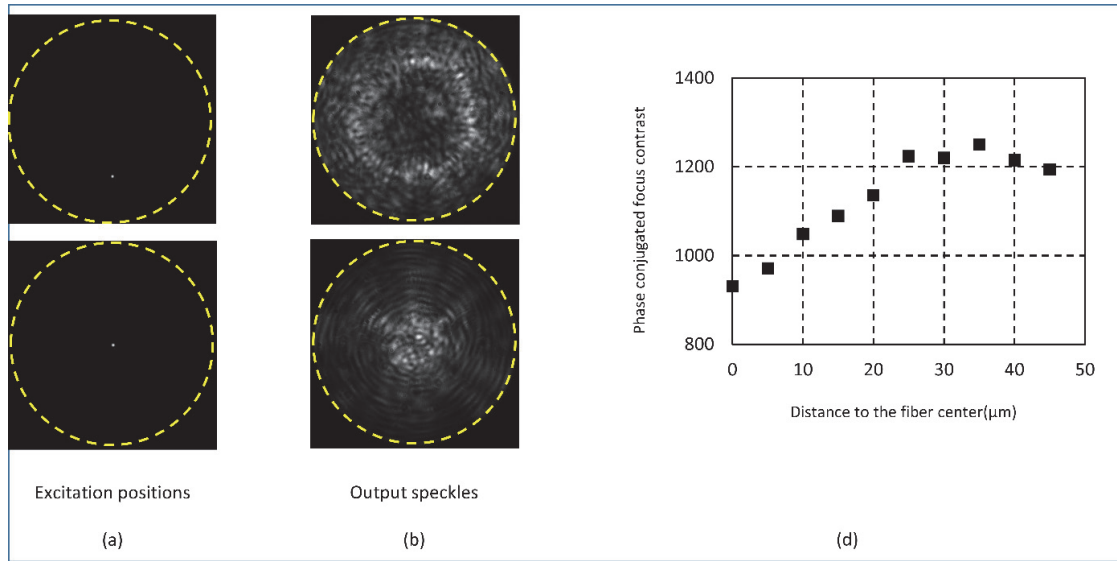


Figure 5-8 Influence of the excitation focus position on the phase conjugated spot. (a) Excitation focus in two different positions (image by reflection on CCD 2 in Figure 5-6). One focus is positioned close to the center of the fiber, the other close to the edge. (b) The corresponding output speckle after propagation through the fiber ((image on CCD 1 in Figure 5-6). The speckle resulting from the more central excitation exhibits less dense variations, indicating that less propagation modes are involved in its creation. (c) Phase conjugation focus enhancement in function of the position. The closer to the edge is the focus, the more modes participate to its formation, better is the enhancement.

We are now able to generate a focused spot at the distal end of the fiber by phase conjugation with a good contrast and stability. The spot position corresponds to the position of the learning focus during the acquisition of the hologram. So by recording the hologram, corresponding to each raster scan position, we can generate a scanning excitation spot at the end of the fiber [35]. We have seen that whatever is the excitation input, the propagation in the MMF generates a random sum of many modes and results in a speckle pattern. However, the output field is not exactly random. If the excitation beam is focused at a radial distance r of the fiber center, the intensity distribution of the output speckle tends to peak at the same radius r (Figure 5-8 (a) and (b)). It influences the contrast of the generated phase conjugated focus. The comparison of the output speckles obtained with the different excitation positions suggest that more modes are involved as the excitation moves away from the center.

The Figure 5-8 (c) shows the spot enhancement as the excitation spot is moved over the end of the fiber. It can be observed that the quality of the contrast is slightly dependent on the position of the fiber. As the external part of the MMF involves a higher number of mode, the phase conjugated focus contrast tends to be better far from the center. As the method we present in this chapter necessitates a constant excitation intensity, we decided to bypass the problem (and the possible need for a laser power compensation) by generating a unique focused spot and scanning the sample.

The excitation focus is generated at the end of the MMF, by scanning the sample and collecting the fluorescence back through the MMF we recreate high resolution lensless fiber endoscopy imaging as previously demonstrated [35]. Before harnessing saturated excitation modulation to imaging through MMF, we present in Figure 5-9 linear fluorescent scanning images of fluorescent beads through multimode fiber.

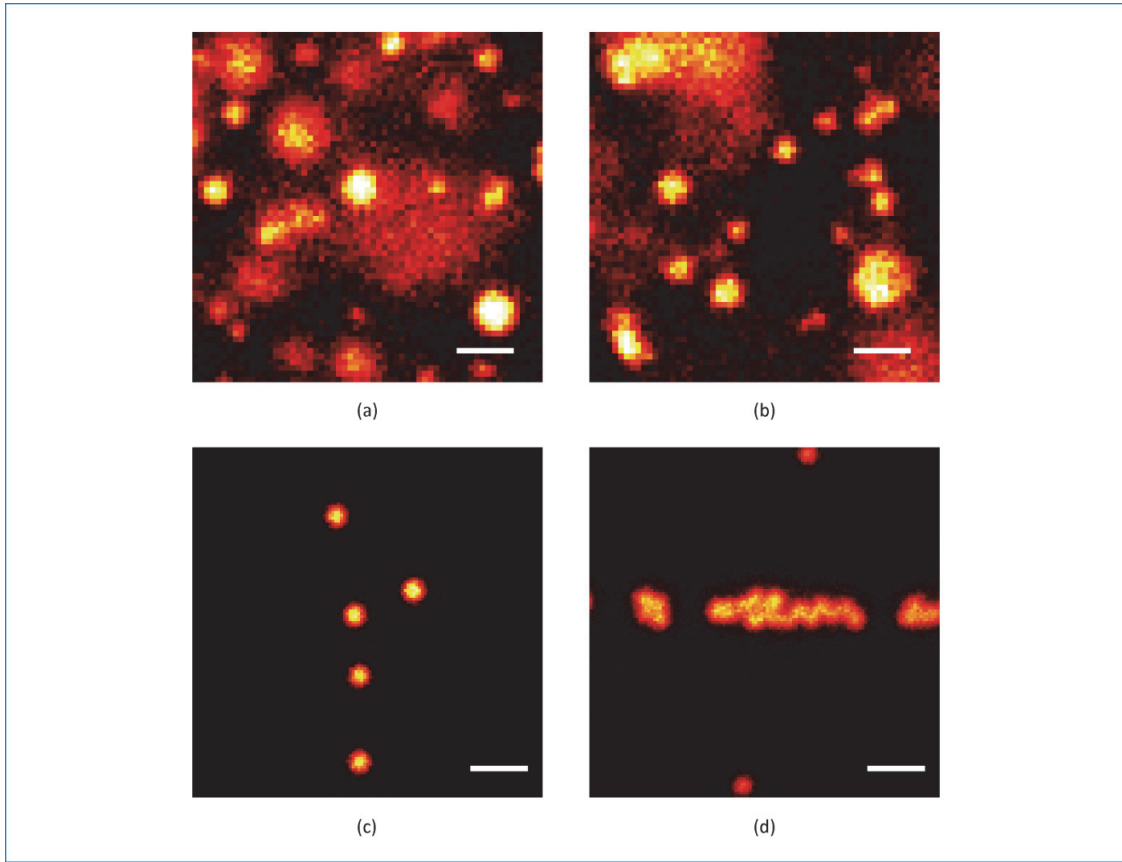


Figure 5-9 Linear fluorescence scanning imaging through multimode fiber. The multimode fiber used was 0.39 NA. The samples are made of red fluorescent beads excited at 532nm. Scale bars are 5μm. (a) and (b) The sample is composed of two layers of beads of different sizes (5μm, 2μm and 1μm). To make the sample, some beads are dried on a glass slide, covered by a 30μm thick PDMS layer, then a second layer of beads is dried on the PDMS. The absence of optical sectioning with MMF imaging by phase conjugation results in out of focus signal. (c) and (d) The sample is composed of 1 μm beads. The variation in shape in the cluster in image (d) indicates that the beads are close to be resolved, but they are not really separated.

In Figure 5-9, the images of different samples shows the properties of scanning imaging through MMF. It illustrates the limitation of the method that we mentioned in the introduction and that we want to improve by using saturated excitation. The first sample is composed of two planes (spaced by 30 μm) of fluorescent beads of different sizes (1, 2 and 5 μm). We can distinguish in Figure 5-9 (a) and (b) the multiple beads with different sizes and brightness. However, in the absence of optical sectioning the signal from the out of focus layer is also recorded and degrades the images. The second sample is composed of 1μm beads dried on a glass slide. In Figure 5-9 (c), the beads spaced a few microns apart are resolved. In Figure 5-9 (d), the structure of the cluster of beads can be distinguished but the individual spheres are not resolved. It indicates a resolution slightly above one micron (below 1 μm has been demonstrated with higher NA fiber [35]). For endoscopic imaging it is very high resolution [162], it could lead to image many cellular structure, but it still needs to be improved to reach typical microscope resolution. After defining the exact resolution we can obtain in MMF imaging, in the next section, we will detail the non-linear method that we used to improve the resolution and eliminate out of focus signal.

5.2.1.5 Linear imaging resolution

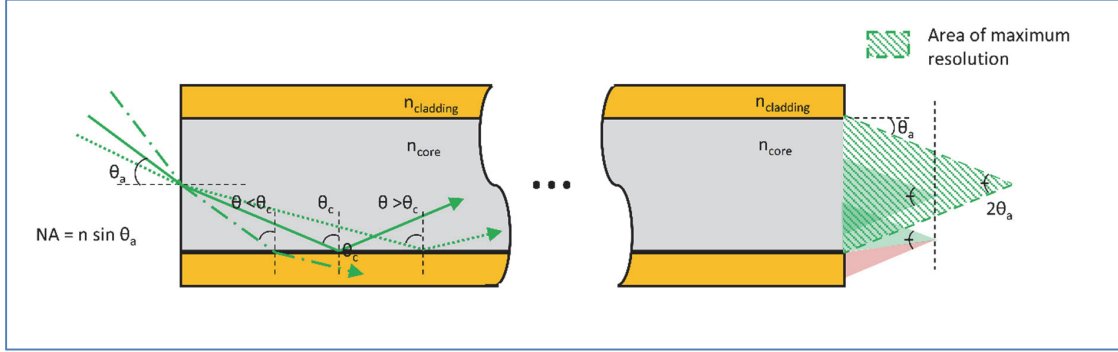


Figure 5-10 Numerical aperture of MMF and resolution of imaging through MMF. (a) A multimode fiber is a cylindrical waveguide. The rays that reach the core-cladding interface with an angle superior to the critical angle are subject to total internal reflection and propagate through the fiber. This guiding condition defines the maximal incident angle of the rays that can be coupled into the fiber. This angle is called acceptance angle θ_a and relates to the NA of the fiber. (b) Equivalently, θ_a is also the maximum angle of the rays that are present at the fiber output. As in microscopy, the maximum angle that can composed the focus leads to a minimal spot size of $0.5 \frac{\lambda}{n \sin \theta_a}$. The acceptance angle defines an area represented in with green stripes where the maximum resolution can be reached.

As in microscopy, the resolution in scanning imaging through MMF is fixed by diffraction and limited by the numerical aperture of the fiber. The NA is linked to the refractive indices of the core and the cladding of the MMF. This relation is illustrated on a geometrical optic point of view in Figure 5-10. All the rays that reach the cladding with an angle larger than the critical angle are totally reflected and remain guided into the fiber, while all the rays below the critical angle leak out and are not guided. Thus, it can be shown (Appendix F) that the maximum angle at the output of the fiber i.e. the numerical aperture of the fiber is:

$$NA = \sqrt{n_{core}^2 - n_{cladding}^2} \quad \text{Equation 5-9}$$

In consequence, the sharper focus that we will be able to generate at the output of the fiber will be composed with the higher angle rays and as for a microscope (Equation 2-3) the imaging resolution at the fiber output will be:

$$FWHM \approx 0.5 \frac{\lambda}{NA} \Rightarrow r \approx 0.61 \frac{\lambda}{NA} \quad \text{Equation 5-10}$$

The numerical aperture is fixed by the materials that compose the fiber, but another parameter that is going to influence the imaging capacity is the fiber diameter. As the fiber core gets larger, the number of modes that can propagate in the fiber increases and can be shown to be about [42]:

$$N_m = 8 \left(\frac{a \cdot NA}{\lambda_0} \right)^2 \propto \frac{a^2}{r^2} \quad \text{Equation 5-11}$$

The number of mode increases proportionally to the ratio of the fiber core area divided by the diffraction limited spot area (Equation 5-11). It means that the density of mode is increasing accordingly with the fiber size so that we will be able to generate the sharpest focused spot over the entire core output facet. In simple words, by increasing the fiber diameter we increase our field of view and keep the resolution imposed by the NA.

An intuitive explanation to understand that the maximal resolution is related to the fiber materials while the field of view is related to the core diameter is to consider the limit of a very small core. If the core is small enough, only one mode is supported: we have a single mode fiber. By reducing the core size of a single mode fiber, the minimal possible size of the fundamental mode that can be reached corresponds to the resolution limit imposed by the NA of the fiber (Appendix G). The single mode fiber situation can be seen as the limit where a single spot can be generated at the output of the fiber in a single position. At the other limit, by increasing the fiber size enough so that the fiber output field is speckled, we can generate, by phase conjugation, all over the fiber core area a

focused spot which is of the size of the speckle grain (that is known to be [179], $\langle r \rangle \approx 0.61 \frac{\lambda}{NA}$).

Thus the resolution at the output of the fiber is given by Equation 5-9 and Equation 5-10. However, in general, it is desirable to image with a certain distance respectively to the fiber facet. By simple geometrical optics consideration, it can be observed that the maximal focusing angle imposed by numerical aperture defines a conic volume in front of the fiber where the maximum resolution can be reached. This is illustrated in the right panel of Figure 5-10. A focus is created at a certain distance of the fiber facet in the plane represented with a black dashed line. If the focus is inside the striped cone, all the rays with highest angles can reach the focus. On the contrary, if the spot is positioned outside the striped cone, the angle content of the focus is lower and the resolution deteriorates. So, as we increase the imaging distance, we reduce the available field of view with maximal resolution. For instance for a typical fiber with 0.39 NA and 200 μm diameter the field of view with maximum imaging resolution is 128 μm large at 100 μm and 42 μm large at 200 μm . Outside this volume for the same reason the collection efficiency is also deteriorated [174]. In all the experiments we present in this chapter, we made sure to remain in the area of optimal resolution.

5.2.2 Saturated excitation microscopy

We have shown in the previous section how to generate a focused spot at a chosen position of the distal end of the MMF. By scanning this spot along the fiber facet and recording the fluorescent signal, diffraction limited images has been acquired. The typical resolution with a multimode fiber is of the order of one micron (Figure 5-9), ideal to resolve cellular structures but still limited compared with the resolution of typical confocal microscope. However, when the fluorescence signal is collected back through the MMF, the spatial information about the fluorescence field is lost because of modal dispersion of incoherent light (Figure 5-11 (a)). The only information available in every scanning position is the total fluorescence intensity.

This absence of spatial information about the reemitted field prevents us from applying the majority of the microscopy techniques we have detailed in the previous chapters. At first, the depth discrimination methods we used previously, i.e. confocal filtering or double helix filtering are based on the spatial imaging of the fluorescence signal and are consequently forbidden. Also, for the same reason, techniques based on structured illumination like CNS are forbidden. On the contrary, STED microscopy is theoretically compatible with imaging through MMF by phase conjugation. Indeed, phase conjugation allows for the reconstruction of the excitation field, independently of its shape. So it is possible, as illustrated in Figure 5-11 (b) to generate a donut shaped beam through MMF by phase conjugation. However, the quality of the donut central zero is a critical parameter for successful STED imaging (Figure 2-12) and even if we could reach the required contrast (Figure 5-11 (c)), the stability of the phase conjugated setup was not sufficient to maintain it in our first tries. In addition, the use of a second wavelength in the digital phase conjugation setup necessitates a second SLM and greatly complicates the implementation. And, above all, conventional STED would have allow to improve the lateral resolution but does not provide optical sectioning. The possible application of this ultrathin endoscope is to image into biological samples. Thence, to improve resolution and also obtain out of focus light filtering we used another microscopy method, first proposed in 2007 [173], named saturable excitation (SAX) microscopy. The principle of SAX microscopy is closely related to CNS microscopy. It also takes advantage of the nonlinearity brought by the absorption fluorescence saturation phenomenon to improve the resolution. The major difference is that the higher frequencies extraction is done in the temporal domain and not in the spatial domain.

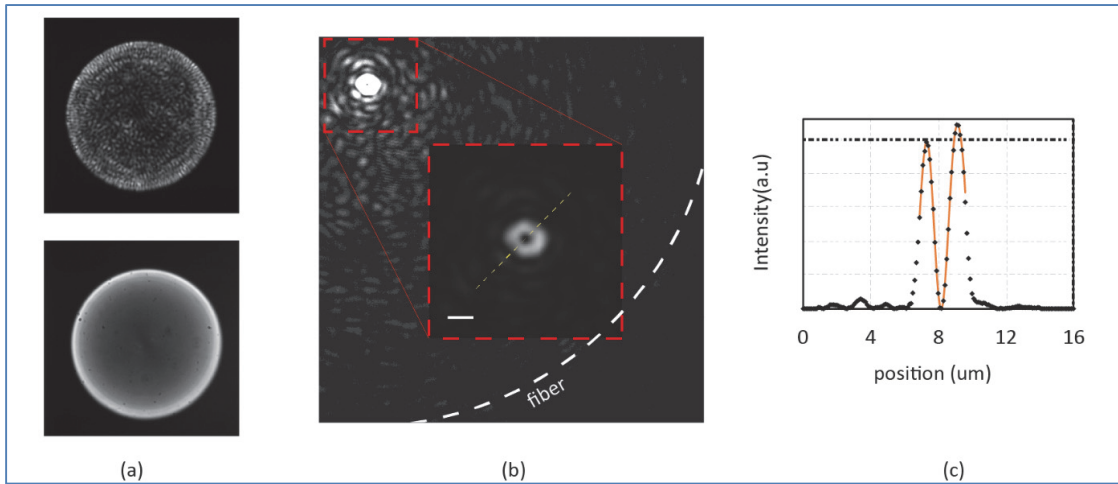


Figure 5-11 Influence of light coherence and generation of a phase conjugated vortex beam. Fiber output after propagation through the MMF. (a) Monochromatic coherent light: the different modes at the output are coherent and interfere to form a speckle pattern as described in the section

5.2.1. (b) Large spectrum fluorescence light, the fiber output is constant due to the incoherent summation of the different modes: the spatial information about the fluorescence field emitted by the sample is lost. (c) Donut shaped beam through multimode fiber by phase conjugation. To show the fiber background, the image is artificially saturated, and the donut beam image is presented without post treatment in the red dotted squared inset. (d) The intensity profile of the phase conjugated donut. We saw in section 2.4.3 that the quality of the central zero is critical for the signal strength in STED imaging. The peak to “zero” ratio intensity measured here is $\epsilon=0.008$. To achieve this contrast we accounted for polarization effect and used an optimization algorithm, (not shown here).

5.2.2.1 Super-resolution by temporal modulation and demodulation

We saw in the previous chapter that at high excitation power the fluorescence signal emitted is not proportional to the excitation. Briefly, at high excitation intensity, the flux of incident photon on the fluorescent molecule is such that after one photon has been absorbed, the next ones are more likely not to be absorbed because the molecule did not relax back to its ground state: this phenomenon is known as saturable absorption. It results in the saturation of the emitted fluorescence signal when the excitation intensity increases. The theoretical curve characteristic of the fluorescence saturation is calculated in detail in Appendix H and the experimental measurement with nanodiamonds containing NV centers has been presented in Figure 4-6. This fluorescence intensity (I_{fluo}) can be expressed in function of the excitation intensity (I_{exc}) as:

$$I_{fluo} = \frac{\sigma_{abs} I_{exc}}{1 + \tau \sigma_{abs} I_{exc}} \quad \text{Equation 5-12}$$

Where σ_{abs} is the absorption cross section and τ the fluorescence lifetime. Equivalently it can be written with a and b constant as:

$$I_{fluo} = \frac{a \cdot I_{exc}}{1 + b \cdot I_{exc}} \sim a \cdot I_{exc} - ab \cdot I_{exc}^2 + ab^2 \cdot I_{exc}^3 - ab^3 \cdot I_{exc}^4 \dots \quad \text{Equation 5-13}$$

The saturated signal is a non-polynomial transition, meaning that it can be approximated by a Taylor expansion with an infinite number of term (Equation 5-13), so it has the potential for theoretical infinite gain in resolution (section 2.2). In CNS microscopy or in SIM the non-linear signal is extracted by analyzing the change in the spatial shape of the reemitted signal compared to the excitation pattern. In SAX microscopy, the idea is to extract the nonlinear fluorescence response in the temporal domain. To understand the principle of the method, let's imagine that on each scanning position we record the dependence of the fluorescence signal on the excitation intensity (Figure 5-12). During the scan, for a given position, the fluorophores localized at the center of the excitation focus will exhibit more saturation than the one on the edge (Figure 5-12 (a)). As the saturation is more pronounced, the curve will deviate from a line to an edge, and higher orders will become non-negligible in the Taylor expansion (Figure 5-12 (b)). Thus, by a simple polynomial fit of the saturated curve it is possible to isolate the contributions proportional to increasing powers of the excitation intensity, leading to improved resolution (Figure 5-12 (c)). This idea has been proposed and demonstrated by Enderlein and all. in 2009 [180], but the lack of accuracy under noisy environment of the high order evaluation by curve fitting limits the application of the method.

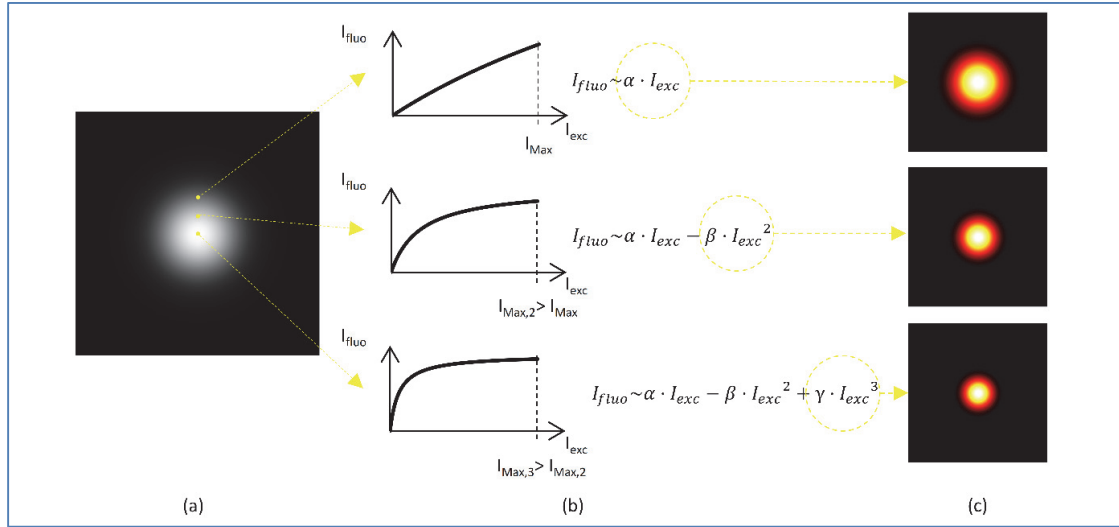


Figure 5-12 Underlying principle of SAX microscopy. (a) The excitation is a diffraction limited focus, so for one scanning position, depending on its localization compared to the center of the excitation focus a fluorophore is not excited with the same intensity. (b) When the excitation intensity is increased, the fluorophore localized in the center experiences a higher maximum intensity: the saturation happens mostly in the center of the focus. The level of saturation can be evaluated by a polynomial fit on the fluorescence dependence on the excitation intensity. (c) Resulting point spread function, by scanning the beam and collecting for each scanning position the first, second and third order of the expansion. As the saturated signal depends nonlinearly on the excitation intensity, by recording high orders the effective PSF is sharpened.

Instead, SAX microscopy is based on time modulated incident light and harmonic demodulation [173,181]. Indeed, the excitation intensity is modulated sinusoidally in time:

$$I_{exc}(t) = 0.5I_{max}(1 + \cos(\omega t))$$

Equation 5-14

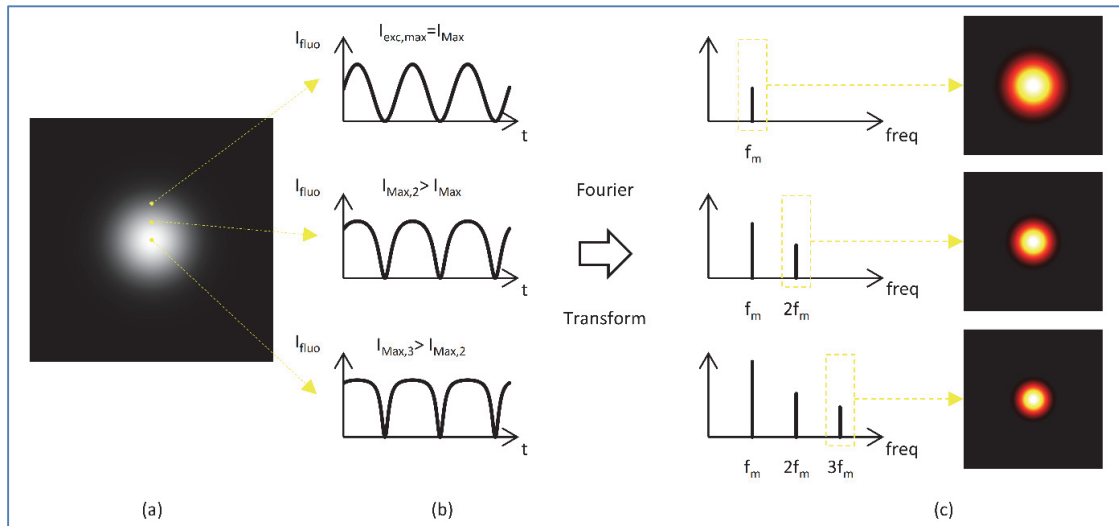


Figure 5-13 Principle of SAX microscopy. (a) Excitation focus. As in Figure 5-13, the saturation occurs mainly in the center of the excitation focus. (b) Fluorescence response curve from fluorophores excited with different intensity level. The excitation intensity is modulated sinusoidally in time at a fundamental frequency. The fluorescence saturation modifies the shape of the fluorescence emitted signal. (c) Demodulation of the fluorescence response and resulting PSFs. The demodulation at the harmonics of the fundamental frequency leads to the extraction of the nonlinear saturated components, proportional to the powers of the excitation intensity (as the curve fitting in the Figure 5-13 but in a much more accurate way, since the noise is spread over the entire frequency spectrum it nearly does not affect the narrow band harmonic signals). Extracting in each scanning position the harmonic signals results in a narrower PSFs. (as in the Figure 5-13, detecting higher harmonics results in isolating contributions proportional to increasing powers of the excitation intensity).

Again, the saturation is more pronounced where the intensity is maximum i.e. in the center of the excitation focus (Figure 5-13 (a)). It modifies the sinusoidal temporal profile and creates components at the harmonics of the modulation frequency (Figure 5-13 (b) and (c)). The demodulated response is calculated by taking the Fourier transform of the fluorescence temporal response. The demodulation brings out the nonlinear component: each harmonic of the modulation frequency corresponds to the contribution proportional to a power of the excitation frequency (Figure 5-14) and leads to an improvement of the resolution [173,181,182].

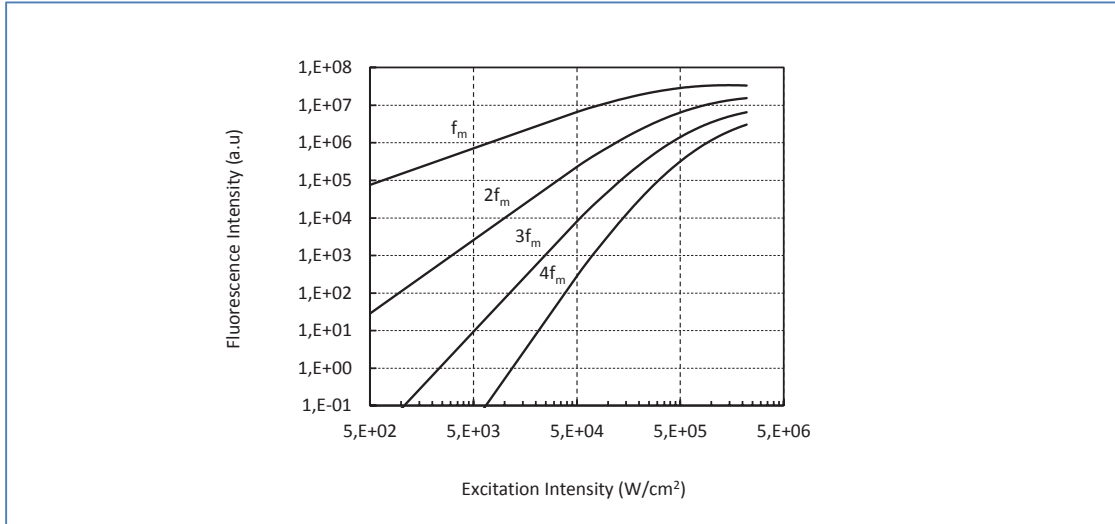


Figure 5-14 Calculated demodulated fluorescence intensity response. The excitation light modulation frequency is f_m and the frequency response is demodulated at the harmonics of the incident light frequency. The sample for the calculation (Appendix H) was a NV center.

The Figure 5-14 shows the calculated demodulated fluorescence intensity response, for a two level fluorophore with the photo-physical properties of a NV center (detailed calculation in Appendix H). The first harmonic (at the modulation frequency) demodulated response corresponds to the linear response which is proportional to the excitation intensity. The other harmonics response correspond to the nonlinear response. The Figure 5-14 is drawn with logarithmic scale, so that the power dependency can be easily visualized. As expected the n^{th} harmonic demodulated signal is proportional the n^{th} power of the excitation. Thus, the highest harmonic that can be recorded will give the highest resolution enhancement. However, two things must be noticed on this curve. First, at high power the nonlinear harmonic demodulated responses also saturate, which means that the maximum intensity of the modulation (I_{max}) must be carefully chosen. If I_{max} is taken too high for the chosen demodulation frequency it will result in a broadening of the PSF because of saturation. Second, the nonlinear demodulated harmonic signals are weak compared to the fundamental signal and get weaker for the higher harmonics. That's why using modulated saturated excitation with harmonic demodulation is practically very important for a successful detection of the nonlinear signal. Indeed, this detection method is equivalent to lock in amplification. The noise tends to be spread over a wider spectrum than the weak narrow band signal. So after integration over several periods, the narrow band harmonic becomes visible in the frequency domain. Thus, the signal that was buried into the noise with a single characterization curve, like in Figure 5-13 can now be recovered.

For the experiment we will use about 50 kW/cm^2 intensity to collect the second harmonic and about 200 kW/cm^2 for the third harmonic. As shown in Figure 5-14, the second harmonic signal is about one order lower than the DC component and the third harmonic signal is about 2 orders of magnitude lower than the DC component.

5.2.2.2 Enhanced resolution: effective point spread function

In this section we calculate the theoretical enhancement in resolution in scanning imaging with saturable excitation. We emphasize the difference with confocal and two photon microscopy in term of resolution gain. As explained above, the fluorescence signal obtained by demodulation at the n^{th} harmonic frequency is proportional to the n^{th} power of the excitation intensity (at the condition that the illumination intensity is low enough in order to not saturate the n^{th} harmonic). So the equivalent point spread function is:

$$PSF_{fiber, SAX^{nm}}(r, z) = (PSF_{exc}(r, z))^n$$

Equation 5-15

Hence, if we approximate the focused beam with a Gaussian, the n^{th} harmonic enhances the resolution by a factor of $\sqrt[n]{n}$. Figure 5-15 (a), shows the lateral intensity profile of the PSFs for different harmonics demodulation. Since the resolution enhancement is related to the nonlinear photoresponse, as in multi-photon microscopy the resolution is also improved in the axial direction. It can be observed in Figure 5-15 (c), that the equivalent excitation PSF size is reduced both in lateral and in axial direction. The numerical approximation of the three dimensional PSF presented in Figure 5-15, has been done using Lomel functions, as proposed in [41] p488. The axial profile has a slightly different shape compared with the lateral profile (Appendix A), but it can still be reasonably approximated with a Gaussian curve, meaning that the axial resolution improvement is also close to a factor $\sqrt[n]{n}$ with the n^{th} harmonic (Figure 5-15).

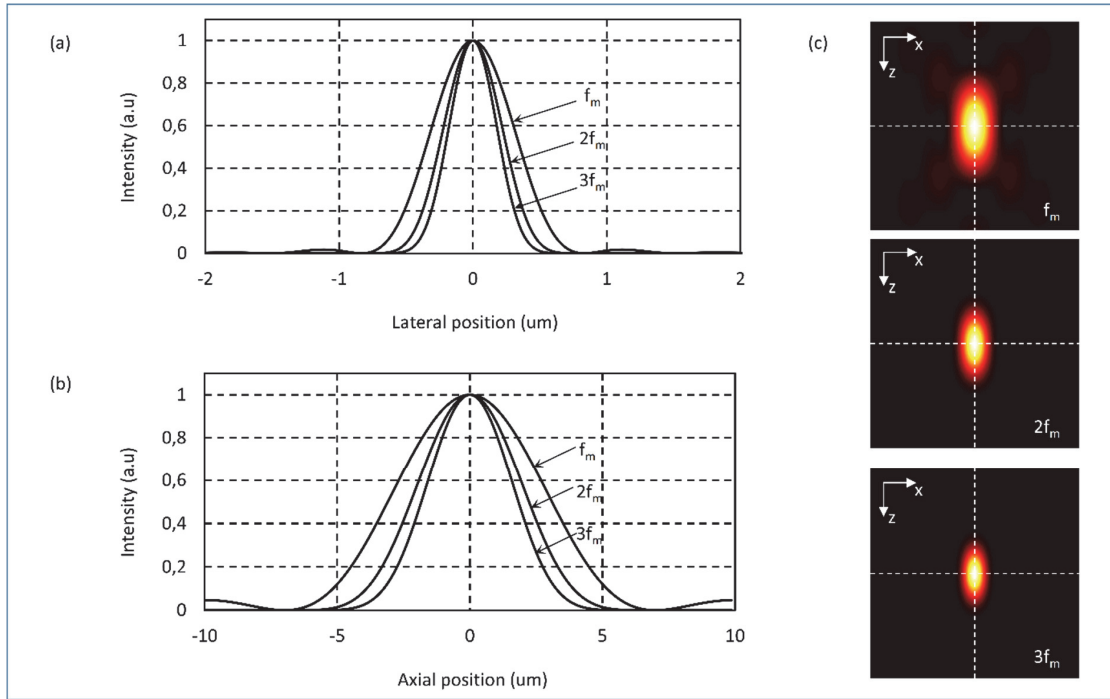


Figure 5-15 Theoretical resolution improvement in SAX microscopy for a 0.39NA and 532nm excitation light. The linear 3D PSF shape is calculated following the numerical approximation proposed in [41] p488. The second harmonic and third harmonic demodulation PSFs are deduced using Equation 5-14 (c) The excitation PSF of a scanning microscope in the (x,z) plane with z the propagation axis at different demodulation frequencies. The f_m demodulation is the linear PSF and the $2f_m$ and $3f_m$ are the PSF with second harmonic and third harmonic demodulation. (a) The lateral profile (x direction) along the white dotted line axis. (b) The axial profile (z direction) along the white dotted line axis.

SAX microscopy have some advantages compared to multiphoton microscopy. For instance it does not require any specific sample, as it is the case with second harmonic generation and it does neither require expensive femtosecond pulsed laser. But the main advantage is in term of resolution. All the harmonics are detected at the same light wavelength as the excitation beam. In contrast, in two photon microscopy the excitation wavelength is usually about twice as long as the one used for single photon absorption, therefore reducing the gain in resolution induced by the nonlinearity. Figure 5-16 (a) shows effective excitation point spread function with diamonds containing NV centers, with the two imaging methods: two photon and SAX. The two photon luminescence of NV centers has been shown to be optimally excited at 835 nm [183] and one photon fluorescence absorption peaks at 532 nm. Because of this large difference in the excitation wavelength, despite the resolution gain due to the nonlinearity the two photon PSF is larger compared with the conventional PSF and even more so compared with the SAX with second harmonic demodulation.

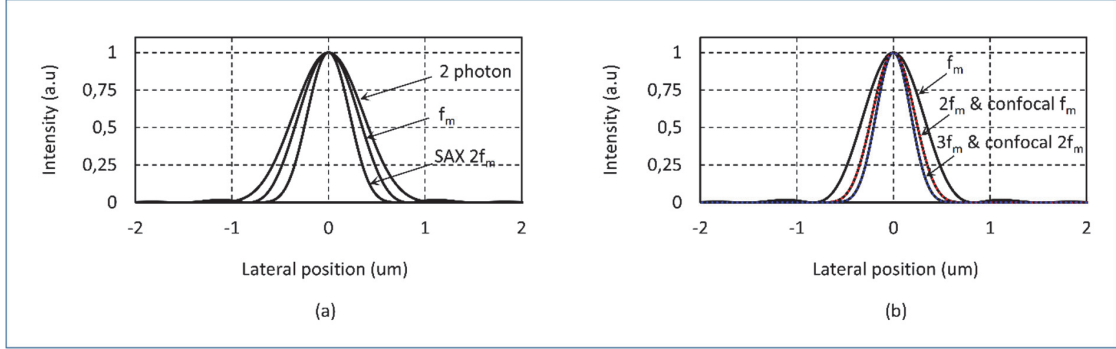


Figure 5-16 Comparison of the PSF with different imaging method with a 0.39NA microscope for NV centers imaging. (a) Lateral profiles of the excitation PSFs with: two-photon excitation at 835nm, one photon excitation at 532nm and second harmonic SAX demodulation with 532nm excitation. (b) Lateral profile of the excitation PSFs with: conventional linear scanning microscopy (f_m), SAX 2nd harmonic scanning microscopy or linear confocal (red dots) and SAX 3rd harmonic scanning microscopy or SAX 2nd harmonic confocal.

After comparing the resolution performance of SAX with two photon imaging, we now make the comparison with confocal imaging. The effective point spread in scanning microscopy is given by the multiplication of the illumination and the detection point spread functions. In the case of a confocal microscope the PSF can be written as:

$$PSF_{conf} = PSF_{exc} \cdot [PSF_{det} \otimes D] \quad \text{Equation 5-16}$$

with D the aperture function of the pinhole and the Point Spread Functions of the confocal microscope (PSF_{conf}), of the excitation (PSF_{exc}) and of the detection (PSF_{det}). The ideal confocal case corresponds to D being a delta-function, so the equivalent PSF is (if we neglect the Stokes shift):

$$PSF_{conf}(r, z) \approx [PSF_{exc}(r, z)]^2 \quad \text{Equation 5-17}$$

As opposed to confocal microscopy, as we underlined in the introduction of section 5.2.2, the imaging through the fiber is a purely scanning image. All the fluorescence collected is integrated on the point detector (with a constant collection efficiency), as if D would be infinitely large:

$$PSF_{fiber}(r, z) = PSF_{exc}(r, z) \quad \text{Equation 5-18}$$

If we consider the range of intensity where the second harmonic demodulated signal is proportional to excitation intensity squared (Equation 5-15), we have:

$$PSF_{fiber, SAX 2f_m}(r, z) = [PSF_{exc}(r, z)]^2 \approx PSF_{conf}(r, z) \quad \text{Equation 5-19}$$

In other words, as illustrated in Figure 5-16 (b), the theoretical gain in resolution obtained with the demodulation of the 2nd harmonic saturated excitation signal is the same than in confocal microscopy with an infinitely small pinhole. It means that SAX confocal microscopy resolution is higher than MMF imaging resolution. However, it also means that MMF imaging benefit proportionally more from the saturated excitation demodulation, since the resolution enhancement factor of SAX 2nd harmonic compared with the linear imaging will be $\sqrt{2} \approx 1.4$ for the MMF while it will be $\sqrt{3}/\sqrt{2} \approx 1.2$ for confocal imaging.

5.2.2.3 Depth discrimination: optical sectioning

Conventional scanning fluorescence imaging through MMF has no optical-sectioning capability which can cause dramatic blurring of the signal when imaging thick sample. That's why confocal microscopy and two-photon microscopy are popular methods, compared to wide field microscope for deep imaging. SAX microscopy in a similar way than two photon microscopy (the saturation signal is created only in the vicinity of the focus) takes benefit of the non-linear fluorescence signal response to provide optical sectioning [184].

To understand optical sectioning [43], we can calculate the signal emitted (I_{thin,layer}) as a fluorescent plane is scanned axially through the excitation PSF (PSF_{exc}):

$$I_{thin,layer}(z) = \int_{r=0}^{\infty} PSF_{exc}(r, z) dr$$

Equation 5-20

Figure 5-17 (a) shows $I_{thin,layer}$ curves for different imaging cases. In the linear case (f_m curve in Figure 5-17), because of energy conservation, the signal is constant as a function of the axial position, illustrating the absence of sectioning. In contrast to the linear case, the integrated intensity of the SAX demodulated signal exhibits a peak in the focal plane (SAX $2f_m$ curve in Figure 5-17). This is the origin of optical sectioning capability with SAX (which is mathematically strictly equivalent to two-photon), it proves that only the fluorophores in the neighborhood of the focus are observed. The sharper response of the SAX curve compared with the two-photon one (dashed curve in Figure 5-17 (a)) shows a better sectioning performance in 2nd harmonic SAX because of the shorter excitation wavelength.

A very thin and homogeneous fluorescent layer is complicated to create, so the practical optical characterization measurement consists in recording the fluorescence intensity as the excitation focus enters into a thick layer of fluorophores (I_{edge}):

$$I_{edge}(z) = \int_{z'=-\infty}^{z'=z} \left\{ \int_r PSF_{exc}(r, z') dr \right\} dz'$$

Equation 5-21

Figure 5-17 (b) displays the calculated edge response (I_{edge}) for the same imaging situation considered for the plane. In the first case (f_m curve), the fluorescence response is linear to the excitation. Assuming an infinitely thick dye layer, the edge response is constant. The $2f_m$ and the dashed curves represent the edge responses for SAX and two photon microscopy respectively. In both cases the signal rises up when the focus enters the edge, illustrating that SAX and two photon microscopy can perform sectioning. Again, the better performance in SAX microscopy is given by the shorter excitation wavelength.

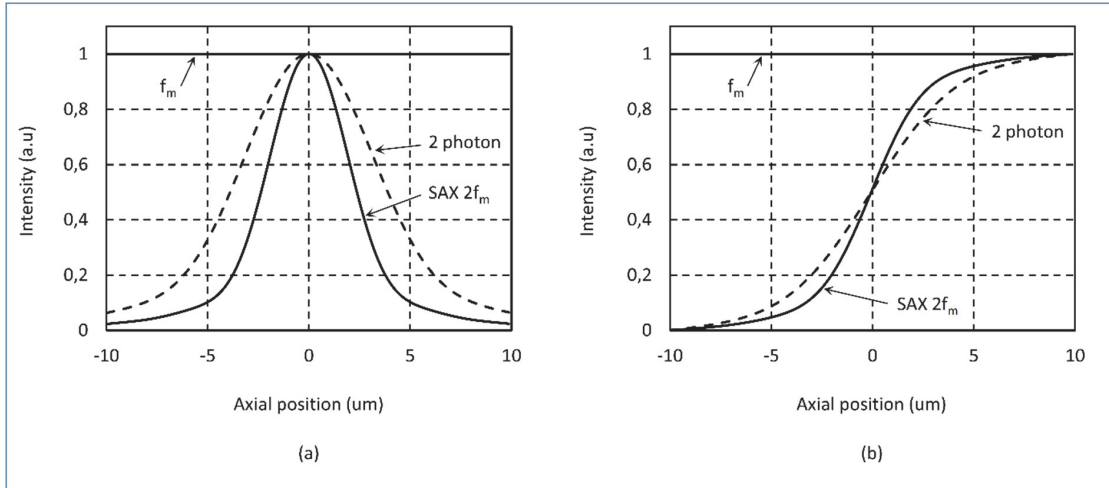


Figure 5-17 Theoretical sectioning performance of SAX and two-photon microscopy. (a) Fluorescence signal as a perfect planar thin object is scanned axially. Linear case (blue) shows the absence of sectioning while the 2nd (red) and 3rd (green) harmonic SAX signal indicate depth discrimination. (b) Edge responses for a 0.39 NA scanning imaging system, with no optical sectioning ability (f_m), with two photon fluorescence response (dashed curve) and saturated fluorescence excitation ($2f_m$).

5.3 Enhanced resolution and optical sectioning through multimode fiber by saturated excitation

5.3.1 Experimental setup

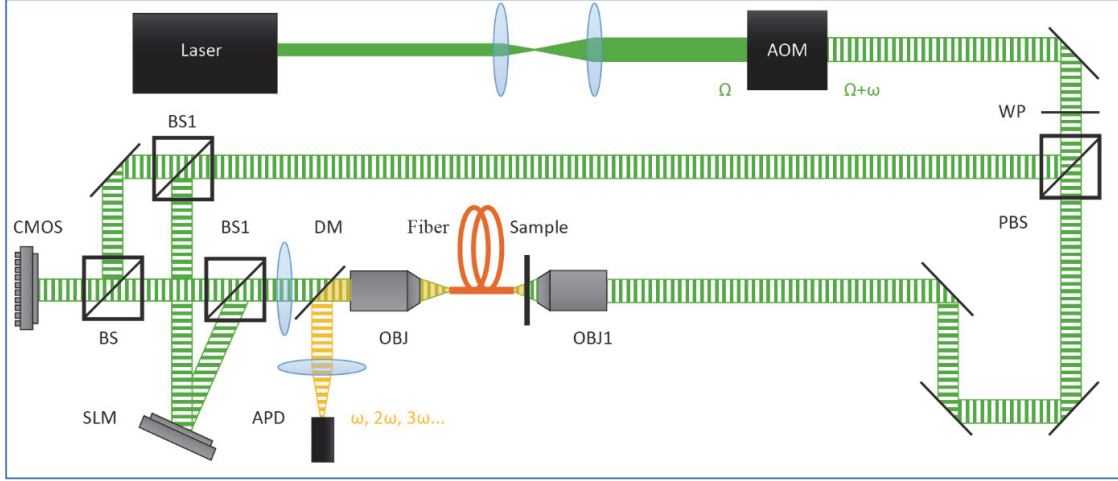


Figure 5-18 1 Schematic of the SAX through MMF imaging setup. We carried out minimal modification on the phase conjugation setup presented in Figure 5-6. To record a fluorescence image, the sample is scanned with a piezoelectric-stage and the light is collected back through the fiber, isolated with a dichroic mirror (DM) and detected with an avalanche photodiode (APD). The beam is modulated in time with an acousto-optic modulator (AOM) and for each scanning position a time trace of the fluorescence signal is recorded and then post-treated to isolate harmonics.

One of the advantage of the method is that its implementation (Figure 5-18) requires minimal changes to the setup presented in Figure 5-6. An acousto-optic modulator is added right after the laser to modulate the beam and the SAX microscopy principle can be directly harnessed to imaging through MMF. The focused spot produced through the MMF is obtained by digital phase conjugation of the field recorded previously on the opposite side with the off-axis holographic setup. The sample is scanned to produce a fluorescence image. The light is modulated sinusoidally in time. As explained above, at low excitation level, the fluorescence response depends linearly on the excitation. When the excitation intensity increases, the fluorescence response saturates and modifies the temporal response of the fluorophores. This leads to the formation of harmonics of the carrier frequency that are extracted to get resolution enhancement.

In the experiment, the beam was sinusoidally modulated in time at $\omega = 2$ kHz with an acousto-optic modulator (AOM). The AOM is placed at the very beginning of the setup so that the induced Doppler shift does not affect the hologram acquisition. To detect the saturated contribution, it is critical that the excitation modulation is a perfect sinusoid in order not to induce any signal at the harmonics frequency. To do so, we calibrated the acousto-optic modulator response and drove it with a radio frequency generator able to envelop the 80 MHz sound wave with an arbitrary kHz modulation (AFG 3102C, Tektronix). A substantial intensity (about 100 kW/cm^2) is necessary to obtain fluorescence saturation, so a high power source (Verdi-V10, Coherent) is used and the losses are minimized. Two (90/10) beam splitters are used to maximize the light sent onto the SLM which is used to excite the fluorescent sample during the scan. As we discussed already in section , the possibility of digitally scanning the beam by using a set of saved patterns has been demonstrated elsewhere [35]. In the experiment we present here, we keep a single phase conjugated excitation spot and we scan the sample with a piezoelectric stage. For each scanning position, the temporal response is recorded during 20 ms with an APD and a fast acquisition card that samples the signal at 100 kHz. The time trace for each scanning position is saved on the computer and the demodulation for each pixel is made off-line on a computer (by simply taking the Fourier transform, and recording the value at the harmonics frequencies).

5.3.2 Resolution improvement

5.3.2.1 Point spread function measurement

We use fluorescent nanodiamonds (120 nm diameter) as imaging probe. In order to characterize the improvement in resolution given by this technique we recorded the PSF by scanning a single nanodiamond into the focused spot produced by the fiber with different excitation intensities.

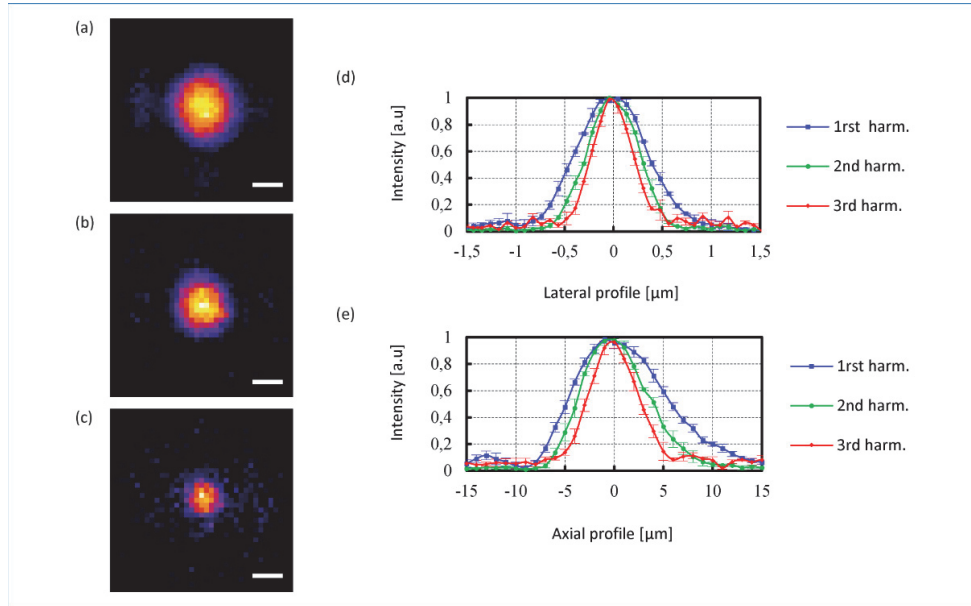


Figure 5-19 Point spread function narrowing with saturated excitation endoscopy. The PSF is measured by making a fluorescent scanning image of a single nanodiamond (with a diameter much smaller than the diffraction limit of the imaging system). Scale bars are 1 μm. (a) Linear image in the focal plane obtained by demodulation at the modulation frequency. (b) Image with second harmonic demodulation (c) Image with third harmonic demodulation. (d) The intensity profiles along the images (a), (b) and (c). The effective point spread function FWHM, decreases as we use higher harmonics for demodulation. The gain in resolution is measured to be about 1.6 times for the third harmonic demodulation compared with the fundamental frequency. Each point on the plot is the average over 5 measurements obtained with different nanodiamonds, the error bars represent \pm the standard deviation. (e) The nanodiamond is also scanned in the axial dimension and the axial intensity profile are plotted. The same resolution improvement factor is obtained in the three dimensions.

It can be observed in Figure 5-19 that both the lateral and axial FWHM decrease with higher harmonics demodulation. We measured the linear lateral FWHM to be 850 nm (the diffraction limit is 700 nm for a 0.39 NA fiber). From the profiles in Figure 5-19 (d) and 3(e), the gain both in lateral and axial resolution is estimated to be about 1.6 with the third harmonic demodulation, close to the theoretical $\sqrt{3}$ expectation (Figure 5-15). The images and the plots in Figure 5-19 are normalized. The higher harmonic frequency components have a signal intensity one to two orders of magnitude lower than the fundamental frequency component (Figure 5-14) and the background that appears in Figure 5-19 (c) is due to shot noise.

5.3.2.2 High resolution Nanodiamonds Imaging

In Figure 5-20 and Figure 5-21, we illustrate the gain in resolving power due to SAX by imaging clusters of nanodiamonds immobilized on a glass slide.

The Figure 5-20 illustrates the resolution enhancement that can be obtained with the second harmonic demodulation and the evolution of the different signal levels. In Figure 5-20, the demodulated signal is shown at the fundamental frequency and at the second and third harmonics. At low power, only the linear signal demodulated at the fundamental frequency is detected, a diffraction limited image is obtained in Figure 5-20 (a). Only noise is present in the Figure 5-20 (b) and (c), it indicates that the excitation modulation is close enough to a perfect sinus in order not to create harmonics. With an excitation intensity of 60 kW/cm² the second harmonic signal can be extracted and a few points must be noticed. First, the saturation of the fluorescence is visible on the fundamental demodulation image Figure 5-20 (d). The deformation of the PSF deteriorates the resolution, that's why saturation is usually avoided in fluorescence microscopy. Second, as expected, the resolution of the second harmonic SAX demodulated image

Figure 5-20 (e) is improved compared with linear imaging Figure 5-20 (a). The improvement can be clearly observed on the details pointed with arrows. Third, the noise floor has increased proportionally less compared to the fundamental signal, it indicates that by increasing more the power the third harmonic should be detected. And, finally since we don't detect any signal with the third harmonic demodulation we probably do not saturate the second harmonic, so the excitation power is optimal for second harmonic demodulation.

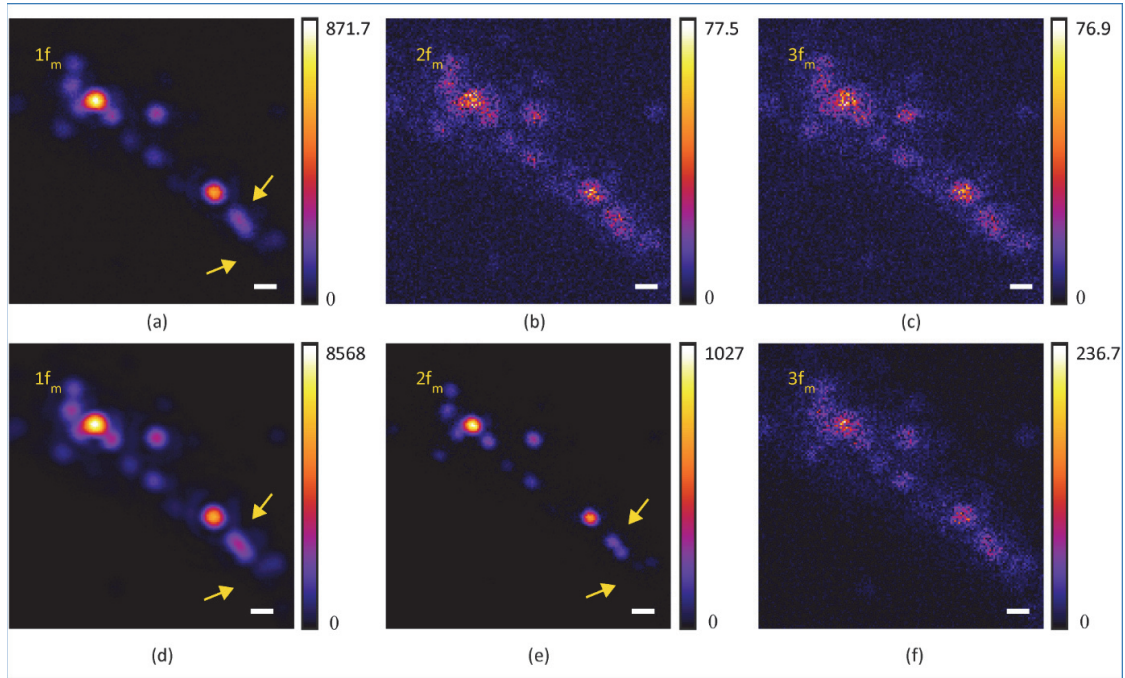


Figure 5-20 Peak intensity influence in SAX endoscopic imaging. Fluorescence images with modulation and demodulation at the fundamental frequency ((a) and (b)), the second harmonic ((b) and (e)) and the third harmonic ((c) and (f)). In the first row, the excitation intensity is low (2 kW/cm^2) the fluorescence response linear and the image resolution limited by diffraction. Only a signal at the fundamental frequency is detected in (a). The second row the excitation is higher (60 kW/cm^2). At the fundamental frequency the image (d) is distorted because of saturation. The second harmonic demodulated signal image (e) has an improved resolution. At this level of saturation, the third harmonic signal is still buried into noise (f).

In Figure 5-21, the fluorescent nanodiamonds were observed at 200 kW/cm^2 and by extracting the third harmonic component. Comparison of the image formed at low light power at the fundamental frequency with the SAX image, confirms the significant improvement of the spatial resolution in SAX microscopy. Some details (arrows in Figure 5-21) of the nanocrystals assembly, invisible with linear imaging are resolved in the demodulated image. The resolution for the third harmonic is about 500 nm and it opens the path for micro-structure observation with MMFs.

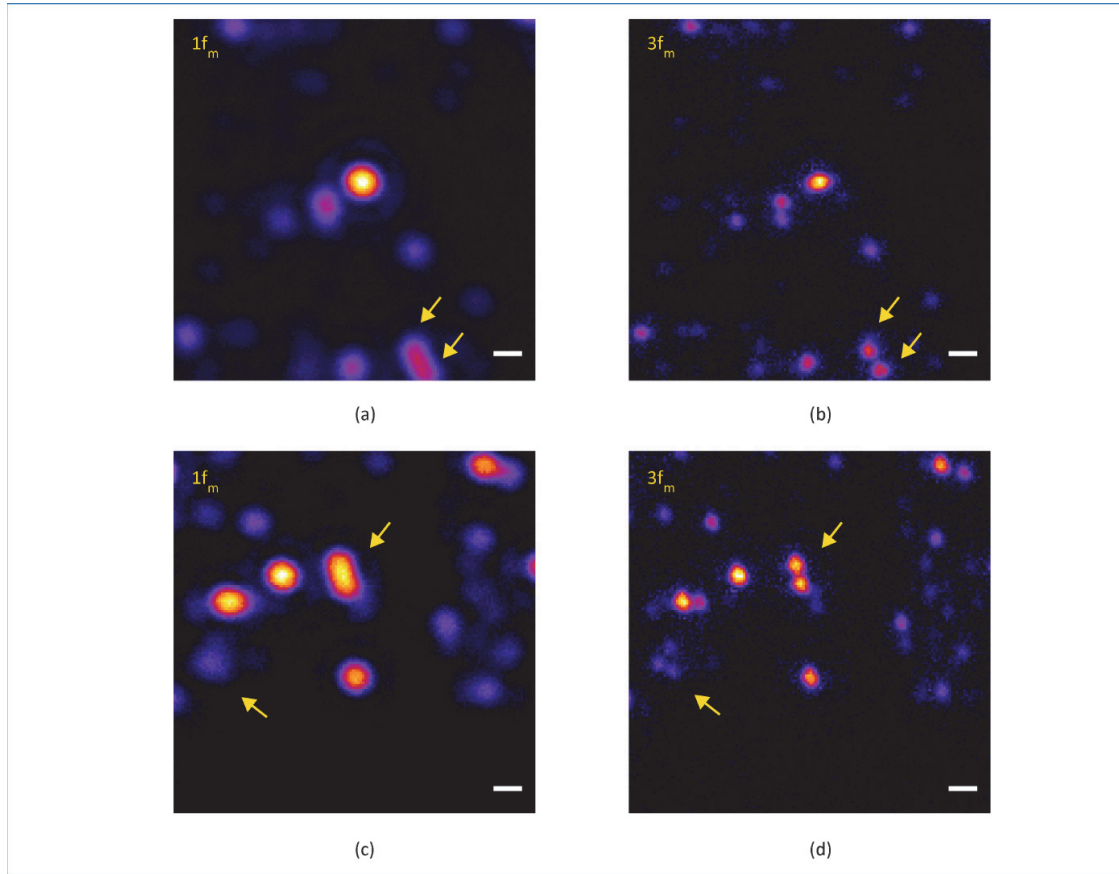


Figure 5-21 Fluorescence images of nanodiamonds immobilized on a glass slide. Scale bars 1 μm. (a) and (c) Linear image. (b) and (d) Saturated excitation image. The excitation intensities for those experiments were about 2 kW/cm² for the linear images and 200 kW/cm² for the SAX images. The arrows points the details where the resolution improvement is clearly visible.

5.3.3 Depth discrimination

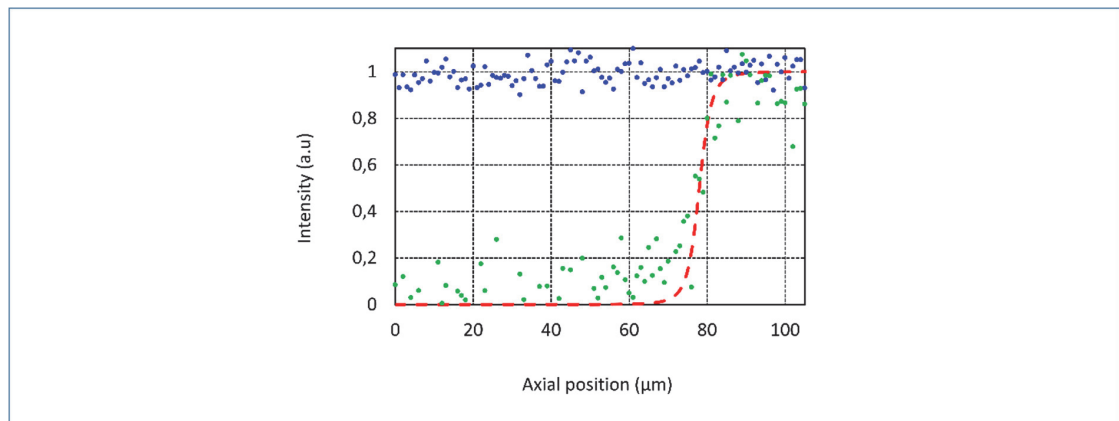


Figure 5-22 Characterization of the sectioning performance: edge response of a Rhodamine 6G dye solution. Edge response from a Rhodamine 6G solution, for linear excitation with demodulation at the excitation frequency (blue points), for saturated excitation with demodulation at the second harmonic (green points) and the theoretical edge response curve (red), equivalently for a linear detection with infinitely small pinhole or for second harmonic SAX demodulation. The integration time was 200 ms per point.

As we detailed in the section 5.2.2.3, SAX can also achieve suppression of out-of-focus light in a similar manner as two-photon fluorescence microscopy and this is in particular importance in our fiber endoscope system since on the contrary to free space

imaging we cannot implement confocal filtering. In order to confirm the depth discrimination capacity and characterize the sectioning performance of our SAX fiber endoscope system we measured the axial edge response. The fluorescence signal collected from a thick dye layer (Rhodamine 6G) while it is scanned along the optical axis is shown in Figure 5-22. The linear response (blue plot) shows the absence of sectioning in the system but the demodulated signal (green plot) at the second harmonic exhibits the edge transition when the focus is entering the dye layer. As predicted in the section 5.2.2.3, the slope of the measured transition with second harmonic demodulation (green plot) is similar to the one given in a confocal microscope with a 0.39 NA objective and an infinitely small pinhole (red plot). However, the out of focus light rejection mechanism takes place in the digital domain and, as we will discuss in the next section, is bound to the available SNR. For this reason, with a thick Rhodamine sample, we were only able to extract the second harmonic signal.

In order to demonstrate that the image contrast can be improved thanks to depth discrimination induced by our method, we made a sample composed of two layers of nanodiamonds separated by 30 μm . When one of the two planes is on focus, background fluorescence light is generated by the out of focus layer (however the out-of-focus fluorophores are not saturated). Thereby, it can be observed in Figure 5-23 (a) and (c) that the out-of-focus signal can deteriorate the linear images. While in Figure 5-23 (b) and (d) the background light is filtered out in the second harmonic demodulated signal and the contrast of the image is greatly improved. As with the edge response measurement, only the second harmonic demodulation could be recorded.

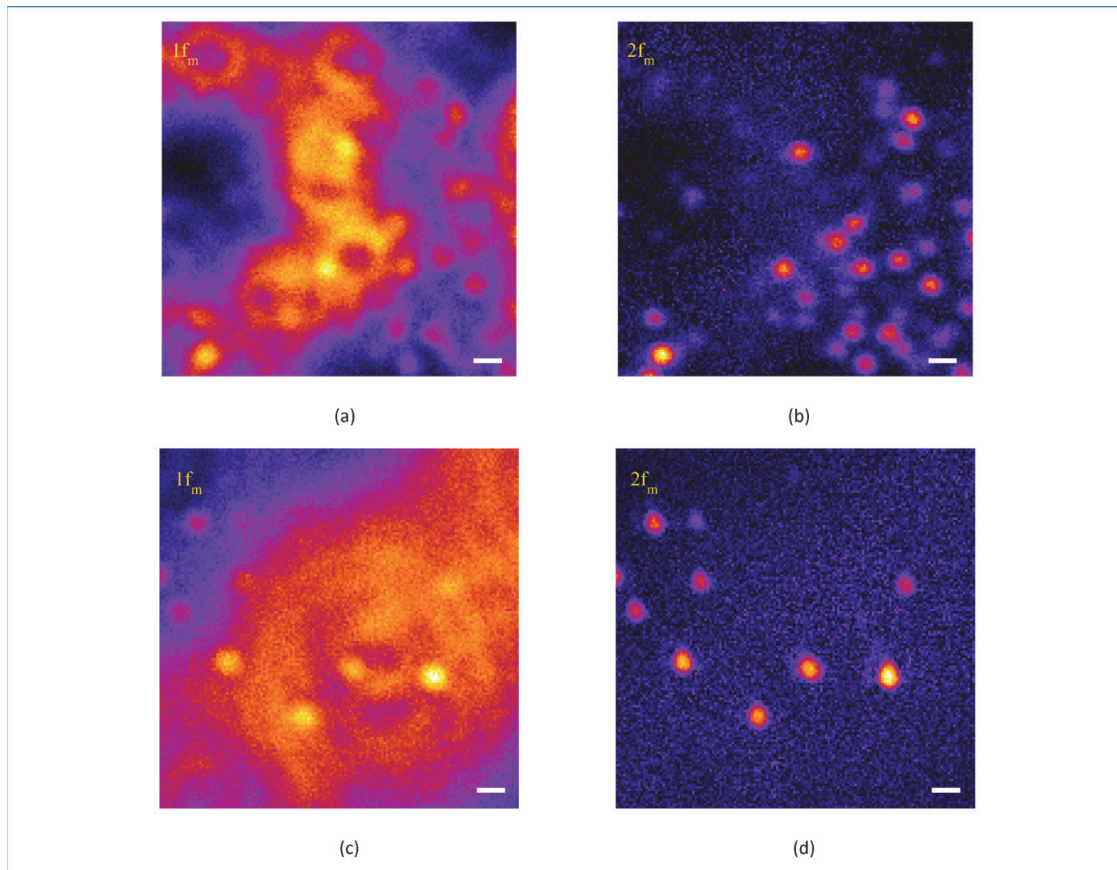


Figure 5-23 Improvement of image contrast by optical sectioning. (a) and (c) Fluorescent image through MMF of fluorescent diamonds: the image is blurred by out of focus signal coming from a cluster of nanodiamonds placed 30 μm deeper. (b) and (d) Saturated excitation image through MMF: second harmonic demodulation rejects out of focus signal and improves significantly the contrast.

5.3.4 SNR limitations

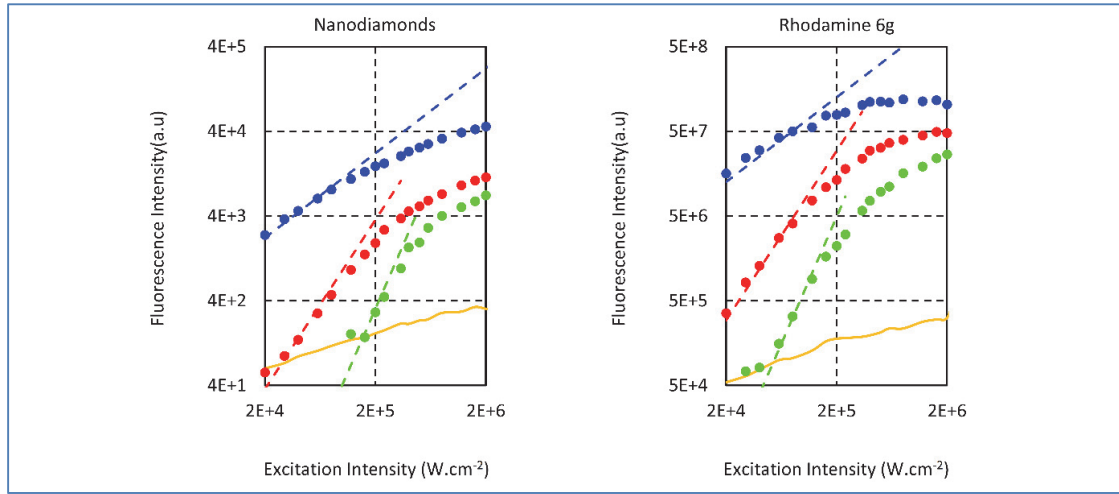


Figure 5-24 Experimentally measured relationship between demodulated fluorescence signal intensity and excitation intensity for two types of dye (fluorescent nanodiamonds with NV centers and Rhodamine 6G). The blue points correspond to the fluorescence signal with demodulation at the fundamental frequency. The red dots to the second harmonic and the green ones to the third. The dashed lines show the gradients of slopes at the beginning of the curve are respectively 1, 2 and 3 (in logarithmic scale), illustrating the nonlinear fluorescence response that results in a gain in resolution. The noise level is taken as the average of the signal in all the frequencies but the harmonics and represented by the yellow curve. Its slope of 0.5 is characteristic of Poisson noise (shot noise).

We have demonstrated that saturated excitation in MMF scanning fluorescence microscopy can lead to resolution increase in all three dimensions. We measured an improvement in resolution by a factor of 1.6, which is close to the theoretical factor of resolution gain of 1.73. The available improvement in resolution can in principle be improved indefinitely by using higher harmonics of the modulation frequency, but the improvement is practically restricted by the available signal to noise ratio. We discuss here what would be needed to improve further the resolution, i.e. to use higher demodulation frequencies.

We present in Figure 5-24 the experimental measurement of the nonlinear response of a single 120 nm nanodiamond containing about 1000 nitrogen vacancies. As presented on the theoretical curve (Figure 5-14), the intensity of the n^{th} harmonic demodulation harmonic increases in proportion with the excitation intensity to the power n (dashed lines in Figure 5-24). The noise floor is measured as the average value over all the frequencies apart from the modulation frequencies and its harmonics. The slope of the noise signal (yellow curve in Figure 5-24), is proportional to the square root of the excitation intensity. This indicates that shot noise from the detector was the main source of noise during nonlinear fluorescence signals demodulation extraction. In traditional fluorescent sample, the photobleaching is the absolute limitation on the available resolution. The modulation frequency and the dwell time must then be optimized to provide sufficient fluorescence saturation without strong photobleaching [185]. However, the case of nonbleaching nanodiamonds greatly simplifies the discussion. Since NDs do not bleach, they give potentially an infinite number of photon. As the demodulated signal increases proportionally to the number of photon faster than the shot noise limit, after a long enough integration time the high order signals can in theory be recorded. In other words by increasing the integration time it pushes back the limit of detection. This is illustrated in Figure 5-25. By increasing the acquisition time to 200 ms (and the excitation intensity) the 4th harmonic can be detected.

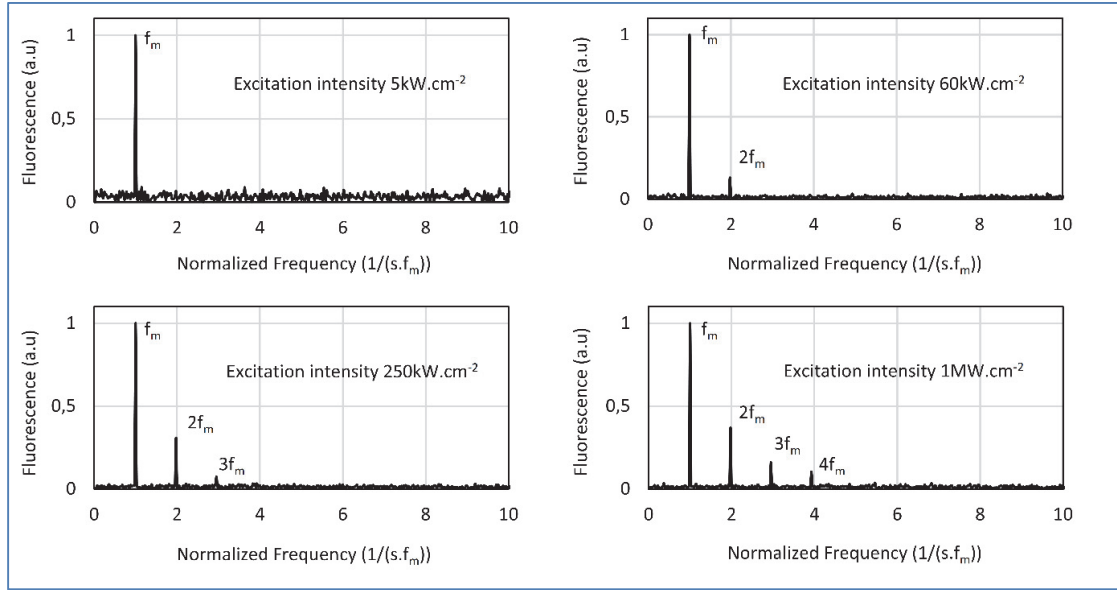


Figure 5-25 Detection of high saturation demodulated orders. Fourier transform of the fluorescence response of a single nanodiamond to a modulated excitation for different maximal excitation intensities. With a long collection time (200ms), the available SNR allows for the detection of the fourth harmonic. (For this characterization measurement, the excitation focus was not obtained with phase conjugation spot, the teaching beam focused with a 0.4NA objective was used to excite the fluorescence.)

However, even if it is in theory possible to improve further the resolution by increasing the integration time on each pixel, the practical interest is limited since it increases dramatically the imaging time. Moreover, the excitation intensity level of signal used to detect the 4th harmonic combined with long immobilization during the acquisition on each pixel comes along with the question of thermal damage in the case of biological sample.

We also demonstrated that besides the resolution improvement, the advantage of saturated excitation imaging method is the ability to remove out of focus light. However, this property suffers from its inability to physically reject out-of-focus light before it reaches the detector. As opposed to two-photon absorption, saturated excitation creates fluorescence signal throughout the entire thickness. Then, as opposed to confocal, the out of focus light rejection is obtained by isolating digitally the signal of interest (i.e. by demodulation of the harmonics generated by the saturation). Thus, in the presence of out of focus light, the level of the high harmonics compared to the fundamental frequency signal is reduced. The stronger the out of focus signal is, the more severe the SNR conditions are for extracting the harmonics signals. The same discussion as in the previous paragraph can apply, whatever is the background signal strength it is in theory possible to recover the demodulated harmonics by increasing the dwell time. However, with a reasonable dwell time of 20 ms the available SNR allowed for background rejection only with the second harmonic in the result section.

5.4 Conclusion

By combining nonlinear sample photoresponse and digital phase conjugation, we created a fiber based endoscope capable of very high lateral resolution. We used saturated excitation, as in CNS microscopy, but with time modulated illumination and harmonic demodulation of the photoresponse. With this purely time-domain implementation, we were able to convert MMF based endoscopes to SAX usage without major modification.

With this method we have demonstrated and improvement in resolution in both the lateral and the axial direction. We reached a lateral resolution of 0.5 μm , which is to our knowledge the best performance for a lensless fiber based endoscope without custom designed fibers. The improved resolution, compatible with any type of fluorophore, highly enhances the imaging possibilities of MMF fiber based endoscopes.

Moreover, in this chapter, we have demonstrated optical sectioning in MMF endoscopic imaging in SAX mode. We have shown that the theoretical sectioning and resolution performance is superior to two photon and confocal imaging (for a practical pinhole size). Dramatic improvement of the image contrast in thick samples has been demonstrated with the SAX mode. Despite this theoretical advantage and the use of CW laser, current development of a commercial version of the MMF endoscope is focused on two photon

excitation. Indeed, as SAX microscopy performance is bound to the available SNR, it makes its application clearly dependent on the specificity of the sample, especially the quantity of the out of focus signal.

In those experiments we have used nonbleaching nanodiamond probes. Even if we believe that nanocrystals have a promising future as biolabels, fluorescent antibodies with organic dyes remain the most popular probes. Consequently, it is a legitimate question to ask whether our method could be used with conventional staining subject to bleaching. With SAX microscope systems, high excitation intensity has been shown to be compatible with the imaging of various biological samples [184,186]. However, the maximum NA of the available MMF on the market is around 0.5. It means that the collection efficiency, which scales as NA^2 , is about one order of magnitude lower in a MMF compared with the microscope systems (implying lower SNR). For endoscopic imaging with conventional labeling it is a reasonable hope to be able to extract one harmonic below what has been demonstrated in the SAX microscopy literature. Thus, we can estimate that SAX MMF endoscopic imaging with organic staining is realistic only using second harmonic demodulation.

In the work we presented here, we have bypassed two obstacles by moving the sample: the power variation of the scanning spot among the fiber surface and the limited scanning speed. The phase conjugation has been shown to be stable over time [163]. Therefore, in a real endoscope based on phase conjugation through a MMF, it should be possible to compensate for the power variation for each scanning position. As for the scanning speed, it is limited by the phase modulating element. To achieve millisecond dwell time, typical in scanning microscopy, digital micro-mirror device can be used instead of a SLM. However, the binary phase encoding results in lower enhancement of the phase conjugated focus and different solutions are currently explored in our lab. The other limitation that must be mentioned is that the speckle pattern depends on the geometrical configuration of the fiber. Thus, each time the fiber is moved a new calibration must be acquired, requiring a rigid guide such as a needle or a dynamic bending compensation mechanism [187].

In conclusion, we suggest a non-linear imaging configuration for MMF fiber endoscopy with saturated modulated excitation and harmonic demodulation. We have demonstrated that this system provides a 1.6 times improvement in resolution and allows for the rejection of out-of-focus of light in the limit of a sufficient SNR.

Chapter 6 Conclusion

6.1 Achieved results

In this thesis we used nanodiamonds crystals to demonstrate various methods to improve the resolution of scanning microscopy.

We identified NVN defects as a potential luminescence source for STED microscopy with a novel emission color (compared with the widely reviewed NV centers). We studied the luminescent properties of NVN color centers in diamond and found that their long lifetime and high photostability lead to efficient and repeatable fluorescence quenching by stimulated emission. We demonstrated superresolved imaging with 70 nm resolution (the size of the particle) using a continuous STED microscope with 590 nm depletion. Considering that the measured depletion characteristics were nearly equivalent to the value reported for the NV defect, we expect that those particles could be used for very high resolution with a high peak intensity pulsed STED setup. We investigated the use of green nanodiamonds for cellular labelling. Here we obtained mixed results. On one hand, green NDs are very promising as bio-labels. Indeed, we did not characterize the phototoxicity rigorously but visual observations seem to indicate that they are not toxic for in vitro experiments (in good agreement with previous report, on a time scale of few hours). They are also perfectly photostable, even under high power depletion beam illumination which is the major advantage compared with traditional fluorescent labels. On the other hand, the long life time and the limited number of defects result in a limited brightness. It is not a problem with well controlled environments with no surrounding autofluorescence however in a cell medium the brightness clearly limits the available SNR and the image quality. Several studies have been published about the increase of the density of NV vacancies in nanodiamonds. For green NDs to become a widely used marker in the future, similar work should succeed in improving (during the GNDs synthesis) the conversion of the available vacancies and nitrogen atoms into NVN color centers.

After identifying nanodiamonds as the ideal fluorescent label for superresolution, we associated existing methods to create a novel superresolution technique with useful properties. Indeed, by combining STED lateral resolution improvement and DH axial localization used in 3D PALM, we have demonstrated isotropic three dimensional imaging of nanodiamonds with a localization of 20 nm in all three dimensions. Since the method does not reduce the axial resolution, it does not compete with 3D superresolution for the imaging of very dense 3D samples. However, for the frequent case of a laterally dense and axially sparse sample, like fluorophores immobilized on a rough surface or a protein cluster on a well-defined interface, DH-STED is more efficient than the existing techniques. Indeed, DH-STED three dimensional images have been obtained after a single lateral scan acquisition. However, the acquisition speed of the method remains limited by the camera sensor frame rate, so the significance of the technique relies on advances in sensor arrays (especially CMOS and APD array) and on the possibility of large parallelization. In our home built setup we demonstrated three dimensional imaging of nanodiamonds and of fluorescent beads filled with organic dye.

After taking advantage of camera detection in scanning microscopy to improve the image in the axial dimension, we investigated its potential for lateral improvement. Several publications had already shown that the resolution of a scanning microscope can be enhanced with a pixelated detector. We built a scanning microscope equipped with a camera detector capable of recording a complete dataset with a 2D image for each scanning position. Thanks to this implementation, we reproduced all the published point scanning SIM methods with digital post treatment. We have shown theoretically and demonstrated experimentally that all the proposed methods result in the same resolution enhancement. For the same reason that SIM allows only for doubling the resolution, those methods are fundamentally limited to a resolution enhancement of a factor of 2. We have demonstrated that as for SIM this limit can be overcome by the use of fluorescence absorption saturation. Saturation was an intelligent way to exploit the lack of photobleaching of NDs since it requires no modification other than increasing the laser intensity. We found that the unique combination of digital and temporal modulation allow the enhancement of the resolution above a factor 2 and we demonstrated gain in resolution by a factor of 2.6. We also found that the shape (and the corresponding spectrum) of the excitation focus results in degradation of the SNR of high frequencies which prevents the extraction of high spatial frequencies that would lead to further resolution enhancement. In order to reach better resolution as demonstrated with saturated SIM different excitation patterns with higher transfer function were investigated. In that perspective we proposed the use of Bessel beam and Hexagonal pattern, however as the generation of those patterns would not be possible on standard microscope the advantage of the method compared with SIM was then less obvious.

To resolve fluorescent structures deep into a material we applied a superresolution microscopy principle to MMF fiber endoscopic imaging. MMFs transmit the information in a nearly optimal way, so those endoscopes are as thin as possible (and so as minimally invasive as it can be). As for free space microscopy, MMF imaging resolution is limited by diffraction and a nonlinear fluorescence photoresponse has been used to enhance the resolution. As for CNS microscopy, we used fluorescence saturation. Harnessing the principle of SAX microscopy to endoscopic imaging through MMF by phase conjugation, we have demonstrated minimally invasive imaging with 0.5 μ m resolution. We also demonstrated the optical sectioning effect as another benefit of SAX imaging through multimode fiber. It allowed us to improve significantly the contrast when imaging a sample composed of several layers of nanodiamonds. However, SAX rejects out-of-focus light in the digital domain, so the application of this method is bound to the available SNR i.e. to the level of out-of-focus signal to eliminate.

6.2 Future developments

The next step with the microscopy methods presented in this thesis would be to test them with biological samples. We discuss here briefly the future developments it implies.

Despite its implementation simplicity, CNS microscopy is not competitive in term of resolution performance. As we described, modifications of the excitation pattern could lead to resolution enhancement, but at the cost of worsening its advantage compared with SIM. Many studies have been published both with nonlinear SIM for high resolution and parallelized linear point scanning SIM for fast and high SNR imaging. We are not convinced there is enough room between those techniques for significant improvement and we do not plan future investigation on the subject.

Dual color STED imaging of nanodiamonds still needs to be demonstrated. Building a two color STED microscope with two depletion lasers is an important investment, however we will soon have the opportunity of testing a Leica prototype with 590 nm and 775 nm depletion lines. We have acquired dual color diamonds containing the two types of defect (green and red), we want to investigate whether two types of vacancy can be resolved into a nanocrystals. Then, we could envisage a long term superresolution colocalization study with red and green FNDs. However, red FNDs are now commercially available with bio-functionalized surface but not green FNDs, so for the moment it would require modification of the surface chemistry by ourselves.

DH-STED could be used for example for cell membrane topography, but the frame rate must be accelerated. We recently acquired a scientific C-MOS camera (Andor Neo 5.5) with low noise and fast acquisition rate and which makes such an experience feasible.

Our current research concerns the MMF. As we pointed out, the optical sectioning provided by SAX microscopy is limited by the SNR, therefore two photon absorption is used today. However, two photon is not the ideal solution, chromatic dispersion of femto-second pulses implies using short fibers or fiber bundle and limits the resolution. We are now working on the adaptation of another microscopy technique to obtain sectioning with CW laser illumination. Indeed, it has been shown that large imaging depth and sectioning can be obtained with linear temporal modulation [188] and is compatible with SAX microscopy [189].

References

1. S. I. Hajdu, "The First Use of the Microscope in Medicine," *Ann. Clin. Lab. Sci.* **32**, 309–310 (2002).
2. S. A. Harris, "The Paper Museum of Cassiano dal Pozzo. Series B: Natural History. Fungi," *J. Hist. Collect.* **18**, 287–288 (2006).
3. Chisholm, Hugh, "Petrology," *Encycl. Br.* **21**, 323–333. (1911).
4. G. T. Shubeita, S. K. Sekatskii, G. Dietler, I. Potapova, A. Mews, and T. Basché, "Scanning near-field optical microscopy using semiconductor nanocrystals as a local fluorescence and fluorescence resonance energy transfer source," *J. Microsc.* **210**, 274–278 (2003).
5. Y. Takaku, H. Suzuki, I. Ohta, D. Ishii, Y. Muranaka, M. Shimomura, and T. Hariyama, "A thin polymer membrane, nano-suit, enhancing survival across the continuum between air and high vacuum," *Proc. Natl. Acad. Sci.* **110**, 7631–7635 (2013).
6. T. A. Klar and S. W. Hell, "Subdiffraction resolution in far-field fluorescence microscopy," *Opt. Lett.* **24**, 954 (1999).
7. M. G. L. Gustafsson, "Surpassing the lateral resolution limit by a factor of two using structured illumination microscopy," *J. Microsc.* **198**, 82–87 (2000).
8. E. Betzig, G. H. Patterson, R. Sougrat, O. W. Lindwasser, S. Olenych, J. S. Bonifacino, M. W. Davidson, J. Lippincott-Schwartz, and H. F. Hess, "Imaging intracellular fluorescent proteins at nanometer resolution," *Science* **313**, 1642–1645 (2006).
9. B. Huang, W. Wang, M. Bates, and X. Zhuang, "Three-Dimensional Super-Resolution Imaging by Stochastic Optical Reconstruction Microscopy," *Science* **319**, 810–813 (2008).
10. J. Requejo-Isidro, "Fluorescence nanoscopy. Methods and applications," *J. Chem. Biol.* **6**, 97–120 (2013).
11. C. Eggeling, K. I. Willig, and F. J. Barrantes, "STED microscopy of living cells – new frontiers in membrane and neurobiology," *J. Neurochem.* **126**, 203–212 (2013).
12. T. A. Klar, R. Wollhofen, and J. Jacak, "Sub-Abbe resolution: from STED microscopy to STED lithography," *Phys. Scr.* **2014**, 014049 (2014).
13. M. G. L. Gustafsson, L. Shao, P. M. Carlton, C. J. R. Wang, I. N. Golubovskaya, W. Z. Cande, D. A. Agard, and J. W. Sedat, "Three-Dimensional Resolution Doubling in Wide-Field Fluorescence Microscopy by Structured Illumination," *Biophys. J.* **94**, 4957–4970 (2008).
14. B. Huang, W. Wang, M. Bates, and X. Zhuang, "Three-dimensional super-resolution imaging by stochastic optical reconstruction microscopy," *Science* **319**, 810–813 (2008).
15. K. Y. Han, K. I. Willig, E. Rittweger, F. Jelezko, C. Eggeling, and S. W. Hell, "Three-Dimensional Stimulated Emission Depletion Microscopy of Nitrogen-Vacancy Centers in Diamond Using Continuous-Wave Light," *Nano Lett.* **9**, 3323–3329 (2009).
16. J. Schneider, J. Zahn, M. Maglione, S. J. Sigrist, J. Marquard, J. Chojnacki, H.-G. Kräusslich, S. J. Sahl, J. Engelhardt, and S. W. Hell, "Ultrafast, temporally stochastic STED nanoscopy of millisecond dynamics," *Nat. Methods* **12**, 827–830 (2015).
17. F. Bergermann, L. Alber, S. J. Sahl, J. Engelhardt, and S. W. Hell, "2000-fold parallelized dual-color STED fluorescence nanoscopy," *Opt. Express* **23**, 211 (2015).
18. B. Yang, F. Przybilla, M. Mestre, J.-B. Trebbia, and B. Lounis, "Large parallelization of STED nanoscopy using optical lattices," *Opt. Express* **22**, 5581 (2014).
19. A. G. York, S. H. Parekh, D. D. Nogare, R. S. Fischer, K. Temprine, M. Mione, A. B. Chitnis, C. A. Combs, and H. Shroff, "Resolution doubling in live, multicellular organisms via multifocal structured illumination microscopy," *Nat. Methods* **9**, 749–754 (2012).
20. O. Schulz, C. Pieper, M. Clever, J. Pfaff, A. Ruhlandt, R. H. Kehlenbach, F. S. Wouters, J. Großhans, G. Bunt, and J. Enderlein, "Resolution doubling in fluorescence microscopy with confocal spinning-disk image scanning microscopy," *Proc. Natl. Acad. Sci.* **110**, 21000–21005 (2013).
21. T. A. Planchon, L. Gao, D. E. Milkie, M. W. Davidson, J. A. Galbraith, C. G. Galbraith, and E. Betzig, "Rapid three-dimensional isotropic imaging of living cells using Bessel beam plane illumination," *Nat. Methods* **8**, 417–423 (2011).
22. M. Ingaramo, A. G. York, P. Wawrzusin, O. Milberg, A. Hong, R. Weigert, H. Shroff, and G. H. Patterson, "Two-photon excitation improves multifocal structured illumination microscopy in thick scattering tissue," *Proc. Natl. Acad. Sci. U. S. A.* **111**, 5254–5259 (2014).
23. T. J. Gould, D. Burke, J. Bewersdorf, and M. J. Booth, "Adaptive optics enables 3D STED microscopy in aberrating specimens," *Opt. Express* **20**, 20998–21009 (2012).
24. X. Hao, C. Kuang, Z. Gu, Y. Wang, S. Li, Y. Ku, Y. Li, J. Ge, and X. Liu, "From microscopy to nanoscopy via visible light," *Light Sci. Appl.* **2**, e108 (2013).
25. S.-J. Yu, M.-W. Kang, H.-C. Chang, K.-M. Chen, and Y.-C. Yu, "Bright Fluorescent Nanodiamonds: No Photobleaching and Low Cytotoxicity," *J. Am. Chem. Soc.* **127**, 17604–17605 (2005).
26. E. Rittweger, K. Y. Han, S. E. Irvine, C. Eggeling, and S. W. Hell, "STED microscopy reveals crystal colour centres with nanometric resolution," *Nat. Photonics* **3**, 144–147 (2009).
27. S. R. P. Pavani, M. A. Thompson, J. S. Biteen, S. J. Lord, N. Liu, R. J. Twieg, R. Piestun, and W. E. Moerner, "Three-dimensional, single-molecule fluorescence imaging beyond the diffraction limit by using a double-helix point spread function," *Proc. Natl. Acad. Sci.* **106**, 2995–2999 (2009).
28. M. G. Gustafsson, "Nonlinear structured-illumination microscopy: wide-field fluorescence imaging with theoretically unlimited resolution," *Proc. Natl. Acad. Sci. U. S. A.* **102**, 13081–13086 (2005).
29. C. J. R. Sheppard, S. B. Mehta, and R. Heintzmann, "Superresolution by image scanning microscopy using pixel reassignment," *Opt. Lett.* **38**, 2889 (2013).
30. C. J. R. Sheppard, "SUPER-RESOLUTION IN CONFOCAL IMAGING," *Optik* **80**, 53–54 (1988).

31. C. B. Müller and J. Enderlein, "Image Scanning Microscopy," *Phys. Rev. Lett.* **104**, 198101 (2010).
32. J. Lu, W. Min, J.-A. Conchello, X. S. Xie, and J. W. Lichtman, "Super-resolution laser scanning microscopy through spatiotemporal modulation," *Nano Lett.* **9**, 3883–3889 (2009).
33. X. Yang, Y. Pu, and D. Psaltis, "Imaging blood cells through scattering biological tissue using speckle scanning microscopy," *Opt. Express* **22**, 3405 (2014).
34. J. Bertolotti, E. G. van Putten, C. Blum, A. Lagendijk, W. L. Vos, and A. P. Mosk, "Non-invasive imaging through opaque scattering layers," *Nature* **491**, 232–234 (2012).
35. I. N. Papadopoulos, S. Farahi, C. Moser, and D. Psaltis, "High-resolution, lensless endoscope based on digital scanning through a multimode optical fiber," *Biomed. Opt. Express* **4**, 260 (2013).
36. Y. Shih, "Quantum Imaging," *IEEE J. Sel. Top. Quantum Electron.* **13**, 1016–1030 (2007).
37. H. Wang, S. Han, and M. I. Kolobov, "Quantum limits of super-resolution of optical sparse objects via sparsity constraint," *Opt. Express* **20**, 23235 (2012).
38. Y. Sonnefraud, H. G. Sinclair, Y. Sivan, M. R. Foreman, C. W. Dunsby, M. A. A. Neil, P. M. French, and S. A. Maier, "Experimental Proof of Concept of Nanoparticle-Assisted STED," *Nano Lett.* **14**, 4449–4453 (2014).
39. F. Wei, D. Lu, H. Shen, W. Wan, J. L. Ponsetto, E. Huang, and Z. Liu, "Wide Field Super-Resolution Surface Imaging through Plasmonic Structured Illumination Microscopy," *Nano Lett.* **14**, 4634–4639 (2014).
40. Z. Liu, S. Durant, H. Lee, Y. Pikus, N. Fang, Y. Xiong, C. Sun, and X. Zhang, "Far-Field Optical Superlens," *Nano Lett.* **7**, 403–408 (2007).
41. M. Born and E. Wolf, *Principles of Optics, 7th (expanded) Ed* (Cambridge U. Press, 1999).
42. "Wiley: Fundamentals of Photonics, 2nd Edition - Bahaa E. A. Saleh, Malvin Carl Teich," <http://eu.wiley.com/WileyCDA/WileyTitle/productCd-0471358320.html>.
43. A. Diaspro, *Confocal and Two-Photon Microscopy: Foundations, Applications and Advances* (Wiley, 2001).
44. E. Rittweger, D. Wildanger, and S. W. Hell, "Far-field fluorescence nanoscopy of diamond color centers by ground state depletion," *EPL Europhys. Lett.* **86**, 14001 (2009).
45. C.J.R. Sheppard, "Super-resolution in confocal imaging," *Opt. - Int. J. Light Electron Opt.* **80**, 53 (1988).
46. T. Wilson, "Confocal microscopy," *Acad. Press Lond. Etc* **426**, 1–64 (1990).
47. S. J. Hewlett and T. Wilson, "Resolution enhancement in three-dimensional confocal microscopy," *Mach. Vis. Appl.* **4**, 233–242 (1991).
48. E. Sánchez-Ortiga, C. J. R. Sheppard, G. Saavedra, M. Martínez-Corral, A. Doblas, and A. Calatayud, "Subtractive imaging in confocal scanning microscopy using a CCD camera as a detector," *Opt. Lett.* **37**, 1280 (2012).
49. Y. Cotte, F. Toy, P. Jourdain, N. Pavillon, D. Boss, P. Magistretti, P. Marquet, and C. Depeursinge, "Marker-free phase nanoscopy," *Nat. Photonics* **7**, 113–117 (2013).
50. K. Y. Han, S. K. Kim, C. Eggeling, and S. W. Hell, "Metastable Dark States Enable Ground State Depletion Microscopy of Nitrogen Vacancy Centers in Diamond with Diffraction-Unlimited Resolution," *Nano Lett.* **10**, 3199–3203 (2010).
51. S.-W. Chu, T.-Y. Su, R. Oketani, Y.-T. Huang, H.-Y. Wu, Y. Yonemaru, M. Yamanaka, H. Lee, G.-Y. Zhuo, M.-Y. Lee, S. Kawata, and K. Fujita, "Measurement of a Saturated Emission of Optical Radiation from Gold Nanoparticles: Application to an Ultra-high Resolution Microscope," *Phys. Rev. Lett.* **112**, 017402 (2014).
52. H. Lee, R. Oketani, Y.-T. Huang, K.-Y. Li, Y. Yonemaru, M. Yamanaka, S. Kawata, K. Fujita, and S.-W. Chu, "Point spread function analysis with saturable and reverse saturable scattering," *Opt. Express* **22**, 26016 (2014).
53. K. Y. Han, K. I. Willig, E. Rittweger, F. Jelezko, C. Eggeling, and S. W. Hell, "Three-Dimensional Stimulated Emission Depletion Microscopy of Nitrogen-Vacancy Centers in Diamond Using Continuous-Wave Light," *Nano Lett.* **9**, 3323–3329 (2009).
54. E. H. Rego, L. Shao, J. J. Macklin, L. Winoto, G. A. Johansson, N. Kamps-Hughes, M. W. Davidson, and M. G. Gustafsson, "Nonlinear structured-illumination microscopy with a photoswitchable protein reveals cellular structures at 50-nm resolution," *Proc. Natl. Acad. Sci.* **109**, E135–E143 (2012).
55. R. Heintzmann and M. G. L. Gustafsson, "Subdiffraction resolution in continuous samples," *Nat. Photonics* **3**, 362–364 (2009).
56. A. S. Trifonov, J.-C. Jaskula, C. Teulon, D. R. Glenn, N. Bar-Gill, and R. L. Walsworth, "Chapter 5 - Limits to Resolution of CW STED Microscopy," in *Advances In Atomic, Molecular, and Optical Physics*, P. R. B. and C. C. L. Ennio Arimondo, ed., *Advances in Atomic, Molecular, and Optical Physics* (Academic Press, 2013), Vol. 62, pp. 279–302.
57. B. Harke, J. Keller, C. K. Ullal, V. Westphal, A. Schönle, and S. W. Hell, "Resolution scaling in STED microscopy," *Opt. Express* **16**, 4154 (2008).
58. M. Leutenegger, C. Eggeling, and S. W. Hell, "Analytical description of STED microscopy performance," *Opt. Express* **18**, 26417 (2010).
59. J. R. Lakowicz, ed., *Principles of Fluorescence Spectroscopy* (Springer US, 2006).
60. G. Donnert, C. Eggeling, and S. W. Hell, "Major signal increase in fluorescence microscopy through dark-state relaxation," *Nat. Methods* **4**, 81–86 (2007).
61. R. T. Borlinghaus, "MRT letter: High speed scanning has the potential to increase fluorescence yield and to reduce photobleaching," *Microsc. Res. Tech.* **69**, 689–692 (2006).
62. A. Giske, "CryoSTED microscopy - a new spectroscopic approach for improving the resolution of STED microscopy using low temperature," <http://archiv.ub.uni-heidelberg.de/volltextserver/7969/>.
63. A. Beveratos, R. Brouri, T. Gacoin, A. Villing, J.-P. Poizat, and P. Grangier, "Single Photon Quantum Cryptography," *Phys. Rev. Lett.* **89**, 187901 (2002).

64. O. Faklaris, D. Garrot, V. Joshi, F. Druon, J.-P. Boudou, T. Sauvage, P. Georges, P. A. Curmi, and F. Treussart, "Detection of Single Photoluminescent Diamond Nanoparticles in Cells and Study of the Internalization Pathway," *Small* **4**, 2236–2239 (2008).
65. B.-M. Chang, H.-H. Lin, L.-J. Su, W.-D. Lin, R.-J. Lin, Y.-K. Tzeng, R. T. Lee, Y. C. Lee, A. L. Yu, and H.-C. Chang, "Highly Fluorescent Nanodiamonds Protein-Functionalized for Cell Labeling and Targeting," *Adv. Funct. Mater.* **23**, 5737–5745 (2013).
66. I. I. Vlasov, A. A. Shiryaev, T. Rendler, S. Steinert, S.-Y. Lee, D. Antonov, M. Vörös, F. Jelezko, A. V. Fisenko, L. F. Semjonova, J. Biskupek, U. Kaiser, O. I. Lebedev, I. Sildos, P. R. Hemmer, V. I. Konov, A. Gali, and J. Wrachtrup, "Molecular-sized fluorescent nanodiamonds," *Nat. Nanotechnol.* **9**, 54–58 (2014).
67. I. Rehor, J. Slegelova, J. Kucka, V. Proks, V. Petrakova, M.-P. Adam, F. Treussart, S. Turner, S. Bals, P. Sacha, M. Ledvina, A. M. Wen, N. F. Steinmetz, and P. Cigler, "Fluorescent Nanodiamonds Embedded in Biocompatible Translucent Shells," *Small* **10**, 1106–1115 (2014).
68. J. Havlik, V. Petrakova, I. Rehor, V. Petrak, M. Gulka, J. Stursa, J. Kucka, J. Ralis, T. Rendler, S.-Y. Lee, R. Reuter, J. Wrachtrup, M. Ledvina, M. Nesladek, and P. Cigler, "Boosting nanodiamond fluorescence: towards development of brighter probes," *Nanoscale* **5**, 3208 (2013).
69. J.-H. Hsu, W.-D. Su, K.-L. Yang, Y.-K. Tzeng, and H.-C. Chang, "Nonblinking green emission from single H3 color centers in nanodiamonds," *Appl. Phys. Lett.* **98**, 193116 (2011).
70. T. A. Klar and S. W. Hell, "Subdiffraction resolution in far-field fluorescence microscopy," *Opt. Lett.* **24**, 954 (1999).
71. X. Hao, C. Kuang, T. Wang, and X. Liu, "Effects of polarization on the de-excitation dark focal spot in STED microscopy," *J. Opt.* **12**, 115707 (2010).
72. S. Deng, L. Liu, Y. Cheng, R. Li, and Z. Xu, "Effects of primary aberrations on the fluorescence depletion patterns of STED microscopy," *Opt. Express* **18**, 1657 (2010).
73. M. Leutenegger, C. Ringemann, T. Lasser, S. W. Hell, and C. Eggeling, "Fluorescence correlation spectroscopy with a total internal reflection fluorescence STED microscope (TIRF-STED-FCS)," *Opt. Express* **20**, 5243 (2012).
74. P. Dedeker, B. Muls, J. Hofkens, J. Enderlein, and J. Hotta, "Orientational effects in the excitation and de-excitation of single molecules interacting with donut-mode laser beams," *Opt. Express* **15**, 3372 (2007).
75. S. Arroyo-Camejo, M.-P. Adam, M. Besbes, J.-P. Hugonin, V. Jacques, J.-J. Greffet, J.-F. Roch, S. W. Hell, and F. Treussart, "Stimulated Emission Depletion Microscopy Resolves Individual Nitrogen Vacancy Centers in Diamond Nanocrystals," *ACS Nano* **7**, 10912–10919 (2013).
76. S. Galiani, B. Harke, G. Vicidomini, G. Lignani, F. Benfenati, A. Diaspro, and P. Bianchini, "Strategies to maximize the performance of a STED microscope," *Opt. Express* **20**, 7362 (2012).
77. A. M. Zaitsev, "Vibronic spectra of impurity-related optical centers in diamond," *Phys. Rev. B* **61**, 12909–12922 (2000).
78. Y. Kuo, T.-Y. Hsu, Y.-C. Wu, and H.-C. Chang, "Fluorescent nanodiamond as a probe for the intercellular transport of proteins in vivo," *Biomaterials* **34**, 8352–8360 (2013).
79. T.-J. Wu, Y.-K. Tzeng, W.-W. Chang, C.-A. Cheng, Y. Kuo, C.-H. Chien, H.-C. Chang, and J. Yu, "Tracking the engraftment and regenerative capabilities of transplanted lung stem cells using fluorescent nanodiamonds," *Nat. Nanotechnol.* **8**, 682–689 (2013).
80. T.-C. Hsu, K.-K. Liu, H.-C. Chang, E. Hwang, and J.-I. Chao, "Labeling of neuronal differentiation and neuron cells with biocompatible fluorescent nanodiamonds," *Sci. Rep.* **4**, (2014).
81. M. Mission, M. F. Rate, and V. M. Model, "Measuring Two Key Parameters of H3 Color Centers in Diamond," *NASA Tech Briefs* 25 (2005).
82. I. Gregor, D. Patra, and J. Enderlein, "Optical Saturation in Fluorescence Correlation Spectroscopy under Continuous-Wave and Pulsed Excitation," *ChemPhysChem* **6**, 164–170 (2005).
83. T.-L. Wee, Y.-W. Mau, C.-Y. Fang, H.-L. Hsu, C.-C. Han, and H.-C. Chang, "Preparation and characterization of green fluorescent nanodiamonds for biological applications," *Diam. Relat. Mater.* **18**, 567–573 (2009).
84. J. Tisler, G. Balasubramanian, B. Naydenov, R. Kolesov, B. Grotz, R. Reuter, J.-P. Boudou, P. A. Curmi, M. Sennour, and A. Thorel, "Fluorescence and spin properties of defects in single digit nanodiamonds," *ACS Nano* **3**, 1959–1965 (2009).
85. Y. Kuo, T.-Y. Hsu, Y.-C. Wu, J.-H. Hsu, and H.-C. Chang, "Fluorescence lifetime imaging microscopy of nanodiamonds in vivo," in *SPIE OPTO* (International Society for Optics and Photonics, 2013), pp. 863503–863503–7.
86. B. R. Smith, D. Gruber, and T. Plakhotnik, "The effects of surface oxidation on luminescence of nano diamonds," *Diam. Relat. Mater.* **19**, 314–318 (2010).
87. S. Rand and L. DeShazer, "Visible color-center laser in diamond," *Opt. Lett.* **10**, 481–483 (1985).
88. E. Rittweger, B. R. Rankin, V. Westphal, and S. W. Hell, "Fluorescence depletion mechanisms in super-resolving STED microscopy," *Chem. Phys. Lett.* **442**, 483–487 (2007).
89. K. I. Willig, B. Harke, R. Medda, and S. W. Hell, "STED microscopy with continuous wave beams," *Nat. Methods* **4**, 915–918 (2007).
90. E. Rittweger, B. Rankin, V. Westphal, and S. Hell, "Fluorescence depletion mechanisms in super-resolving STED microscopy," *Chem. Phys. Lett.* **442**, 483–487 (2007).
91. L.-J. Su, C.-Y. Fang, Y.-T. Chang, K.-M. Chen, Y.-C. Yu, J.-H. Hsu, and H.-C. Chang, "Creation of high density ensembles of nitrogen-vacancy centers in nitrogen-rich type Ib nanodiamonds," *Nanotechnology* **24**, 315702 (2013).
92. Y. Tzeng, O. Faklaris, B. Chang, Y. Kuo, J. Hsu, and H. Chang, "Superresolution Imaging of Albumin-Conjugated Fluorescent Nanodiamonds in Cells by Stimulated Emission Depletion," *Angew. Chem. Int. Ed.* **50**, 2262–2265 (2011).
93. E. Neu, D. Steinmetz, J. Riedrich-Möller, S. Gsell, M. Fischer, M. Schreck, and C. Becher, "Single photon emission from silicon-vacancy colour centres in chemical vapour deposition nano-diamonds on iridium," *New J. Phys.* **13**, 025012 (2011).

94. F. Göttfert, C. A. Wurm, V. Mueller, S. Berning, V. C. Cordes, A. Honigmann, and S. W. Hell, "Coaligned Dual-Channel STED Nanoscopy and Molecular Diffusion Analysis at 20 nm Resolution," *Biophys. J.* **105**, L01–L03 (2013).
95. G. Lukinavičius, L. Reymond, E. D'Este, A. Masharina, F. Göttfert, H. Ta, A. Güther, M. Fournier, S. Rizzo, H. Waldmann, C. Blaukopf, C. Sommer, D. W. Gerlich, H.-D. Arndt, S. W. Hell, and K. Johnsson, "Fluorogenic probes for live-cell imaging of the cytoskeleton," *Nat. Methods* **11**, 731–733 (2014).
96. Y. Sonnefraud, H. G. Sinclair, Y. Sivan, M. R. Foreman, C. W. Dunsby, M. A. A. Neil, P. M. French, and S. A. Maier, "Experimental Proof of Concept of Nanoparticle-Assisted STED," *Nano Lett.* **14**, 4449–4453 (2014).
97. A. Chmyrov, J. Keller, T. Grotjohann, M. Ratz, E. d'Este, S. Jakobs, C. Eggeling, and S. W. Hell, "Nanoscopy with more than 100,000 'doughnuts,'" *Nat. Methods* **10**, 737–740 (2013).
98. T. Grotjohann, I. Testa, M. Leutenegger, H. Bock, N. T. Urban, F. Lavoie-Cardinal, K. I. Willig, C. Eggeling, S. Jakobs, and S. W. Hell, "Diffraction-unlimited all-optical imaging and writing with a photochromic GFP," *Nature* **478**, 204–208 (2011).
99. F. Bergermann, L. Alber, S. J. Sahl, J. Engelhardt, and S. W. Hell, "2000-fold parallelized dual-color STED fluorescence nanoscopy," *Opt. Express* **23**, 211 (2015).
100. B. Yang, F. Przybilla, M. Mestre, J.-B. Trebbia, and B. Lounis, "Large parallelization of STED nanoscopy using optical lattices," *Opt. Express* **22**, 5581 (2014).
101. T. A. Klar, S. Jakobs, M. Dyba, A. Egner, and S. W. Hell, "Fluorescence microscopy with diffraction resolution barrier broken by stimulated emission," *Proc. Natl. Acad. Sci.* **97**, 8206–8210 (2000).
102. K. Y. Han, K. I. Willig, E. Rittweger, F. Jelezko, C. Eggeling, and S. W. Hell, "Three-Dimensional Stimulated Emission Depletion Nanoscopy of Nitrogen-Vacancy Centers in Diamond Using Continuous-Wave Light," *Nano Lett.* **9**, 3323–3329 (2009).
103. C.J.R. Sheppard, "Super-resolution in confocal imaging," *Opt. - Int. J. Light Electron Opt.* **80**, 53 (1988).
104. A. Jesacher, M. Ritsch-Marte, and R. Piestun, "Three-dimensional information from two-dimensional scans: a scanning microscope with postacquisition refocusing capability," *Optica* **2**, 210 (2015).
105. P. W. Winter, A. G. York, D. D. Nogare, M. Ingaramo, R. Christensen, A. Chitnis, G. H. Patterson, and H. Shroff, "Two-photon instant structured illumination microscopy improves the depth penetration of super-resolution imaging in thick scattering samples," *Optica* **1**, 181 (2014).
106. S. Roth, C. J. Sheppard, K. Wicker, and R. Heintzmann, "Optical photon reassignment microscopy (OPRA)," *ArXiv Prepr. ArXiv13066230* (2013).
107. G. M. De Luca, R. M. Breedijk, R. A. Brandt, C. H. Zeelenberg, B. E. de Jong, W. Timmermans, L. N. Azar, R. A. Hoebe, S. Stallinga, and E. M. Manders, "Re-scan confocal microscopy: scanning twice for better resolution," *Biomed. Opt. Express* **4**, 2644–2656 (2013).
108. A. G. York, S. H. Parekh, D. Dalle Nogare, R. S. Fischer, K. Temprine, M. Mione, A. B. Chitnis, C. A. Combs, and H. Shroff, "Resolution doubling in live, multicellular organisms via multifocal structured illumination microscopy," *Nat. Methods* **9**, 749–754 (2012).
109. O. Schulz, C. Pieper, M. Clever, J. Pfaff, A. Ruhlandt, R. H. Kehlenbach, F. S. Wouters, J. Großhans, G. Bunt, and J. Enderlein, "Resolution doubling in fluorescence microscopy with confocal spinning-disk image scanning microscopy," *Proc. Natl. Acad. Sci.* **110**, 21000–21005 (2013).
110. S. R. P. Pavani, A. Greengard, and R. Piestun, "Three-dimensional localization with nanometer accuracy using a detector-limited double-helix point spread function system," *Appl. Phys. Lett.* **95**, 021103 (2009).
111. S. R. P. Pavani, M. A. Thompson, J. S. Biteen, S. J. Lord, N. Liu, R. J. Twieg, R. Piestun, and W. Moerner, "Three-dimensional, single-molecule fluorescence imaging beyond the diffraction limit by using a double-helix point spread function," *Proc. Natl. Acad. Sci.* **106**, 2995–2999 (2009).
112. S. R. P. Pavani and R. Piestun, "Three dimensional tracking of fluorescent microparticles using a photon-limited double-helix response system," *Opt. Express* **16**, 22048–22057 (2008).
113. A. Greengard, Y. Y. Schechner, and R. Piestun, "Depth from diffracted rotation," *Opt. Lett.* **31**, 181 (2006).
114. Y. Y. Schechner, R. Piestun, and J. Shamir, "Wave propagation with rotating intensity distributions," *Phys. Rev. E* **54**, R50–R53 (1996).
115. R. Piestun, Y. Y. Schechner, and J. Shamir, "Propagation-invariant wave fields with finite energy," *J. Opt. Soc. Am. A* **17**, 294 (2000).
116. O. Svelto, *Principles of Lasers* (Springer US, 2010).
117. S.-H. Lee, Y. Roichman, G.-R. Yi, S.-H. Kim, S.-M. Yang, A. van Blaaderen, P. van Oostrum, and D. G. Grier, "Characterizing and tracking single colloidal particles with video holographic microscopy," *Opt. Express* **15**, 18275 (2007).
118. M. Badieirostami, M. D. Lew, M. A. Thompson, and W. E. Moerner, "Three-dimensional localization precision of the double-helix point spread function versus astigmatism and biplane," *Appl. Phys. Lett.* **97**, 161103 (2010).
119. G. Grover, K. DeLuca, S. Quirin, J. DeLuca, and R. Piestun, "Super-resolution photon-efficient imaging by nanometric double-helix point spread function localization of emitters (SPINDLE)," *Opt. Express* **20**, 26681 (2012).
120. S. R. P. Pavani and R. Piestun, "High-efficiency rotating point spread functions," *Opt. Express* **16**, 3484–3489 (2008).
121. G. Grover and R. Piestun, "New approach to double-helix point spread function design for 3D super-resolution microscopy," in J. Enderlein, I. Gregor, Z. K. Gryczynski, R. Erdmann, and F. Koberling, eds. (2013), p. 85900M.
122. G. Grover, S. R. P. Pavani, and R. Piestun, "Performance limits on three-dimensional particle localization in photon-limited microscopy," *Opt. Lett.* **35**, 3306–3308 (2010).
123. P. Zhang, P. M. Goodwin, and J. H. Werner, "Fast, super resolution imaging via Bessel-beam stimulated emission depletion microscopy," *Opt. Express* **22**, 12398 (2014).

124. M. A. Thompson, M. D. Lew, M. Badieirostami, and W. E. Moerner, "Localizing and Tracking Single Nanoscale Emitters in Three Dimensions with High Spatiotemporal Resolution Using a Double-Helix Point Spread Function," *Nano Lett.* **10**, 211–218 (2010).
125. S. T. Hess, T. P. Girirajan, and M. D. Mason, "Ultra-high resolution imaging by fluorescence photoactivation localization microscopy," *Biophys. J.* **91**, 4258–4272 (2006).
126. T. Wilson, *Confocal Microscopy* (Acad. Press, 1990).
127. M. Dyba and S. W. Hell, "Photostability of a Fluorescent Marker Under Pulsed Excited-State Depletion through Stimulated Emission," *Appl. Opt.* **42**, 5123 (2003).
128. G. Donnert, C. Eggeling, and S. W. Hell, "Major signal increase in fluorescence microscopy through dark-state relaxation," *Nat. Methods* **4**, 81–86 (2007).
129. K. I. Willig, B. Harke, R. Medda, and S. W. Hell, "STED microscopy with continuous wave beams," *Nat. Methods* **4**, 915–918 (2007).
130. M. Leutenegger, C. Eggeling, and S. W. Hell, "Analytical description of STED microscopy performance," *Opt. Express* **18**, 26417 (2010).
131. R. T. Borlinghaus, "MRT letter: High speed scanning has the potential to increase fluorescence yield and to reduce photo-bleaching," *Microsc. Res. Tech.* **69**, 689–692 (2006).
132. A. Barsic, G. Grover, and R. Piestun, "Sparse reconstructions of overlapping three-dimensional point spread functions using overcomplete dictionaries," arXiv:1308.6826 (2013).
133. C. Maurer, A. Jesacher, S. Bernet, and M. Ritsch-Marte, "What spatial light modulators can do for optical microscopy," *Laser Photonics Rev.* **5**, 81–101 (2011).
134. M. A. Lauterbach, M. Guillon, A. Soltani, and V. Emiliani, "STED microscope with Spiral Phase Contrast," *Sci. Rep.* **3**, (2013).
135. G. Moneron, R. Medda, B. Hein, A. Giske, V. Westphal, and S. W. Hell, "Fast STED microscopy with continuous wave fiber lasers," *Opt. Express* **18**, 1302–1309 (2010).
136. I. Heller, G. Sitters, O. D. Broekmans, G. Farge, C. Menges, W. Wende, S. W. Hell, E. J. Peterman, and G. J. Wuite, "STED nanoscopy combined with optical tweezers reveals protein dynamics on densely covered DNA," *Nat. Methods* **10**, 910–916 (2013).
137. C. B. Müller and J. Enderlein, "Image scanning microscopy," *Phys. Rev. Lett.* **104**, 198101 (2010).
138. M. G. Gustafsson, "Surpassing the lateral resolution limit by a factor of two using structured illumination microscopy," *J. Microsc.* **198**, 82–87 (2000).
139. C. J. Sheppard, S. B. Mehta, and R. Heintzmann, "Superresolution by image scanning microscopy using pixel reassignment," *Opt. Lett.* **38**, 2889–2892 (2013).
140. R.-W. Lu, B.-Q. Wang, Q.-X. Zhang, and X.-C. Yao, "Super-resolution scanning laser microscopy through virtually structured detection," *Biomed. Opt. Express* **4**, 1673–1682 (2013).
141. C.-H. Yeh and S.-Y. Chen, "Resolution enhancement of two-photon microscopy via intensity-modulated laser scanning structured illumination," *Appl. Opt.* **54**, 2309 (2015).
142. B.-J. Chang, L.-J. Chou, Y.-C. Chang, and S.-Y. Chiang, "Isotropic image in structured illumination microscopy patterned with a spatial light modulator," *Opt. Express* **17**, 14710–14721 (2009).
143. R. Heintzmann and M. G. Gustafsson, "Subdiffraction resolution in continuous samples," *Nat. Photonics* **3**, 362–364 (2009).
144. R. Heintzmann, T. M. Jovin, and C. Cremer, "Saturated patterned excitation microscopy—a concept for optical resolution improvement," *JOSA A* **19**, 1599–1609 (2002).
145. M. Ingaramo, A. G. York, E. Hoogendoorn, M. Postma, H. Shroff, and G. H. Patterson, "Richardson–Lucy Deconvolution as a General Tool for Combining Images with Complementary Strengths," *ChemPhysChem* **15**, 794–800 (2014).
146. M. A. A. Neil, R. Juskaitis, and T. Wilson, "Method of obtaining optical sectioning by using structured light in a conventional microscope," *Opt. Lett.* **22**, 1905 (1997).
147. B. Thomas, M. Momany, and P. Kner, "Optical sectioning structured illumination microscopy with enhanced sensitivity," *J. Opt.* **15**, 094004 (2013).
148. P. W. Winter, A. G. York, D. D. Nogare, M. Ingaramo, R. Christensen, A. Chitnis, G. H. Patterson, and H. Shroff, "Two-photon instant structured illumination microscopy improves the depth penetration of super-resolution imaging in thick scattering samples," *Optica* **1**, 181 (2014).
149. K. A. Lidke, B. Rieger, T. M. Jovin, and R. Heintzmann, "Superresolution by localization of quantum dots using blinking statistics," *Opt. Express* **13**, 7052 (2005).
150. I. M. Vellekoop and A. P. Mosk, "Focusing coherent light through opaque strongly scattering media," *Opt. Lett.* **32**, 2309–2311 (2007).
151. Z. Yaqoob, D. Psaltis, M. S. Feld, and C. Yang, "Optical phase conjugation for turbidity suppression in biological samples," *Nat. Photonics* **2**, 110–115 (2008).
152. S. M. Popoff, G. Leroosey, M. Fink, A. C. Boccara, and S. Gigan, "Controlling light through optical disordered media: transmission matrix approach," *New J. Phys.* **13**, 123021 (2011).
153. X. Xu, H. Liu, and L. V. Wang, "Time-reversed ultrasonically encoded optical focusing into scattering media," *Nat. Photonics* **5**, 154–157 (2011).
154. O. Katz, E. Small, and Y. Silberberg, "Looking around corners and through thin turbid layers in real time with scattered incoherent light," *Nat. Photonics* **6**, 549–553 (2012).
155. K. Si, R. Fiolka, and M. Cui, "Fluorescence imaging beyond the ballistic regime by ultrasound-pulse-guided digital phase conjugation," *Nat. Photonics* **6**, 657–661 (2012).

156. B. Judkewitz, Y. M. Wang, R. Horstmeyer, A. Mathy, and C. Yang, "Speckle-scale focusing in the diffusive regime with time reversal of variance-encoded light (TROVE)," *Nat. Photonics* **7**, 300–305 (2013).
157. S. Kang, S. Jeong, W. Choi, H. Ko, T. D. Yang, J. H. Joo, J.-S. Lee, Y.-S. Lim, Q.-H. Park, and W. Choi, "Imaging deep within a scattering medium using collective accumulation of single-scattered waves," *Nat. Photonics* **9**, 253–258 (2015).
158. T. Čížmár and K. Dholakia, "Exploiting multimode waveguides for pure fibre-based imaging," *Nat. Commun.* **3**, 1027 (2012).
159. S. Bianchi and R. D. Leonardo, "A multi-mode fiber probe for holographic micromanipulation and microscopy," *Lab. Chip* **12**, 635–639 (2012).
160. Y. Choi, C. Yoon, M. Kim, T. D. Yang, C. Fang-Yen, R. R. Dasari, K. J. Lee, and W. Choi, "Scanner-Free and Wide-Field Endoscopic Imaging by Using a Single Multimode Optical Fiber," *Phys. Rev. Lett.* **109**, 203901 (2012).
161. B. A. Flusberg, E. D. Cocker, W. Piyawattanametha, J. C. Jung, E. L. M. Cheung, and M. J. Schnitzer, "Fiber-optic fluorescence imaging," *Nat. Methods* **2**, 941–950 (2005).
162. G. Oh, E. Chung, and S. H. Yun, "Optical fibers for high-resolution in vivo microendoscopic fluorescence imaging," *Opt. Fiber Technol.* **19**, 760–771 (2013).
163. I. Papadopoulos, "Dynamic control of light transmission through multimode fibers," (2014).
164. R. N. Mahalati, R. Y. Gu, and J. M. Kahn, "Resolution limits for imaging through multi-mode fiber," *Opt. Express* **21**, 1656–1668 (2013).
165. I. N. Papadopoulos, S. Farahi, C. Moser, and D. Psaltis, "Increasing the imaging capabilities of multimode fibers by exploiting the properties of highly scattering media," *Opt. Lett.* **38**, 2776 (2013).
166. Y. Choi, C. Yoon, M. Kim, J. Yang, and W. Choi, "Disorder-mediated enhancement of fiber numerical aperture," *Opt. Lett.* **38**, 2253 (2013).
167. S. Bianchi, V. P. Rajamanickam, L. Ferrara, E. Di Fabrizio, C. Liberale, and R. Di Leonardo, "Focusing and imaging with increased numerical apertures through multimode fibers with micro-fabricated optics," *Opt. Lett.* **38**, 4935 (2013).
168. M. T. Myaing, D. J. MacDonald, and X. Li, "Fiber-optic scanning two-photon fluorescence endoscope," *Opt. Lett.* **31**, 1076 (2006).
169. D. R. Rivera, C. M. Brown, D. G. Ouzounov, I. Pavlova, D. Kobat, W. W. Webb, and C. Xu, "Compact and flexible raster scanning multiphoton endoscope capable of imaging unstained tissue," *Proc. Natl. Acad. Sci.* **108**, 17598–17603 (2011).
170. E. E. Morales-Delgado, S. Farahi, I. N. Papadopoulos, D. Psaltis, and C. Moser, "Delivery of focused short pulses through a multimode fiber," *Opt. Express* **23**, 9109 (2015).
171. A. F. Gmitro and D. Aziz, "Confocal microscopy through a fiber-optic imaging bundle," *Opt. Lett.* **18**, 565 (1993).
172. D. Loterie, S. Farahi, I. Papadopoulos, A. Goy, D. Psaltis, and C. Moser, "Digital confocal microscopy through a multimode fiber," *ArXiv150204172 Phys.* (2015).
173. K. Fujita, M. Kobayashi, S. Kawano, M. Yamanaka, and S. Kawata, "High-Resolution Confocal Microscopy by Saturated Excitation of Fluorescence," *Phys. Rev. Lett.* **99**, 228105 (2007).
174. I. N. Papadopoulos, S. Farahi, C. Moser, and D. Psaltis, "Focusing and scanning light through a multimode optical fiber using digital phase conjugation," *Opt. Express* **20**, 10583 (2012).
175. J. W. Goodman, W. H. H. Jr, D. W. Jackson, and M. Lehmann, "WAVEFRONT-RECONSTRUCTION IMAGING THROUGH RANDOM MEDIA," *Appl. Phys. Lett.* **8**, 311–313 (1966).
176. E. N. Leith and J. Upatnieks, "Holographic Imagery Through Diffusing Media," *J. Opt. Soc. Am.* **56**, 523 (1966).
177. H. Kogelnik and K. S. Pennington, "Holographic Imaging Through a Random Medium," *J. Opt. Soc. Am.* **58**, 273 (1968).
178. A. Yariv and D. M. Pepper, "Amplified reflection, phase conjugation, and oscillation in degenerate four-wave mixing," *Opt. Lett.* **1**, 16 (1977).
179. "Wiley: Statistical Optics - Joseph W. Goodman," <http://eu.wiley.com/WileyCDA/WileyTitle/productCd-0471399167.html>.
180. J. Humpolíčková, A. Benda, and J. Enderlein, "Optical Saturation as a Versatile Tool to Enhance Resolution in Confocal Microscopy," *Biophys. J.* **97**, 2623–2629 (2009).
181. M. Yamanaka, Y.-K. Tzeng, S. Kawano, N. I. Smith, S. Kawata, H.-C. Chang, and K. Fujita, "SAX microscopy with fluorescent nanodiamond probes for high-resolution fluorescence imaging," *Biomed. Opt. Express* **2**, 1946–1954 (2011).
182. S. Kawano, N. I. Smith, M. Yamanaka, S. Kawata, and K. Fujita, "Determination of the Expanded Optical Transfer Function in Saturated Excitation Imaging and High Harmonic Demodulation," *Appl. Phys. Express* **4**, 042401 (2011).
183. Y. Y. Hui, B. Zhang, Y.-C. Chang, C.-C. Chang, H.-C. Chang, J.-H. Hsu, K. Chang, and F.-H. Chang, "Two-photon fluorescence correlation spectroscopy of lipid-encapsulated fluorescent nanodiamonds in living cells," *Opt. Express* **18**, 5896 (2010).
184. M. Yamanaka, Y. Yonemaru, S. Kawano, K. Uegaki, N. I. Smith, S. Kawata, and K. Fujita, "Saturated excitation microscopy for sub-diffraction-limited imaging of cell clusters," *J. Biomed. Opt.* **18**, 126002–126002 (2013).
185. Y. Yonemaru, M. Yamanaka, N. I. Smith, S. Kawata, and K. Fujita, "Saturated Excitation Microscopy with Optimized Excitation Modulation," *ChemPhysChem* **15**, 743–749 (2014).
186. M. Yamanaka, S. Kawano, K. Fujita, N. I. Smith, and S. Kawata, "Beyond the diffraction-limit biological imaging by saturated excitation microscopy," *J. Biomed. Opt.* **13**, 050507–050507–3 (2008).
187. S. Farahi, D. Ziegler, I. N. Papadopoulos, D. Psaltis, and C. Moser, "Dynamic bending compensation while focusing through a multimode fiber," *Opt. Express* **21**, 22504 (2013).
188. N. Chen, C.-H. Wong, and C. J. Sheppard, "Focal modulation microscopy," *Opt. Express* **16**, 18764 (2008).
189. W. Gong, K. Si, N. Chen, and C. J. R. Sheppard, "Improved spatial resolution in fluorescence focal modulation microscopy," *Opt. Lett.* **34**, 3508 (2009).
190. M. Müller, *Introduction to Confocal Fluorescence Microscopy, Second Edition* (SPIE, 2005).

191. A. Marian, F. Charrière, T. Colomb, F. Montfort, J. Kühn, P. Marquet, and C. Depeursinge, "On the complex three-dimensional amplitude point spread function of lenses and microscope objectives: theoretical aspects, simulations and measurements by digital holography," *J. Microsc.* **225**, 156–169 (2007).
192. R. Dorn, S. Quabis, and G. Leuchs, "Sharper Focus for a Radially Polarized Light Beam," *Phys. Rev. Lett.* **91**, 233901 (2003).
193. J. Humpolíčková, A. Benda, and J. Enderlein, "Optical Saturation as a Versatile Tool to Enhance Resolution in Confocal Microscopy," *Biophys. J.* **97**, 2623–2629 (2009).
194. I. Gregor, D. Patra, and J. Enderlein, "Optical Saturation in Fluorescence Correlation Spectroscopy under Continuous-Wave and Pulsed Excitation," *ChemPhysChem* **6**, 164–170 (2005).
195. I. Papadopoulos, "Dynamic control of light transmission through multimode fibers," STI (2014).
196. J. M. Senior and M. Y. Jamro, *Optical Fiber Communications: Principles and Practice* (Pearson Education, 2009).
197. D. Marcuse, "Loss Analysis of Single-Mode Fiber Splices," *Bell Syst. Tech. J.* **56**, 703–718 (1977).

Appendix A: Analytical light distribution at the focus of a microscope objective and the validity of the approximations.

We gave in the main text the analytical expression for intensity distribution at the focus of an objective lens [41,190]:

$$I[0, \nu] = \left[\frac{2J_1(\nu)}{\nu} \right]^2 \cdot I_0, \text{ where } \nu \text{ is the optical unit with } \nu = r \frac{2\pi}{\lambda} NA \text{ with } r = \sqrt{x^2 + y^2} \text{ and } NA = \sin \alpha \quad \text{Equation App 1}$$

And its corresponding axial profile expression can also be expressed as:

$$I[u, 0] = \left[\frac{\sin(u/4)}{u/4} \right]^2 \cdot I_0, \text{ where } u \text{ is the optical unit with } u = z \frac{2\pi}{\lambda} \frac{NA^2}{n} \quad \text{Equation App 2}$$

The detailed derivation for those expression is given in Chapter 8 of [41] and it requires several approximations. First, the derivation uses paraxial approximation i.e. assumes ray with small angles to the optical axis i.e. $\sin \alpha \approx \alpha$.

Second, it also uses Debye approximation, which is valid for point close to the optical axis and for Fresnel number much larger than unity ($f \gg a \gg \lambda$ and $\frac{a^2}{\lambda f} \gg 1$, where f is the focal length and a the aperture size.).

The Debye approximation is valid for large angle but not the paraxial approximation. In consequence, the analytical expression Equation App 1 and Equation App 2, has been shown to give very accurate estimation only for NA below 0.7 [191]. Above this value, more accurate method like full scalar theory calculation yield to significantly different PSF size estimation. For instance the lateral PSF FWHM for a high NA=1.3, oil immersion ($n=1.518$) microscope objective is found to be 0.39λ with the classical approximation and 0.34λ with full diffraction theory calculation (Chapter B. [190]).

One more approximation used to derive Equation App 1 and Equation App 2 is that the field amplitude is constant over the aperture which experimentally is never exactly the case. Indeed, laser beams have generally a Gaussian intensity profile.

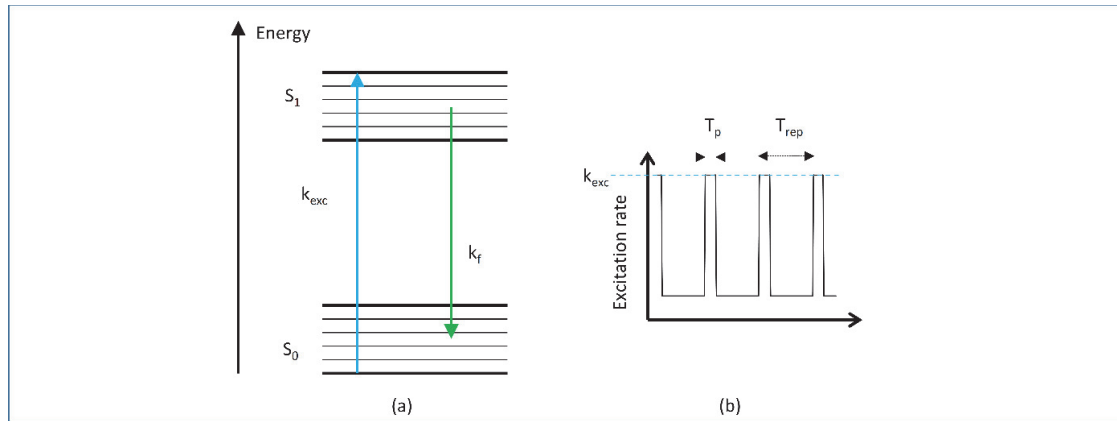
Finally, all those calculations are from scalar diffraction theory, meaning that the effects of polarization are not taken into account. For high NA objectives this has a strong influence on the final focal distribution [191]. For instance, incident linear polarization results in broader orthogonal component and incident radial polarization results in sharper longitudinal focus in high NA objectives [192].

Nevertheless, those basic formula provide first order practical approximations for the resolution of microscopes and are often sufficient for qualitative description. In the thesis, we used high NA objective only for STED microscopy (the consequence of focusing vortex beam with high NA are described in [71] and discussed in the main text section 2.4.3). For the other experiments, this description was in reasonable agreement with our experimental measurements.

Appendix B: Fluorescence saturation under high power excitation.

Fluorescence saturation is used in Chapter 3, Chapter 4 and Chapter 5 in order to enhance the resolution of the imaging system. We derive here in detail the fluorescence response of a typical fluorophore under high excitation for CW and pulsed excitation [193,194].

We consider a two-state model of a fluorescent molecule (Figure_app 1(a)), with a ground state S_0 and an excited state S_1 (we neglect other transitions like the formation of Triplet state). Under laser illumination the molecule absorbs some photons and is promoted from the ground state to the excited state with an excitation rate k_{exc} . It can also relax from the excited state to the ground state by emitting fluorescence. The fluorescence rate is noted k_f (k_f is equal to the inverse of the fluorescence lifetime $k_f = \frac{1}{\tau_f}$).



Figure_app 1 (a) Two level Jablonski diagram with k_{exc} the excitation rate and k_f the fluorescence rate. (b) Simplified model of the train of pulse, we consider a square wave function with T_p the pulse width and T_{rep} the wave period.

Thus, the kinetic of S_0 and S_1 formation can be written:

$$\begin{aligned} \frac{dS_0}{dt} &= -k_{exc}S_0 + k_fS_1 \\ \frac{dS_1}{dt} &= k_{exc}S_0 - k_fS_1 \end{aligned} \quad \text{Equation App 3}$$

Where S_0 and S_1 stand for the probability of finding the molecule in the respective states. We assume the total fluorophores population remains constant and we consider only the transition between the two states, therefore the sum of the both populations is constant and the probability to find the molecule in one of the both state is 1. In consequence, we can write:

$$\frac{dS_0}{dt} = -k_{exc}S_0 + k_f[1 - S_0] \quad \text{Equation App 4}$$

The solution of this differential equation is:

$$S_0(t) = \frac{k_f}{k_f + k_{exc}} \left(1 + \alpha e^{-(k_{exc} + k_f)t} \right) \quad \text{Equation App 5}$$

CW illumination:

Under continuous illumination with intensity I_{exc} , the excitation rate is constant $k_{exc} = \sigma_{abs} I_{exc}$ (where σ_{abs} is the molecule absorption cross section) and the previous equation can reach its steady state solution:

$$S_0 = \frac{k_f}{k_f + k_{ex}} \Rightarrow S_1 = 1 - S_0 = \frac{k_{ex}}{k_{ex} + k_f}$$

Equation App 6

The fluorescence intensity is proportional to the number of excited fluorophore and is equal to:

$$I_{fl} = \phi_f \cdot k_f \cdot S_1$$

Equation App 7

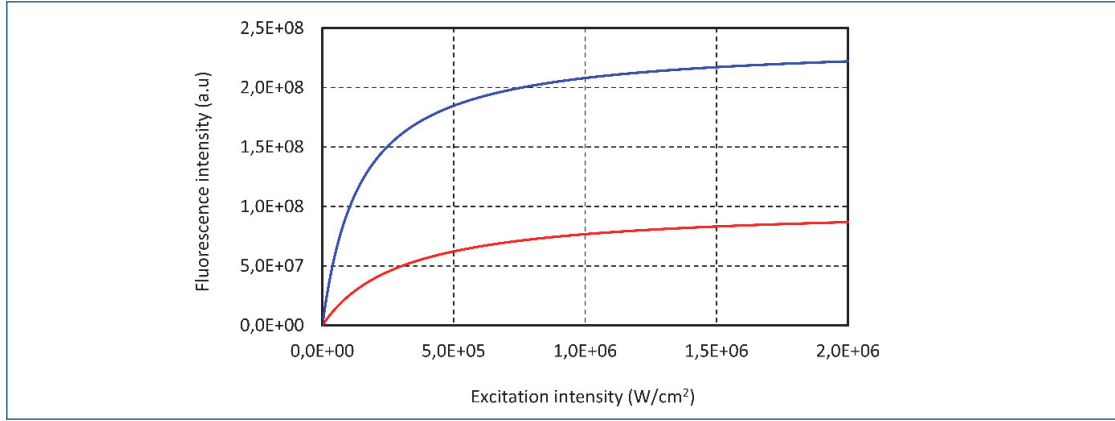
With Φ_f the fluorescence quantum yield, which is different for each the fluorophores. Here, we consider a perfect emitter with a quantum yield equal to 1 therefore the fluorescence signal is equal to:

$$I_{fl} = k_f \cdot S_1 = \frac{k_f k_{ex}}{k_{ex} + k_f} = \frac{k_f \sigma_{abs} I_{exc}}{k_f + \sigma_{abs} I_{exc}} = \frac{\sigma_{abs} I_{exc}}{1 + \sigma_{abs} \tau I_{exc}}$$

Equation App 8

This is the Equation 5-12 in the main text.

As an example we show in the Figure_app 2 the saturation characteristic curve of a Nitrogen Vacancy into diamond crystal. ($\tau=10$ ns, $\sigma_{abs}=1 \cdot 10^{-16}$ cm²) and Texas Red ($\tau=4.2$ ns, $\sigma_{abs}=5 \cdot 10^{-16}$ cm²).



Figure_app 2 Fluorescence signal intensity (a.u) in function of the excitation intensity (W/cm2). Red curve: NDs, Blue curve: Texas red.

The model is in good agreement with the experimental curve shown in the main text in Figure 4-6 (a).

Pulsed excitation:

In the case of pulse excitation the pulse width is comparable with typical fluorescence decay time, so the transient regime has an important role. In consequence we derive again the saturation curve but taking into account the influence of the pulse width. We approximate the pulsed excitation by a periodic train of square pulses (Figure_app 1 (b)). Therefore, we assume a constant approximation rate k_{ex} during the pulse duration (T_p) and a constant fluorescence rate k_f . The repetition period is noted T_{rep} .

So during the pulse excitation ($0 \leq t \leq T_p$), we have the same initial equation described above:

$$S_{0,pulse}(t) = \frac{k_f}{k_f + k_{ex}} \left(1 + \alpha e^{-(k_{ex} + k_f)t} \right)$$

Equation App 9

And, after the pulse, $k_{ex}=0$, so for ($T_p \leq t \leq T_{rep}$), we have:

$$\frac{dS_0}{dt} = +k_f [1 - S_0] \Rightarrow S_{0,relax}(t) = \left(1 + \beta e^{-k_f t} \right)$$

Equation App 10

In order to determine the coefficients α and β we assume that the interpulse time is long enough to let the molecule entirely relax. Hence we have the boulder conditions:

$$S_{0,pulse}(0) = S_{0,relax}(T_{rep})$$

$$S_{0,pulse}(T_p) = S_{0,relax}(T_p)$$

Equation App 11

The solution of those equation is:

$$\alpha = \frac{(e^{k_f T_p} - e^{k_f T_{rep}}) k_{ex}}{(e^{(-k_{ex}-k_f)T_p + k_f T_p} - e^{k_f T_{rep}})(k_{ex} + k_f)}$$

$$\beta = \frac{e^{k_f T_p + k_f T_{rep}} (-1 + e^{(-k_{ex}-k_f)T_p}) k_{ex}}{(e^{(-k_{ex}-k_f)T_p + k_f T_p} + e^{k_f T_{rep}})(k_{ex} + k_f)}$$

Equation App 12

The fluorescence intensity is proportional to the number of excited fluorophore, so we calculate the average probability of the fluorophore to be in the excited state during the laser cycle:

$$\overline{S_1} = \frac{1}{T_{rep}} \int_0^{T_{rep}} (1 - S_0(t)) dt$$

Equation App 13

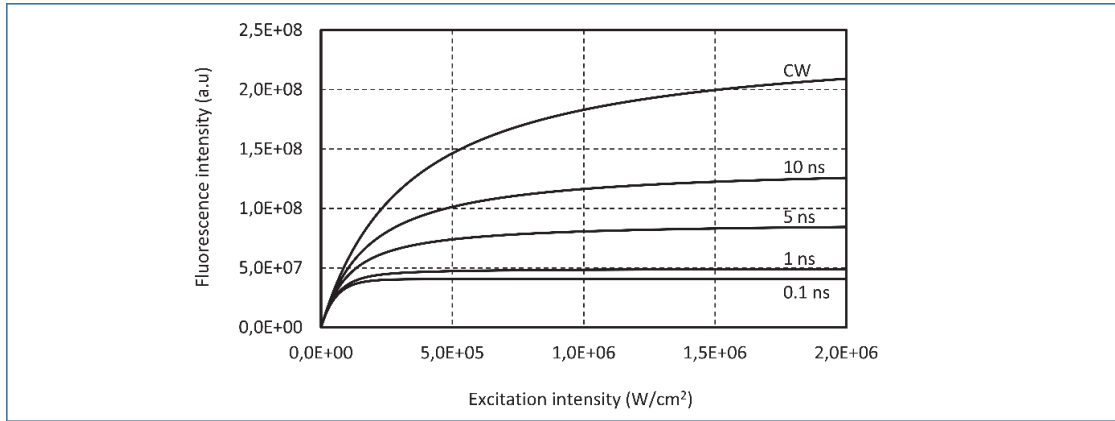
Which leads to the fluorescence intensity (with a quantum yield equal to 1):

$$I_{fl} = \phi_f \cdot k_f \cdot \overline{S_1} = \frac{e^{(-k_f T_p)} \left(e^{k_{ex} T_p + k_f (T_p + T_{rep})} k_{ex} (k_{ex} + k_f (k_{ex} + k_f) T_p) - k_{ex} \left(e^{(k_{ex} + 2k_f) T_p} k_{ex} + e^{k_f T_{rep}} k_{ex} + e^{k_f T_p} (-k_{ex} + k_f (k_{ex} + k_f) T_p) \right) \right)}{(-1 + e^{k_{ex} T_p + k_f T_{rep}}) (k_{ex} + k_f)^2 T_{rep}}$$

Equation App 14

This is the Equation 2-19 in the main text.

In the Figure_app 3 we show the saturation curve for Atto 647N ($\tau=4.1$ ns, $\sigma_{abs}=3.1 \cdot 10^{-16} \text{cm}^2$) excited with a laser with a repetition rate of 40MHz and different pulse widths:



Figure_app 3 Fluorescence signal intensity (a.u) in function of the average excitation intensity (W/cm²). $\overline{I_{exc}} = \sigma_{abs} \cdot I_{ex} \cdot T_{rep}/T_p$. Pulse width: 100ps, 1ns, 5ns, 10ns, CW.

Appendix C: Complete expression Gauss Laguerre modes.

We introduced the Double Helix wavefront in Chapter 3, through the concept of rotating beam that we decomposed in the Gauss-Laguerre modes. We give here the complete expression of the Gauss-Laguerre solutions to the paraxial equation:

$$U_{n,m} = G(\hat{\rho}, \hat{z}) R_{n,m}(\hat{\rho}) \Phi_m(\varphi) Z_n(\hat{z})$$

Equation App 15

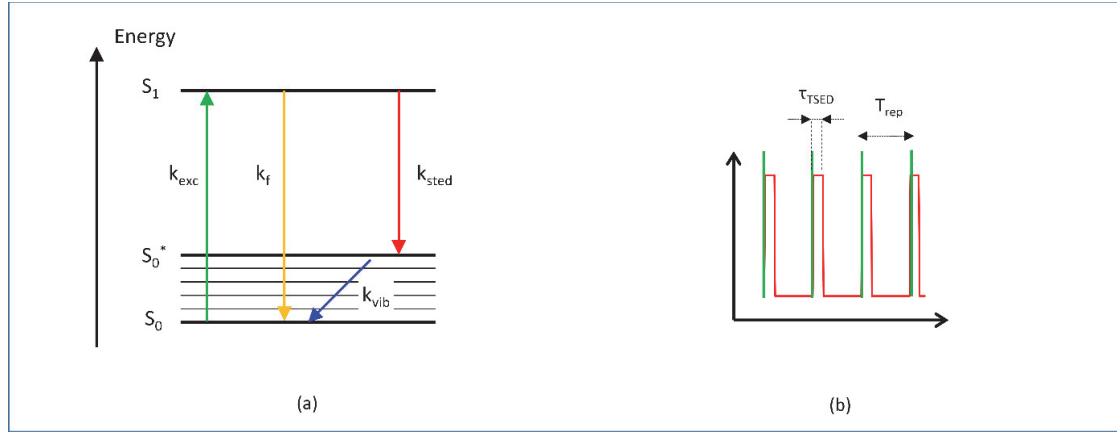
$$\text{where } \left\{ \begin{array}{l} G(\rho, z) = \frac{w_0}{w(\hat{z})} e^{-\hat{\rho}^2} e^{i\hat{\rho}^2 \hat{z}} e^{-i\psi(\hat{z})} \\ R_{n,m}(\hat{\rho}) = (\sqrt{2}\hat{\rho})^{|m|} L_{(n-|m|)/2}^{|m|}(2\hat{\rho}^2) \text{ with } L_{(n-|m|)/2}^{|m|} \text{ generalized Laguerre polynomial.} \\ \Phi_m(\varphi) = e^{-im\varphi} \\ Z_n(\hat{z}) = e^{-in\psi(\hat{z})} \end{array} \right.$$

$$\text{with } \left\{ \begin{array}{l} \hat{\rho} = \frac{\rho}{w(\hat{z})} \\ w(\hat{z}) = w_0 \sqrt{1 + \hat{z}^2} \\ \hat{z} = \frac{z}{z_0} \\ z_0 = \frac{\pi w_0^2}{\lambda} \\ \psi(\hat{z}) = \arctan(\hat{z}) \end{array} \right.$$

The notations follows the one in [114].

Appendix D: Influence of pulse width on depletion efficiency.

In order to derive the analytical expression that describes the Stimulated Emission Depletion process with pulsed laser, we consider a three-level model [58] (Figure_app 4). As for Appendix B, the fluorophore ground state is noted S_0 and the excited state S_1 . From the excited state S_1 , the fluorophore can transit to S_0 either via spontaneous decay with a rate k_f either be sent to a higher vibrational level S_0^* via stimulated emission. The subsequent vibrational transition occurs with a rate k_{vib} .



Figure_app 4 (a) Jablonski diagram illustrating the transition involved in STED microscopy. k_{exc} and k_{sted} are the absorption rate for the excitation beam and the depletion beam respectively, k_f is the spontaneous fluorescence emission rate, k_{vib} is the a rate of the non-radiative transition between vibrational sub level. (b) The pulse train is composed of two lasers with repetition rate $1/T_{rep}$, the excitation laser is assumed to have infinitely short pulse and the depletion laser has a pulse width τ_{STED} .

Here, we consider an instantaneous excitation pulse followed with a depletion pulse lasting for τ_{STED} and a pulse intensity I_{sted} . The lasers have a repetition rate $1/T_{rep}$. During the depletion pulse, the corresponding population rate equations are (the equations take also into account the undesired excitation from S_0^* to S_1 by the depletion beam itself that is not represented in Figure_app 4):

For $0 \leq t \leq \tau_{STED}$,

$$\frac{\partial S_1}{\partial t} = -k_f S_1 - k_{STED} S_1 + k_{STED} S_0^* \quad \text{Equation App 16}$$

$$\frac{\partial S_0^*}{\partial t} = -k_{vib} S_0^* + k_{STED} S_1 - k_{STED} S_0^* \quad \text{Equation App 17}$$

Where S_0^* and S_1 stand for the probability of finding the molecules in the respective states. Because $k_{vib} \gg k_{STED}$ the equilibrium of the S_0^* population is quasi immediate:

$$0 = -k_{vib} S_0^* + k_{STED} S_1 - k_{STED} S_0^* \Rightarrow S_0^* = \frac{k_{STED}}{k_{STED} + k_{vib}} S_1 \quad \text{Equation App 18}$$

Injecting Equation App 18 into Equation App 16, we obtain:

$$\frac{\partial S_1}{\partial t} = -k_f S_1 - \frac{k_{STED} k_{vib}}{k_{STED} + k_{vib}} S_1 \quad \text{Equation App 19}$$

We assume that the excitation promotes all the fluorophores to the excited state, therefore $S_{1,t < \tau_{STED}}(0) = 1$. The solution is then written:

$$S_{1,t < \tau_{STED}} = e^{-\left(k_f + \frac{k_{STED}k_{vib}}{k_{STED} + k_{vib}}\right)t} \quad \text{Equation App 20}$$

After the depletion pulse the molecules spontaneously relax ($k_{STED} = 0$) and the Equation App 16 becomes:

For $\tau_{STED} \leq t \leq T_{rep}$,

$$\frac{\partial S_1}{\partial t} = -k_f S_1 \Rightarrow S_{1,t > \tau_{STED}} = e^{\frac{k_{STED}k_{vib}}{k_{STED} + k_{vib}}\tau_{STED}} e^{-k_f t} \quad \text{Equation App 21}$$

As in Appendix B, the fluorescence intensity is proportional to the number of excited fluorophore, so we calculate the average probability of the fluorophore to be in the excited state during the laser cycle:

$$\overline{S_1} = \frac{1}{T_{rep}} \left(\int_0^{\tau_{STED}} (S_1(t)) dt + \int_{\tau_{STED}}^{T_{rep}} (S_1(t)) dt \right) \quad \text{Equation App 22}$$

And the corresponding fluorescence intensity is:

$$I_{fl} = \phi_f \cdot k_f \cdot \overline{S_1} = \frac{\phi_f k_f}{T_{rep}} \left(\frac{e^{-\frac{k_{STED}k_{vib}\tau_{STED}}{k_{STED} + k_{vib}} - k_f(T_{rep} + \tau_{STED})} (e^{k_f T_{rep}} - e^{k_f \tau_{STED}})}{k_f} + \frac{(1 - e^{-\frac{(k_{STED}k_{vib} + k_f(k_{STED} + k_{vib}))\tau_{STED}}{k_{STED} + k_{vib}}})(k_{STED} + k_{vib})}{k_{STED}k_{vib} + k_f(k_{STED} + k_{vib})} \right) \quad \text{Equation App 23}$$

In order to quantify the depletion efficiency, we want to calculate the suppression factor (η) (i.e. the fraction of fluorescence which is not depleted). η is given by the ratio $I_{fl}(\tau_{STED}) / I_{fl}(0)$ where $I_{fl}(0)$ is the fluorescence intensity in the absence of depletion beam.

For the undisturbed molecule, we have:

$$I_{fl}(0) = \frac{\phi_f}{T_{rep}} (1 - e^{-k_f T_p}) \quad \text{Equation App 24}$$

Therefore the suppression factor is:

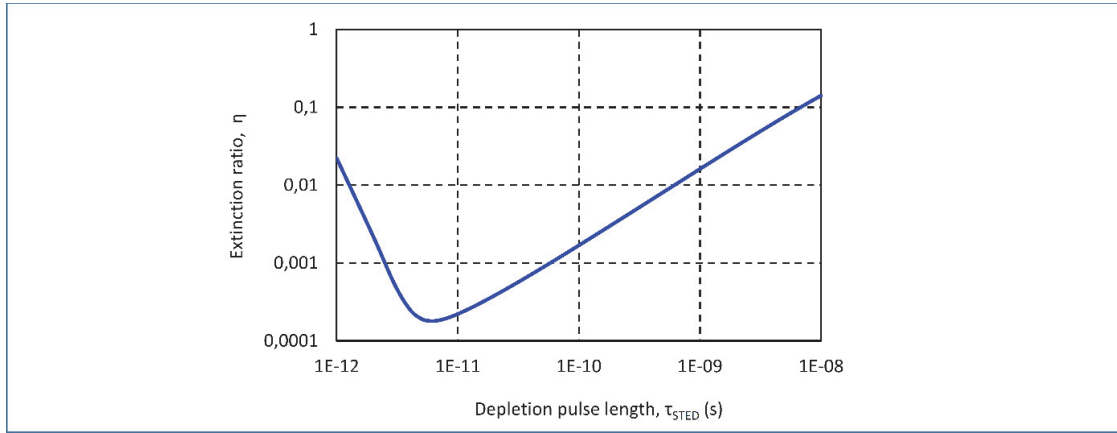
$$\eta = k_f \left(\frac{e^{-\frac{k_{STED}k_{vib}\tau_{STED}}{k_{STED} + k_{vib}} - k_f(T_{rep} + \tau_{STED})} (e^{k_f T_{rep}} - e^{k_f \tau_{STED}})}{k_f} + \frac{(1 - e^{-\frac{(k_{STED}k_{vib} + k_f(k_{STED} + k_{vib}))\tau_{STED}}{k_{STED} + k_{vib}}})(k_{STED} + k_{vib})}{k_{STED}k_{vib} + k_f(k_{STED} + k_{vib})} \right) (1 - e^{-k_f T_p})^{-1} \quad \text{Equation App 25}$$

This analytical expression describes the STED dynamics. The interesting point is then to find the optimal use of the available power.

The average power of the laser is equal to:

$$\langle P_{STED} \rangle = P_{STED, peak} \frac{\tau_{STED}}{T_{rep}} \propto I_{STED} \frac{\tau_{STED}}{T_{rep}} \text{ and } k_{STED} = I_{STED} \sigma_{STED} \text{ (with } \sigma_{STED} \text{ the STED cross section)} \quad \text{Equation App 26}$$

Hence, for a constant laser repetition rate the average power scales linearly with $k_{STED} \tau_{STED}$ which represents the number of potential STED de-excitation during one cycle. Therefore, to estimate the depletion process efficiency we draw the spontaneous emission probability in function of the laser pulse width for a constant $k_{STED} \tau_{STED}$ value. It can be observed in Figure_app 5 that η_{sp} curve goes through a minimum, meaning that there is an optimal pulse width in term of depletion efficiency.



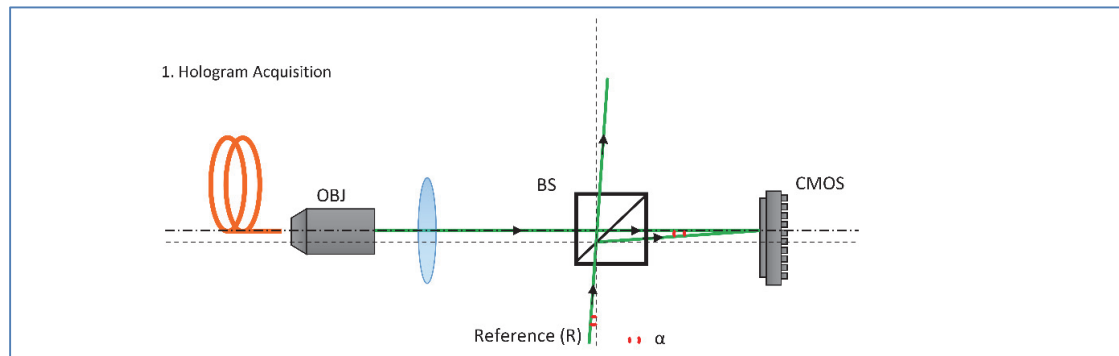
Figure_app 5 Fluorescence depletion efficiency dependence on the depletion width for a constant depletion average power $k_{STED} \tau_{STED} = 16$ $k_{vib} = 5 / (1ps)$ $k_f = 1 / (4ns)$ $T_{rep} = 1 / (80MHz)$.

This curve is identical to the blue curve of Figure 3-18 in the main text and the physical interpretation is done 3.4.1.

Appendix E: Alignment procedure in digital phase conjugation

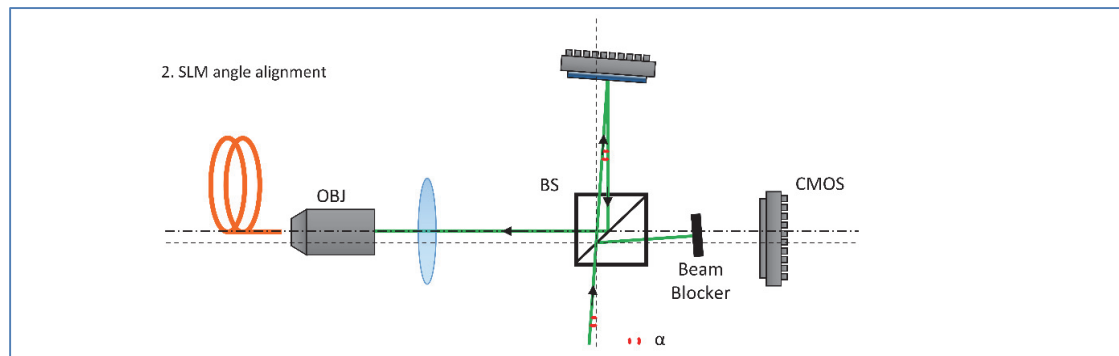
Digital phase conjugation requires a very precise alignment in order to perform the exact back propagation that recomposes the excitation focus. First the modulation device (SLM) and the recording device must be pixel matched to apply the correct phase modulation. Second the SLM angle must be tuned so that the light is sent into the fiber exactly in the opposite direction it escaped during the propagation step. This appendix details the alignment procedure used to achieve digital phase conjugation.

For the translational alignment, both the camera and the SLM are centered onto the beam to match their lateral position (for the SLM a ring pattern is projected and aligned on the edges of the beam). For the angle alignment, the key is to align the beam splitter previously very carefully to be exactly at 45° of the optical axis. Then, the alignment is straight forward: the recorded hologram recorded and the phase conjugated pattern projected on the SLM share the same grating phase pattern induced by the angle between the optical axis and the reference (angle α in Figure_app 6).



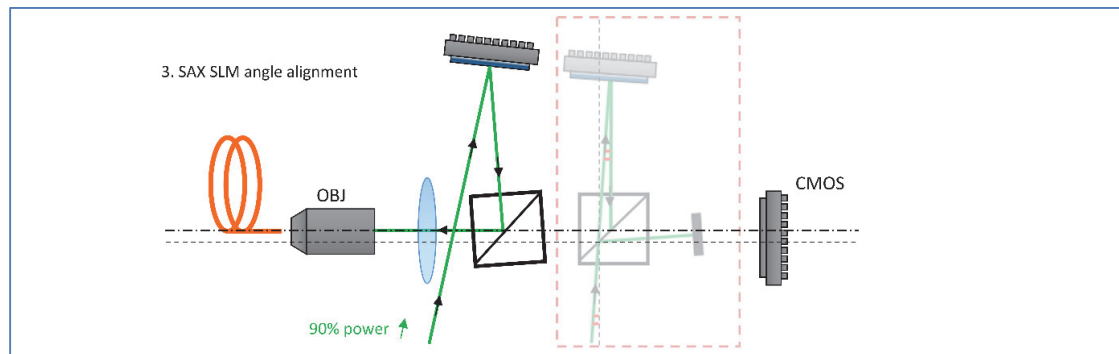
Figure_app 6 Hologram acquisition: the carrier frequency of the hologram is given by the angle between the reference and the optical axis.

Therefore, the field reflected on the SLM with the phase conjugated pattern is deflected by the angle α . In consequence, in order to find the correct angle, the SLM should be tilted so that it is perpendicular to the incoming reference Figure_app 7. It can be done easily by assigning a constant phase on the SLM and with typical iris alignment. Then the phase conjugation pattern is assigned onto the SLM. This procedure has been developed by Y. Papadopoulos and is described in more details in [163].



Figure_app 7 SLM alignment: the SLM surface should be perpendicular to the incident reference beam so that it acts as a phase conjugation mirror.

In our SAX setup, in order to minimize the losses we used two 90/10 beam splitters and avoided the double pass in the central BS. In order to perform the angle alignment we used the above procedure as an intermediate step and then aligned the beam reflected on the second SLM with the one reflected on the first one (Figure_app 8).



Figure_app 8 Alignment of the high power optical line with the help of the first SLM.

Finally the z position of the SLM is optimized manually to maximize the strength of the phase conjugated focus spot.

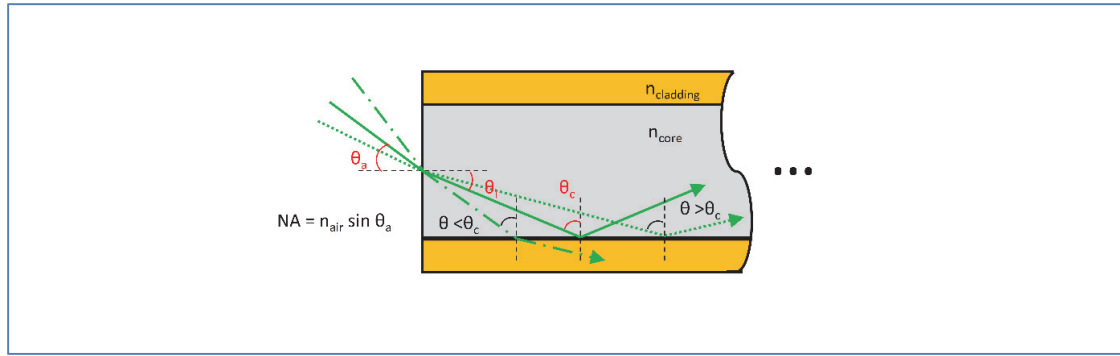
Appendix F: Numerical aperture in MMF

The numerical aperture of the fiber is determined by the maximum angle a ray can enter and propagate into the fiber (so called acceptance angle θ_a).

$$NA = n_{air} \sin \theta_a$$

Equation App 27

Where n_{air} is the external refractive index. We show here, how the numerical aperture relates to the core and cladding refractive indices.



Figure_app 9 The rays propagate through reach the core-cladding interface with an angle superior to the critical angle.

From Figure_app 9, at the interface between the core (n_{core}) and the cladding (n_{clad}) we have (Snell's law):

$$n_{core} \sin \theta_c = n_{clad}$$

Equation App 28

Where θ_c is the critical angle. At the interface air-core we have:

$$n_{air} \sin \theta_a = n_{core} \sin \theta_i$$

Equation App 29

Then, θ_i and θ_c being the two acute angles of a right triangle, we have:

$$\cos \theta_i = \sin \theta_c = \frac{n_{clad}}{n_{core}} \Rightarrow \sin \theta_i = \sqrt{1 - \frac{n_{clad}^2}{n_{core}^2}}$$

Equation App 30

Assuming $n_{air}=1$ and using Equation App 30 in Equation App 29, we have:

$$NA = \sin \theta_a = n_{core} \sqrt{1 - \left(\frac{n_{clad}}{n_{core}} \right)^2}$$

Equation App 31

Therefore, we have the well-known formulae of the numerical aperture of a multimode fiber:

$$NA = \sqrt{n_{core}^2 - n_{clad}^2}$$

Equation App 32

Appendix G: Information confinement in single mode and multimode fiber

We make here the parallel between the number of modes in a multimode fiber and the minimal mode size of a single mode fiber to illustrate both the fact that resolution is only a matter of material indices and the fact that the information that is transmitted into the MMF is optimally constrained. We present here the derivation for the both.

Confinement in single mode fiber: mode radius dependence on the core size.

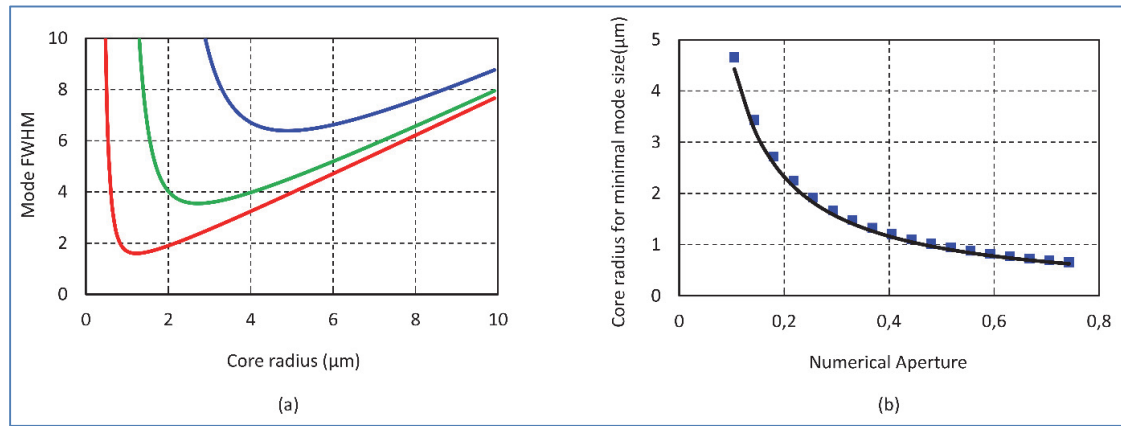
For single mode (step-index) the mode radius is well estimated by the empirical Marcus formulae (p73 of [195] and original paper [196]):

$$\frac{w}{a} \approx 0.65 + \frac{1.619}{V^{3/2}} + \frac{2.879}{V^6} \quad \text{Equation App 33}$$

Where a is the core radius, w the mode radius and V is the V-parameter defined as:

$$V = \frac{2\pi}{\lambda} a \cdot NA = \frac{2\pi}{\lambda} a \cdot \sqrt{n_{core}^2 - n_{clad}^2} \quad \text{Equation App 34}$$

The dependency of the mode radius in function of the core size is shown in Figure_app 10 (a), for constant numerical aperture (i.e. for constant core and cladding refractive indices). For large core, the mode radius decreases with the core radius. However, this is not true for small cores. When the core gets too small, the mode deviates from its approximate Gaussian shape and the mode radius increases. This corresponds to the limit of confinement. We can observe that the core size for the minimum mode radius, follows the rule $0.3\lambda/NA$, which corresponds roughly to a mode size at the usual resolution limit $0.5\lambda/NA$.



Figure_app 10 Minimal mode size in single mode fiber. (a) Mode FWHM for constant NA in function of the core size (blue curve NA=0.1, green curve NA=0.2, red curve NA=0.4). The curves exhibit minima that corresponds to the minimal mode size achievable with a contrast of refractive index. (b) The core size for the minimal mode in function of NA (blue dots), it follows the black curve $0.3\lambda/NA$.

Confinement in MMF: Number of mode dependence on the core size.

As the diameter of a step index fiber is increased, the more modes can propagate into the MMF and it can be shown that the number of guided mode (N) is well approximated by p338 [42]:

$$N = \frac{4V^2}{\pi^2} \quad \text{Equation App 35}$$

The modes are defined by Bessel functions and the higher order modes are less confined in space. However to make the parallel with the single mode fiber in term of information confinement, we can calculate the average core space used for a mode to propagate as the core area divided by the number of mode:

$$\sim \frac{a^2}{N} = \frac{a^2 \pi^2}{4V^2} = \left(\frac{\lambda}{4NA} \right)^2$$

Equation App 36

Therefore, the average mode “core size” as:

$$0.5 \sqrt{\frac{a^2}{N}} = 0.5 \frac{\lambda}{NA}$$

Equation App 37

Hence for large number of mode, the average “core size” used for each mode to propagate is again roughly equal to the classical limit of resolution indicating that the information is optimally confined when propagating in MMF. This optimal confinement results in the same resolution limit that with free space objectives.

Appendix H: Analytical expression of SAX coefficient.

We saw in the Appendix B that in the case of continuous excitation the fluorescence, for a two level Jablonski diagram system the fluorescence intensity can be expressed as:

$$I_{fluor} = \frac{a \cdot I_{exc}}{1 + b \cdot I_{exc}} \quad \text{Equation App 38}$$

So it can be approximate as:

$$I_{fluor} \sim a \cdot I_{exc} - ab \cdot I_{exc}^2 + ab^2 \cdot I_{exc}^3 - ab^3 \cdot I_{exc}^4 \dots \quad \text{Equation App 39}$$

If we consider a modulation:

$$I_{exc}(t) = 0.5 I_{max} (1 + \cos(\omega t)) \quad \text{Equation App 40}$$

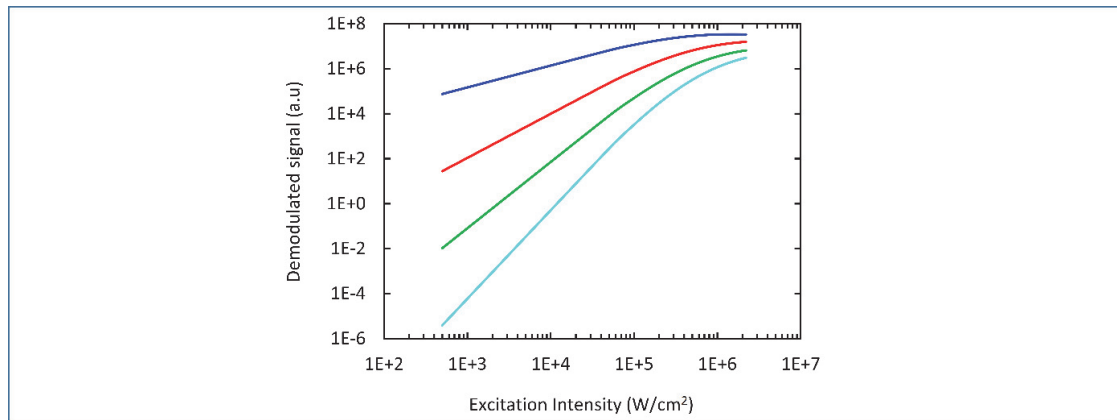
We have:

$$I_{fluor}(t) \sim 0.5a(I_{max} + I_{max} \cos(\omega t)) - 0.25ab(I_{max} + I_{max} \cos(\omega t))^2 + 0.125ab^2(I_{max} + I_{max} \cos(\omega t))^3 - 0.0625ab^3(I_{max} + I_{max} \cos(\omega t))^4 + \dots \quad \text{Equation App 41}$$

Which can be expanded into:

$$\begin{aligned} I_{fluor}(t) \sim & (0.5a I_{max} - 0.375ab I_{max}^2 + 0.3125ab^2 I_{max}^3 - 0.273438ab^3 I_{max}^4) \\ & + (0.5a I_{max} - 0.5ab I_{max}^2 + 0.46875ab^2 I_{max}^3 - 0.4375ab^3 I_{max}^4) \cos(\omega t) \\ & + (-0.125ab I_{max}^2 + 0.1875ab^2 I_{max}^3 - 0.21875ab^3 I_{max}^4) \cos(2\omega t) \\ & + (0.03125ab^2 I_{max}^3 - 0.0625ab^3 I_{max}^4) \cos(3\omega t) \\ & + (-0.0078125ab^3 I_{max}^4) \cos(4\omega t) + \dots \end{aligned} \quad \text{Equation App 42}$$

Hence, the terms that multiply every cosines at the harmonics frequencies can be isolated by demodulation and used for SAX microscopy. The demodulated coefficients are drawn in Figure_app 11 (identical to the Figure 5-14 in the main text).



Figure_app 11 SAX demodulated coefficient in function of the excitation intensity. The fourth first harmonics are represented, blue curve is demodulation at the fundamental frequency f_m , red is $2f_m$, green is f_m and turquoise is $4f_m$.

What must be understood is that the coefficient that can be used depends on the level of saturation. Indeed, as the saturation increases more terms become non negligible, only the last term of the expression that scales with a single power of the excitation intensity can be used. Therefore, experimentally the maximum power the maximum intensity must be chosen carefully, to obtain the maximum signal at the targeted order while keeping the single power dependency.

Curriculum Vitae

CONTACT INFORMATION

Grégoire Laporte,
Chemin des clochetons 18,
1004 Lausanne.
Tel: 00041 (0)215583029

EDUCATION

- High School: Lycée Marc Chagall Reims, France
- University: Ecole Nationale Supérieure de Physique Grenoble (PHELM), France
- Graduate School: Ecole Polytechnique Fédérale de Lausanne, Suisse

PROFESSIONAL QUALIFICATIONS

- Certifications and Accreditations: Master in Optics and Radiofrequency (University Joseph Fourier Grenoble).
- Computer Skills: Matlab, beam propagation method, Comsol, L-Edit, Solid-Works, Mathematica, Labview.

PUBLICATIONS

- Double-helix enhanced axial localization in STED nanoscopy, Optics express, 2013
- Resolution enhancement in nonlinear scanning microscopy through post-detection digital computation, Optica, 2014
- Enhanced resolution in a multimode fiber imaging system, Optics express, 2015
- STED imaging of green fluorescent Nanodiamonds containing Nitrogen-Vacancy-Nitrogen centers, Biomedical Optics Express, under review.

